Cosmic Explosions: Observations Of Infant Hydrogen-Free Supernovae Towards An Understanding Of Their Parent Systems

Thesis by
Yi Cao

In Partial Fulfillment of the Requirements for the
degree of
Doctor of Philosophy

CALIFORNIA INSTITUTE OF TECHNOLOGY
Pasadena, California

2016
Defended 3 May 2016

Yi Cao
ORCID: 0000-0002-8036-84910

ACKNOWLEDGEMENTS

Foremost, I would like to recognize that my thesis work resulted from substantial support by the whole intermediate Palomar Transient Factory collaboration. Without dedication and hard work from everyone in the team, I would not have been able to complete my thesis.

I would like to express my sincere gratitude to my wonderful and unique thesis advisor Prof. S. R. Kulkarni, for creating an environment fulfilled with dedication and hard work, for encouraging me to discover my unique way of researching, for providing guidance, support, and resources to my research and life, and for dispassionate and insightful assessment of strengths and weaknesses. His advice, point of view, and business approach to research and life have helped me become a better person.

I also feel grateful to Prof. Mansi Kasliwal for hands-on instructions on performing astronomic measurements, collaboration on various research projects, discussions on my researches, and patiently and enthusiastically marking up my papers and proposals.

My thank also goes to my co-advisor Prof. Peter Nugent for his guidance, support, and resources on developing the realtime image subtraction pipeline (a core component that enables my thesis), hospitality at the Lawrence Berkeley Lab, and helpful discussions on my research.

Thanks to the iPTF team members, especially Prof. Avishay Gal-Yam, Prof. Eran Ofek, Dr. Iair Arcavi, Dr. Sagi Ben-Ami, Prof. Ariel Goobar, Dr. Joel Johansson, Prof. Brad Cenko, Dr. Andy Howell, Dr. Tom Barlow, Dr. Assaf Horesh, Dr. Daniel Perley, Dr. Sumin Tang, Dr. Adam Miller, and Dr. Lin Yan, for sharing experiences, excitements, passions, and pains.

Thanks to the Caltech astronomy community, especially to my fellow graduate students, for making a home away from home, although I still abstain from eating donuts and drinking alcohol like an American. Thanks to Prof. Judy Cohen, Prof. Fiona Harrison, Prof. Christian Ott, Prof. Sterl Phinney, and Prof. Tom Prince, for serving on my candidacy and defense committees. Thanks to the supporting teams at Palomar Observatory and Keck Observatory for making the observation experience smooth and enjoyable.

Finally, my family. Words are powerless to express my gratitude to my parents for giving birth to me, raising me, and wholeheartedly supporting me at all times, and to my wife for accompanying me, encouraging me, comforting me, and bringing a little angel into our life.

ABSTRACT

Radiation in the first days of supernova explosions contains rich information about physical properties of the exploding stars. In the past three years, I used the intermediate Palomar Transient Factory to conduct one-day cadence surveys, in order to systematically search for infant supernovae. I show that the one-day cadences in these surveys were strictly controlled, that the realtime image subtraction pipeline managed to deliver transient candidates within ten minutes of images being taken, and that we were able to undertake follow-up observations with a variety of telescopes within hours of transients being discovered. So far iPTF has discovered over a hundred supernovae within a few days of explosions, forty-nine of which were spectroscopically classified within twenty-four hours of discovery.

Our observations of infant Type Ia supernovae provide evidence for both the single-degenerate and double-degenerate progenitor channels. On the one hand, a low-velocity Type Ia supernova iPTF14atg revealed a strong ultraviolet pulse within four days of its explosion. I show that the pulse is consistent with the expected emission produced by collision between the supernova ejecta and a companion star, providing direct evidence for the single degenerate channel. By comparing the distinct early-phase light curves of iPTF14atg to an otherwise similar event iPTF14dpk, I show that the viewing angle dependence of the supernova-companion collision signature is probably responsible to the difference of the early light curves. I also show evidence for a dark period between the supernova explosion and the first light of the radioactively-powered light curve. On the other hand, a peculiar Type Ia supernova iPTF13asv revealed strong near-UV emission and absence of iron in the spectra within the first two weeks of explosion, suggesting a stratified ejecta structure with iron group elements confined to the slow-moving part of the ejecta. With its total ejecta mass estimated to exceed the Chandrasekhar limit, I show that the stratification and large mass of the ejecta favor the double-degenerate channel.

In a separate approach, iPTF found the first progenitor system of a Type Ib supernova iPTF13bvn in the pre-explosion *HST* archival mages. Independently, I used the early-phase optical observations of this supernova to constrain its progenitor radius to be no larger than several solar radii. I also used its early radio detections to derive a mass loss rate of $3 \times 10^{-5} M_{\odot}\,\mathrm{yr}^{-1}$ for the progen-

itor right before the supernova explosion. These constraints on the physical properties of the iPTF13bvn progenitor provide a comprehensive data set to test Type Ib supernova theories. A recent *HST* revisit to the iPTF13bvn site two years after the supernova explosion has confirmed the progenitor system.

Moving forward, the next frontier in this area is to extend these single-object analyses to a large sample of infant supernovae. The upcoming Zwicky Transient Facility with its fast survey speed, which is expected to find one infant supernova every night, is well positioned to carry out this task.

PUBLISHED CONTENT AND CONTRIBUTIONS

1. Cao, Y. et al. (2012). " Classical Novae in Andromeda: Light Curves from the Palomar Transient Factory and GALEX". In: *ApJ* 752, pp. 17, doi: 10.1088/0004-637X/752/2/133.

   Y.C. initiated the study, reduced the PTF data, performed the data analysis, and prepared the manuscript.

2. Cao, Y. et al. (2013). "Discovery, Progenitor and Early Evolution of a Stripped Envelope Supernova iPTF13bvn". In: *ApJ* 775, pp. 7, doi: 10.1088/2041-8205/775/1/L7.

   Y.C. built the realtime data processing pipeline that enabled the discovery of the supernova, performed data analysis, and prepared the manuscript.

3. Cao, Y. et al. (2015). "A strong ultraviolet pulse from a newborn type Ia supernova". In: *Nature* 521, 328–331, doi: 10.1038/nature14440

   Y.C. participated in the conception of the project, built the realtime data processing pipeline, reduced and analyzed the data, and prepared the manuscript.

TABLE OF CONTENTS

LIST OF ILLUSTRATIONS

LIST OF TABLES

Chapter 1

INTRODUCTION

A supernova (SN) is a destructive stellar explosion that may briefly outshine the entire galaxy light of its residence. This explosion occurs roughly once per century in a galaxy like our Milky Way. Historical studies have established two major SN explosion mechanisms: thermonuclear explosions of CO white dwarfs (Type Ia) and core collapses of massive stars (Type Ibc and II). Filippenko (1997) provides a general review on spectral evolution of different types of SNe.

Not only do SNe mark the evolutionary endpoints of certain stellar systems, but they are also responsible to synthesize heavy elements in the Universe and to recycle stellar material into the interstellar medium. Thermonuclear SNe have also been extensively utilized for cosmographic distance measurements.

Thanks to various synoptical surveys in the last decade, we have found a few times more SNe than those discovered in the proceeding one thousand years. However, the underlying physical processes that drive SN explosions and that produce the SN observables remain unclear. The fundamental piece of information that underpins our understanding towards these physical processes is the link between progenitor stars and the type of SNe they produce at the end of their lives (see Langer 2012 for a recent theoretical review).

1.1 Fortuitous pre-explosion imaging

Since late 1990's, the SN community has been extensively searching archives for high resolution and deep images of nearby galaxies which host SNe, in order for direct identification of their progenitor stars. In practice, this method usually relies exclusively on availability of pre-explosion images of nearby galaxies taken by *Hubble Space Telescope* (*HST*), as *HST* is the only telescope capable to resolve brightest stars (absolute magnitude > -5 in the visible band) in nearby galaxies up to $\simeq 20\,\mathrm{Mpc}$.

Thermonuclear Supernovae

Recent observations have provided solid evidence that the primary exploding star in a Type Ia SN is a CO white dwarf (Nugent *et al.*, 2011; Bloom *et al.*, 2012). There are two major channels that lead to ignition of unstable CO burning in the white dwarf (Hillebrandt and Niemeyer, 2000; Maoz *et al.*, 2014). In the single-degenerate (SD) channel, a white dwarf accretes material from a non-degenerate companion star, which is either a main-sequence star or a giant. When the mass of the white dwarf approaches an unknown critical value, the resulting increase in its central temperature and pressure ignites thermonuclear runaway that eventually explodes and destructs the whole white dwarf. One possibility of the critical mass here is the Chandrasekhar limit ($\simeq 1.4 M_\odot$ where $M_\odot = 1.99 \times 10^{33}$ g is the solar mass). In the double-degenerate (DD) scenario, two white dwarfs collides or merges in a binary or even a triple system to produce a supernova. Since white dwarfs are very faint, the direct imaging method is to look for the companion star in the SD channel and does not anticipate to detect anything from the DD channel.

In one of the nearest Type Ia SN2011fe (a.k.a. PTF11kly) in M101 at 6 Mpc[1], nothing was found at the location of the SN in pre-explosion *HST* images. The detection upper limit excludes a luminous red giant or anything brighter as a companion star (Figure 1.1; Li *et al.* 2011a). This non-detection together with other observations of SN2011fe favors the DD channel (see Chomiuk 2013 for a review).

More recently, candidates of companion stars in two low-velocity thermonuclear SNe (SNe Iax; Foley *et al.* 2013) are suggested in their pre- or post-explosion *HST* images (McCully *et al.*, 2014; Foley *et al.*, 2014). If verified, both candidates will be the first known companion stars of thermonuclear SNe.

Core-Collapse Supernovae

The existence of pre-explosion images has allowed direct identification of the progenitors of eighteen Type II core-collapse SNe (hydrogen-rich; Figure 1.2). These progenitor stars form a sample to establish a link that final core-collapses of red supergiants produce the most common class of Type II SNe. This observational link shows compatibility with stellar evolutionary model predictions

[1]SN2014J in M82 at 4 Mpc experiences severe extinction due to dust. Therefore the detection upper limit for the progenitor of SN2014J is not as deep as that for the progenitor of SN2011fe.

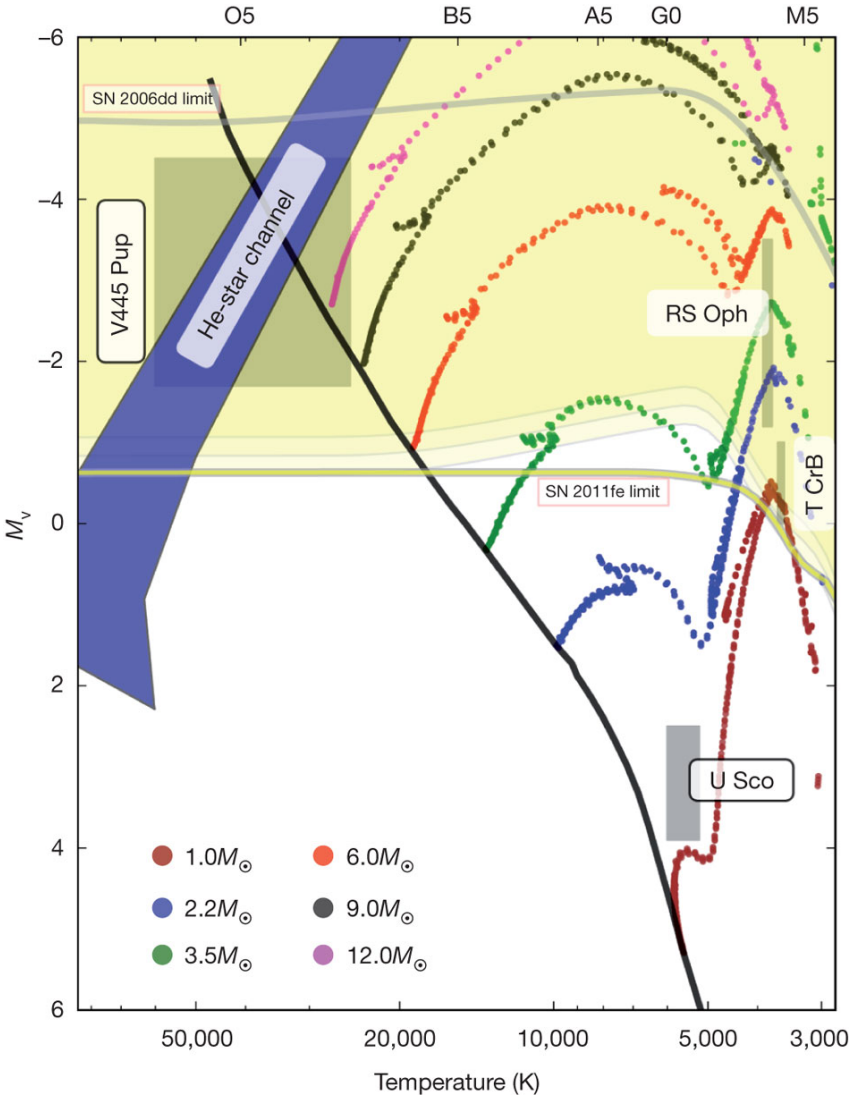

Figure 1.1: Progenitor system constraints of SN2011fe in a Hertzsprung-Russell diagram. The thick yellow line is the 2-σ limit in M_V against effective temperature at the SN location from the *HST* images. Regions of possible Type Ia progenitor systems are also labeled in this figure. [Figure 2 in Li *et al.* (2011a)]

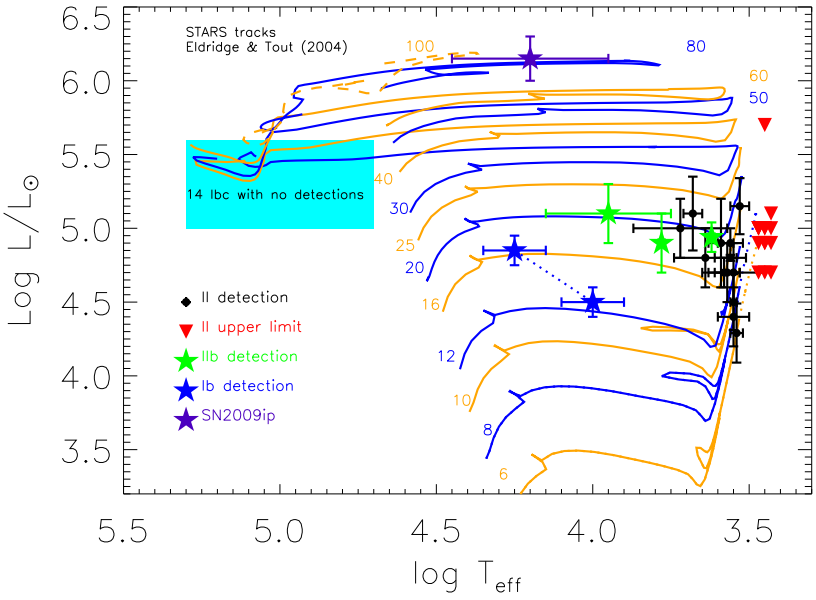

Figure 1.2: The positions of detected progenitors and upper limits to core-collapse SNe in the Hertzsprung-Russell diagram. The stellar evolutionary tracks are from Eldridge and Tout (2004). The two positions of the SN Ib progenitor detection, joined by the dotted line, is for iPTF13bvn which will be discussed in detail in Chapter 6. The non-detection limits for Type Ibc SN progenitor are not quantitatively marked here and are listed in Table 1.1. [Figure 3 in Smartt (2015)]

(see Smartt 2009 and Smartt 2015 for reviews of recent progresses).

More than a dozen nearby Type Ibc core-collapse SNe (hydrogen-free) also have existing archival pre-explosion images. As summarized in Table 1.1, however, no progenitor has been identified in these images. The deepest non-detection limit is $M_B > -4.4$ mag in a Type Ic SN2002ap.

On the theory side, Wolf-Rayet stars have been proposed a long time ago as progenitors of Type Ibc SNe, as they lose their hydrogen and possibly helium envelopes through radiatively line-driven stellar windes (see Crowther 2007 for a review of Wolf-Rayet stars). The detection upper limits of the progenitors in Table 1.1 are consistent with Wolf-Rayet stars in the Milky Way and Magellanic Clouds. An alternative progenitor scenario is less massive helium stars in binary systems which strip off their hydrogen layers through interaction with companion stars (Dessart *et al.*, 2012; Yoon *et al.*, 2012). However, the observational counterpart of these helium star binaries remains

Table 1.1. Detection upper limits of progenitors of Type Ibc SNe in nearby galaxies [Table 4 in Eldridge *et al.* (2013)]

SN	Type	Host	Dist (Mpc)	E(B − V)	$M_{\rm U}$ (mag)	$M_{\rm B}$ (mag)	$M_{\rm V}$ (mag)	$M_{\rm R}$ (mag)	$M_{\rm I}$ (mag)
2000ew	Ic	NGC 3810	18.2 ± 3.3	0.04	···	···	···	−6.81	···
2001B	Ib	IC 391	25.5 ± 2.5	0.14	···	···	−8.25	···	···
2002ap	Ic	NGC 628	9.3 ± 1.8	0.09	−8.85[a]	−4.4[a]	···	−5.5[a]	···
2003jg	Ic	NGC 2997	12.5 ± 1.2	0.11	···	−6.30	···	−6.16	−6.99
2004gn	Ic	NGC 4527	14.2 ± 1.3	0.07	···	···	···	−5.55	···
2004gt	Ibc	NGC 4038	22 ± 3	0.07	−9.15	−7.44	−6.07	···	−7.49
2005V	Ibc	NGC 2146	17.1 ± 3.2	0.90	···	−10.60	···	−8.80	−9.93
2007gr	Ic	NGC 1048	10.6 ± 1.3	0.08	···	−6.7	···	···	−8.6
2010br	Ibc	NGC 4051	12.7 ± 2.0	0.04	···	···	···	−4.92	···
2011am	Ib	NGC 4219	24.5 ± 5.6	0.06	···	···	···	−7.44	···
2011hp	Ic	NGC 4219	24.5 ± 5.6	0.50	···	···	···	−7.46	···
2012au	Ib	NGC 4790	23.6 ± 2.0	0.04	···	−8.0	···	−7.5	−8.6

[a]The broad-band magnitudes are ground-based observations in the standard Johnson-Cousins broad-band filters, i.e., U – $F366W$, B – $F450W$, V – $F555W$, R – $F606W$, I – $F814W$.

in debate (see Yoon 2015 for a recent review on this scenario).

Summary

Given the facts that the volume-limited event rates of Type Ia and Ibc SNe are half and one third of the Type II SN rate (Li *et al.*, 2011c) and that the intrinsic brightnesses of progenitor systems of Type Ia and Ibc SNe are probably much fainter than red supergiants, one may have to wait for a long time before identifying one system in the pre-explosion images to a Type Ia or Ibc SN, not to mention building samples of Type Ia and Ibc progenitors. Therefore, new approaches are warranted to constrain the physical properties of Type Ia and Ibc SN progenitors.

1.2 Physics of infant SNe

Both theoretical and observational results in recent years have shown that SN radiation within a few days of its explosion (infant SN) contains rich information about the physical properties of its progenitor system. In this section, we briefly review recent progress in theory. We will cover the observations of infant SNe in the next section.

In core-collapse SNe and some thermonuclear SNe (for example, Type Ia SNe from the delayed-detonation transition; Piro *et al.* 2010), the SN explosion begins with a SN shock breakout. A radiation-driven shock wave propagates outwards within the progenitor star, which heats up and accelerates the progenitor envelope. Once the photon diffusive timescale in the post-shock region becomes shorter than the shock wave travel timescale, i.e., the opacity in front of the shock drops to $\sim c/v_s$ where c is the speed of light and v_s is the shock wave velocity, the envelope of the progenitor star cannot hold the photons behind the shock any more. As a result, these photons soon break out of the surface of the progenitor, producing a bright flash in X-ray. The rise timescale of the X-ray flash, denoted as $t_{\rm breakout}$, is roughly the light crossing timescale of the progenitor R_*/c where R_* is the radius of the progenitor. For a red supergiant of radius $500R_\odot$ where $R_\odot = 6.955 \times 10^{10}$ cm is the radius of the Sun, $t_{\rm breakout} \sim 20$ min; for a Wolf-Rayet star of radius $5R_\odot$, $t_{\rm breakout} \sim 10$ seconds; for a white dwarf, $t_{\rm breakout}$ is less than a second.

Following the SN shock breakout, the stellar envelope expands and rapidly cools down in a quasi-adiabatic manner. As the photosphere penetrates into the outer shells of the envelope, the radiative energy stored within the envelope

escapes via thermal radiation, leading to an early emission in the ultraviolet (UV) and optical. This early emission has been modeled from both numerical calculations (e.g., Falk, 1978; Ensman and Burrows, 1992; Blinnikov *et al.*, 2000) and analytical models (e.g., Waxman *et al.*, 2007; Rabinak and Waxman, 2011). One of the main advantages of analytical models over numerical calculations is that it provides explicit analytic expressions for the dependence of the emission on model parameters, thus making both the use of observation data for determining model parameters and the identification of model uncertainties much easier and more straightforward. In a simplified analytical model (Waxman *et al.*, 2007), the photospheric temperature $T_{\rm ph}$ of the expanding envelope depends mainly on the progenitor's radius R_* and on the opacity of the enevelop, i.e., $T_{\rm ph}$ approximately proportional to $R_*^{1/4}$. The luminosity L is approximately proportional to $(E/M)R_*$, where E is the explosion energy and M is the ejecta mass. Since SN spectra can be used to infer the chemical composition of the envelop and thus the opacity, we may derive the progenitor radius R_* and the ratio E/M directly from the early UV/optical light curve of a SN. Later, Rabinak and Waxman (2011) extended the model to include a more realistic description of the opacity and its variation with time due to recombination, and to include photon diffusion, which causes the emitted spectrum to deviate from a blackbody. Nakar and Piro (2014) and Piro (2015) also provide analytical expressions of SN emission in this cooling phase for SNe embedded in massless circumstellar shells.

The adiabatic cooling phase ends when the radiative energy from ^{56}Ni decay diffuses to the photosphere. The duration of the cooling phase depends on the location of the shallowest layer where ^{56}Ni is deposited. In a Type Ia or Ibc SN, the cooling phase lasts for hours to a few days.

Furthermore, many SNe are born in close binary systems. For instance, observations of galactic massive O stars show that more than 70% of all massive stars have mass exchange with a companion star and that binary interaction dominates the evolution of massive stars (Sana *et al.*, 2012). In a SD progenitor system of a Type Ia SN, a donor star is also needed to increase the mass of the primary white dwarf. If the companion star remains present at the time of the SN explosion, the SN ejected material will inevitably slam into the companion star immediately after the explosion. This collision produces a luminous X-ray flash from the non-thermal collision process which lasts for

tens of minutes (this X-ray flash is very difficult to capture with current X-ray telescopes), and a diffusive thermal emission that peaks in the UV and decays in a couple of days after the collision (Kasen, 2010). In particular, in a Type Ia SNe, SN-companion collision signatures serve as a "smoking gun" for the SD progenitor channel, as such signatures are not expected in the DD explosions.

1.3 Observations of infant SNe

Previous surveys were optimized with cadences of a few days or longer and to cover large sky areas, in order to discover as many SNe as possible. These surveys were driven partly to explore the diversity of supernovae and other transients (e.g., Kasliwal 2011) and partly to use Type Ia supernovae around peak to measure cosmological distances (e.g., Phillips 1993). Figure 1.3 summarizes cadences and survey depths of some recent transient surveys. As a result of the long cadence, most SNe were discovered around maximum brightnesses in these experiments. The few SNe that were discovered at very early phases were either from serendipitous discovery or from small-scale fast-cadence experiments. Despite the small number of these infant SNe, they have greatly enhanced our knowledge about SNe and their progenitors.

Soderberg *et al.* (2008) reported the serendipitous discovery of a Type Ibc SN2008D at the time of the explosion by *Swift*, as marked by an extremely luminous X-ray outburst, and attributed the outburst to the breakout of the SN shock from the progenitor star. The rise time of the X-ray outburst $t_{\rm breakout} \simeq 63\,{\rm seconds}$ corresponded to a shock breakout radius $ct_{\rm breakout} \sim 10^{12}\,{\rm cm}$. Immediate follow-up observations in the UV, optical and radius allowed the authors to establish the Type Ibc classification of SN2008D and to estimate the radius of the compact progenitor to be $10^{11}\,{\rm cm}$. The authors subsequently attributed the different radii derived from shock breakout timescale and from cooling-phase emission to the circumstellar medium sounding the SN. Since the circumstellar medium was established by last-stage mass loss of the progenitor before the SN explosion, the follow-up X-ray and radio observations allow the authors to estimate a mass loss rate of $10^{-5} M_{\odot}\,{\rm yr}^{-1}$ for the progenitor. Finally, although no progenitor is identified in any pre-explosion image, the authors concluded that the physical properties of SN2008D progenitor, as derived from optical, X-ray and radio observations of the SN in its infant period, are consistent with those of known Wolf-Rayet stars.

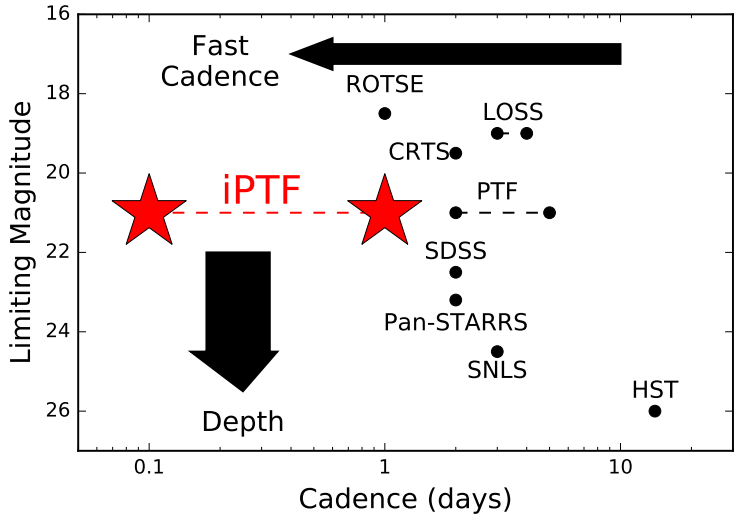

Figure 1.3: Depth versus cadence for iPTF and surveys prior to iPTF. References: ROTSE: the Robotic Optical Transient Search Experiment (Akerlof *et al.*, 2003); LOSS: the Lick Observatory Supernova Search (Li *et al.*, 2000); CRTS: the Catalina Real-time Transient Survey (Drake *et al.*, 2009); PTF: the Palomar Transient Factory (Law *et al.*, 2009); SDSS: the SDSS Supernova Survey (Frieman *et al.*, 2008); Pan-STARRS: transient search in the Pan-STARRS medium deep survey (Rest *et al.*, 2014); SNLS: Supernova Legacy Survey (Astier *et al.*, 2006); *HST*: the *HST* supernova surveys (Riess *et al.*, 2004, 2007); iPTF: the intermediate Palomar Transient Factory (this work).

In another Type Ic SN PTF10vgv, even without direct detection of the cooling phase, Corsi *et al.* (2012) compared the observed light curve and deep pre-discovery non-detection limits, which set upper limits on emission in the cooling phase, against analytical and numerical models of the post-shock-breakout cooling-phase luminosity of a Type Ic SN, and managed to derive an upper limit of $\lesssim 4.5 R_\odot$ on the radius of the progenitor star. Such a tight upper limit rules out giant and supergiant stars as progenitors of this Type Ic SN.

Moreover, in a Type Ia SN2011fe (a.k.a., PTF11kly) discovered only twelve hours after the SN explosion (Nugent *et al.*, 2011), its early emission follows the freely expanding fireball model in which the temperature remains constant and the luminosity increases as $\propto t^2$. Comparing the SN light curve and pre-discovery upper limits to post-shock-breakout emission models, Bloom *et al.* (2012) constrained the radius of the exploding star to be $< 0.02 R_\odot$ (Figure 1.4). Given an ejecta mass of $\sim 1 M_\odot$, the authors derived a mean density of $> 10^5\,\mathrm{g\,cm^{-3}}$ for the progenitor. Such a high density indicates conclusively

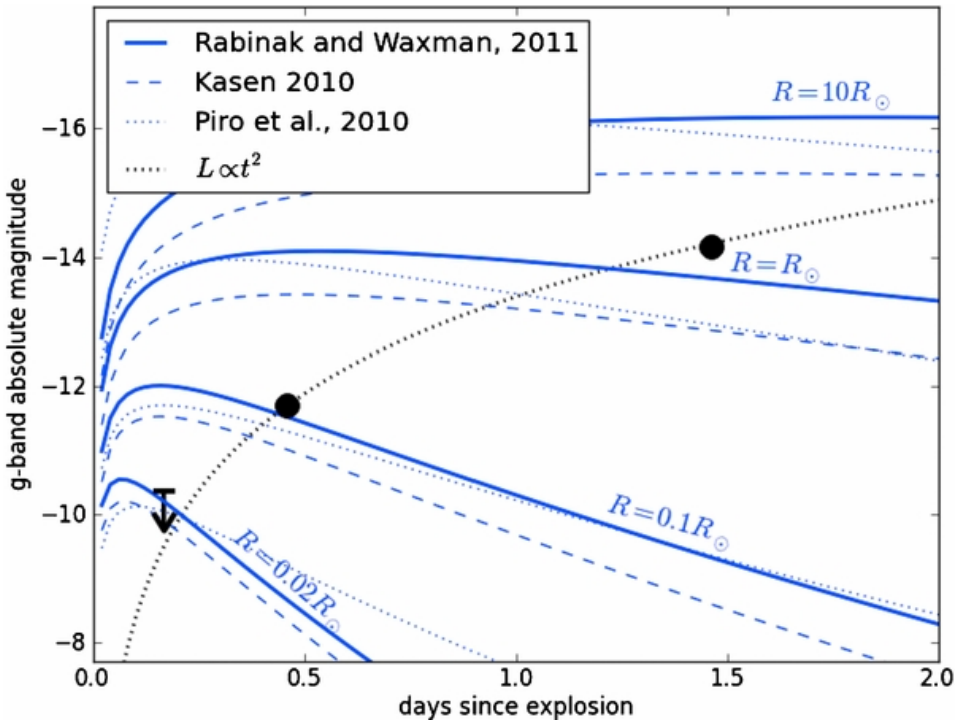

Figure 1.4: Absolute g-band magnitude of SN2011fe versus time since explosion in three theoretical models of the early-time shock-heated evolution of Type Ia SNe. The black line shows the $L \propto t^2$ radioactive-heating behavior seen in later-time PTF data, consistent with the non-detection. The post-shock-breakout emission models are taken from Rabinak and Waxman (2011) and Piro *et al.* (2010).The ejecta mass in these models is assumed to be $1M_\odot$ (a higher ejecta mass will lead to a more compact progenitor). In the (Kasen, 2010) companion interaction model, R denotes the separation distance between the two stars, and the light curve is shown for an observer aligned with the collision axis, which produces the brightest observed luminosity. [Figure 2 in Bloom *et al.* (2012)]

that only a degeneracy-supported compact object, such as a white dwarf, is viable as the primary star of SN2011fe. A caveat here is that the constraint on the progenitor radius depends on the SN explosion date which is derived from extrapolation of its early light curve (Nugent *et al.*, 2011). Piro and Nakar (2014) suggested a dark time of ∼1 day between the SN explosion and the rise of its radioactively powered light curve and hence that the progenitor can be as large as $\sim 1R_\odot$. Furthermore, if SN2011fe arises from a SD system, the early UV observations also allowed Brown *et al.* (2012a) to put a non-detection upper limit on the SN-companion interaction signature, which rules out a solar mass companion at a distance of a few solar radii.

Both theoretical and observational achievements on constraining progenitor properties from observations of infant SNe motivate us to carry out systematic fast-cadence transient surveys. In addition, as shown in Figure 1.3, the sub-day dynamic sky is yet to be explored. As trailblazers, our surveys may uncover surprises in this new phase space.

1.4 Outline of this thesis

In spring and fall observing seasons in 2013 – 2015, I used the intermediate Palomar Transient Factory to conduct fast-cadence transient surveys. Chapter 2 describes the survey designs, operations and performances. Chapters 3, 4, 5 and 6 present observations of three infant Type Ia SNe and one infant Type Ib SN and discuss the implications to their progenitor systems. Chapter 7 summarizes the progress to date with an eye towards the future.

Chapter 2

FAST-CADENCE TRANSIENT SEARCH IN THE INTERMEDIATE PALOMAR TRANSIENT FACTORY†

Yi Cao[1], P. E. Nugent[2,3], M. M. Kasliwal[1]

[1] California Institute of Technology, Pasadena, CA 91125, USA

[2] Department of Astronomy, University of California, Berkeley, CA 94720-3411, USA

[3] Lawrence Berkeley National Laboratory, 1 Cyclotron Road, MS 50B-4206, Berkeley, CA 94720, USA

Abstract

In this paper, we present the fast-cadence transient surveys in the intermediate Palomar Transient Factory systematically search for infant supernovae and fast-evolving transients, including (1) cadence control and field selection of these surveys, (2) the fast-turnaround pipeline that delivers transient candidates within ten minutes of images being taken, and (3) the rapid-response follow-up observations of transients within hours of discovery. In the first three years of operation, we discovered over a hundred supernovae within three days of their explosions. About half of them obtained their first spectroscopic observations on the same night or the night following discovery. Our infant supernova sample provides unique preview into progenitor physics.

2.1 Introduction

In the spring of 2013, we started a new collaboration called the intermediate Palomar Transient Factory (iPTF), after PTF completed its mission at the end of 2012. The new collaboration uses the same hardware as PTF, including the Palomar 48-inch Schmidt telescope (P48) equipped with the CFH12K camera as the discovery machine (Law *et al.* 2009). The CFH12K camera had eleven working CCDs (each has 2048×4096 pixels with $1.01''\,\mathrm{pixel}^{-1}$) and covered $7.26\,\mathrm{deg}^2$ in a snapshot. However, due to an electronic issue, one CCD failed in

†An edition of this chapter is going to be submitted to the *Publications of the Astronomical Society of the Pacific* shortly.

the early spring 2015. This failure reduced the total field of view to $6.60\,\mathrm{deg}^2$. The camera has two filters: Mould R and SDSS g. The exposure time is currently chosen to be 60 seconds. A single snapshot can reach a survey depth of $R \simeq 20.5\,\mathrm{mag}$ or $g \simeq 21\,\mathrm{mag}$ under a median seeing of $2''.0$. The mean overhead time for readout and telescope slew is about 40 seconds.

iPTF implements an end-to-end strategy tailored for infant supernovae (SNe) and fast transients. The nightly cadence is strictly controlled. A fast-turnaround realtime data processing pipeline — which uses high performance computing resources, databases, and machine learning algorithms — delivers transient candidates within minutes of images being taken. We also have pre-approved target-of-opportunity (ToO) programs with a variety of telescopes to perform follow-up observations within hours of transients being discovered.

This paper is organized as follows: Section 2.2 describes the fast discovery and follow-up procedures. Then Section 2.3 summarizes science performance of the fast-cadence surveys. Finally, Section 2.4 summarizes important lessons learned from iPTF with an eye towards the upcoming Zwicky Transient Facility (ZTF).

2.2 Operation and performance

Given the weather pattern at Palomar Observatory and the location of the Milky Way on the sky as well as moon constraints, we undertake the fast-cadence transient surveys during dark and grey periods in spring and fall observing seasons[1]. In each observing season (about four months in length), we monitor a selected list of fields with P48 multiple times every night in either g or R band. The multiple visits in every single night allow us to detect intra-night variation of transients and moving object. In every observing season, only one filter is used to avoid filter exchange and to maximize the light curve information in a single band (color information is collected by follow-up observations).

Figure 2.1 presents an overview of the iPTF data flow. Immediately after each exposure, the images are transferred to both the National Energy Research Scientific Computing Center (NERSC) and the Infrared Processing and Analysis Center (IPAC). NERSC hosts a realtime image subtraction pipeline for

[1]The bright time of each month is used to survey galaxies within 200 Mpc with Hα filters (Kasliwal 2011; Cook et al. in prep.).

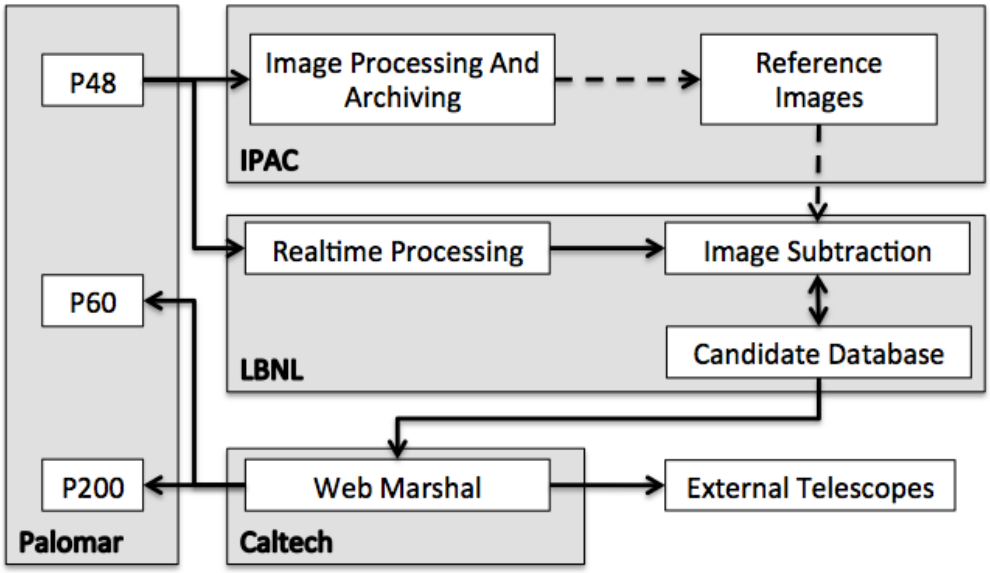

Figure 2.1: **iPTF data flow.** The solid arrows represent realtime activities while the dashed arrows represent post-night activities.

fast turnaround discovery of transients, and IPAC performs detailed post-night processing and archives images. IPAC also provides high-quality stacked reference images for the NERSC pipeline. Once a transient candidate is identified from the NERSC pipeline, we immediately undertake comprehensive follow-up observations with the 60-inch and 200-inch telescopes at Palomar Observatory as well as other ground-based and space telescopes.

A transient survey consists of three independent and equally important components: cadence and area, transient identification and follow-up observations. In the following, we describe these three components for our fast-cadence survey.

Cadence And Area

About 80% of P48 time in spring and fall is used to perform several different fast-cadence transient surveys, as summarized in Table 2.1. In these surveys, the nightly cadence is strictly maintained. The interruption to our cadence includes bad weather, other observation programs that uses the remaining 20% telescope time, and occasional P48 ToO triggers for GRBs (Singer *et al.*, 2015) and LIGO events (Kasliwal *et al.*, 2016). In order to minimize the impact from observations of other experiments, we manually set up a fixed nightly observing schedule for each lunation.

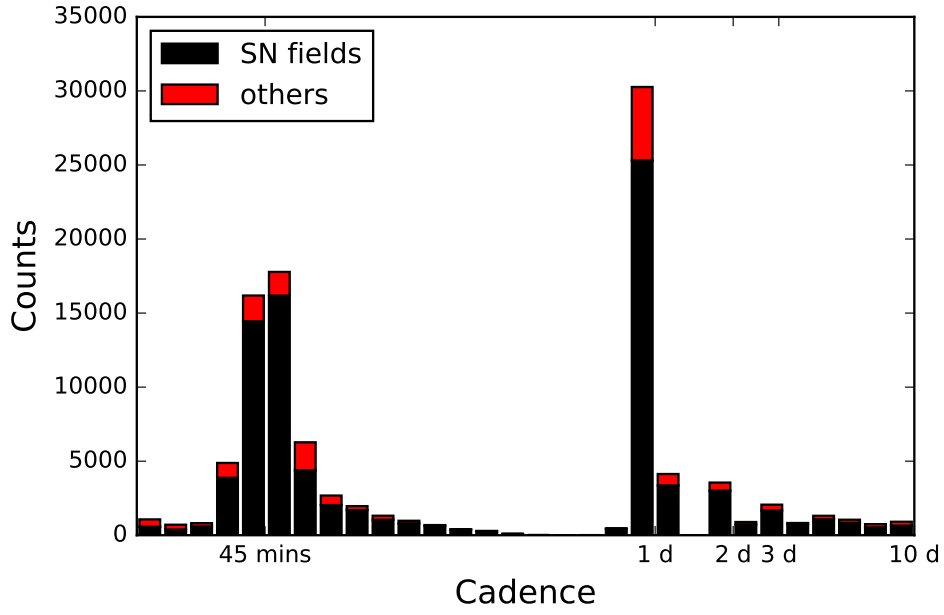

Figure 2.2: **Histogram of time intervals for adjacent visits to a same field.** The x-axis is in a logarithmic scale with a bin width is $10^{0.1}$ day.

Figure 2.2 presents a histogram of the actual time intervals between two adjacent visits of same fields for all P48 observations, including both SN surveys and other programs on the same telescope. In this histogram, the broad peak around 45 min reflects the intra-night revisit timescales. The narrow and sharp peak at 1 day is the designed nightly cadence, which shows that the cadence is controlled strictly. The histogram also illustrates that observations from other experiments have small impact to the SN surveys.

For a fixed amount of telescope time, cadence and survey area are mutually repelling factors. The faster the survey cadence, the smaller the survey area. A useful parameter to quantify the effective survey area for a given time baseline τ is the total sky area Ω that is visited twice separated by τ. Then the expected rate for a given type of events is $\Omega\tau f$ where f is the surface rate density of such events. The theoretical value of $\Omega(45\ \mathrm{min})$ and $\Omega(1\ \mathrm{day})$ for a perfect weather-free experiment that visits every field twice every night can be estimated as follows: each season has roughly four months, and in each month our survey is undertaken for 25 nights (except for five nights around full moon). Given the exposure time and overhead of the camera, in an average night in spring or fall, P48 takes 300 individual exposures and equivalently monitors 150 fields.

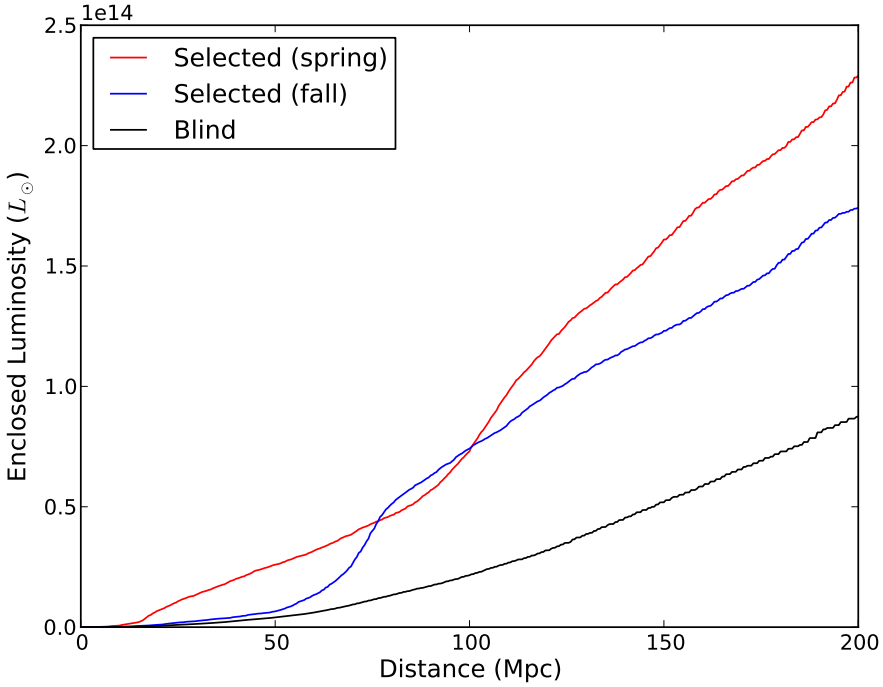

Figure 2.3: **Enclosed B-band luminosities of the selected survey fields as a function of distance in spring and fall 2013.** In comparison, the enclosed B-band luminosity for blind pointings is shown in black.

Therefore, with 11 CCDs,

$$\Omega(\tau = 45 \text{ min}) = 7.26\,\text{deg}^2 \times 150 \times 25 \times 4 = 1.09 \times 10^5\,\text{deg}^2 \ , \tag{2.1}$$

$$\Omega(\tau = 1 \text{ day}) = 7.26\,\text{deg}^2 \times 150 \times 24 \times 4 = 1.04 \times 10^5\,\text{deg}^2 \ , \tag{2.2}$$

where the first term in the expressions is the P48 field of view, the second is the total number of fields, the third is the number of visit pairs separated by τ, and the fourth is the length of an observing season in months. With 10 CCDs, $\Omega(\tau = 45 \text{ min}) = 9.90 \times 10^4\,\text{deg}^2$ and $\Omega(\tau = 1 \text{ day}) = 9.50 \times 10^4\,\text{deg}^2$. We compare these theoretical values to actual values computed in Table 2.1 and find that our actual values are about 30%–50% of the ideal values. Since the impacts from non-SN observations are negligible (Figure 2.2), we conclude that the weather at Palomar deteriorates our cadence performance by a factor of 50%–70%.

Our field selection is optimized in two ways. In spring and fall 2013, we used a Census of the Local Universe (CLU) catalog for galaxies within 200 Mpc

Table 2.1. Transient surveys

Observing season	Nightly epochs	Filter	Ω(45 min) (deg^2)	Ω(1 day) (deg^2)
2013 Spring	3	Mould R	8.65×10^4	4.15×10^4
2013 Fall	2	Mould R	7.55×10^4	4.37×10^4
2014 Spring	2	Mould R	6.04×10^4	5.41×10^4
2014 Fall	2	SDSS g	4.19×10^4	2.96×10^4
2015 Spring	2	SDSS g	4.01×10^4	3.07×10^4
2015 Fall (until Nov 1, 2015)[a]	2	SDSS g	2.42×10^4	1.85×10^4

[a]Analysis in this paper was performed with data taken between Feb 1, 2013 and Nov 1, 2015.

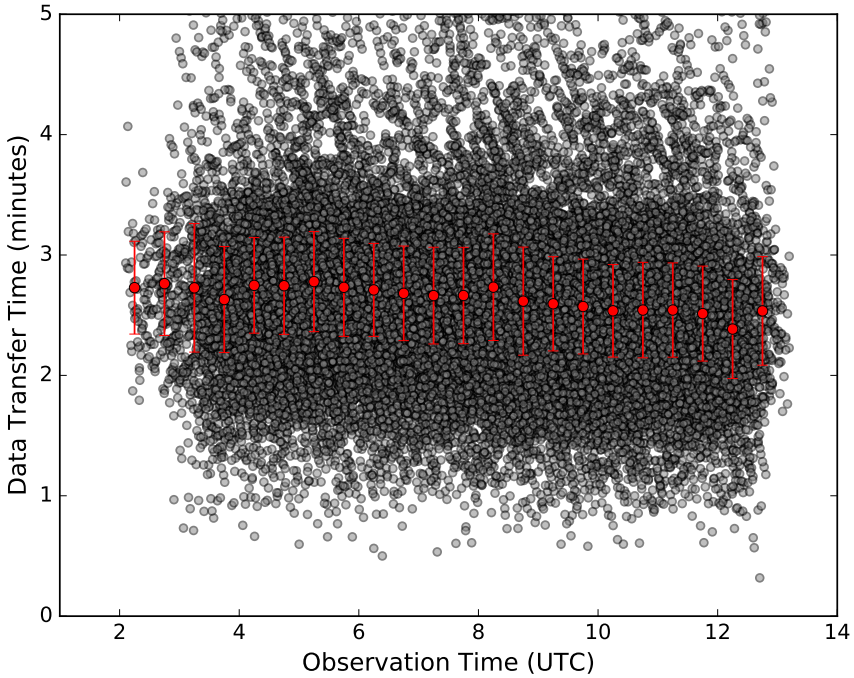

Figure 2.4: **Data transfer time from Palomar Observatory to NERSC.** Individual measurements of the data transfer time as a function of observation time are shown in gray. The median data transfer time in each 0.5 hour bins with its median absolute deviation is shown in red.

(Kasliwal 2011; Cook et al. in prep.) to maximize the included B-band luminosity in the fields. This selection enhances the rates of events related to massive stars. Figure 2.3 shows the B-band luminosity gain as a function of distance in these two seasons. Alternatively in the other observing seasons, we select continuous tiles of fields to cover galaxies in a wide range of stellar mass and star formation rates, in order for unbiased sampling of events in different environments.

Discovery

Upon completion of each P48 exposure, a pack of CCD images is immediately transferred via high-speed microwave links to the San Diego Supercomputer Center and then to both NERSC and IPAC via Internet. The median time for data transfer from Palomar Observatory to NERSC is 2.6 mins with a distribution shown in Figure 2.4. We find slightly longer transfer time in the first half of a night than in the second half, probably due to human activities.

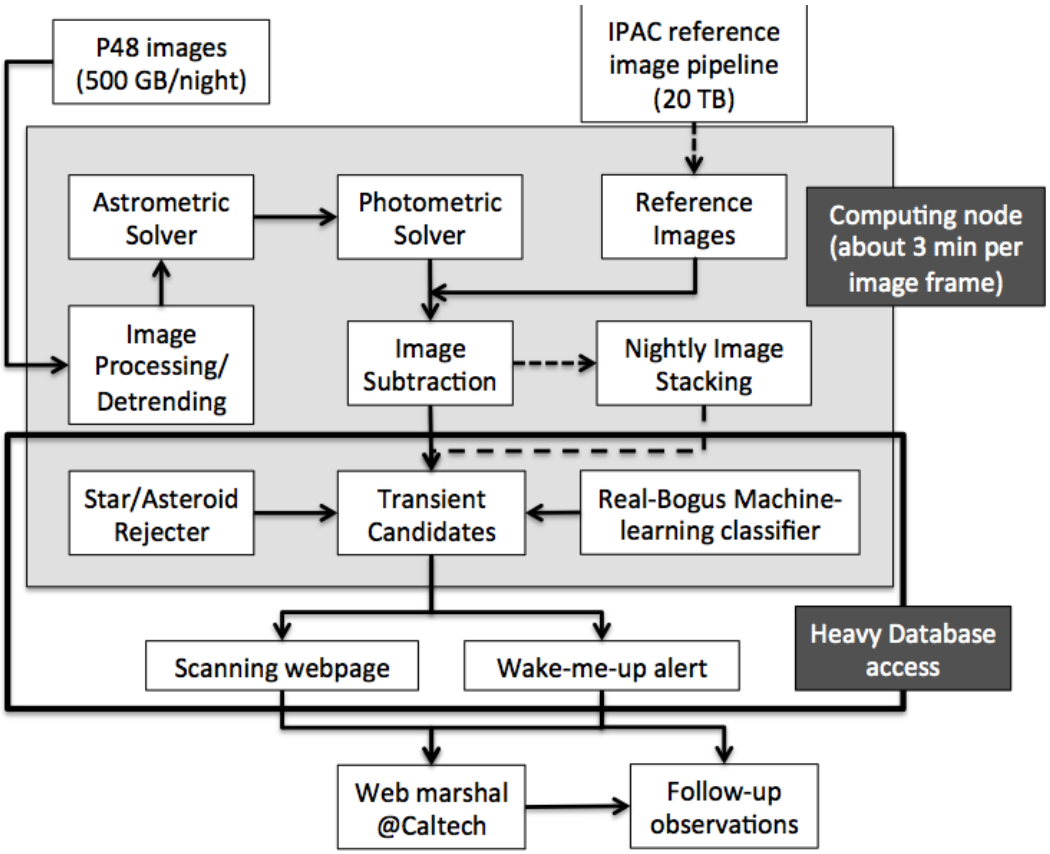

Figure 2.5: **Overview of the NERSC image subtraction pipeline.** The gray region highlights the realtime pipeline running on the NERSC supercomputer. The black box highlights intercommunication to the database. Solid arrows represent realtime operations and dashed arrows represent post-night operations in the pipeline.

Upon arrival of these images at NERSC, our automated image subtraction pipeline processes them and displays transient candidates on an internal webpage for further examination and follow-up within several minutes.

NERSC Realtime Image Subtraction Pipeline

The NERSC realtime image subtraction pipeline makes uses of high-performance computing resources, high-speed I/O filesystems, efficient databases, and advanced algorithms to minimize the false positive rates and to shorten the turnaround time between observations and actual discoveries. Figure 2.5 provides a schematic view of the NERSC pipeline.

The top level of the pipeline is a scheduler program. It recognizes new images upon arrival, submits a processing job for each received pack of images to

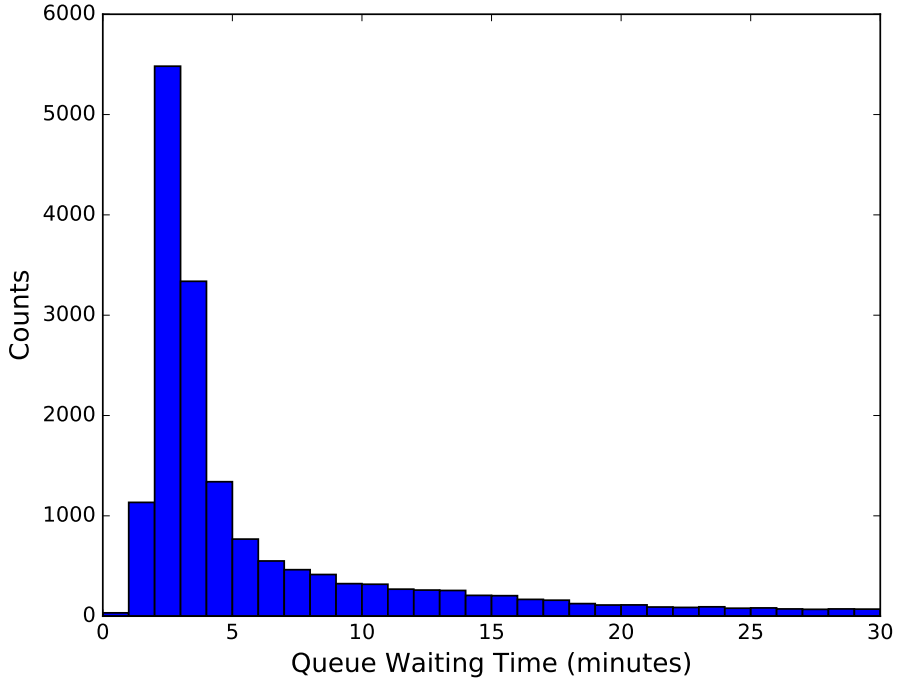

Figure 2.6: **Histogram of wait time at NERSC.** This wait time includes wait times in both the pipeline scheduler and the supercomputer queuer.

the supercomputer queue, monitors the total number of concurrent processing jobs in order to not overload the database, and logs the nightly processing activities. It also archives raw and processed data to the tape and generates processing reports at the end of a night. Upon submission of a processing job, based on the job priority, the supercomputer queuer allocates a computing node with multiple CPU cores for the job.

Both the pipeline scheduler and the supercomputer queuer have response latency times. In order to minimize the former latency, the pipeline scheduler runs every 30 seconds during the night. For the latter, we have acquired a special supercomputer queue with dedicated computing nodes from NERSC to minimize the wait time in the supercomputer queue. As shown in Figure 2.6, most processing jobs can be executed within five minutes of images being received at NERSC.

At each computing node, the processing job allocates a child process for each individual CCD image with one CPU core and sufficient memory. In this case, all CCD images of an exposure are processed almost in parallel, with an

exception for the astrometric solver which has to run serially. In the following, we describe major steps in the image subtraction pipeline:

- **Image preprocessing** – We perform routine procedures of overscan subtraction, bias subtraction and flat-field correction to each raw image. The bias and flat-field frames are generated every ten days by a separate program that runs in parallel in the daytime. For each CCD, this program stacks most recent 100 bias images to make a super bias, and also stacks most recent 100 science images in g or R filters to make super flats in these filters.

- **Astrometric and photometric solvers** – Given that each CCD covers $0.57^\circ \times 1.15^\circ$ sky area, the software `astrometry.net`[2] with appropriate index files is well suited to solve the astrometry. The success rate of `astrometry.net` is $> 99\%$ and the resulting astrometric solution is accurate to about half a pixel. The disadvantage here is that the current version of `astrometry.net` does not support parallel computing. Running an independent process of `astrometry.net` for each CCD image would require an unaffordable large memory and could also be delayed by the memory access speed. Here we are forced to synchronize all child processes after image preprocessing to run `astrometry.net` on a single CPU core in serial. After the astrometric solver, each child process extracts a catalog with the software `SExtractor`[3] for sources with signal-to-noise ratios (SNRs) > 20 in order to calibrate the photometry with respect to the PTF-IPAC catalog (Ofek *et al.*, 2012b). A median zero-point across each CCD image is then calculated. A caveat here is that some CCD images may have non-negligible spatial variation in the zero-point (Ofek *et al.*, 2012a).

- **Image registration** – In preparation for image subtraction, we solve the relative astrometry of the science image with respect to its corresponding reference image by matching their `SExtractor` catalogs with the software `Scamp`. `Scamp` works best for catalogs down to similar depth, so we truncate the reference catalog at the limiting magnitude of the science image. Using the updated astrometric solution, we resample the

[2] `astrometry.net` is available at `http://astrometry.net`.

[3] `SExtractor`, `Scamp` and `SWarp` are available at `http://www.astromatic.net`.

reference image to the same pixel coordinate system of the new image with the software `SWarp`.

- **Image subtraction** – We perform image subtraction between the new image and resampled reference image by using point spread function (PSF) matching with the software `HOTPANTS`[4]. In order to minimize the noise, the PSF on the resampled r eference image is convoluted into the PSF on the new image with a PSF convolution kernel. The convolution kernel is parameterized by linear combination of Gaussian basis functions with different widths, and is built with a list of image stamps centered at high-SNR stars across the image. These high-SNR stars are pre-selected from the `SExtractor` catalog. `HOTPANTS` also models low-spatial-frequency variation of PSFs on both images with low-order polynomials. The input `HOTPANTS` parameters are listed in Table 2.2. Since our primary goal here is to detect transients, we only perform positive subtraction, i.e., subtracting the reference image off from the new image. Transient candidates with SNR$>$ 5 are extracted from the subtracted images with `SExtractor`.

- **Real-bogus classification** – Misalignment of astrometric solutions, imperfect convolution kernels, Poisson noises of bright objects, cosmic rays, and defects in the reference images may produce artifacts in the resulting subtracted images. In order to remove these image-based artifacts, we developed a real-bogus classifier using a supervised random forest algorithm. The classifier utilizes 42 features derived from `SExtractor` outputs. The "real" training set consists of detections of variable stars and spectroscopically classified supernovae, and the "bogus" set is selected randomly in our candidate database and confirmed by visual inspection. This classifier achieves a 1% false positive rate at a cost of 5% false negative rate (Brink *et al.*, 2013; Rebbapragada *et al.*, 2015).

- **matching to external catalogs** – After cleaning artifacts in each the transient candidate list, the main contaminations are real celestial objects, including asteroids, variable stars and active galaxy nuclei (AGNe). Thus we further cross-match the transient candidates to the minor planet

[4] `HOTPANTS` is available at `http://www.astro.washington.edu/users/becker/v2.0/hotpants.html`

catalog and the SDSS spectroscopic catalogs for stars and AGNe. Recently, a new random-forest star-galaxy separator is developed on IPAC reference images, which uses `SExtractor` features and which is trained by spectroscopically confirmed stars in SDSS (Miller et al. in prep.), to reject variable stars outside the SDSS footprints. Additionally, since the absolute magnitude and environment of a transient candidate also provide valuable information about the nature of the transient, we spatially associate transient candidates to nearby galaxies in the CLU catalog.

- **Subtraction quality check** – A "byproduct" from matching to external catalogs is to assess the quality of a subtracted image using the following two metrics: the ratios between the numbers of transient candidates and field stars, and the fraction of transient candidates with high real-bogus scores (in practice, we define a threshold value for high real-bogus scores at 1% false positive rate and 5% false negative rate). We further assume that the fraction of variable sources r_{v*} is roughly a constant across the sky, and that half of the variable sources are brighter than their counterparts in the reference images and therefore appear as positive sources in the subtracted images. Since variable sources outnumber real transients substantially, for a good subtracted image, the former metric value should be close to $r_{v*}/2$ and the latter metric value should be close to zero.

- **Post-night image stacking** – After nightly realtime processing, we stack the multiple subtracted images of each field with `Swarp` in order to deepen our detection limits by about half a magnitude. These stacked images are used to search for transients slightly below the single-image detection limits, to provide better SNRs for detected transients in single images, and to provide deeper detection limits for non-detections.

The elapsed time of each step in the pipeline is summarized in Figure 2.7. As can be seen in individual panels of this figure, except for the preprocessing step which involves only matrix operations, the elapsed time of each step is correlated with galactic latitudes of fields. This is probably because, since the density of celestial objects is roughly correlated with galactic latitude, the more celestial objects in an image, the longer these steps take. The scattering in the elapsed times depends not only on the actual density of celestial object

Table 2.2. `HOTPANS` parameters

Parameter	Value	Note
r	$2.5 \times$ seeing	convolution kernel half width (pixel)
rss	$6 \times$ seeing	half width of substamp to extract around stars (pixel)
tu	recorded in the reference header	upper valid data count of the reference image
tl	median(reference)$-10 \times \sigma_{\mathrm{reference}}$[1]	lower valid data count of the reference image
iu	45000	upper valid data count of the science image
il	median(science)$-10 \times \sigma_{\mathrm{science}}$[1]	lower valid data count of the science image

[1] σ denotes the median absolute deviation.

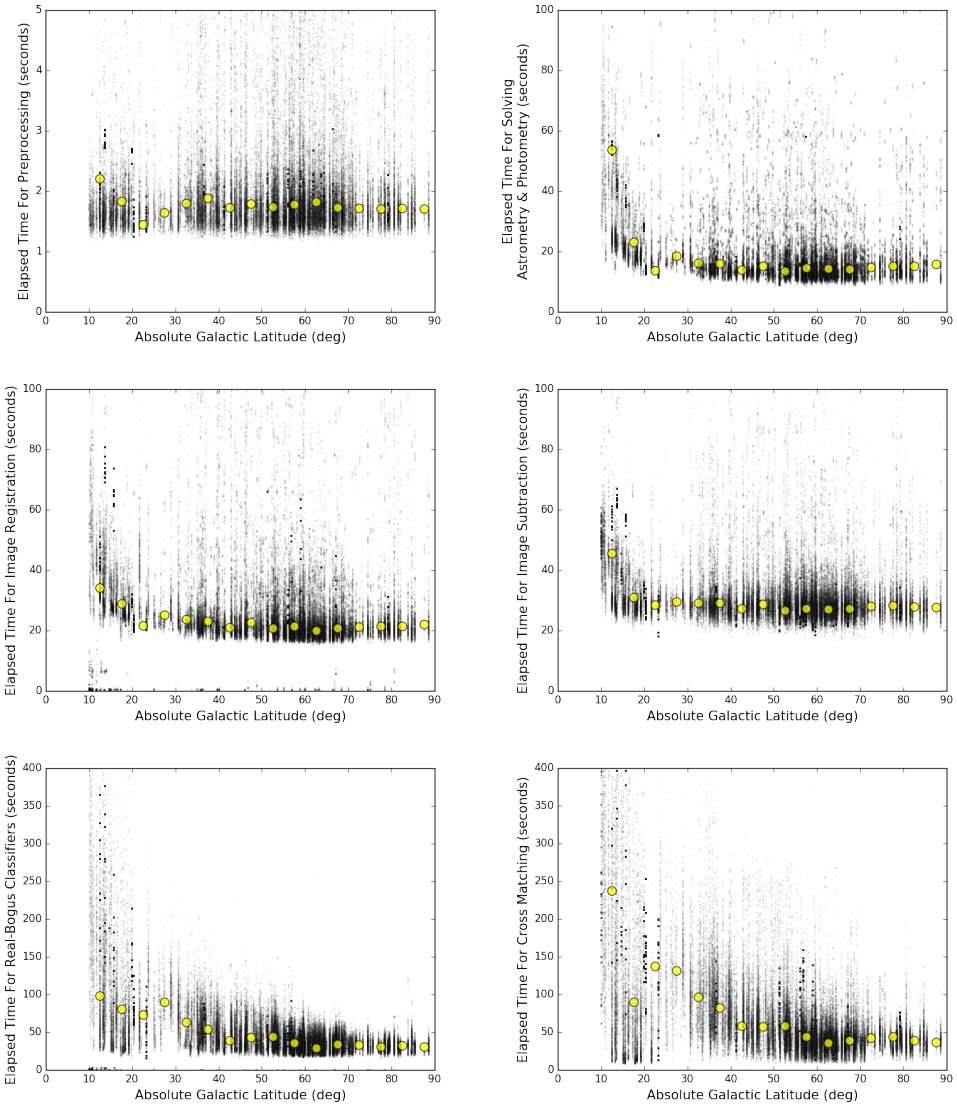

Figure 2.7: **Elapsed times of individual steps in the pipeline.** The data were taken between April 1 and July 31, 2015. The gray dots are real data and the yellow circles are median values in bins of 5 degrees in absolute galactic latitudes.

of each field, but also on the input/output (I/O) speed to the spinning disk at different times.

The whole processing job takes a median time of 4.5 minutes with a distribution show in Figure 2.8. The latest version of this pipeline, which was delivered in early 2015, can process more than 90% of images within 5 minutes. Taken into account the data transfer time and wait time in the supercomputer queue, the distribution of total turnaround time from completion of an exposure to

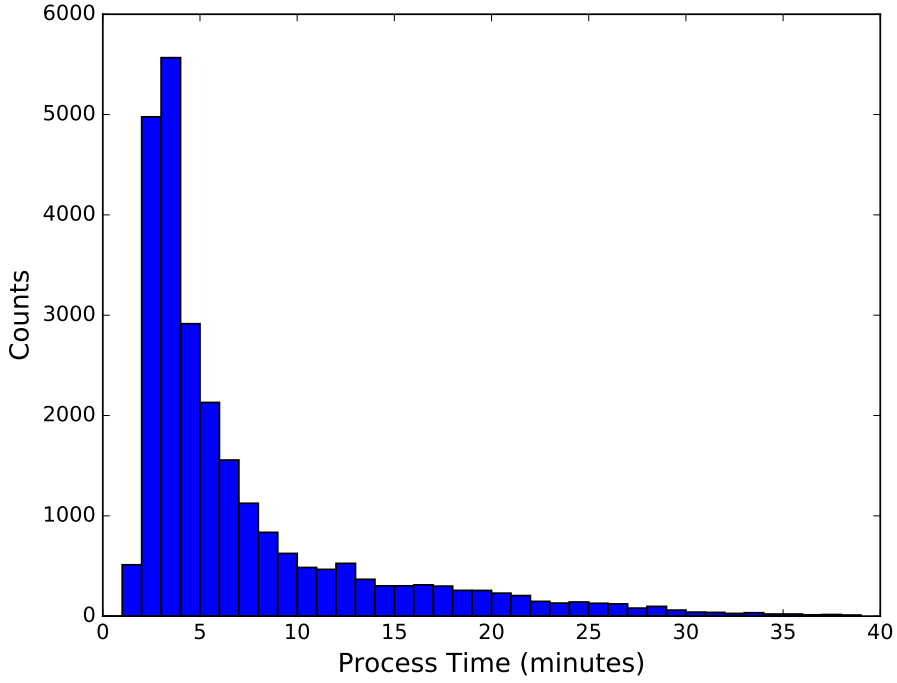

Figure 2.8: **Histograms of NERSC pipeline processing time.**

candidates with real-bogus scores in the database is shown in Figure 2.9. With the latest version of this pipeline, the total turnaround time is usually under ten minutes.

There are a few technical limitations in the current pipeline that could be improved in future. First, the pipeline uses existing astronomy software that involves heavy I/O on spinning disks. As such the processing time can be affected substantially by the I/O speed of the spinning disks. It would become faster if the whole processing is carried out in the memory and only I/O's necessary files in the spinning disks. Second, Python is used as a pipeline wrapper and also performs simple algebraic calculations in the pipeline. The execution of an interpreted script in Python is generally much slower than a machine-language executable from a compiled language. Loading Python modules from the spinning disk can also be impacted by the I/O speed. In addition, there is plenty of room to improve the image subtraction algorithms to reduce false positive rates. For example, a new image differencing algorithm is recently being implemented at IPAC (Masci et al. in prep.).

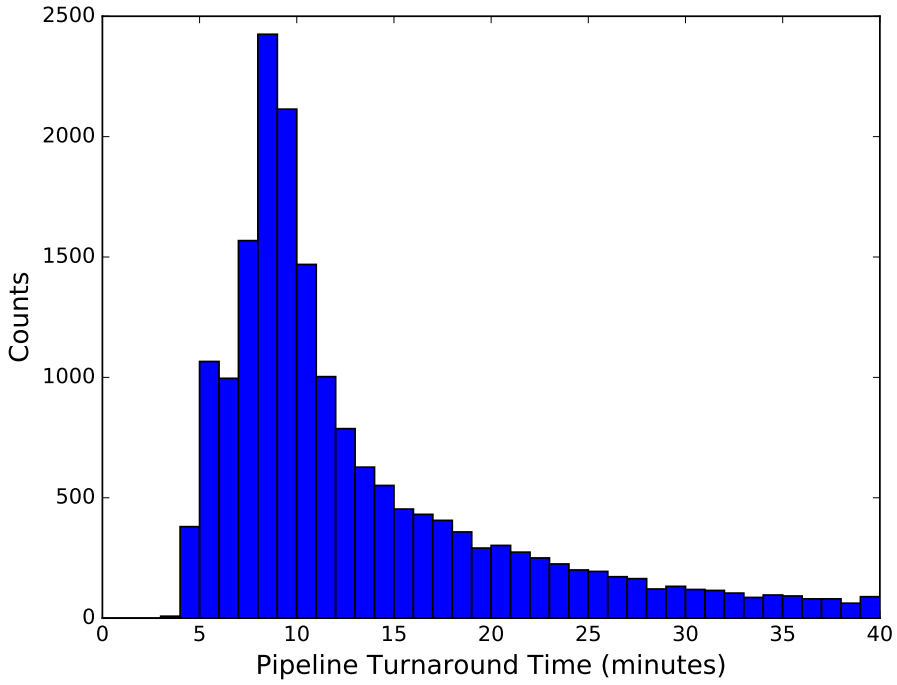

Figure 2.9: **Histogram of turnaround time from completion of an exposure to output candidates from the pipeline.**

Transient candidate vetting

Our realtime image subtraction pipeline produces $\simeq 10^4$ candidates every night. In addition to image-based processing as described above, we add some post-processing criteria to further purify the transient candidate list.

- Due to incompleteness of the asteroid catalog down to $\simeq 21$ mag, uncatalogued moving objects are among the most commonly-seen false positives, especially when our fields are close to the ecliptic plane. Most of them can be removed by requiring two detections at the same location separated by at least half an hour.

- Due to absence of an all-sky star catalog down to $\simeq 21$ mag (SDSS only covers 14,555 square degrees), our candidate list is also heavily contaminated by variable stars. Our recently developed star-galaxy classifier has greatly reduced the number of variable stars brighter than 20 mag (Miller et al. in prep.).

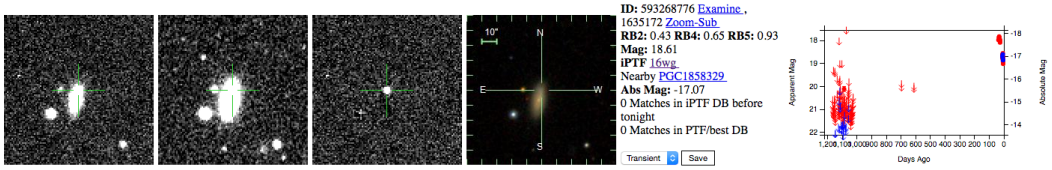

Figure 2.10: **Screenshot of the scanning page.** For each candidate, this page displays $10'' \times 10''$ cutouts of its new, reference and subtracted images centered at the candidate as well as a cutout of SDSS image of the same size when available. This page also shows relevant information such as apparent and absolute magnitudes, real-bogus scores, links to external databases (MPChecker, NED, Simbad, VizieR), and a historical light curve at the location of each candidate.

- A third type of false positives in the transient candidate list is AGNe. Thanks to the rich archival data since PTF, these false positives can be visually removed by examining their historical light curves, since most of them have long history of activities.

After the post-processing stage, we take two ways forward. In one approach, we developed a robotic program called "treasurer" that automatically saves the best candidates **within a minute** of them becoming available in the database, triggers multi-color follow-up observations with the Palomar 60-inch telescope, and alerts our team members by email or text message to trigger further follow-up observations on bigger telescopes. The best candidates here are defined as sources (1) with two detections both having false positive rates $< 0.1\%$, (2) spatially associated with nearby galaxies, and (3) having non-detections in the previous night.

In the other approach, we lower our candidate selection bar for completeness. The only selection criterion is two detections with real-bogus scores above a threshold that corresponds to a false positive rate of 1%. This criterion leads to a list of 100–300 candidates per night. These candidates are displayed on an internal webpage when available (a screenshot of the webpage is shown Figure 2.10), and one or two team members in Sweden or Israel visually inspect them every 15 to 30 minutes during the California night. Once a promising transient candidate is found, the scanning person alerts the whole team for follow-up observations.

Examples of breakdown of candidate numbers at each processing and post-processing stage as well as triggering follow-up observations can be found in

Singer *et al.* (2013, 2015) and Kasliwal *et al.* (2016).

Follow-up

Successes of previous supernovae searches have shown that follow-up observations are as important as discoveries. Since our discovery telescope only provides limited photometric information of a transient in a single band, timely and detailed photometric and spectroscopic observations in optical and other wavelengths are warranted for understanding the nature of the transient. Therefore, we have approved fast-response ToO programs on a variety of ground-based and space-based telescopes, as summarized in Table 2.3. These programs allow us to perform rapid and comprehensive follow-up observations to transients within hours of discovery.

2.3 Results

Compared to previous transient surveys, the unique strength of iPTF is the fast turnaround capability from discovery to follow-up observations on sub-day timescales. Figure 2.11 gives a real example of our discovery and fast-response follow-up observations of an infant Type Ia supernova.

Between 2013 and 2015, we have discovered and spectroscopically confirmed 433 SNe within redshift 0.1 (the redshift cut here is to remove distant SNe at peak). For each SN, we measure two metrics to assess our fast-response performance: the time interval $\Delta t_{\rm discovery}$ between its last non-detection and discovery, and the time interval $\Delta t_{\rm followup}$ between discovery and first spectroscopic follow-up. Here the discovery time is defined as the time when the SN is identified by either our robot or human scanning. $\Delta t_{\rm discovery}$ approximates the age of the SN at discovery and depends on combination of our cadence and turnaround time of our discovery mechanism. $\Delta t_{\rm followup}$ reflects how rapidly we carry out follow-up observation upon discovery. As demonstrated in the histograms of Figures 2.12 and 2.13, in 2013 – 2015, we discovered more than a hundred supernovae with $\Delta t_{\rm discovery} \leq 3\,{\rm days}$. Twenty of them acquired their first spectroscopic follow-up within the same night as discovery ($\Delta t_{\rm followup} < 0.5\,{\rm day}$), and another twenty-nine of them were observed spectroscopically in the night following discovery ($0.5\,{\rm day} < \Delta t_{\rm followup} < 1.5\,{\rm day}$),.

Our discovery efficiency can be estimated by using infant Type Ia SNe, which is quantified here as events dimmer than $-16.5\,{\rm mag}$ upon discovery. Given the iPTF detection limits of $R \simeq 20.5\,{\rm mag}$ and $g \simeq 21$, iPTF can detect

Table 2.3. TOO follow-up programs

Telescope	P.I.	Observation type
Palomar 60-inch	S. R. Kulkarni	Optical photometry
Palomar 200-inch	S. R. Kulkarni	Optical spectroscopy
Keck I & Keck II	S. R. Kulkarni	Optical spectroscopy / Adaptive Optics
Gemini-North and South	M. M. Kasliwal	Optical spectroscopy
LCOGT network	D. A. Howell	Optical photometry and spectroscopy
Nordic Optical Telescope	J. Sollerman	Optical photometry and spectroscopy
APO ARC-3.5m	M. M. Kasliwal	Optical spectroscopy
TNG	F. Taddia	Optical spectroscopy
VLT	R. Amanullah	Optical/IR spectroscopy
Magellan	M. M. Kasliwal	Optical/IR photometry and spectroscopy
Spizter	M. M. Kasliwal	IR photometry
JVLA	A. Horesh	Radio
CARMA	A. Horesh	Radio
Swift	M. M. Kasliwal & Y. Cao	X-ray / UV photometry and spectroscopy
HST	A. Gal-Yam & S. R. Kulkarni	UV spectroscopy

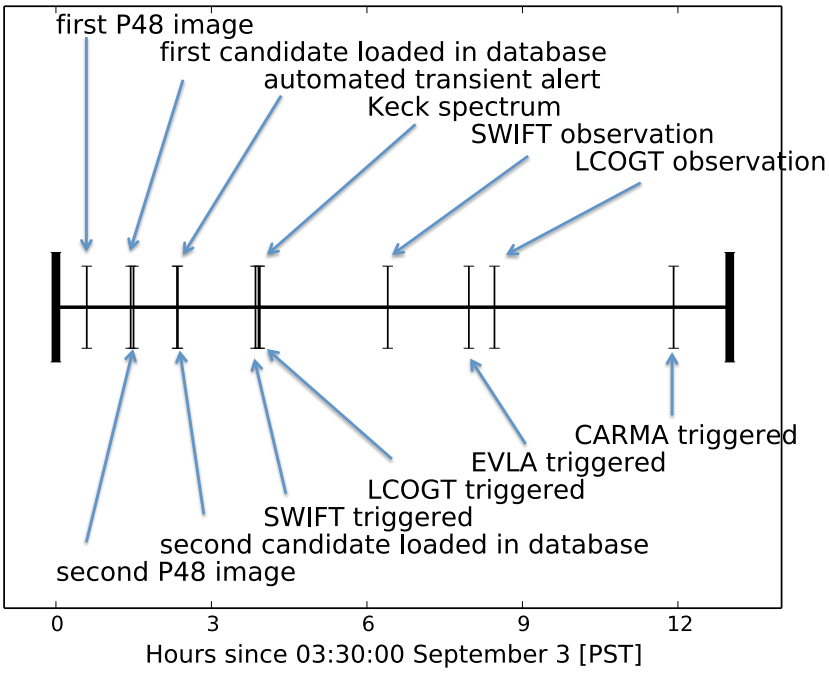

Figure 2.11: **Timeline of discovery and follow-up observations of iPTF13dge.** iPTF13dge is an infant Type Ia supernova discovered within three days of explosion in 2013.

such events up to $10^{2.5}$ Mpc (which corresponds to redshift 0.074). With a volumetric Type Ia SN rate of $3 \times 10^{-5}\,\mathrm{Mpc}^{-3}\,\mathrm{yr}^{-1}$ (Li *et al.*, 2011b) and the Ω(1 day) column in Table 2.1, we estimate that iPTF should find 40 ± 6 such infant Type Ia SNe. In reality, we have discovered 42 Type Ia SNe within redshift 0.074 that had an absolute magnitude dimmer than -16.5 mag upon discovery in our surveys. As a result, we probably have found almost all infant Type Ia SNe in our survey. A detailed Monte Carlo simulation to estimate the discovery efficiency of different types of transients is under investigation (Nugent et al. in prep.).

The infant SNe discovered by our fast-turnaround discovery pipeline have led to a number of papers. Table 2.4 lists all publications thus far directly related to infant SNe discovered in iPTF.

2.4 Summary and future

In this paper, we present the iPTF fast-cadence transient surveys and describe the three essential components in these surveys: cadence and survey area,

Table 2.4. iPTF publications on infant SNe and fast transients

Objects	Publications	Titles
57 Type II Supernovae	Rubin *et al.* (2016)	Type II Supernova Energetics and Comparison of Light Curves to Shock-cooling Models
84 Type II Supernovae	Khazov *et al.* (2016)	Flash Spectroscopy: Emission Lines from the Ionized Circumstellar Material around $<$ 10-day-old Type II Supernovae
iPTF14atg	Cao *et al.* (2015)	A strong ultraviolet pulse from a newborn type Ia supernova
iPTF13ebh	Hsiao *et al.* (2015)	Strong near-infrared carbon in the Type Ia supernova iPTF13ebh
iPTF14yb	Cenko *et al.* (2015)	iPTF14yb: The First Discovery of a Gamma-Ray Burst Afterglow Independent of a High-energy Trigger
iPTF13beo	Gorbikov *et al.* (2014)	iPTF13beo: the double-peaked light curve of a Type Ibn supernova discovered shortly after explosion
iPTF13ast	Gal-Yam *et al.* (2014)	A Wolf-Rayet-like progenitor of SN 2013cu from spectral observations of a stellar wind
iPTF13bvn	Fremling *et al.* (2014)	The rise and fall of the Type Ib supernova iPTF13bvn. Not a massive Wolf-Rayet star
iPTF14jj	Goobar *et al.* (2014)	The Rise of SN 2014J in the Nearby Galaxy M82
iPTF13bvn	Cao *et al.* (2013b)	Discovery, Progenitor and Early Evolution of a Stripped Envelope Supernova iPTF13bvn

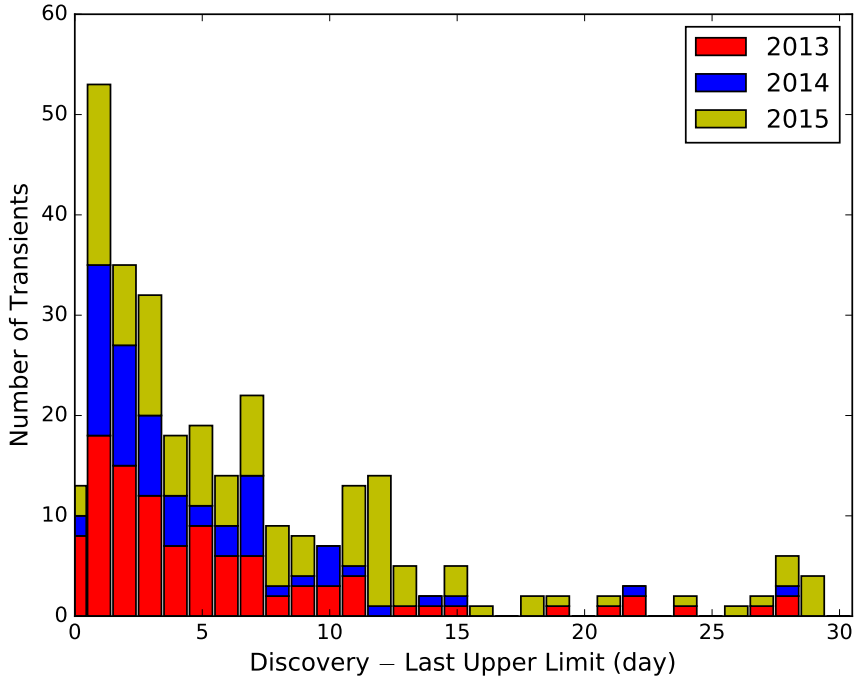

Figure 2.12: **Histogram of time intervals between last non-detection and discovery for spectroscopically confirmed SNe within redshift** 0.1**.**

realtime transient discoveries, and follow-up observations. We show:

- Our cadences are strictly controlled, after we implement a fixed nightly observing schedule for each lunation. However, our efficiency is deteriorated by bad weather to 30%–50%.
- Our realtime image subtraction pipeline manages to deliver transient candidates within ten minutes of images being taken at the telescope. We have found over a hundred supernovae within a few days of their explosions in the first three years of operation.
- Our fast-response mechanism equipped with approved target-of-opportunity programs on a variety of telescopes allows us to acquire immediate and comprehensive follow-up observations of supernovae. We have acquired spectroscopic follow-up observations for forty-nine supernovae within the same night of or the night following discovery.

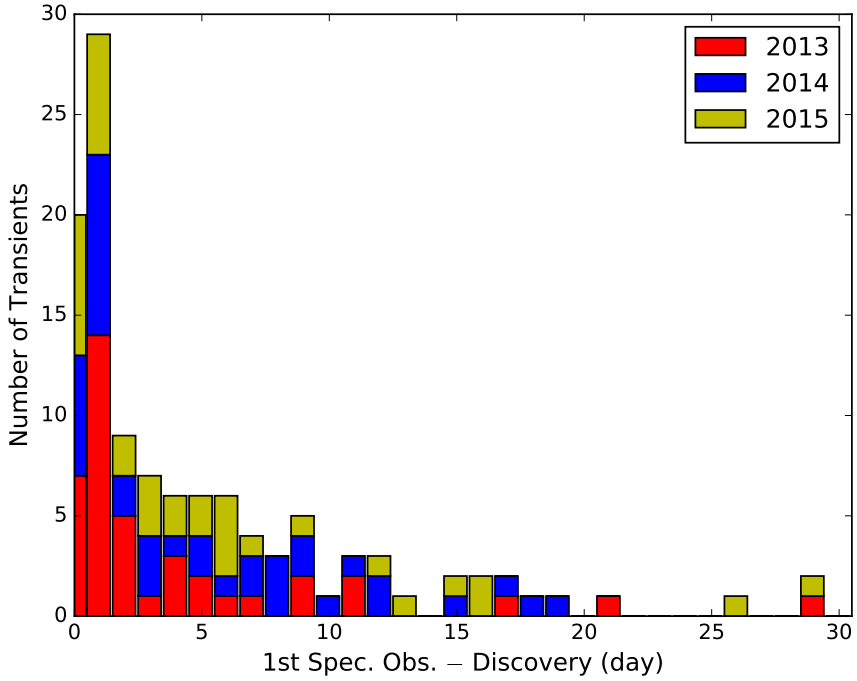

Figure 2.13: **Histogram of time interval between discovery and first spectroscopic observations for SNe with non-detection limits within three days of discovery.**

A few lessons are learned from these fast-cadence surveys in iPTF: first, software in a time-domain survey is as important as hardware, since it efficiently converts raw data to scientifically useful data and sets up a upper limit on the response speed of follow-up observations. Second, since survey data is unlikely to provide sufficient information about the interesting phenomena, fast-cadence surveys need also be partnered with rapid-response follow-up plans in order to maximize scientific return out of the survey.

The iPTF project will cease operation in February 2017 and make way for the Zwicky Transient Facility (ZTF; Smith *et al.* 2014; Bellm *et al.* 2015), which will mount a new camera on the P48 telescope that will have a field of view of 47 square degrees. Taking into its faster readout and shorter exposure time, the survey speed in ZTF will be ten times faster than that in iPTF. ZTF will be able to survey the entire northern sky down a depth similar to iPTF every eight hours. Since iPTF discovers one infant supernova per week or so, ZTF is estimated to find one infant supernova every night. ZTF is poised to chart the phase space on sub-day timescales. Accordingly, we are

also organizing a systematic global follow-up network, with the GROWTH (Global Relay of Observatories Watching Transients Happen) program, that is focused on fast transients, young supernovae and asteroids within the first 24 hours of discovery.

Quick discovery pipelines and rapid follow-up observations will continue to be critical in the ZTF success. The data rate in ZTF will be fourteen times higher than in iPTF, which will challenge the ZTF realtime image subtraction pipeline and its corresponding databases. By coupling the astronomical pipelines with more advanced high-performance-computing resources, we are well on our way to delivering this capability for ZTF.

Acknowledgement

YC and PEN acknowledge support from the DOE under grant DE-AC02-05CH11231, Analytical Modeling for Extreme-Scale Computing Environments. YC and MMK acknowledge support from the National Science Foundation PIRE program grant 1545949. We thank the iPTF scanning team (T. Petrushevska, R. Ferretti, C. Fremling, L. Hangard, E. Karamehmetoglu, A. Nyholm, S. Papadogiannakis, R. Roy, A. Horesh, D. Khazov, S. Knezevic, J. Johansson, G. Leloudas, I. Manulis, A. Rubin, M. Soumagnac, P. Vreeswijk, O. Yaron J. Sollerman, A. Goobar, A. Gal-Yam, E. O. Ofek) for monitoring the data stream every night. We thank the IPAC team (F. Masci, R. Laher, J. Surace) for reference image generation. We thank the machine learning team at LANL (P. Wozniak) and JPL (U. Rebbapragada, B. Bue, G. Doran). The intermediate Palomar Transient Factory project is a scientific collaboration (PI: S. R. Kulkarni) among the California Institute of Technology, Los Alamos National Laboratory, the University of Wisconsin, Milwaukee, the Oskar Klein Center, the Weizmann Institute of Science, the TANGO Program of the University System of Taiwan, and the Kavli Institute for the Physics and Mathematics of the Universe.

Chapter 3

A STRONG ULTRAVIOLET PULSE FROM A NEWBORN TYPE IA SUPERNOVA[†]

Yi Cao[1], S. R. Kulkarni[1,2], D. Andrew Howell[3,4], Avishay Gal-Yam[5], Mansi M. Kasliwal[6], Stefano Valenti[3,4], J. Johansson[7], R. Amanullah[7], A. Goobar[7], J. Sollerman[8], F. Taddia[8], Assaf Horesh[5], Ilan Sagiv[5], S. Bradley Cenko[9], Peter E. Nugent[10,11], Iair Arcavi[3,12], Jason Surace[13], P. R. Wozniak[14], Daniela I. Moody[14], Umaa D. Rebbapragada[15], Brian D. Bue[15] & Neil Gehrels[9]

[1] Astronomy Department, California Institute of Technology, Pasadena, CA 91125, USA

[2] Caltech Optical Observatories, California Institute of Technology, Pasadena, CA 91125, USA

[3] Las Cumbres Observatory Global Telescope Network, 6740 Cortona Dr., Suite 102, Goleta, CA 93117, USA

[4] Department of Physics, University of California, Santa Barbara, CA 93106, USA

[5] Department of Particle Physics and Astrophysics, Weizmann Institute of Science, Rehovot 76100, Israel

[6] Observatories of the Carnegie Institution for Science, 813 Santa Barbara Street, Pasadena, CA 91101, USA

[7] The Oskar Klein Centre, Department of Physics, Stockholm University, SE-106 91 Stockholm, Sweden

[8] The Oskar Klein Centre, Department of Astronomy, Stockholm University, SE 106 91 Stockholm, Sweden

[9] Astrophysics Science Division, NASA Goddard Space Flight Center, Mail Code 661, Greenbelt, MD 20771, USA

[10] Lawrence Berkeley National Laboratory, Berkeley, California 94720, USA

[11] Astronomy Department, University of California, Berkeley, 501 Campbell Hall, Berkeley, CA 94720, USA

[12] Kavli Institute for Theoretical Physics, University of California, Santa Barbara, CA 93106, USA

[†]An edition of this chapter was published on *Nature*, vol. 521, 328 – 331 (2015).

[13] Spitzer Science Center, California Institute of Technology, Pasadena, CA 91125, USA

[14] Los Alamos National Laboratory, Los Alamos, NM 87545, USA

[15] Jet Propulsion Laboratory, California Institute of Technology, Pasadena, CA 91109, USA

Abstract

Type Ia supernovae (Filippenko, 1997) are destructive explosions of carbon oxygen white dwarfs (Nugent *et al.*, 2011; Maoz *et al.*, 2014). Although they are used empirically to measure cosmological distances (Riess *et al.*, 1998; Perlmutter *et al.*, 1999; Sullivan *et al.*, 2011), the nature of their progenitors remains mysterious (Maoz *et al.*, 2014). One of the leading progenitor models, called the single degenerate channel, hypothesizes that a white dwarf accretes matter from a companion star and the resulting increase in its central pressure and temperature ignites thermonuclear explosion (Maoz *et al.*, 2014; Whelan and Iben, 1973; Wang and Han, 2012). Here we report observations of strong but declining ultraviolet emission from a Type Ia supernova within four days of its explosion. This emission is consistent with theoretical expectations of collision between material ejected by the supernova and a companion star (Kasen, 2010), and therefore provides evidence that some Type Ia supernovae arise from the single degenerate channel.

3.1 Discovery

On UTC (Coordinated Universal Time) 2014 May 3.29 iPTF discovered an optical transient, internally designated as iPTF14atg, at α(J2000)= $12^{\rm h}52^{\rm m}44^{\rm s}.8$ and δ(J2000)= $+26°28'13''$, about $10''$ east with no measurable offset in declination from the apparent host galaxy IC 831. It had an R-band magnitude of 20.3 in the discovery image. No source was detected at the same location on images taken on UT 2014 May 02.25 and 02.29 down to a limiting magnitude of $R \simeq 21.4$ mag (99.9999% confidence level), indicating that the SN likely exploded between May 2.29 and 3.29. No activity had been found at this location in the iPTF archival data in 2013 (3 epochs) and 2014 (101 epochs) down to similar limiting magnitudes. Our follow-up spectroscopic campaign established that iPTF14atg was a Type Ia supernova (SN). This SN was also independently discovered by ASASSN on May 22 (Holoien *et al.*, 2014) and classified as a SN 1991bg-like Type Ia SN on June 3 (Wagner *et al.*, 2014).

SDSS (Data Release 12) measured the redshift of IC 831 to be 0.02129 (Bolton *et al.*, 2012). With the cosmological parameters measured by Planck ($H_0 = 67.8\,\mathrm{km\,s^{-1}\,Mpc^{-1}}$, $\Omega_m = 0.307$, $\Omega_\Lambda = 0.691$ and $\Omega_\nu = 0.001$; Planck Collaboration *et al.* 2014), we calculate a co-moving distance of 93.7 megaparsecs and a distance modulus of 34.9 mag for IC 831. No redshift-independent distance measurement is available for this galaxy, according to the NASA/IPAC Extragalactic Database (NED).

3.2 Observations and data reduction

Swift

Upon discovery we triggered observations with the Ultraviolet/Optical Telescope (UVOT) and the X-ray Telescope (XRT) on the *Swift* space observatory (Gehrels *et al.*, 2004). As summarized in Table 3.1, *Swift* observed iPTF14atg for fourteen epochs in May and June 2014. In order to subtract the host galaxy contamination, *Swift* took reference images at the same site six months later. Visual inspection to the reference images ensures that the SN has faded below the detection limit.

Photometric measurements of the UVOT images were undertaken with the `uvotsource` routine in the HEASoft package[1]. Instrumental fluxes of iPTF14atg were extracted with an aperture of radius 3″ centered at the location determined by the iPTF optical images and the sky background is calculated with an aperture of radius 20″ in the vicinity of iPTF14atg. The instrumental fluxes were then corrected by the growth curves of UVOT point spread functions (PSFs) and for coincidence loss. Then the instrumental fluxes were converted to physical fluxes using the most recent calibration (Breeveld *et al.*, 2011). The host galaxy flux is measured with the same aperture and following the same procedure in the reference images, and is subtracted off in the flux space.

The XRT data were analyzed with the `Ximage` program in the HEASoft package. In circumstances of non-detections, we estimated count rate upper limits at a 99.7% CL at the location of iPTF14atg. Then we used WebPIMMS[2] to convert the XRT upper limit measured on May 6 to a physical flux limit. The optical and UV data taken on the same day can be approximated by a blackbody model with a temperature $T_{eff} = 1.0 \times 10^4\,\mathrm{K}$ and a radius $4 \times 10^3 R_\odot$

[1]The HEASoft package is available at `http://heasarc.nasa.gov/heasoft`

[2]WebPIMMS is available at `http://heasarc.gsfc.nasa.gov/cgi-bin/Tools/w3pimms/w3pimms.pl`

(See Section 3.3 for details). Using this blackbody model with the radius fixed to the above value and setting the interstellar column density of hydrogen to as is appropriate towards this direction (Kalberla *et al.*, 2005), we find that the XRT upper limit of counting rate agrees with the blackbody temperature.

Ground-based facilities

As described in 3.1, P48 monitored the iPTF14atg site in the R band every night (weather-permitting) until 2014 July 2. The host galaxy light in the P48 images was removed with the aid of a reference image that was built by stacking twelve pre-SN P48 images. We performed the PSF photometry on the subtracted images and calibrated it to the PTF-IPAC catalog (Ofek *et al.*, 2012a).

We also triggered LCOGT to follow up iPTF14atg in *griBV* filters. Since reference images were not available, we used image-based models that includes a PSF and a low-order polynomial to simultaneously model the SN fluxes and its underlying galaxy background. The photometry is then calibrated to the SDSS catalog.

Our spectroscopic observations span from a few to two hundred days after the iPTF14atg explosions and are logged in Table 3.2. Spectroscopic data were reduced and calibrated with standard routines in IRAF and IDL.

We also observed iPTF14atg with the Jansky Very Large Array on May 16 at both 6.1 GHz (C-band) and 22 GHz (K-band). The observation was performed in the A configuration using J1310+3220 as a phase calibrator and 3C286 as a flux calibrator. The data were reduced using standard routines in the CASA software. The observation resulted in a null-detection at both bands with an upper limit of 30 μJy (99.7% CL). Note that the radio observation is taken more than ten days after iPTF14atg discovery.

3.3 Early UV pulse from infant iPTF14atg

As can be seen in Figure 3.1, the UV brightness of iPTF14atg declined substantially in the first two observations. A rough energy flux measure in the UV band is provided by $\nu f_\nu \simeq 3 \times 10^{-13}\,\mathrm{ergs\,cm^{-2}\,s^{-1}}$ in the *uvm2* band. Starting from the third epoch, the UV and optical emission began to rise again in a manner similar to that seen in other Type Ia SNe. The XRT did not detect any X-ray signal at any epoch (Table 3.1). We thus conclude that iPTF14atg

Table 3.1. *Swift* observation of iPTF14atg

UT Time	UVOT (counts/sec)[a]						XRT (counts/sec)[b]
	uvw2	*uvm2*	*uvw1*	*u*	*b*	*v*	
May 06.67 – 06.74	0.297 ± 0.028	0.176 ± 0.014	0.399 ± 0.044	1.251 ± 0.116	2.354 ± 0.168	1.491 ± 0.131	$< 3.7 \times 10^{-3}$
May 08.53 – 08.61	0.112 ± 0.019	0.096 ± 0.014	0.324 ± 0.041	1.374 ± 0.151	2.444 ± 0.212	1.472 ± 0.163	$< 4.9 \times 10^{-3}$
May 12.98 – 13.12	0.208 ± 0.019	0.182 ± 0.019	0.578 ± 0.044	2.971 ± 0.152	4.515 ± 0.194	2.288 ± 0.136	$< 5.2 \times 10^{-3}$
May 15.25 – 15.38	0.351 ± 0.057	0.296 ± 0.041	0.681 ± 0.100	3.636 ± 0.414	5.557 ± 0.531	2.945 ± 0.371	$< 2.2 \times 10^{-3}$
May 18.99 – 19.05	0.452 ± 0.051	0.297 ± 0.024	1.081 ± 0.094	5.381 ± 0.372	6.600 ± 0.417	3.580 ± 0.285	$< 8.8 \times 10^{-3}$
May 20.31 – 20.46	0.404 ± 0.034	0.325 ± 0.024	0.956 ± 0.067	5.758 ± 0.307	7.084 ± 0.347	3.178 ± 0.214	$< 6.5 \times 10^{-3}$
May 21.45 – 21.46	0.437 ± 0.067	0.262 ± 0.042	0.809 ± 0.115	6.015 ± 0.578	7.454 ± 0.669	3.178 ± 0.407	$< 2.4 \times 10^{-2}$
May 25.45 – 25.65	0.166 ± 0.019	0.156 ± 0.014	0.483 ± 0.041	4.228 ± 0.219	6.808 ± 0.291	3.590 ± 0.195	$< 3.6 \times 10^{-3}$
May 27.65 – 27.85	0.124 ± 0.023	0.084 ± 0.014	0.440 ± 0.053	3.595 ± 0.274	6.804 ± 0.400	3.494 ± 0.266	$< 6.8 \times 10^{-3}$
May 30.24 – 30.52	0.078 ± 0.018	0.029 ± 0.009	0.352 ± 0.045	2.551 ± 0.227	4.883 ± 0.330	3.490 ± 0.257	$< 7.0 \times 10^{-3}$
Jun 07.38 – 07.65	0.041 ± 0.011	0.019 ± 0.006	0.187 ± 0.028	1.101 ± 0.119	2.936 ± 0.195	2.279 ± 0.162	$< 3.8 \times 10^{-3}$
Jun 17.39 – 17.60	0.052 ± 0.014	0.027 ± 0.009	0.143 ± 0.023	0.859 ± 0.102	2.235 ± 0.168	1.782 ± 0.196	$< 5.4 \times 10^{-3}$
Jun 21.37 – 21.45	0.039 ± 0.011	0.023 ± 0.006	0.127 ± 0.024	0.833 ± 0.107	2.377 ± 0.176	1.851 ± 0.143	$< 4.9 \times 10^{-3}$
Jun 25.24 – 25.53	0.045 ± 0.012	0.018 ± 0.007	0.120 ± 0.026	0.801 ± 0.113	1.624 ± 0.153	0.413 ± 0.039	$< 4.6 \times 10^{-3}$
Nov 12.04 – 12.11[c]	0.004 ± 0.010	0.017 ± 0.008	0.080 ± 0.025	0.559 ± 0.115	1.576 ± 0.189	0.953 ± 0.156	

[a]The uncertainties are at a 66.8% CL.

[b]The upper limits are at a 99.7% CL.

[c]This is a reference epoch to remove host galaxy contamination.

Table 3.2. Spectroscopic observations of iPTF14atg

Date (UT)	Telescope/Instrument	Resolution (Å)	Wavelength Coverage (Å)	Observer	Data Reducer
May 6.32	ARC-3.5m/DIS[a]	10	3500 – 9500	Cao	Cao
May 6.96	NOT/ALFOSC[b]	16.2	3500 – 9000	Smirnova	Taddia
May 9.25	ARC-3.5m/DIS[a]	10	3500 – 9500	Kasliwal	Cao
May 11.04	NOT/ALFOSC[b]	16.2	3500 – 9000	Martinez	Taddia
May 15.96	NOT/ALFOSC[b]	16.2	3500 – 9000	Nyholm	Papadogiannakis
May 21.31	ARC-3.5m/DIS[a]	10	3500 – 9500	Cao	Cao
May 24.21	Hale/DBSP[c]	10	3300 – 10000	Waszczak	Rubin & Yaron
May 26.35	Keck-II/DEIMOS[d]	1.5	5700 – 8200	Cao	De Cia
May 28.33	Keck-I/LRIS[e]	7	3300 – 10000	Perley	Perley
June 3.15	ARC-3.5m/DIS[a]	10	3500 – 9500	Cao	Cao
June 6.23	Hale/DBSP[c]	10	3300 – 10000	Waszczak	Yaron
June 29.30	Keck-I/LRIS[e]	7	3300 – 5500	Cao & Duggan	Perley
		4.7	5800 – 7400		
July 30.24	Keck-I/LRIS[e]	4	3300 – 5500	Cao	Perley
		2.5	5400 – 7000		
August 20.24	Gemini-N/GMOS[f]	3	4000 – 9000		Kasliwal
Dec 21	Keck-II/DEIMOS[d]	3.5	4500 – 9500		

[a]The Dual Image Spectrograph (DIS) on the ARC-3.5m telescope at the Apache Observatory, New Mexico, USA.

[b]The Andalucia Faint Object Spectrograph and Camera (ALFOSC) on the Nordic Optical Telescope at La Palma, Spain.

[c]The Double Spectrograph (DBSP; Oke and Gunn 1982) on the Palomar 200-inch Hale telescope at Palomar Observatory, California, USA.

[d]The DEep Imaging Multi-Object Spectrograph (DEIMOS; (Faber *et al.*, 2003)) on the Keck-II telescope at Mauna Kea, Hawaii, USA.

[e]The Low Resolution Imaging Spectrometer (LRIS; (Oke *et al.*, 1995)) on the Keck-I telescope at Mauna Kea, Hawaii, USA.

[f]The Gemini Multi-Object Spectrograph (GMOS; Hook *et al.* 2004) on the Gemini-N telescope at Mauna Kea, Hawaii, USA.

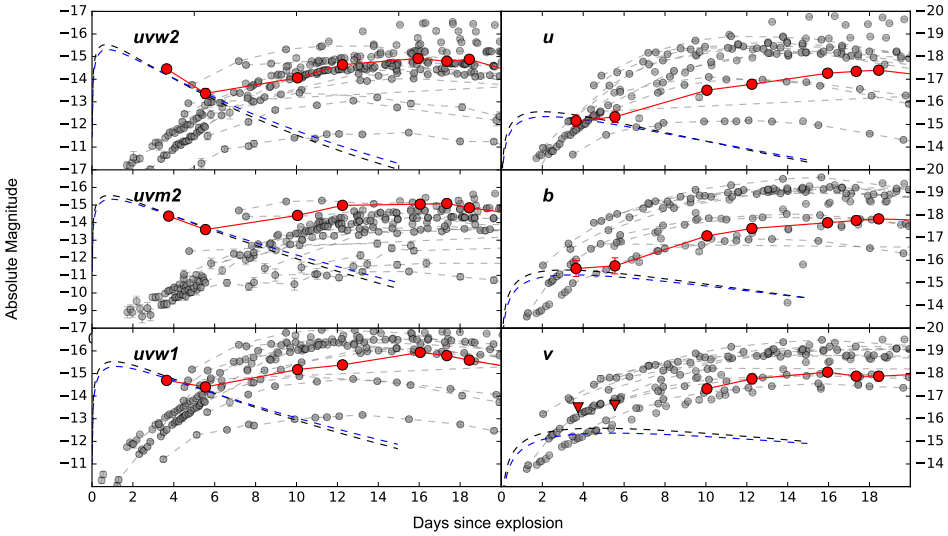

Figure 3.1: **Swift/UVOT light curves of iPTF14atg**. iPTF14atg light curvs are shown in red circles and lines and are compared with those of other Type Ia SNe (gray circles). The magnitudes are in the AB system. The 1-σ error bars include both statistical and systematic uncertainties in measurements. Lightcurves of other SNe and their explosion dates are taken from previous studies (Brown *et al.*, 2012a,b). In each of the three UV bands (uvw2, uvm2, and uvw1), iPTF14atg stands out for exhibiting a decaying flux at early times. The blue (Model A) and black (Model B) dashed curves show two theoretical light curves derived from companion interaction models (Kasen, 2010).

emitted a pulse of radiation primarily in the UV band. This pulse with an observed luminosity of $L_{\rm UV} \simeq 3 \times 10^{41}\,{\rm ergs\,s^{-1}}$ was probably already declining by the first epoch of the Swift observations (within four days of its explosion).

Figure 3.1 also illustrates that such an early UV pulse from a SN Ia within four days of its explosion is unprecedented (Milne *et al.*, 2010; Brown *et al.*, 2012a). We now seek an explanation for this early UV pulse.

Spherical models

In this subsection we consider models spherically symmetric with respect to the SN explosion center to interpret the early UV excess seen in iPTF14atg. In the first model, we investigate the possibility that the UV pulse is powered by radioactive decay. The rise time of a SN peak is roughly characterized by the diffusive timescale from the radioactive layer to the photosphere, i.e.,

$$\tau \propto \left(\frac{\kappa M_{ej}}{c v_{exp}} \right)^{1/2} , \tag{3.1}$$

where M_{ej} is the mass of ejecta outside the radioactive layer, κ is the mean opacity of the ejecta, c is the speed of light and v_{exp} is the mean expansion velocity. To further simplify the situation, we assume that κ remains roughly constant in the rise phase of a SN. If the mean expansion velocity v_{exp} also does not change significantly, then the UV pulse of iPTF14atg within four days of its explosion and its primary optical peak observed about twenty days after explosion indicate two distinct radioactive layers that powered the SN emission on different timescales. The shallow layer at about 4% of the total ejected mass below the surface drove the UV pulse. If we further assume that the radioactive element in the shallowest layer is ^{56}Ni, then the UV luminosity of $L_{\rm UV} \simeq 3 \times 10^{41}\,{\rm ergs\,s^{-1}}$ requires a ^{56}Ni mass of $0.01 M_{\odot}$. Such a configuration has been widely discussed in double-detonation models where a carbon-oxygen white dwarf accretes mass from a helium star. After the helium shell on the surface of the white dwarf reaches a critical mass, helium burns in a detonation wave with such force that a detonation is also ignited in the interior of the white dwarf, making a SN explosion with sub-Chandrasekhar mass. However, nuclear burning on the surface not only synthesizes ^{56}Ni, but a layer containing iron-group elements. These elements have a vast number of optically thick lines in the UV to effectively absorb and reprocess UV photons into longer wavelengths. Therefore we would not have observed the UV pulse at the early time in this scenario (Kromer *et al.*, 2010). In addition, some double-detonation models predict weak Si II 6355 Å absorption near the SN peak (Nugent *et al.*, 1997), which contradicts the observed deep Si II absorption in iPTF14atg. Therefore we consider this model as not consistent with observations.

A second model is that the emission arises from circumstellar gas around the progenitor. The circumstellar gas is heated up by either high energy photons from the SN shock breakout (Case A) or the SN shock itself (Case B). We assume that the circumstellar gas is optically thin and thus the plausible radiation mechanism is bremsstrahlung. Consider a simple model of a sphere of radius R_s and temperature T that contains pure-element gas with an atomic number Z and a mass number A. The material is completely ionized, so the electron density n_e and the ion density n_i are related by $n_e = Z n_i$. The bremsstrahlung luminosity is

$$L_{ff} = 1.4 \times 10^{-27} T^{1/2} n_e n_i Z^2 \times \frac{4\pi}{3} R_s^3 \,, \tag{3.2}$$

where all physical quantities are in CGS units. We further assume the critical case that the optical depth of the sphere is unity, i.e.,

$$\tau_s = n_e \sigma_T R_s = 1 \ , \tag{3.3}$$

where σ_T is the Thompson scattering cross section. Then we can derive analytical expressions for the luminosity, the total mass of the sphere M and the thermal energy of Q in terms of A, Z, R_s and T, namely

$$L_{ff} = 5.0 \times 10^{41} Z R_{17} T_5^{1/2} \,\mathrm{ergs\,s^{-1}} \ , \tag{3.4}$$

$$M = \frac{4\pi}{3} R_s^3 \times n_i A u = 53 \frac{A}{Z} R_{17}^2 M_\odot \ , \tag{3.5}$$

$$Q = \frac{4\pi}{3} R_s^3 \times (n_i + n_e) \times \frac{3}{2} k_B T = 1.3 \times 10^{48} \frac{Z+1}{Z} R_{17}^2 T_5 \,\mathrm{ergs} \ , \tag{3.6}$$

where $R_s = R_{17} \times 10^{17}\,\mathrm{cm}$, $T = T_5 \times 10^5\,\mathrm{K}$, and u is the atomic mass unit. Since no hydrogen is seen in the iPTF14atg spectra, we assume that the sphere is dominated by helium, and hence $A = 4$ and $Z = 2$.

In Case A, the circumstellar gas is heated up by the high energy photons from the SN shock breakout. The temperature of the gas is roughly $1.0 \times 10^4\,\mathrm{K}$ as determined by the optical-UV spectral energy distribution (SED; Figure 3.1). In order to account for a UV luminosity of $3 \times 10^{41}\,\mathrm{ergs\,s^{-1}}$, the radius R_s has to be as large as $3 \times 10^{16}\,\mathrm{cm}$. The total mass of the sphere would be ten solar mass and the total thermal energy 10^{47} ergs. If the optical depth of the sphere is larger than unity, then we would end up with an even more massive sphere. So we are forced to invoke a sphere containing a mass much larger than a typical SN Ia. Absence of strong Na I D absorption lines in the spectra also argue against such a massive circumstellar material. In addition, the elliptical host galaxy with no star forming activity excludes existence of massive stars.

In Case B, the circumstellar gas is ionized by the SN shock. The SN shock has a typical velocity between $20,000\,\mathrm{km\,s^{-1}}$ and $5,000\,\mathrm{km\,s^{-1}}$. Thus, in four days of the SN explosion, the SN shock traveled to $R_s \sim 10^{15}\,\mathrm{cm}$. To account for the UV pulse, this small radius would lead to an extremely high temperature of $10^7\,\mathrm{K}$, which is inconsistent with the observed SED. Therefore we discard this model.

Since these spherical models are unable to explain the observed UV pulse, next we turn to asymmetric models in which the UV emission comes from particular directions.

SN-companion collision model

A reasonable physical model is UV emission arising in the ejecta as the ejecta encounters a companion (Kasen, 2010; Pan *et al.*, 2012). When the rapidly moving ejecta slams into the companion, a strong reverse shock is generated in the ejecta and heats up the surrounding material. Thermal radiation from the hot material, which peaks in the UV, can then be seen for a few days until the fast-moving ejecta engulfs the companion and blocks the reverse shock region. We compare a semi-analytical model (Kasen, 2010) to the Swift/UVOT light curves[3]. For simplicity, the explosion date is fixed to May 3. We assume that the exploding white dwarf is close to the Chandrasekhar mass limit ($1.4M_{\odot}$) and that the SN explosion energy is 2.5×10^{50} ergs. These values lead to a mean expansion velocity of $5 \times 10^{3}\,\mathrm{km\,s^{-1}}$ for the ejecta. Since the temperature at the collision location is so high that most atoms are ionized, the opacity is probably dominated by electron scattering. To further simplify the case, we assume that the emission from the reverse shock region is blackbody and isotropic. Under these assumptions, in order to explain the UV light curves, the companion star should be located $70R_{\odot}$ away from the white dwarf (Model A; black dashed curves in Figure 3.1).

There are several caveats in this simple semi-analytical model. First, the model parameters are degenerate. For example, if we reduce the SN energy to 1.6×10^{50} ergs and increase the binary separation to $90R_{\odot}$, the model light curve can still account for the observed UV luminosities (Model B; blue dashed curves in Figure 1). Second, the emission from the reverse shock region is not isotropic. The UV photons can only easily escape through the conical hole carved out by the companion star and therefore the emission is more concentrated in this direction. The isotropic assumption roughly corresponds to a viewing angle of 20°–30° from the direction of the companion (Kasen, 2010). Third, the actual explosion date is not well constrained, so that when the companion collision happened is not clear. Our multi-wavelength observations soon after discovery of the SN provide a good data set for detailed modeling of the SN-companion collision.

We also construct the SED from the photometry and spectrum of iPTF14atg obtained on the same day of the first UVOT epoch and compare it with the blackbody spectra derived from Models A and B. As can be seen in Figure 3.2,

[3]We note that a factor of π is missing in calculating the blackbody spectra in Cao *et al.* (2015)

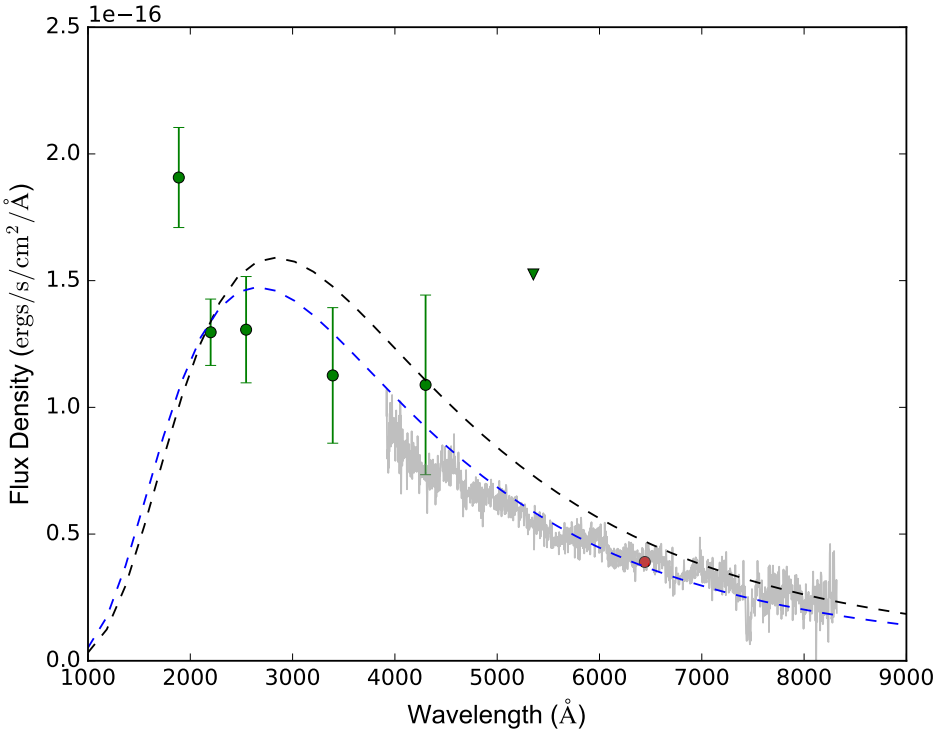

Figure 3.2: **SED of young iPTF14atg**. The spectral energy distribution of iPTF14atg on May 6 (three days after explosion) is constructed by using the PTF r-band magnitude (red), an optical spectrum (gray), and Swift/UVOT measurements (green circle) and upper limit (green triangle). The error bars denote 1-σ uncertainties. The blue and black blackbody spectra correspond to the model light curves of the same color in Figure 3.1.

the model blackbody spectra are roughly consistent with the overall shape of the SED (The blackbody spectrum from Model B is slightly better than that from Model A), indicating that the emitting regions can be approximated by a blackbody with a temperature of 1.0×10^4 K and a radius of $4 \times 10^3 R_\odot$.

3.4 SN specifics

Next we investigate the specifics of iPTF14atg. Figure 3.3 shows its multi-color light curves and Figure 3.4 shows its spectral evolution. We note that there is a difference between the PTF Mould R-band and LCOGT r-band magnitudes. We calculated synthetic photometry using the iPTF14atg spectra and the filter transmission curves and found that this difference was mainly due to the filter difference.

First, the existence of characteristic spectral absorption features from inter-

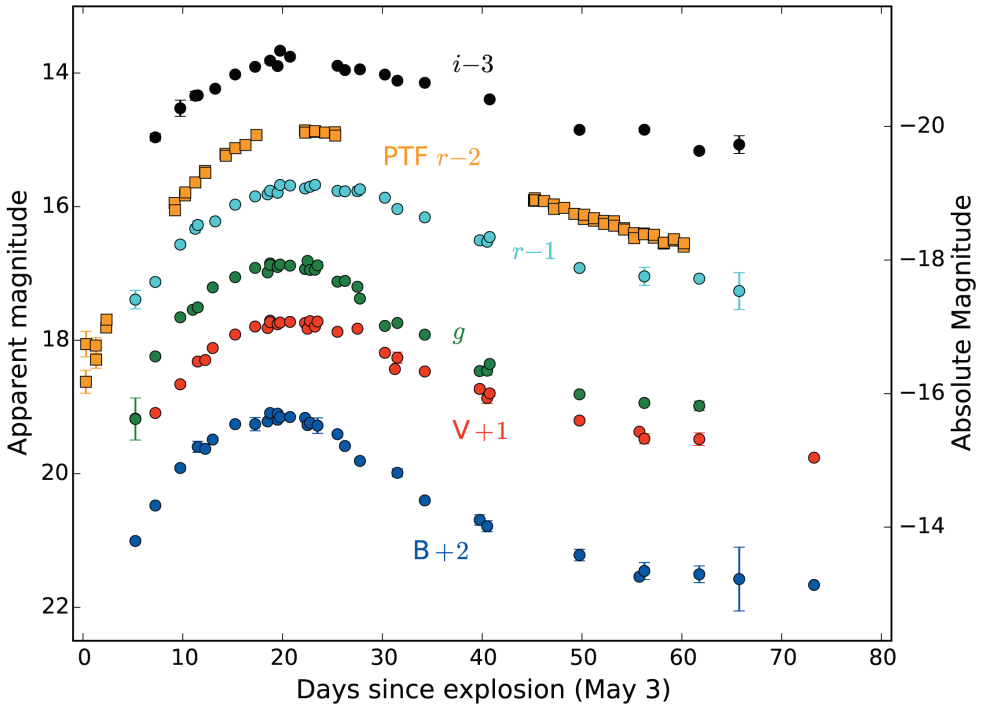

Figure 3.3: **Multi-color light curves of iPTF14atg**. Following the convention, the magnitudes in B and V bands are in the Vega system while those in g, r and i in the AB system. Error bars represent 1-σ uncertainties.

mediate mass elements in the pre-maximum spectra, such as Si II and S II, indicates that iPTF14atg is spectroscopically classified as a Type Ia SN (Filippenko, 1997). Second, its peak B-band absolute magnitude is fainter than normal Type Ia SNe that are used in cosmography (Yasuda and Fukugita, 2010). Subluminous Type Ia SNe have three major families with prototypical events being SN1991bg (Filippenko *et al.*, 1992a), SN2002cx (Li *et al.*, 2003; Foley *et al.*, 2013), and SN2002es (Ganeshalingam *et al.*, 2012). Below we present a comparative analysis on both light curves and spectra between iPTF14atg and the three families to show that iPTF14atg probably belongs to the SN2002es family.

photometry

Since iPTF14atg is not a normal SN Ia, the usual light curve fitting tools for normal Type Ia SNe, such as SALT2 (Guy *et al.*, 2007) and SNooPy2 (Burns *et al.*, 2011), are not suitable to determine the light-curve features. Thus we fit

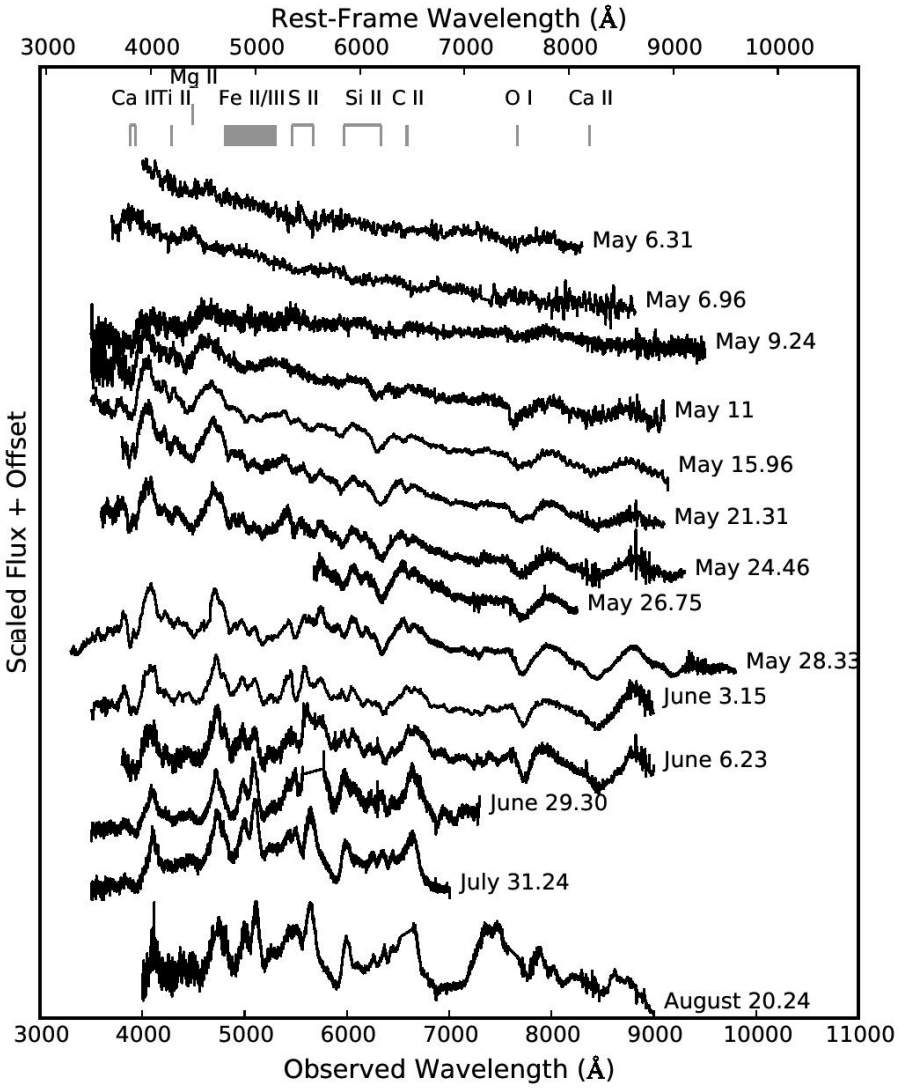

Figure 3.4: **Spectral evolution of iPTF14atg**. Ticks at the top of the figure label major spectra features in the spectra.

a 5th-order polynomial to the B-band light curve and derived a B-band peak magnitude of 17.1 mag on May 22.15 and $\Delta m_{15} = 1.2$ mag. Next we infer that the line-of-sight extinction is low, since the Galactic extinction in this direction is $A_B = 0.032$, and since we do not see any sign of strong Na I D absorption in all of our low- and medium-resolution spectra of iPTF14atg. As such, given the host galaxy distance modulus of 34.9 mag, we calculated an absolute B-band peak magnitude of -17.8 mag for iPTF14atg. We also concluded that iPTF14atg is a subluminous outlier of the well-established relation between the peak magnitude and Δm_{15} (Phillips, 1993).

Figure 3.5 compares light curves of iPTF14atg, SN1991bg, SN2005hk (a typical SN2002cx-like event) and SN2002es. We can see that: (1) the peak magnitude of iPTF14atg is brighter than that of SN1991bg, similar to that of SN2005hk, and fainter than that ofSN2002es. However, both SN2002cx and SN2002es families show large ranges of peak magnitudes (Foley *et al.*, 2013; White *et al.*, 2015). (2) The light curve shape of iPTF14atg is apparently much broader than that of SN1991bg, indicating slower evolution in both rise and decline phases. (3) iPTF14atg has a slower rise than SN2005hk. The very early-phase light curve of iPTF14atg is probably distorted by the SN-companion collision signature. (4) Unlike SN2002es, iPTF14atg does not show a faster decline in the light curve about 30 days after the peak.

Figure 3.6 presents the near-UV (NUV) and optical color evolution of iPTF14atg in comparison with that of SN2011fe (an optically normal but NUV-blue event; Brown *et al.* 2012a; Vinkó *et al.* 2012), SN1991bg, SN2005hk, and SN2002es. According to this figure, iPTF14atg was initially bluer in the $uvm2 - uvw1$ color by more than two magnitudes than SN2011fe. Though SN2011fe gradually becomes NUV bluer while approaching its peak, iPTF14atg remains a nearly constant NUV color and still bluer at peak than SN2011fe by one magnitude. The NUV color of iPTF14atg is also not consistent with that of SN2005hk. The $B - V$ color of iPTF14atg was initially red, and then quickly became blue in a few days. It starts to roughly follow the $B - V$ color evolution of both SN2002es and SN1991bg about two weeks before maximum. In contrast, though SN2011fe was also red initially, it gradually became blue during the SN rise, reached its bluest color near the SN peak and turned red later on. SN2005hk also looks bluer in the optical than iPTF14atg before +10 days.

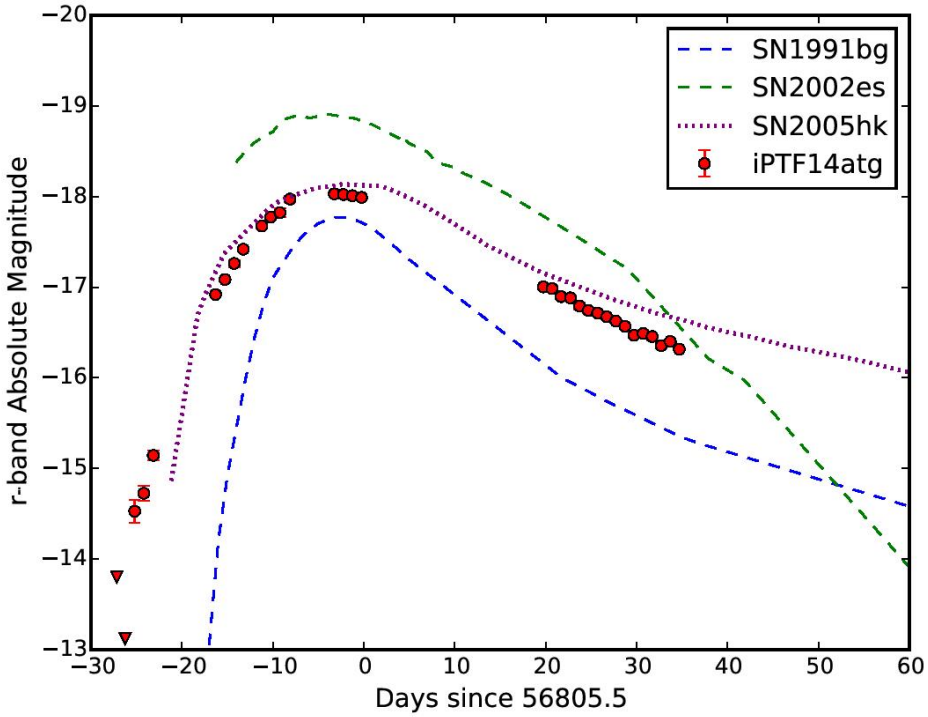

Figure 3.5: **The iPTF14atg light curve compared to those of well-studied subluminous events**. The SN1991bg spectra were taken from the Nugent templates (Nugent *et al.*, 2002), a typical SN2002cx-like event SN2005hk, and SN2002es. The red triangles are upper limits at a 99.9999% CL for non-detections of iPTF14atg. The error bars denote 1-σ uncertainties.

Spectroscopy

The iPTF14atg spectral sequence is shown in Figure 3.4. We compare them to those of well-studied subluminous events at similar phases in Figure 3.7, including SN1991bg, SN2005hk, and SN2002es.

Four days after the explosion, the spectrum of iPTF14atg consisted of a blue continuum superposed by some weak and broad absorption features. As shown in Figure 3.2, the optical spectrum is consistent with the blackbody spectrum estimated by the spectral density distribution (SED) in the UV. This indicates that the emission of iPTF14atg at this early phase is dominated by the thermal emission from the SN-companion interaction. None of the known subluminous Type Ia SNe have been observed at such early time for appropriate comparison, so we turned to a young normal Type Ia SN2011fe (Nugent *et al.*, 2011). Unlike iPTF14atg, the spectra of SN2011fe taken within two days after explosion show

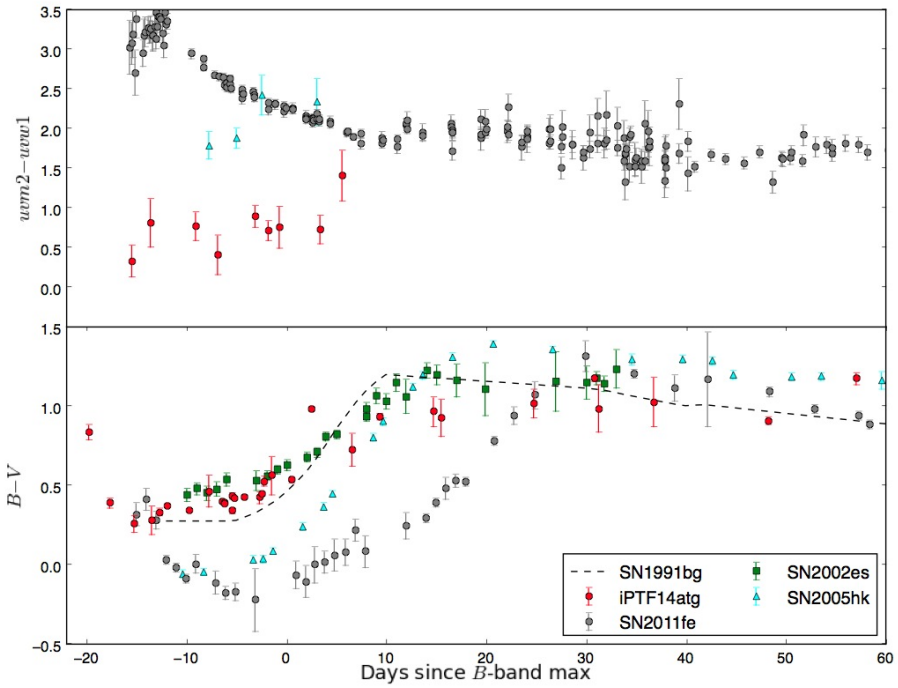

Figure 3.6: **Color evolution of iPTF14atg.** The color curves of iPTF14atg are compared to those of SN1991bg, SN2005hk, SN2002es, and a normal event SN2011fe. The error bars denote 1-σ uncertainties.

clear absorption features commonly seen in a pre-max SN Ia, such as SI II, S II, O I, and Ca II.

In the next spectrum taken three days later after the first epoch, iPTF14atg started to show characteristic spectral features like Si II and Ca II. In the spectrum taken on eleven days before maximum, we clearly identified Si II absorption around 6100 Å. Its minimum corresponds to an expansion velocity of $10,000\,\mathrm{km\,s^{-1}}$. This velocity is lower than that of SN2011fe at a similar phase (Parrent *et al.*, 2012).

In the spectrum one week before its maximum brightness (first panel of Figure 3.7), we identify absorption features such as Si II, the S II "W" profile around 5000 Å, and O I. The spectral features match well to the SN1991bg spectrum at a similar phase. However, the velocities of the absorption lines in iPTF14atg are lower than those in SN1991bg by about $3,000\,\mathrm{km\,s^{-1}}$. The Ti II trough in iPTF14atg around 4200 Å is also not as deep as that in SN1991bg. On the other hand, this iPTF14atg spectrum is distinct from that of the SN2002cx-like

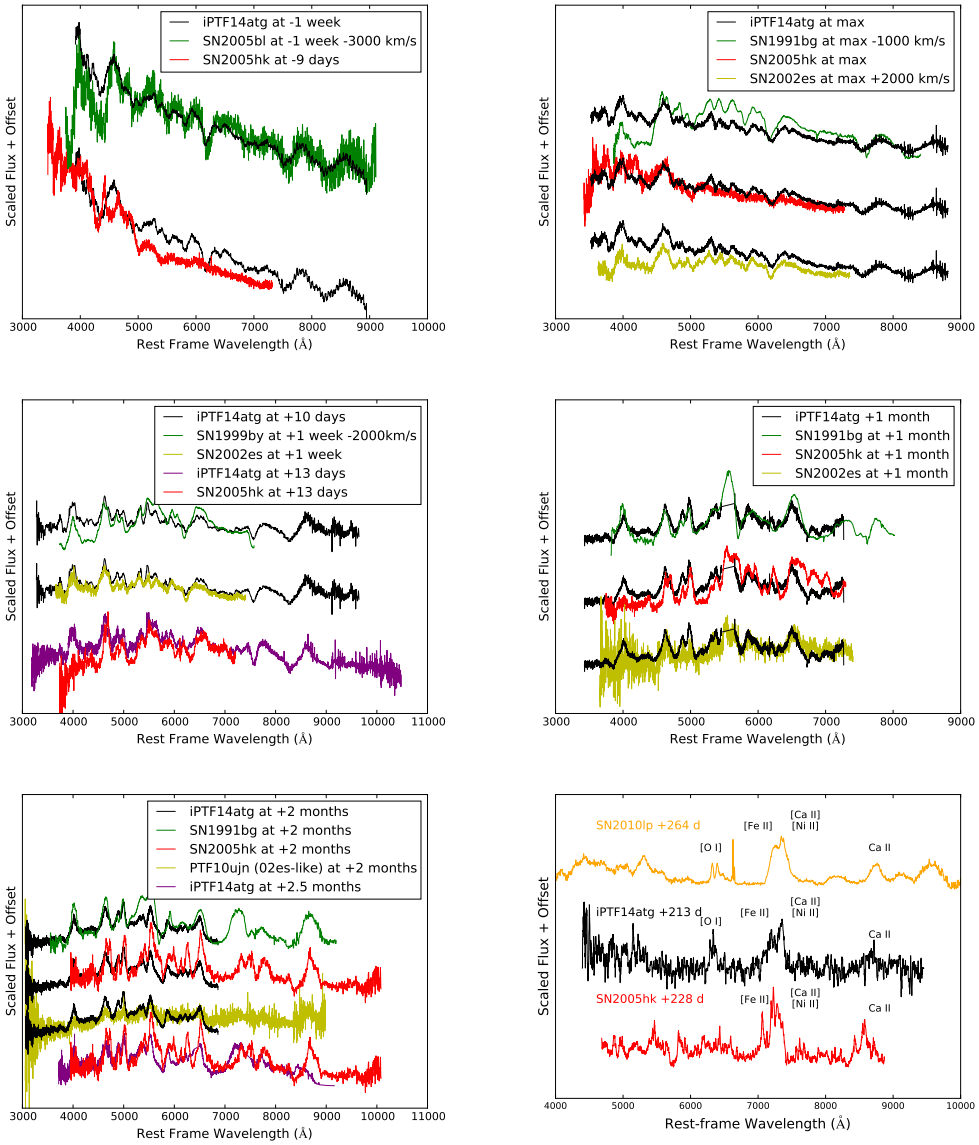

Figure 3.7: **Spectral comparison between iPTF14atg and well-studied subluminous SNe.** iPTF14atg spectra in comparison to those of SN1991bg family (SN1991bg, SN2005bl), SN2002es family (SN2005hk), and SN2002es family (SN2002es, SN2010lp, PTF10ujn) at similar phases.

SN2005hk which shows very weak Si II absorption and no Ti II.

Near the SN peak (second panel of Figure 3.7), the spectrum of iPTF14atg shares similar absorption features with all the three subluminous families, though the depth of the absorptions and the continuum shapes differed among them. iPTF14atg had line velocities in between those of SN1991bg (higher velocities) and SN2005hk (lower velocities). The best match to the overall spectral shape was found between iPTF14atg and SN2002es.

The post-maximum spectral evolution (third to fifth panels of Figure 3.7) shows that iPTF14atg shares many spectral similarities with SN2002cx-like events, but we do see distinct differences in the near infrared wavelengths in the late-time spectra two months after the SN peak (fifth panel of Figure 3.7).

Furthermore, at the nebular phase (sixth panel of Figure 3.7), iPTF14atg show nebular lines from [O I], [Fe II], [Ni II] and Ca II which are all seen in the nebular spectrum of subluminous SN2010lp (subtype unknown). The [O I] is not seen in the SN2005hk spectrum at a similar phase.

To sump up, based on both light curve and spectral similarities, we conclude that iPTF14atg matches best to SN2002es-like events.

Carbon feature

One interesting spectral feature of iPTF14atg is the strong and persistent C II 6580 Å absorption. The C II absorption is seen in pre-max spectra of $\simeq$ 30% normal Type Ia SNe and always disappears before the SN peak (Thomas *et al.*, 2011a; Silverman and Filippenko, 2012). Only in very few cases (Cartier *et al.*, 2014) did the carbon absorption feature persist after maximum light. The C II feature has also been reported in pre-max or max spectra of SN2002cx-like events but not in post-max spectra (Foley *et al.*, 2010; Parrent *et al.*, 2011). In the case of SN2002es, weak C II absorption maybe exist three days after maximum (Ganeshalingam *et al.*, 2012). In our case, the C II 6580 Å absorption is first seen at a velocity of $11,000\,\mathrm{km\,s^{-1}}$ in the iPTF14atg spectrum taken about 12 days before maximum light. Its velocity gradually decreased to $6,000\,\mathrm{km\,s^{-1}}$ near maximum. Then its velocity kept decreasing to $4,000\,\mathrm{km\,s^{-1}}$ two weeks after maximum, until the C II absorption disappeared. The long-lasting C II feature indicates that both high-velocity shallow layers and low-velocity deep layers of the iPTF14atg ejecta are carbon-rich, hinting incomplete burning extending deep into the ejecta. The

incomplete burning is consistent with a pure deflagration of a WD(Gamezo *et al.*, 2003).

Host galaxy

The host galaxy IC831 is morphologically classified as an elliptical galaxy (Scodeggio *et al.*, 1998) or an S0 galaxy (Huchra *et al.*, 2012). Its SDSS spectrum shows very weak Hα and [O III] emission. This suggests that the host galaxy has little star forming activity. iPTF14atg occurred about 4.6 kiloparsecs from the center of IC831. In all iPTF14atg spectra, we did not detect any Hα emission either at the SN location or underlying in the galaxy background, suggesting that iPTF14atg was born in an old population. This strongly argues against that iPTF14atg is a core-collapse SN. Furthermore, since SN2002cx-like events prefer star-forming regions while SN2002es-like events are all found in the passive galaxies (White *et al.*, 2015), the host galaxy of iPTF14atg is also consistent with those in the SN2002es family.

3.5 Implications

Our work along with recent results on possible detections of companion stars in SN2008ha (Foley *et al.*, 2014) and SN2012Z (McCully *et al.*, 2014) suggests that subluminous low-velocity SNe, such as SN2002cx- and SN2002es-like families, arise from the single degenerate channel. In contrast, there is mounting evidence that some Type Ia SNe result from the double degenerate channel (Li *et al.*, 2011a; González Hernández *et al.*, 2012). As such, Type Ia SNe may have multiple channels and determining the fraction of different channels will become the next frontier of this field. Counting the fraction of Type Ia SNe with companion interaction signatures provides a viable method to estimate the branch fraction of the single degenerate channel, as such signatures are not expected in the double degenerate channel. Prior to our discovery, searches for companion interaction have been carried out in both UV (Brown *et al.*, 2012a; Foley *et al.*, 2012; Brown *et al.*, 2012b) and ground-based optical data (Hayden *et al.*, 2010; Bianco *et al.*, 2011). However, the sample of extraordinarily early UV light curves of Type Ia SNe is very limited. Our discovery of the UV pulse demonstrates the existence of SN-companion collision signature and will also motivate future transient surveys to enlarge the UV light curve sample. Our optical observations of iPTF14atg also demonstrates that the interaction signature is not distinctive in the optical bands.

Moving forward, a fast-cadence UV transient survey will be ideal to systematically probe the companion interaction signatures of Type Ia SNe. Given the observed UV flux of iPTF14atg, ULTRASAT (a proposed space telescope aimed at undertaking fast-cadence observations of the UV sky; Sagiv *et al.* 2014) should detect such events up to 300 megaparsecs. Factoring in its field-of-view of 210 square degrees, ULTRASAT will detect three dozen Type Ia SNe of all kinds within this volume during its two-year mission lifetime. In fact, the UV flux of the SN-companion interaction is brighter at earlier phases. Thus, ULTRASAT may discover more such events at greater distances. Since up to a third of Type Ia SNe are subluminous (Foley *et al.*, 2013), ULTRASAT survey could definitively determine the fraction of events with companion interaction and thus the rate of events from the single degenerate channel.

Acknowledgement

We thank A. L. Piro, M. Kromer and J. Cohen for helpful discussion. We also thank A. Waszczak, A. Rubin, O. Yaron, A. De Cia, D. Perley, G. Duggan, O. Smirnova, S. Papadogiannakis, A. Nyholm, Y. F. Martinez, and the staff at the Nordic Optical Telescope and Gemini for observation and data reduction. Some of the data presented here were obtained at the W. M. Keck Observatory, which is operated as a scientific partnership among the California Institute of Technology, the University of California and NASA. The observatory was made possible by the generous financial support of the W. M. Keck Foundation. Some data were obtained with the Nordic Optical Telescope, which is operated by the Nordic Optical Telescope Scientific Association at the Observatorio del Roque de los Muchachos, La Palma, Spain. This work also makes use of observations from the LCOGT network. Research at California Institute of Technology is supported by the National Science Foundation. D.A.H. acknowledges support from the National Science Foundation. A.G.-Y. acknowledges support from the EU/FP7 via an ERC grant, the "Quantum Universe" I-Core program, ISF, Minerva and Weizmann-UK grants, and the Kimmel Award. M.M.K. acknowledges generous support from the Carnegie-Princeton fellowship. Supernova research at the OKC is supported by the Swedish Research Council and by the Knut and Alice Wallenberg Foundation. The National Energy Research Scientific Computing Center, which is supported by the Office of Science of the US Department of Energy under contract No. DE-AC02-05CH11231, provided staff, computational resources,

and data storage for this project. LANL participation in iPTF is supported by the US Department of Energy as part of the Laboratory Directed Research and Development program. A portion of this work was carried out at the Jet Propulsion Laboratory under a Research and Technology Development Grant, under contract with the National Aeronautics and Space Administration.

Chapter 4

SEEING SN2002ES-LIKE SUPERNOVAE AT DIFFERENT VIEWING ANGLES[†]

Yi Cao[1] & S. R. Kulkarni[1,2]

[1] Astronomy Department, California Institute of Technology, Pasadena, CA 91125, USA

[2] Caltech Optical Observatories, California Institute of Technology, Pasadena, CA 91125, USA

Abstract

In this letter, we investigate initial rise behavior of optical light curves of two SN2002es-like Type Ia supernovae, iPTF14atg and iPTF14dpk. Although these two events resemble each other around and after maximum, they show distinct early-phase behavior in the R-band. On the one hand, the steady rise of iPTF14atg lasted for 22 days with a mean rise rate of $0.2 \sim 0.3\,\mathrm{mag\,day^{-1}}$ before it reached the R-band peak (-18.05 mag). On the other hand, iPTF14dpk rose rapidly to -17 mag within a day of discovery and then slowly to its peak (-18.19 mag) with a rise rate similar to iPTF14atg. The apparent total rise time of iPTF14dpk is therefore only 16 days. We show that the emission before -17 days with respect to maximum, which is seen in iPTF14atg but missing in iPTF14dpk, can be entirely attributed to the SN-companion interaction signature. If both supernovae arise from the same progenitor channel, then the absence of the earliest emission in iPTF14dpk is a natural consequence of an unfavored viewing angle along which the supernova-companion interaction is blocked by the optically thick supernova ejecta. We further show existence of a gap phase between the onset of a supernova explosion and the first light of its radioactively powered light curve. In iPTF14atg, this gap phase is masked by emission from supernova-companion interaction.

[†]An edition of this chapter is going to be submitted to the *Astrophysical Journal letters* shortly.

4.1 Introduction

Following the discovery of a strong and declining UV pulse from a SN2002es-like supernova (SN) iPTF14atg within four days of explosion (Cao *et al.*, 2015), it becomes particularly interesting to examine the early-phase light curve of other SN2002es-like events. If the UV pulse in iPTF14atg indeed arises from collision between the SN ejected material and a companion star, due to the viewing angle effect, it should be invisible in most of other SN2002es-like events.

Thanks to nightly-cadence surveys conducted in the intermediate Palomar Transient Factory (iPTF; Rau *et al.* 2009; Law *et al.* 2009), we found two SN2002es-like events in 2013–2015, internally designated as iPTF14atg and iPTF14dpk. Both events have well-sampled optical light curves and spectroscopic coverage. In this letter, we analyze the early-phase rise behavior of these two events.

The letter is organized as follows: in §4.2 we establish their similarities to SN2002es. In §4.3 we present the different rise behavior of the two events and seek an explanation. We conclude this letter in §4.4.

4.2 Similarity of the two events

The observations of iPTF14atg and iPTF14dpk were obtained in the Mould-R filter with the 48-inch Schmidt telescope at Palomar Observatory. The host galaxy light is subtracted with pre-SN reference images by using the image differencing technique. The light curves are produced by the PTF-IPAC forced photometry pipeline which performs point-spread-function photometry at the location of a transient on the difference images. All magnitudes are in the AB system and calibrated to the SDSS catalog.

The spectra of iPTF14atg were published in Cao *et al.* (2015) and presented in Chapter 3. The spectra of iPTF14dpk were obtained at -10 days with the double spectrograph (DBSP; Oke and Gunn 1982) on the Palomar 200-inch Hale telescope, and at +20 and +50 days with the Low-Resolution Imaging Spectrometer (LRIS; Oke *et al.* 1995). The spectra were reduced using standard IRAF/IDL routines. All spectra are corrected for the Galactic extinction with $R_V = 3.1$ (Fitzpatrick, 1999). The spectra are made public on WISeREP (Yaron and Gal-Yam, 2012).

In order to correct for the Galactic extinction, we use the Fitzpatrick (1999)

Table 4.1. Two SN2002es-like Events in iPTF

Name	Coordinate (J2000)	Redshift	μ[a]	Host Type	$E(B-V)$[b]	Peak MJD[c]	Peak Mag.[c]
iPTF14atg	$12^h52^m44.84^s$ $+26°28'13.0''$	0.0213	34.92	E-S0	0.011	56802.1	-18.05 ± 0.02
iPTF14dpk	$16^h45^m19.35^s$ $+40°09'41.3''$	0.0387	36.23	Starburst	0.012	56878.1	-18.19 ± 0.02

[a]The distance moduli μ are calculated with $H = 67.77\,\mathrm{km\,s^{-1}\,Mpc^{-1}}$ (Planck Collaboration *et al.*, 2014). No redshift-independent distance measurement is available for the host galaxies of these events on the NASA/IPAC Extragalactic Database (NED).

[b]The Galactic extinction map is given by Schlafly and Finkbeiner (2011).

[c]The peak modified Julian dates (MJD) and magnitudes are measured from the PTF r-band light curves. The peak magnitudes do not include uncertainties from μ.

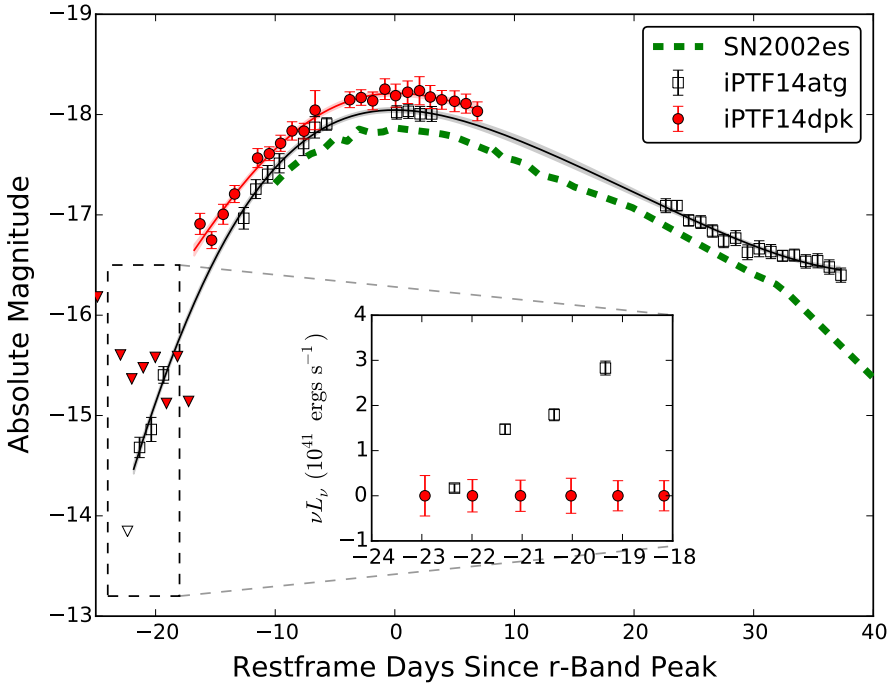

Figure 4.1: ***R*-band Light curves of iPTF14atg and iPTF14dpk.** Black empty squares are iPTF14atg and red filled stars denote iPTF14dpk. Detection upper limits (5-σ) of pre-SN non-detections for iPTF14atg and iPTF14dpk are denoted by black empty and red filled downward triangles, respectively. The best interpolated light curves of iPTF14atg and iPTF14dpk with uncertainties from the Gaussian process regression are shown in red and black curves, respectively. For comparison, the green dashed curve shows the r-band light curve of SN2002es. The inset zooms in the early-phase light curves of iPTF14atg and iPTF14dpk in the νL_ν space.

model with $R_V = 3.1$. We do not see obvious Na I D absorption in our SN spectra. Since Na I D absorption is correlated with the local extinction (Poznanski *et al.*, 2012), neither iPTF14atg nor iPTF14dpk is embedded in a dusty circumstellar medium. Therefore we do not correct for local extinction in our following analysis.

The primary data of the two events are summarized in Table 4.1. Their light curves and spectra are shown in Figures 4.1 and 4.2, respectively.

Next, in order to determine their peak magnitudes and dates, we use Gaussian process regression to interpolate the light curves. A squared exponential function is chosen as the autocorrelation function and the autocorrelation length is determined by the maximum likelihood estimation based on available data

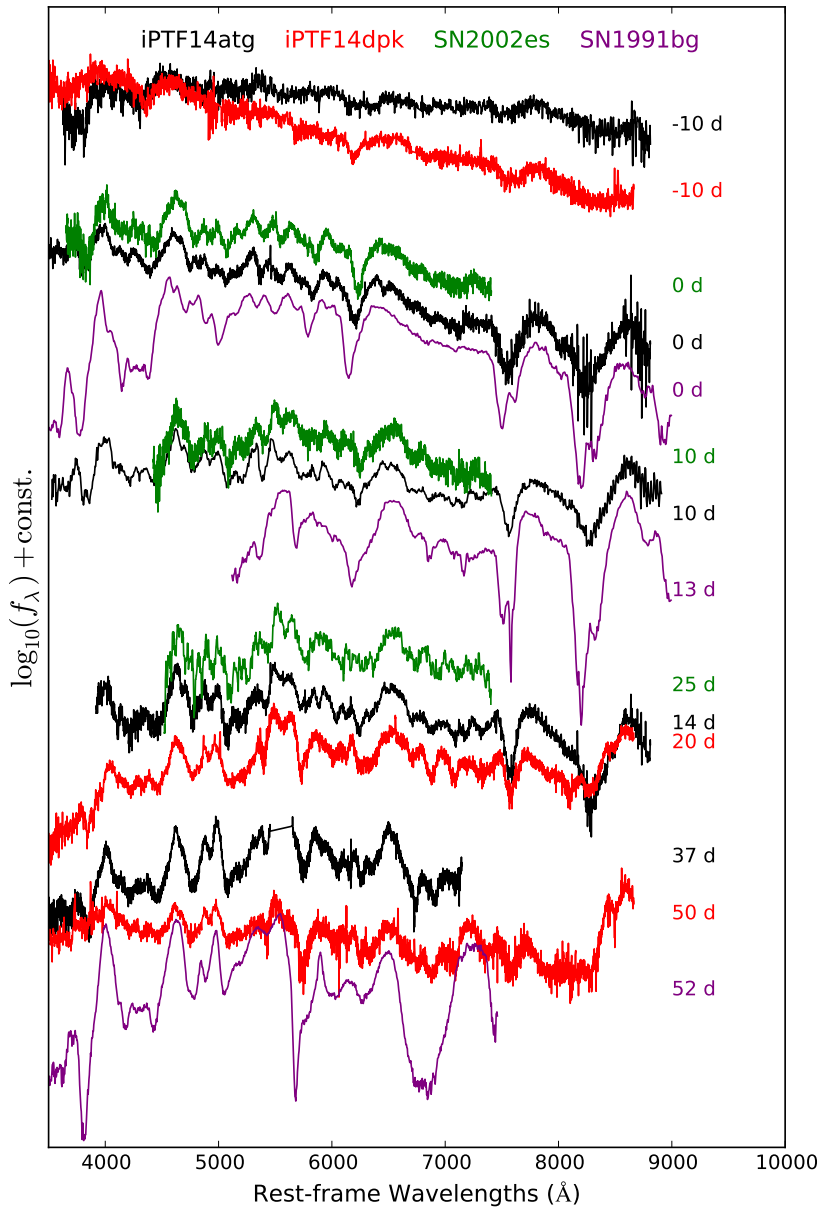

Figure 4.2: **Spectral sequences of iPTF14atg and iPTF14dpk.** The iPTF14atg spectra are taken from Cao *et al.* (2015) and shown in black while the iPTF14dpk spectra are in red. For comparison, we also show spectra of SN2002es (green; Ganeshalingam *et al.* 2012) and SN1991bg (purple, Filippenko *et al.* 1992a). The phase of each spectrum is shown next to the spectrum.

(Figure 4.1). Thanks to the almost nightly photometric sampling, the regression analysis determines both the peak dates and magnitudes with small uncertainties, as shown in Table 4.1.

We calculate k-correction in the R-band for these two SNe at phases when spectra are available, and find that the k-correction is $\lesssim 0.2$ mag. As a result, going forward, we neglect the k-correction.

As shown in Figure 4.1, apart from the first few days after explosions, the light curves of both iPTF14atg and iPTF14dpk are quite similar. Both light curves also resemble that of SN2002es around maximum, though iPTF14atg does not show the fast decline seen in SN2002es after $t \simeq 30$ days. The R-band peak magnitudes of iPTF14atg (-18.05 mag), iPTF14dpk (-18.19 mag) and SN2002es (-18.35 mag) are also comparable.

As can be seen in Figure 4.2, the spectra of iPTF14atg and iPTF14dpk around and after maxima also match those of SN2002es at similar phases. In particular, both iPTF14atg and iPTF14dpk show the low-velocity absorption lines and Ti II troughs, hallmark of SN2002es-like SNe. Next, the spectra of iPTF14atg and iPTF14dpk taken at -10 days share broad absorption features, although the continuum emission of iPTF14dpk looks bluer than that of iPTF14atg. This color difference might be due to residuals from imperfect subtraction of galaxy light in the spectra of iPTF14dpk, as iPTF14dpk is located close to the center of its very blue host galaxy in an interacting galaxy pair. In subsequent spectra, the spectral features and absorption lines of iPTF14atg and iPTF14dpk both match quite well to those of SN2002es.

Integrating the spectra and calibrating to the broadband photometry, we obtain an optical luminosity of $3 \times 10^{42}\,\mathrm{ergs\,s^{-1}}$ for both SNe around maximum. Since SN radiation around maximum is concentrated in the optical, the optical luminosity is a good approximation to the bolometric luminosity. In the case of iPTF14atg, the explosion date is tightly constrained by the SN-companion collision and therefore its rise time to the r-band maximum is 22 days. Following Scalzo *et al.* (2012), we estimate a total ^{56}Ni mass of $0.14 M_{\odot}$. In contrast, as discussed in §4.3, iPTF14dpk may experience a "dark" period after the explosion. Therefore its light curve only provides a lower limit to the actual explosion date and hence a lower limit to the ^{56}Ni mass of $0.11 M_{\odot}$.

In addition, the main difference of SN2002es-like events from classical sub-

luminous SN1991bg-like events is that the former exhibit low velocity absorption features. As shown in Figure 4.2, around maximum, although the overall spectral shapes look similar among SN2002es-like events and SN1991bg, the velocities of the absorption lines, such as Si II, are obviously lower in SN2002es-like events than in SN1991bg by several thousand $\mathrm{km\,s^{-1}}$. At late time, SN2002es-like events develop multiple narrow features between 5000 Å and 7000 Å while these features are blended in the spectra of SN1991bg-like events (Jha *et al.*, 2006).

4.3 Light curves at early phases

As noted in the previous section, iPTF14atg and iPTF14dpk exhibit distinct behavior at early phases. it took iPTF14atg more than a week to rise to -17 mag with a mean rise rate of $0.2 \sim 0.3\,\mathrm{mag\,day^{-1}}$. In contrast, iPTF14dpk shows a steep rise to $r = -16.9$ mag within one day of its last non-detection of $r > -15.1$ mag, indicating an initial rise rate $> 1.8\,\mathrm{mag\,day^{-1}}$. In the subsequent epoch, the seemingly decline in the light curve is not statistically significant.

At first blush, the pre-SN 5-σ upper limits of iPTF14dpk in the magnitude plot may mislead the readers into concluding that the upper limits of iPTF14dpk are consistent with the early detections of iPTF14atg. However, when viewed by νL_ν, the early detections of iPTF14atg are distinct from the non-detections of iPTF14dpk at similar epochs by more than 3 σ (see the inset of Figure 4.1). If we approximate measurement noises with Gaussian distributions, the probability that iPTF14dpk pre-SN non-detections are consistent with the early-phase detections of iPTF14atg is less than 3×10^{-9}.

Given the spectroscopic typing and almost identical light curves (apart from the early rise), we make a simple and reasonable assumption that *all* SN2002es-like events arise from the same progenitor family. As noted in §4.1, the observed early declining UV pulse from iPTF14atg provides evidence for the SD progenitor channel.

In the case of iPTF14atg, the Rayleigh-Jeans tail of the early UV pulse, which arises from the SN-companion collision, also dominates SN emission in the optical. In order to show this, we first fit the SN-companion collision model (Kasen, 2010) to the observed UV pulse. Following Chapter 3, a good fit is obtained with an explosion energy of 3×10^{50} ergs, an ejecta mass of $1.4M_\odot$, and

a binary separation of $70R_{\odot}$. Then we calculate the r-band light curve from the best-fit model and compare it to the observed light curve of iPTF14atg. As shown in the upper panel of Figure 4.3, the light curve before -17 days can be entirely attributed to the Rayleigh-Jeans tail emission from the SN-companion collision. After that, radioactive energy from ^{56}Ni decay heats up the SN photosphere and powers the rest part of its light curve.

Given a binary separation of $70R_{\odot}$ and an ejecta velocity of $5 \times 10^3\,\mathrm{km\,s^{-1}}$, the SN ejecta hit the companion star within three hours of SN explosion. Here the SN-companion signature provides a more accurate approximation to the explosion date for a Type Ia SN than any explosion date derived from model-dependent extrapolation of SN light curves.

Since the SN-companion collision is responsible to the optical emission earlier than -17 days, there exists a gap phase between the explosion at -22 days and visibility of the radioactively powered light curve starting which is seen at -17 days or later. If iPTF14atg had been observed in an unfavored viewing angle along which the SN-companion collision is blocked by the optically thick ejecta, the SN would end up with a "dark" period of a few days after the SN explosion but before the radioactively powered SN emission becomes visible. This viewing angle effect provides a natural explanation to the absence of emission from iPTF14dpk at -17 days or earlier.

In fact, as noted in Kasen (2010), given typical mass ratios of a few for SD progenitor binaries for Type Ia SNe, only $< 10\%$ of the resulting explosions would have geometry that would allow the SN-companion collision signature to be seen by a randomly located observer. For the remaining $> 90\%$ events, there is little light emission at this stage until the radioactive decay energy brightens the SN.

Not only in iPTF14dpk and iPTF14atg, the "dark" period has also been proposed in the normal SN2011fe in analysis of its spectral line velocity evolution (Hachinger *et al.*, 2013; Piro and Nakar, 2014). This " dark" period can be understood by considering locations of the receding photosphere and the outgoing energy diffusive front which originates at the shallowest layer where ^{56}Ni is deposited. The "dark" period ends when the energy diffusive front meets and heats up the photosphere. As shown in a toy model in Figure 4.4, a deep deposition of ^{56}Ni can delay the first light of a SN by a few days, compared to a shallow deposition.

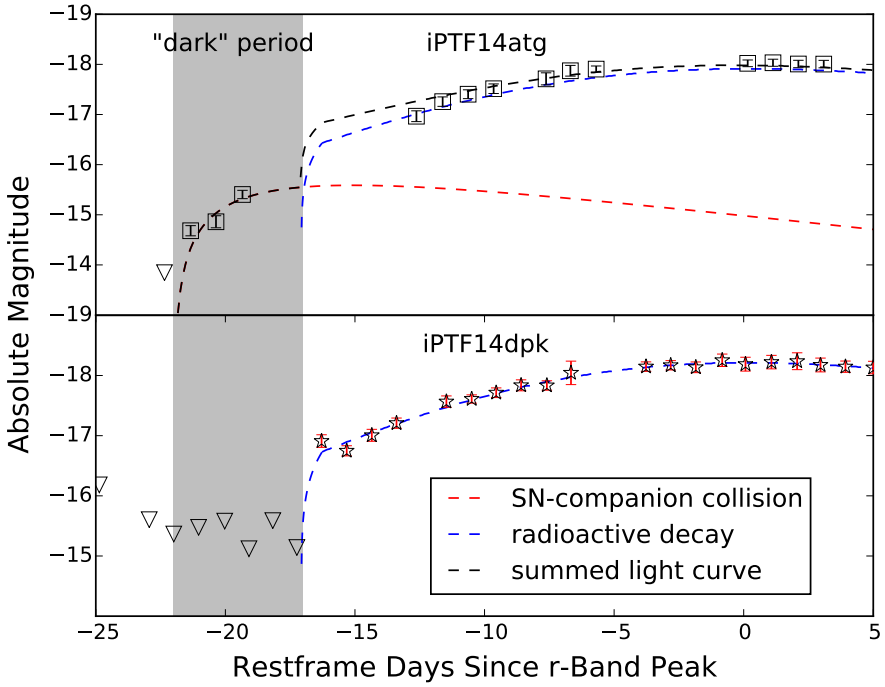

Figure 4.3: **Light curve analysis of iPTF14atg and iPTF14dpk.** *Upper panel:* The early r-band light curve of iPTF14atg has two component: the earlier component (red dashed curve) is the Rayleigh-Jeans tail of the thermal emission computed from SN-companion collision model. The later component (blue dashed curve), powered by ^{56}Ni, is represented by the iPTF14dpk light curve offset by 0.3 mag to match the peak magnitude of iPTF14atg. *Lower panel:* The early r-band light curve of iPTF14dpk is purely powered by ^{56}Ni. The post-explosion "dark" period is highlighted in gray.

Very recently, Piro and Morozova (2015) performed conceptually similar but more sophisticated calculations on the durations of the "dark" period for normal Type Ia SNe with different ^{56}Ni depositions. They used more realistic WD models from MESA (Paxton *et al.*, 2011), added ^{56}Ni at different deposition depths, and performed radiative transfer calculations with SNEC (Morozova *et al.*, 2015). They found that deep deposition of ^{56}Ni in a normal Type Ia SN may lead to a "dark" period of a couple of days.

A Side Note About iPTF14dpk

The sharp rise of iPTF14dpk was initially considered to be a possible SN-companion interaction signature, but our further analysis soon denied this hypothesis. According to the scaling relations in Kasen (2010), the luminosity

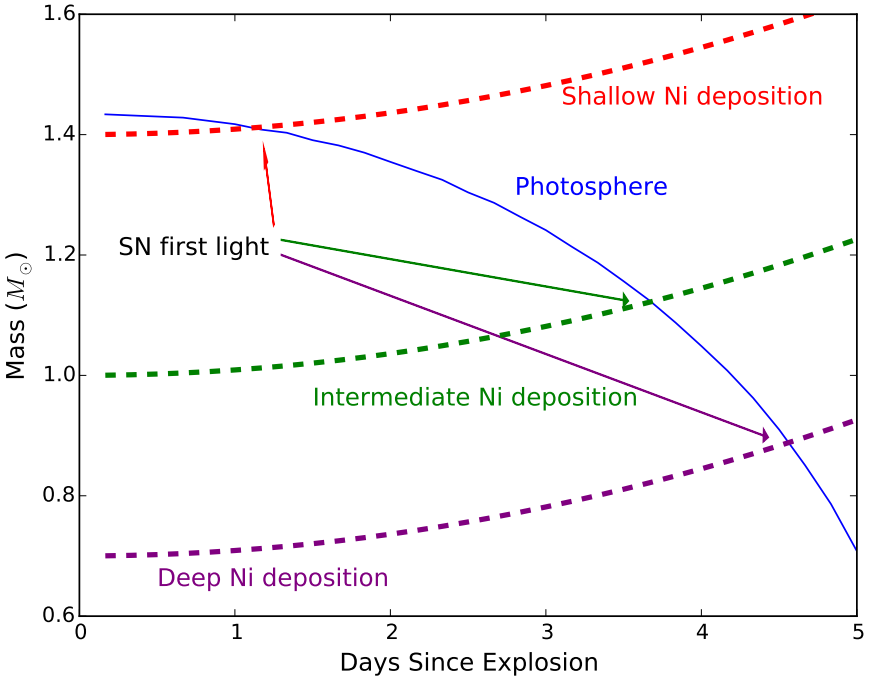

Figure 4.4: **Locations of photosphere and diffusive fronts as a function of time since explosion.** The y-axis is the mass coordinate of the SN ejecta. The location of photosphere (blue solid curve) is calculated for a $1.44M_\odot$ white dwarf model with a constant opacity $0.2\,\mathrm{cm^2\,g^{-1}}$ and a SN expansion velocity $10^5\,\mathrm{km\,s^{-1}}$. The dashed red, green, and purple curves correspond to diffusive wavefronts for the shallowest ^{56}Ni layer located at $1.4M_\odot$, $1.0M_\odot$, and $0.7M_\odot$. The propagation of the diffusive wavefront is approximated by $\Delta M \propto t^2$. The intersection points between the solid curve and the dash curves represent the time of SN first light.

from a SN-companion collision $L \propto aE^{7/8}M^{-7/8}$ and the effective temperature $T \propto a^{-1/4}$, where a is the binary separation, E is the explosion energy and M is the total ejecta mass. Since the temperature is very high, the radiation flux in the R band can be approximated by the Rayleigh-Jeans law, i.e., $f_\nu \simeq L/(\sigma T^4) \times 2kT\nu^2/c^2 \propto LT^{-3} \propto E^{7/8}M^{-5/8}a^{1/4}$. As such, the r-band flux is insensitive to the binary separation. If iPTF14dpk has an ejecta mass similar to iPTF14atg, then in order to fit the first detection of $R = -17\,\mathrm{mag}$ of iPTF14dpk, its explosion energy has to be $E \gtrapprox 2 \times 10^{51}\,\mathrm{ergs}$. Such a large explosion energy would then lead to an expansion velocity significantly higher than the low expansion velocity of iPTF14dpk derived from its spectral lines. Furthermore, as the effective temperature remains high, the expansion of the

SN would make the R-band flux increase rapidly with time. However, we do not see a fast-rising light curve after the first epoch of iPTF14dpk.

4.4 Discussion and conclusion

In this letter, we compare R-band light curves of two low-velocity SN2002es-like Type Ia SNe, iPTF14atg and iPTF14dpk, from the intermediate Palomar Transient Factory. Both are photometrically and spectroscopically similar to the prototypical SN2002es (Ganeshalingam *et al.*, 2012). Despite their similarities around and after maximum, we observed distinct initial rise behaviors in these two events. While iPTF14atg experiences a steady and slow rise which lasts for 22 days, iPTF14dpk shows a sharp initial rise to -16.9 mag within a day of discovery and then joins the rise behavior of iPTF14atg. The observed rise time of iPTF14dpk is only 16 days.

Based on the spectroscopic typing and similar photometric evolution, and based on the observed early declining ultraviolet pulse in iPTF14atg (Cao *et al.*, 2015), we make a reasonable assumption that all SN2002es-like events arise from the single-degenerate progenitor channel. By analyzing the early R-band light curve of iPTF14atg and iPTF14dpk, we show that:

- Due to deep deposition of ^{56}Ni, SN2002es-like events experience a post-explosion gap phase before radioactive decay energy brightens the SNe.
- In the case of iPTF14atg, since the event was observed along a favorable viewing angle, the gap phase was masked by Rayleigh-Jeans emission from the SN-companion collision.
- Like most other SN2002es-like SNe, iPTF14dpk did not show SN-companion collision signature because the viewing angle is not preferred. As a result, it experienced a "dark" period in the gap phase before it became visible. The duration of this "dark" period depends on the shallowest deposition depth of ^{56}Ni.

Moving forward, a large sample of young SN2002es-like light curves will be valuable to verify the viewing geometry effect as well as the "dark" period scenario. Furthermore, this sample will also put constraints on the geometry of the SD progenitor systems for SN2002es-like events. The upcoming Zwicky Transient Facility (Smith *et al.*, 2014) and the planned wide-field fast-cadence

ultraviolet surveys, such as ULTRAIST (Sagiv *et al.*, 2014), will provide opportunities to collect the sample in both the optical and UV, respectively. Additionally, since the presence of a companion star in a SN explosion also affects the spherical symmetry of the SN ejecta, spectropolarimetric follow-up observations of SN2002es-like SNe will also provide independent constraint on the viewing angles (Kasen *et al.*, 2004).

Acknowledgement

The research in the SRK group at Caltech is partly funded by the National Science Foundation.

Chapter 5

ABSENCE OF FAST-MOVING IRON IN AN INTERMEDIATE TYPE Ia SUPERNOVA BETWEEN NORMAL AND SUPER-CHANDRASEKHAR†

Yi Cao[1], J. Johansson[2], Peter E. Nugent[3,4], A. Goobar[5], Jakob Nordin[6], S. R. Kulkarni[1], S. Bradley Cenko[7,8], Ori D. Fox[4,9], Mansi M. Kasliwal[1,10], C. Fremling[11], R. Amanullah[5], E. Y. Hsiao[12,13], D. A. Perley[1], Brian D. Bue[14], Frank J. Masci[15], William H. Lee[16], Nicolas Chotard[17]

[1] Astronomy Department, California Institute of Technology, Pasadena, CA 91125, USA

[2] Benoziyo Center for Astrophysics, Weizmann Institute of Science, 76100 Rehovot, Israel

[3] Computational Cosmology Center, Computational Research Division, Lawrence Berkeley National Laboratory, 1 Cyclotron Road, MS 50B-4206, Berkeley, CA 94720, USA

[4] Department of Astronomy, University of California Berkeley, Berkeley, CA 94720-3411, USA

[5] Oskar Klein Centre, Physics Department, Stockholm University, SE-106 91 Stockholm, Sweden

[6] Institut für Physik, Humboldt-Universität zu Berlin, Newtonstr. 15, 12489 Berlin, Germany

[7] Astrophysics Science Division, NASA Goddard Space Flight Center, Mail Code 661, Greenbelt, Maryland 20771, USA

[8] Joint Space-Science Institute, University of Maryland, College Park, MD 20742, USA

[9] Space Telescope Science Institute, 3700 San Martin Drive, Baltimore, MD 21218, USA

[10] Observatories of the Carnegie Institution for Science, 813 Santa Barbara Street, Pasadena, California 91101, USA

[11] Department of Astronomy, The Oskar Klein Center, Stockholm University, AlbaNova, 10691 Stockholm, Sweden

†An edition of this chapter has been accepted for publication on the *Astrophysical Journal*.

[12] Department of Physics, Florida State University, Tallahassee, FL 32306, USA

[13] Department of Physics and Astronomy, Aarhus University, Ny Munkegade 120, 8000 Aarhus C, Denmark

[14] Jet Propulsion Laboratory, California Institute of Technology, Pasadena, CA 91125, USA

[15] Infrared Processing and Analysis Center, California Institute of Technology, MS 100-22, Pasadena, CA 91125, USA

[16] Instituto de Astronomía, Universidad Nacional Autónoma de México, Apdo. Postal 70-264 Cd. Universitaria, México DF 04510, México

[17] Université de Lyon, F-69622, France ; Université de Lyon 1, Villeurbanne ; CNRS/IN2P3, Institut de Physique Nucléaire de Lyon

Abstract

In this paper, we report observations of a peculiar Type Ia supernova iPTF13asv (a.k.a., SN2013cv) from the onset of the explosion to months after its peak. The early-phase spectra of iPTF13asv show an absence of iron absorption, indicating that synthesized iron group elements are confined to low-velocity regions of the ejecta, which, in turn, implies a stratified ejecta structure along the line of sight. By comparing its light curves and spectra to those of well-studied Type Ia supernovae, we show that iPTF13asv is an intermediate case between normal and super-Chandrasekhar events. On the one hand, its light curve shape (B-band $\Delta m_{15} = 1.03 \pm 0.01$) and overall spectral features resemble those of normal Type Ia supernovae. On the other hand, it resembles super-Chandrasekhar events in the large peak optical and UV luminosity ($M_B = -19.84\,\mathrm{mag}$, $M_{uvm2} = -15.5\,\mathrm{mag}$), the low but almost constant Si II velocities (about $10,000\,\mathrm{km\,s^{-1}}$ around peak), and its persistent C II signatures. We estimate a ^{56}Ni mass of $0.81^{+0.10}_{-0.18} M_\odot$ and a total ejecta mass of $1.59^{+0.45}_{-0.12} M_\odot$. The large ejecta mass of iPTF13asv and its stratified ejecta structure together seemingly favor a double-degenerate progenitor channel.

5.1 Introduction

Recent observations have provided mounting evidence that Type Ia supernovae (SNe) have multiple progenitor channels (see Maoz *et al.* 2014 for a review). In the single-degenerate (SD) channel, a WD accretes material from a companion star and explodes when its mass approaches the Chandrasekhar limit

(Whelan and Iben, 1973). This channel is supported by possible detections of companion stars in pre- or post-SN images (McCully *et al.*, 2014; Foley *et al.*, 2014), likely signatures of SN-companion collisions (Cao *et al.*, 2015; Marion *et al.*, 2016), and observations of variable Na I D absorption (Patat *et al.*, 2007; Sternberg *et al.*, 2014). In the double-degenerate (DD) channel, in contrast, two WDs collide or merge in a binary or even triple system to produce a Type Ia SN (e.g., Nomoto and Iben, 1985; Kushnir *et al.*, 2013). This channel is consistent with observations of two nearby Type Ia SN2011fe and SN2014J (e.g., Li *et al.*, 2011a; Brown *et al.*, 2012a; Shappee *et al.*, 2013; Margutti *et al.*, 2014; Kelly *et al.*, 2014; Goobar *et al.*, 2015; Lundqvist *et al.*, 2015). Despite these interesting constraints from individual events, the progenitors of Type Ia SNe are still unknown.

In the SD channel, rigid rotation may provide additional support for a WD of a mass slightly larger than the Chandrasekhar limit, and differential rotation may support for a even more massive WD. However, the theoretical viability of massive, rotation-supported WDs is much less clear in reality (Yoon and Langer, 2004; Saio and Nomoto, 2004; Piro, 2008; Justham, 2011; Di Stefano *et al.*, 2011; Hachisu *et al.*, 2012). In the DD channel, in contrast, the exploding WD binary may allow SN ejecta mass much higher than the Chandrasekhar limit. In fact, more than a handful of SNe have been found to have total ejecta masses significantly exceeding the Chandrasekhar limit (Howell *et al.*, 2006; Hicken *et al.*, 2007; Yuan *et al.*, 2010; Yamanaka *et al.*, 2009; Scalzo *et al.*, 2010; Silverman *et al.*, 2011; Scalzo *et al.*, 2014a). However, these super-Chandrasekhar SNe show distinctive characteristics compared to normal events: they are overluminous in both the optical and UV, implying a large amount of synthesized ^{56}Ni. They show low expansion velocities and long rise times, leading to massive ejecta. They also show persistent absorption from unburned carbon.

In this paper, we present observations of a peculiar Type Ia SN, iPTF13asv, which shares observational characteristics with both super-Chandrasekhar and normal Type Ia SN. It was discovered with $R = 20.54 \pm 0.16$ mag at $\alpha = 16^h22^m43^s.19$, $\delta = +18°57'35.0''$ (J2000) in the vicinity of a dwarf galaxy SDSS J162243.02+185733.8 on UTC 2013 May 1.44 (hereafter May 1.44) by the intermediate Palomar Transient Factory (iPTF; Law *et al.* 2009; Rau *et al.* 2009). No activity was seen at the same location down to 5-σ detection thresh-

olds of $R \simeq 21.0$ mag on images taken on April 30.5 and earlier. iPTF13asv was independently discovered and classified as a peculiar Type Ia by Zhou *et al.* (2013), and was designated as SN2013cv.

The apparent host galaxy of iPTF13asv does not have a redshift-independent distance measurement in the NASA/IPAC Extragalactic Database. In order to have a better comparison to other SNe, we adopt a fiducial value of the Hubble constant $H_0 = 72\,\mathrm{km\,s^{-1}\,M}pc^{-1}$. Thus the redshift 0.036 leads to a distance modulus of 35.94 mag. The peculiar motion of the host galaxy at $\sim$100 km s^{-1} introduces an uncertainty of $\lessapprox 0.05$ mag to the distance modulus. The Galactic line-of-sight extinction is $E(B-V) = 0.045$ (Schlafly and Finkbeiner, 2011). We correct for the Galactic extinction by using the parameterized model in Fitzpatrick (1999) with $R_V = 3.1$.

This paper is organized as follows: the observational data are presented in §5.2. The photometric and spectroscopic properties are analyzed in §5.3, and we construct its bolometric light curve and estimate the total ejecta mass in §5.4. A discussion of the nature of iPTF13asv is given in §5.5 and our conclusions are summarized in §5.6.

5.2 Observations

The nightly cadence survey of iPTF (weather permitting) with the 48-inch telescope at the Palomar Observatories (P48) provides a well-sampled R-band light curve of iPTF13asv covering the pre-SN history and its rise phase. Upon discovery, we utilized the Palomar 60-inch telescope (P60; Cenko *et al.* 2006), Andalusia Faint Object Spectrograph and Camera (ALFOSC) on the Nordic Optical Telescope (NOT), and the RATIR camera mounted on the OAN/SPM 1.5-meter Harold L. Johnson telescope for multi-band photometric follow-up observations. In these images, light contamination from the host galaxy is removed with pre- or post-explosion reference images by using the image subtraction technique. Point-spread-function (PSF) photometry is then performed on subtracted images. The instrumental fluxes are then calibrated either to the SDSS catalog or by using Landolt photometric standard stars. The magnitudes in $UBVJH$ bands are in Vega system. Those in other bands are in AB system. The light curves are presented in Figure 5.1.

We also triggered target-of-opportunity observations of the *Swift* spacecraft for X-ray and UV follow-up. We used the `HEASoft` package to perform aperture

photometry on the *Swift*/UVOT images. The instrumental fluxes are corrected for coincident loss and with the PSF growth curve, and are converted to physical magnitudes with the latest calibration (Breeveld *et al.*, 2011). Post-SN reference images are acuiqred to remove host galaxy contamination. In cases of non-detection, we estimated 3-σ upper limits. We also used the `XImage` software to analyze the XRT data. In cases of non-detection, upper limits at a 99.7% confidence level are estimated. The *Swift* measurements are presented in Table 5.1.

Spectroscopic observations were undertaken with the SN Integral Field Spectrograph (SNIFS; Lantz *et al.* 2004) on the 2.2 m telescope of the University of Hawaii, the Dual Imaging Spectrograph (DIS) on the ARC 3.5 m telescope at Apache Point Observatory (APO), the Double Spectrograph (DBSP; Oke and Gunn 1982) on the 200-inch Hale telescope (P200) at Palomar Observatory, and the Folded-port InfraRed Echellette (FIRE) on the Magellan Baade Telescope at Las Campanas Observatory. The long-slit spectra taken by APO/DIS, P200/DBSP and Magellan/FIRE are extracted through the usual routines in IRAF and IDL and calibrated using observations of spectroscopic flux standard stars. Data reduction of SNIFS is outlined in Aldering *et al.* (2006). However, due to bad weather, flux calibration of SNIFS spectra was not complete. Therefore, we interpolate the multi-band light curves and "warp" the spectra with low-order polynomials to match photometric data. The spectral sequence is presented in Figure 5.2.

The light curves and spectra are made publicly available via WISeREP[1] (Yaron and Gal-Yam, 2012).

5.3 Analysis

Initial Rise and Explosion Date

In order to determine the explosion date of iPTF13asv, we follow Nugent *et al.* (2011) and model the early PTF R-band light curve of iPTF13asv as a freely expanding fireball where the luminosity increases as $\propto t^2$ and the temperature remains constant. Restricting ourselves to the light curve within four days of discovery, we find a best fit (the inset in Figure 5.1) at an explosion date of April 29.4$\pm$0.3 (95% confidence interval) with a fitting $\chi^2 = 4.3$ for five degrees of freedom. The best-fit light curve is also consistent with the non-detection

[1]WISeREP is available at `http://www.weizmann.ac.il/astrophysics/wiserep/`.

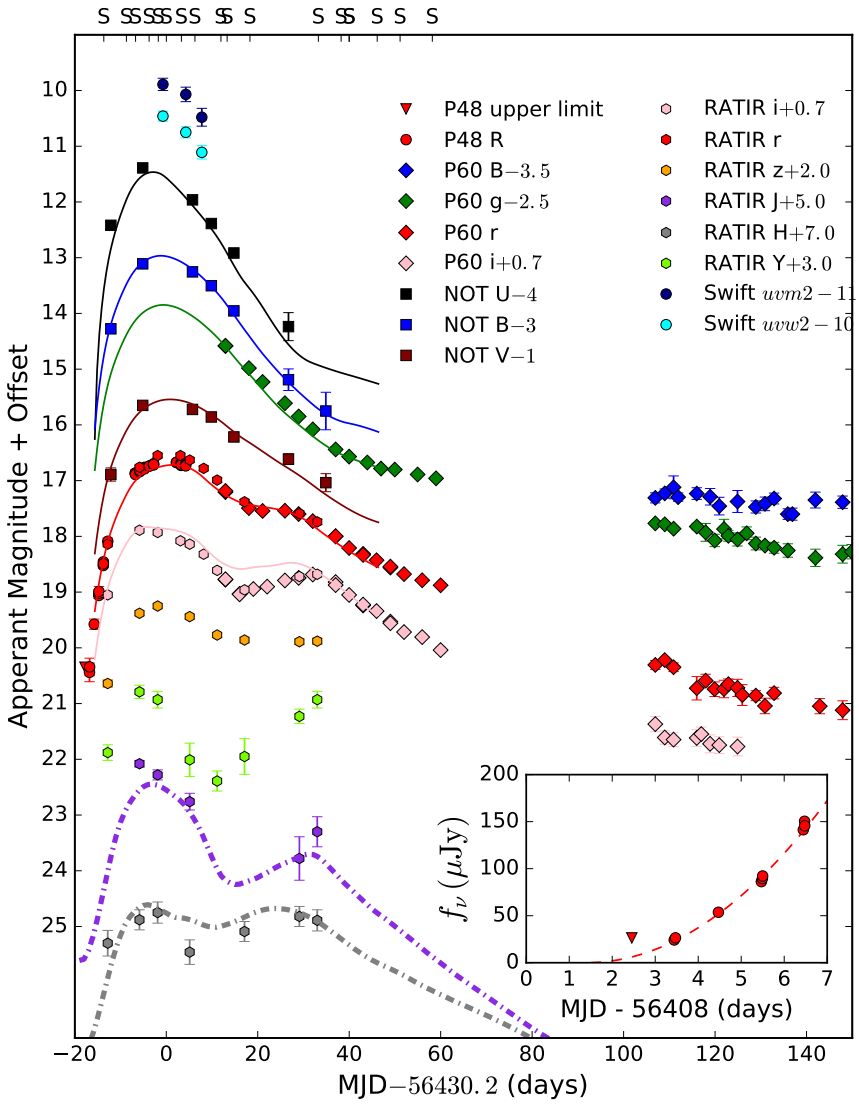

Figure 5.1: **Multi-color light curves of iPTF13asv.** Colors and shapes represent different filters and instruments, respectively. A deviation of $\simeq 0.1$ mag between the P48 R-band (red circles) and P60 r-band (red diamonds) is due to the difference between the P48 Mould R filter and the P60 SDSS r filter. The "S" ticks on the top axis denote spectroscopic observation epochs. The solid curves are SALT2 best-fit light curves in corresponding filters. The dashed-dotted curves are the IR template from Stanishev *et al.* (2015). The inset zooms into the very early phases of the PTF R-band light curve. The dashed curve in the inset shows the best t^2 law fit to the early light curve.

Table 5.1. *Swift* observations

Obs. Date	UVOT/*uvm2*		UVOT/*uvw2*		XRT	
	exp. time (s)	mag (AB)	exp. time (s)	mag (AB)	exp. time (s)	counts ($\mathrm{cnts\,s^{-1}}$)
May 17.4	1386	21.02 ± 0.08	1540	20.59 ± 0.08	2971	$< 3.6 \times 10^{-3}$
May 22.6	1154	21.25 ± 0.10	1193	20.92 ± 0.09	2382	$< 8.0 \times 10^{-3}$
May 25.9	1298	21.83 ± 0.12	1274	21.39 ± 0.10	2625	$< 4.3 \times 10^{-3}$
June 02.7	646	< 22.20	604	< 22.36	1264	$< 9.0 \times 10^{-3}$
June 10.5	462	< 21.98	464	< 22.18	928	$< 1.2 \times 10^{-2}$
June 13.4	612	< 22.37	674	< 22.46	1326	$< 8.7 \times 10^{-3}$

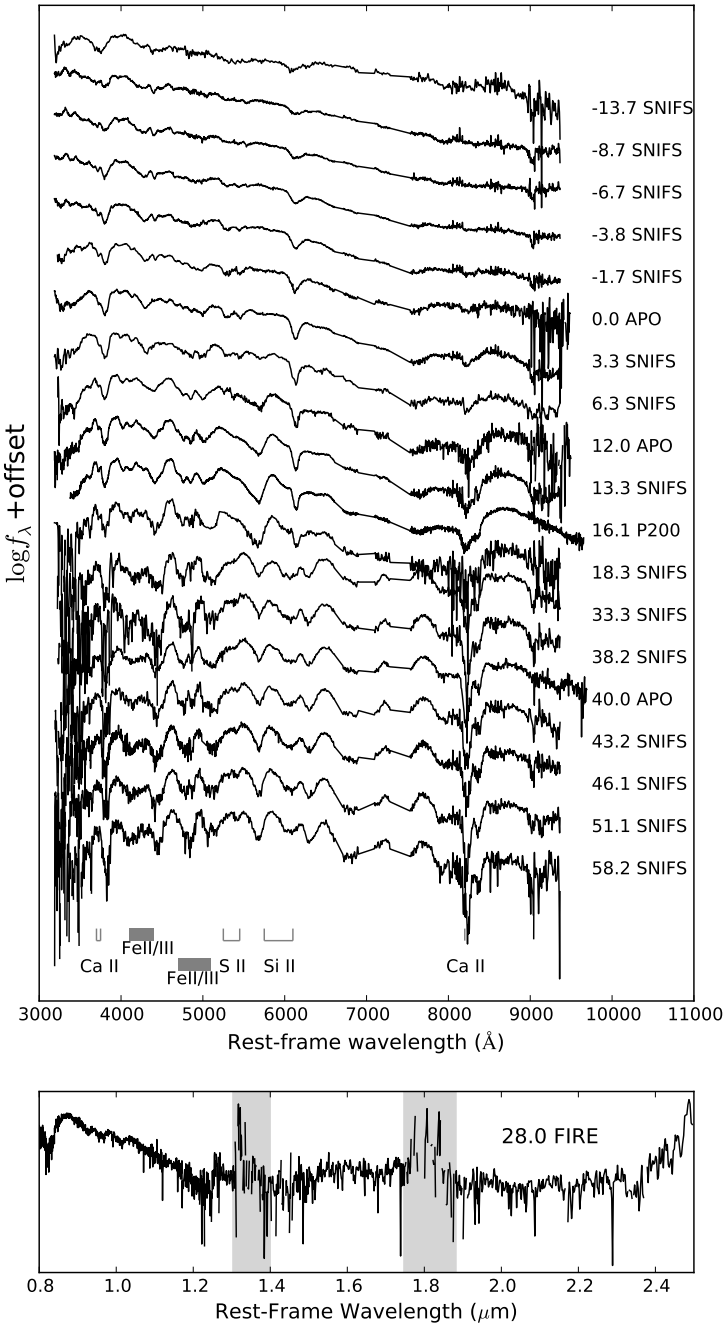

Figure 5.2: **Optical and near-IR spectral evolution of iPTF13asv.** Ticks at the bottom denote the main spectral features. The phases and telescopes/instruments are labeled next to the corresponding spectra.

upper limit on April 30.4.

If we generalize the t^2 model with a power-law model, we obtain strong degeneracy between the explosion date and the power-law index over a large range of the parameter space. In fact, Firth *et al.* (2015) analyzed the rise behavior of a large sample of Type Ia SNe with the power-law model and also found that the power-law indices have large uncertainties with a mean value of 2.5, which hints that SN photospheres are heats up by shallow-deposited ^{56}Ni. Furthermore, there could be a dark time between the SN explosion and the SN light curve powered by radioactive decay on the diffusive timescale for the shallowest deposition of ^{56}Ni in the ejecta (Piro 2012; Piro and Morozova 2015; Chapter 4). Thus, it is nontrivial to estimate the exact explosion date purely from the early light curve. Since the following analysis and discussion are not very sensitive to the exact explosion date, for simplicity, we adopt the explosion date determined by the t^2 model.

Absence of Iron in Early-phase Spectra

The most striking feature of these early-phase spectra is absence of iron absorption. We used a forward-modeling of SN spectroscopy data called SYN++ (Thomas *et al.*, 2011b) to perform spectral feature identification on the spectrum taken eleven days after explosion (or equivalently, -9.2 days with respect to the B-band maximum which is determined later in this section). As highlighted by the gray regions in Figure 5.3, the SYN++ analysis shows that the iPTF13asv spectrum shows no sign of either Fe II or Fe III.

We also compare early-phase spectra of iPTF13asv to those of well-studied normal and over-luminous Type Ia events in the top two panels of Figure 5.4. Most spectra in comparison, including the spectrum of the super-Chandrasekhar SN2009dc at -7 days, clearly show the existence of iron absorption features. The exceptions are two super-Chandrasekhar events, SN2006gz and SN2007if, which may have weak or no iron absorption. As shown in the bottom two panels of Figure 5.4, iron features appear in the iPTF13asv spectra around and after maximum.

As a result of nucleosynthesis and mixing during SN explosions, iron commonly manifests itself as absorption features in SN spectra, either as Fe II at low effective temperatures or as Fe III at high temperatures. The absence of iron at early phases implies that weak mixing during the SN explosion confines

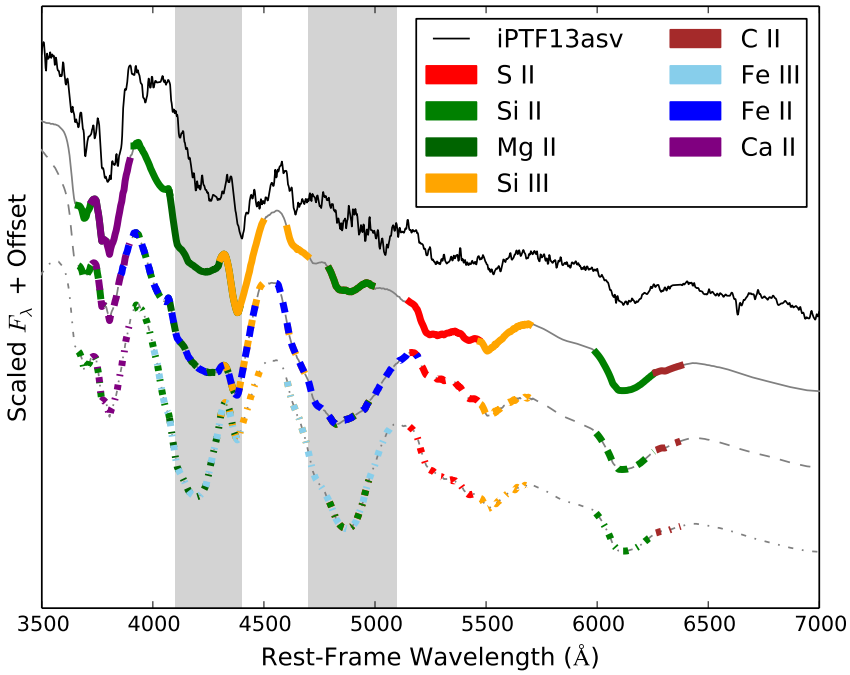

Figure 5.3: **SYN++ synthetic SN spectrum fit to iPTF13asv at -9.2 days.** From top to bottom are the observed spectrum, the synthetic spectrum without Fe (solid), the synthetic spectrum with Fe II (dashed) and the synthetic spectrum with Fe III (dash-dotted). The absorption features from different species are illustrated in different colors. The Fe II and Fe III absorption wavelength ranges are highlighted in light gray.

synthesized iron group elements in low-velocity regions of the ejecta.

The centric concentration of iron can be verified by strong UV emission at the same time, as the iron group elements are the main absorbers of photons below 3500 Å. However, we did not trigger *Swift* observations at early phases because the SN is located beyond our trigger criterion of within 100 Mpc. In comparison to the spectral shape of SN2011fe, the spectral shape of iPTF13asv at −7 days (top right panel of Figure 5.4) shows stronger fluxes towards shorter wavelengths, hinting a strong emission in the UV.

The weak mixing of iron in the SN explosion may have strong implications for the explosion mechanism and will be discussed shortly. In the next few subsections, we investigate the specifics of iPTF13asv.

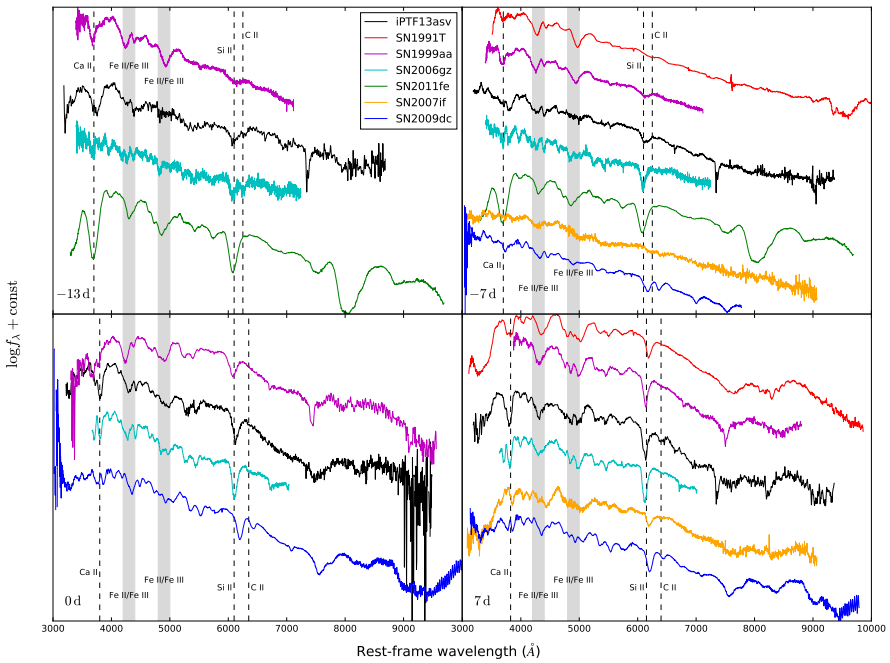

Figure 5.4: **Spectral comparison between iPTF13asv and well-studied SNe.** The well-studied SNe included normal SN2011fe (Pereira *et al.*, 2013), over-luminous SN1991T (Mazzali *et al.*, 1995) and SN1999aa (Matheson *et al.*, 2008), and super-Chandrasekhar events SN2006gz (Hicken *et al.*, 2007), SN2007if (Blondin *et al.*, 2012) and SN2009dc (Taubenberger *et al.*, 2011). The phases of the spectra are shown at the lower left corner of each panel.

Light Curves

In order to determine the light curve shape parameters of iPTF13asv, we use the SALT2 software (Guy *et al.*, 2007) to fit its optical light curve (see Figure 5.1 for the SALT2 best-fit light curves). The best-fit light curve gives a rest-frame B-band peak magnitude $m_B = 16.28 \pm 0.03$ on May 18.12 ± 0.09. We set this B-band peak date as $t = 0$ for the rest of this paper. The fit also gives a color term $c = -0.16 \pm 0.02$, and two shape parameters $x_0 = 0.0055 \pm 0.0001$ and $x_1 = 0.37 \pm 0.09$. Based on the fitted SALT2 light curve, we derive a color $(B - V)_0 = -0.14 \pm 0.03$ at the B-band maximum and $\Delta m_{15} = 1.03 \pm 0.01$ from x_1 by using the relation in Guy *et al.* (2007).

The local extinction in the host galaxy of iPTF13asv is negligible for several reasons. First, Figure 5.5 compares the $B - V$ colors between iPTF13asv ($\Delta m_{15} = 1.03$ mag) and SN2011fe ($\Delta m_{15} = 1.10$ mag). Since SN2011fe is

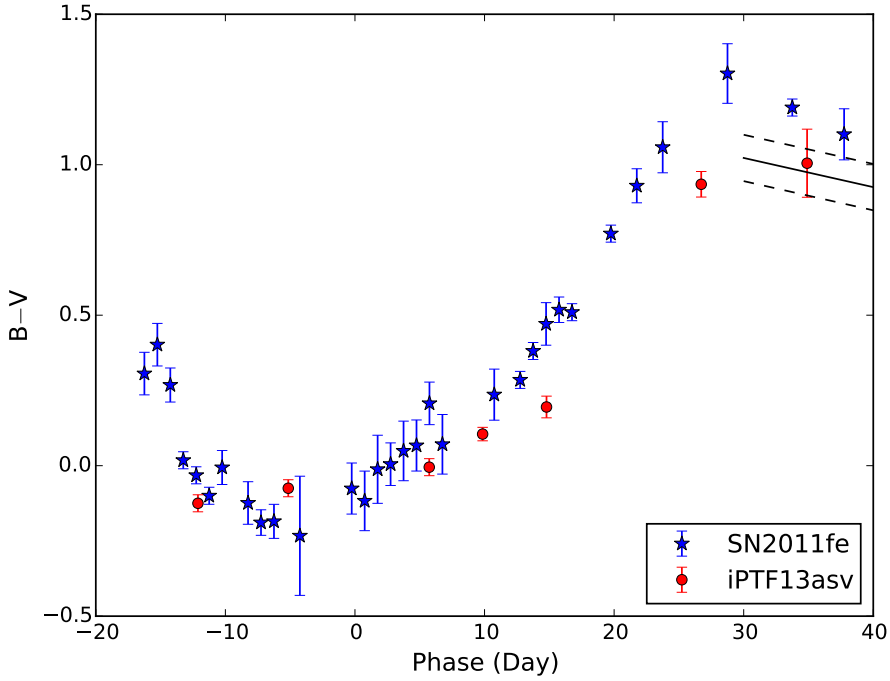

Figure 5.5: $B-V$ **color evolution of SN2011fe and iPTF13asv.** The galactic absorption is corrected for both events. The solid line shows the Lira relation from Burns *et al.* (2014) and the dashed lines corresponding to its 0.06 mag scattering.

unreddened by its host (Nugent *et al.*, 2011; Vinkó *et al.*, 2012), similar colors around maximum suggest that iPTF13asv also has little local extinction. After the maximum, iPTF13asv has a slightly blue color compared to SN2011fe, probably due to the different stretch of these two events (Nobili and Goobar, 2008), until they join the Lira relation after +30 days. Second, the intrinsic color $B-V = 0.95$ mag of iPTF13asv at +35 days is consistent with the latest calibration of the Lira relation (Burns *et al.*, 2014). Third, the absence of Na I D absorption in the low-resolution optical spectra also implies weak extinction in the host galaxy. Given a typical velocity dispersion of 10 km s^{-1} for a dwarf galaxy (Walker *et al.* 2007), we derive from the highest signal-to-noise ratio spectrum that the equivalent width for each of the Na I D lines is less than 0.2 Å (5-σ). Using the empirical relation in Poznanski *et al.* (2012), we find that the extinction $E(B-V) < 0.06$. Therefore, in what follows, we neglect the local extinction correction.

After correction for Galactic extinction we derive an absolute peak magnitude

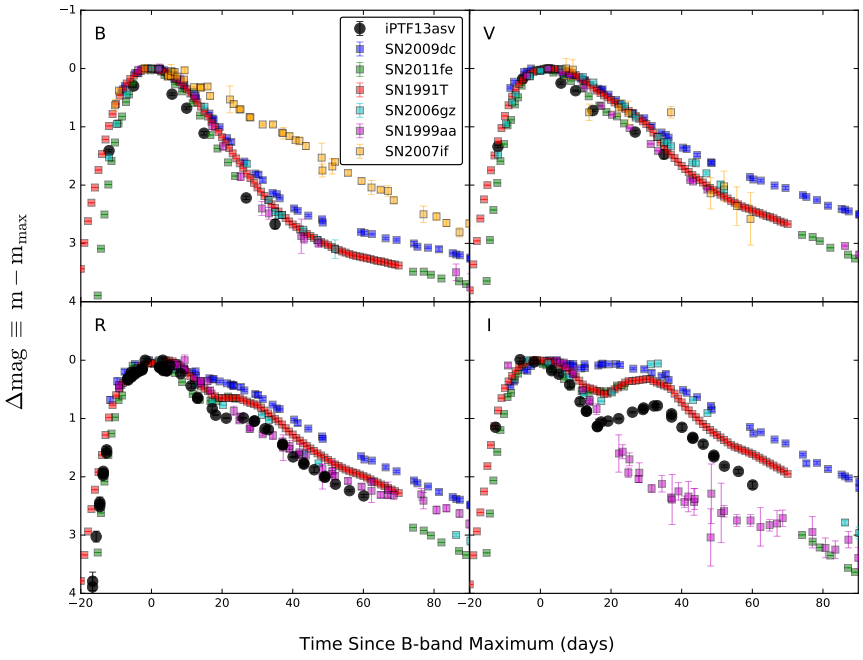

Figure 5.6: **Light curve comparison of iPTF13asv to well-studied normal and over-luminous events.** Light curve comparison of iPTF13asv to normal SN2011fe (Pereira *et al.*, 2013), over-luminous SN1991T (Nugent template) and SN1999aa (Krisciunas *et al.*, 2000), and super-Chandrasekhar events SN2006gz (Hicken *et al.*, 2007), SN2007if (Scalzo *et al.*, 2010) and SN2009dc (Silverman *et al.*, 2011). The legend colors are the same as in Figure 5.4.

of iPTF13asv in its rest-frame B-band to be -19.84 ± 0.06. This is about 0.5 mag brighter than normal Type Ia SNe at peak.

Before we compare iPTF13asv light curves to those of well-studied SNe, we establish that the k-correction in the UV and optical wavelengths is negligible. Synthetic photometry using both the Nugent SN Ia template (Nugent *et al.*, 2002) and the observed *HST* UV spectra of SN2011fe (Mazzali *et al.*, 2014). shows that the k-correction is < 0.1 mag in the optical and < 0.2 mag in the *Swift*/UVOT UV filters.

In Figure 5.6, the optical light curves of iPTF13asv are compared to those of well-studied SNe, including normal SN2011fe; overluminous SN1999aa and SN1991T; and super-Chandrasekhar SN2006gz, SN2007if, and SN2009dc. All light curves have been offset to match their peak magnitudes and shifted to

match the epoch of the B-band maxima. Figure 5.6 illustrates that (1) the light curve width of iPTF13asv is similar to those of normal events and narrower than those of overluminous and super-Chandrasekhar events, except for SN2006gz, (2) iPTF13asv shows an isolated secondary maximum in the I-band whose strength is weaker than those observed in SN2011fe and SN1991T, and (3) iPTF13asv matches well to the super-Chandrasekhar SN2006gz in the B- and V-band light curves, but SN2006gz has a much stronger near-IR secondary peak.

Figure 5.7 compares iPTF13asv in the *Swift*/UVOT $uvm2$ and $uvw2$ filters to a large sample of both normal, overluminous, and super-Chandrasekhar Type Ia SNe observed by *Swift* (Milne *et al.*, 2013; Brown, 2014). Although the $uvw2$ filter has a non-negligible leakage in long wavelengths, the $uvm2$ filter does not have a significant leakage and therefore provides the best available measurements of the UV flux. The figure shows that, like super-Chandrasekhar events, iPTF13asv is more luminous in the UV than the majority of normal events. Furthermore, Milne *et al.* (2013) divided Type Ia SNe into different subclasses based on their *Swift*/UVOT colors. We cannot make a direct comparison here because only $uvm2$ and $uvw2$ data are available for iPTF13asv. An indirect comparison is that iPTF13asv is brighter than SN2011fe by half a magnitude in the optical and by $\simeq 0.7$ mag in the UV. Since SN2011fe is a NUV-blue event (Brown *et al.*, 2012a), iPTF13asv probably belongs to the same subclass.

We also compare the IR light curves of iPTF13asv in the J- and H-band to the most recent light curve template for normal Type Ia events (Figure 5.1; Stanishev *et al.* 2015) and find that the sparsely sampled light curves of iPTF13asv roughly follow the template. The peak magnitudes of iPTF13asv are $M_J = -18.83 \pm 0.08$ and $M_H = -18.16 \pm 0.19$, compared to the median peak magnitudes of $M_J = -18.39$ and $M_H = -18.36$ with rms scatters of $\sigma_J = 0.116 \pm 0.027$ and $\sigma_H = 0.085 \pm 0.16$ for normal Type Ia SNe (Barone-Nugent *et al.*, 2012). The secondary maximum of iPTF13asv is clearly seen in the J-band and H-band light curves. The strong IR secondary peak indicates concentration of iron group elements in the central region of the ejecta (Kasen, 2006), consistent with the conclusion from the early-phase spectra.

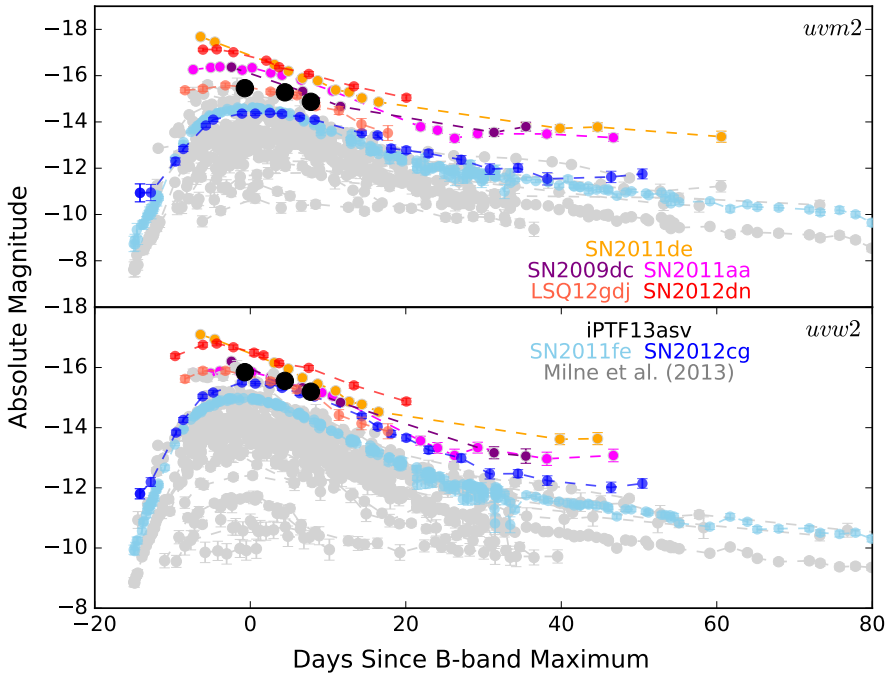

Figure 5.7: **UV light curve comparison between iPTF13asv and other SNe Ia.** A sample of SNe Ia from Milne *et al.* (2013) are shown in gray. Highlighted by different colors are light curves of iPTF13asv (black), SN2011fe (sky blue; Brown *et al.* 2012a), SN2012cg (blue), super-Chandrasekhar events SN2009dc, SN2011aa and LSQ12gdj (purple; Brown *et al.* 2014), and the most UV-luminous event SN2011de (orange; Brown 2014). All magnitudes are in the AB system.

Spectra

Spectral Cross-matching

We use the latest versions of both SN Identification (SNID; Blondin and Tonry 2007) and SuperFit (Howell *et al.*, 2005) to spectroscopically classify iPTF13asv. Before −5 days, unsurprisingly, neither programs find a good match for iPTF13asv spectra partly because they do not have many early-phase SNe in their templates and partly because the absence of iron absorption in the early-phase spectra of iPTF13asv has not been seen before. Around and after maximum, both SNID and SuperFit find that iPTF13asv matches to normal Type Ia SNe (Table 5.2).

Table 5.2. SNID results

Phase	First Five Best Matches[1]				
−6.8	05eu@−5.2 (normal)	03ic@−4.1 (normal)	08Z@−4.3 (normal)	05na@−1.5 (normal)	06cc@−9.7 (normal)
0.0	96ai@+2.2 (normal)	07F@+3.0 (normal)	94ae@0.0 (normal)	03cg@−2.1 (normal)	94ae@+0.9 (normal)
+6.8	08Z@+7.6 (normal)	05na@+3.4 (normal)	99aa@+1.8 (peculiar)	01fe@+6.2 (normal)	06cz@−2.0 (91T-like)
+13.3	08Z@+12.3 (normal)	07ca@+13.3 (normal)	07bj@+12.0 (normal)	03fa@+13.4 (91T-like)	03kf@+13.4 (normal)

[1]The format in this column is name@phase (sub-class).

Spectral comparison to well-studied SNe

Figure 5.4 compares iPTF13asv spectra to those of well-studied SNe at different epochs: normal SN2011fe (Pereira *et al.*, 2013); over-luminous SN1991T (Filippenko *et al.*, 1992b) and SN1999aa (Garavini *et al.*, 2004; Matheson *et al.*, 2008); and super-Chandrasekhar SN2006gz (Hicken *et al.*, 2007), SN2007if (Scalzo *et al.*, 2010), and SN2009dc (Taubenberger *et al.*, 2011). At −13 days (top left panel of Figure 5.4), although both SN2006gz and iPTF13asv have weak or no absorption from iron, iPTF13asv shows strong Ca II H and K absorption but SN2006gz does not. The absorption of C II is apparently weaker in iPTF13asv than in SN2006gz. Both SN1999aa and SN2011fe at similar phases show strong Ca II and iron absorptions.

At a week before maximum (top right panel of Figure 5.4), except for the prominent absence of iron in iPTF13asv, the overall spectral features of iPTF13asv are similar to those of normal SNe. Unlike the near-absence of Ca II and Si II lines in SN1991T, iPTF13asv shows apparent Ca II and Si II absorption, the strengths of which are weaker than those seen SN1991T. Besides this, its C II feature in the iPTF13asv spectrum becomes weaker.

Around maximum (lower left panel of Figure 5.4), we find good spectral matches between iPTF13asv and SN2011fe. The strength of Si II absorption in iPTF13asv is apparently between the weak absorption in SN1991T and the strong one in SN2011fe.

One week after maximum (lower right panel of Figure 5.4), the spectrum of iPTF13asv is similar to those of normal events, but with C II absorption.

Si II velocities

We further measure the expansion velocity evolution of iPTF13asv by fitting a Gaussian kernel to the Si II 6355 line in each spectrum. The continuum is modeled by a linear regression to regions at both sides of the line. Then we fit a linear model to the velocities between −10 and +10 days as a function of time and estimate a velocity of $(1.0 \pm 0.1) \times 10^4\,\mathrm{km\,s^{-1}}$ and a negligible velocity gradient at peak.

Figure 5.8 shows that Si II velocities at maximum versus peak magnitudes. As can be seen in the figure, iPTF13asv has a Si II velocity lower than the majority of normal Type Ia SNe and similar to super-Chandrasekhar events. Figure 5.9

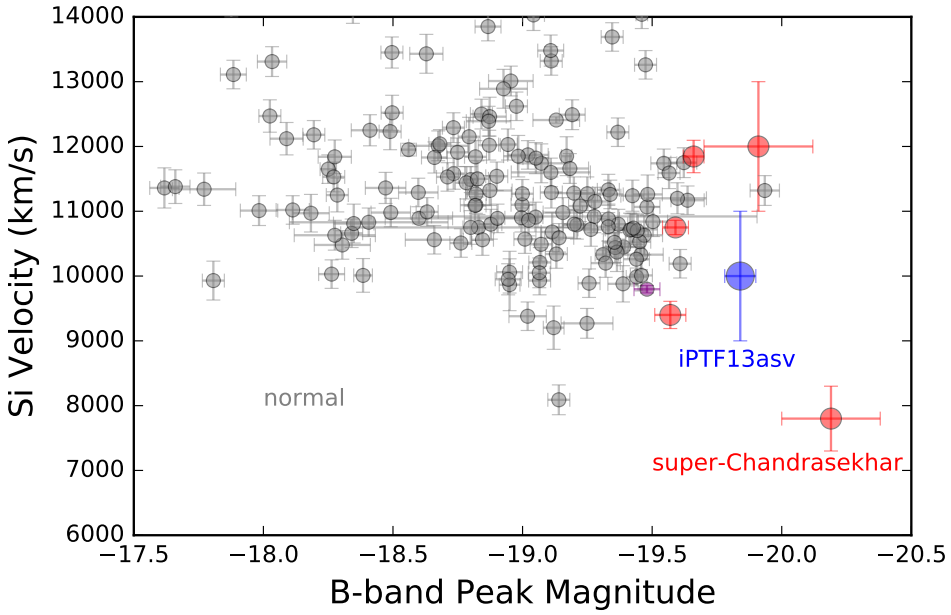

Figure 5.8: **Si II velocities at maximum vs. peak magnitude.** The gray points are measurements taken from Foley *et al.* (2011) and Scalzo *et al.* (2014b). Note that Foley *et al.* (2011) did not correct the local extinction. The red points are taken from Scalzo *et al.* (2012).

compares Si II velocity gradients at maximum versus peak magnitudes. Like super-Chandrasekhar events, iPTF13asv has a velocity gradient close to zero, lower than the majority of normal events.

Carbon signatures

We also note that iPTF13asv shows weak but persistent C II absorption features until at least a week after maximum. Figure 5.10 shows SYN++ fits to iPTF13asv spectra of high signal-to-noise ratios, demonstrating the existence of C II 6580 and C II 7234 lines. The velocity of these C II lines changes from $\simeq 14,000\,\mathrm{km\,s^{-1}}$ at -13.7 days to $\simeq 11,000\,\mathrm{km\,s^{-1}}$ at $+6.3$ days.

About 30% of normal SNe are estimated to reveal the C II 6580 and C II 7234 absorption notches in early phases (Thomas *et al.*, 2011a; Parrent *et al.*, 2011; Silverman and Filippenko, 2012). These C II features usually disappear before maximum. In contrast, some super-Chandrasekhar events show strong and persistent C II features even after maximum. Figure 5.11 compares the spectra of iPTF13asv at one week after maximum to those of well-studied

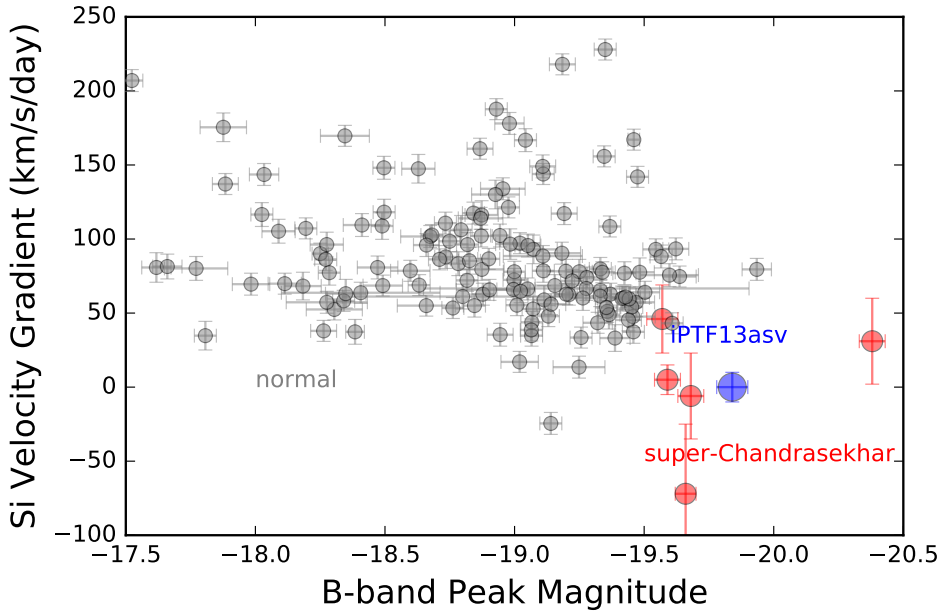

Figure 5.9: **Si II velocity gradient at maximum vs. peak magnitude** The gray points are measurements taken from Foley *et al.* (2011). Note that Foley *et al.* (2011) did not correct the local extinction. The red points are taken from Scalzo *et al.* (2012).

SNe at similar phases. As can be seen, on the one hand, neither SN1991T nor SN1999aa has the carbon feature at this phase; on the other hand, the carbon signature in iPTF13asv is not as strong as those seen in the super-Chandrasekhar SN2009dc.

Host Galaxy

After iPTF13asv faded away, we obtained a low signal-to-noise ratio spectrum of its apparent host galaxy SDSS J162254.02+185733.8. The spectrum only shows Hα emission at the redshift of iPTF13asv. We fit a Gaussian profile to the Hα line and measure a luminosity of $3 \times 10^{38}\,\mathrm{ergs\,s^{-1}}$. We adopt the empirical relation between Hα luminosity and star formation rate (Kennicutt, 1998) and obtain a star formation rate of $2 \times 10^{-3}\,M_{\odot}\,\mathrm{yr}^{-1}$ for the host galaxy.

Next, we construct the spectral energy distribution (SED) of the host galaxy with optical photometry from SDSS and near-IR photometry measured on the post-SN reference images. The SED is then modeled with a galaxy synthesis code called the Fitting and Assessment of Synthetic Templates (Kriek *et al.* 2009). We assume an exponentially decaying star formation history and a solar

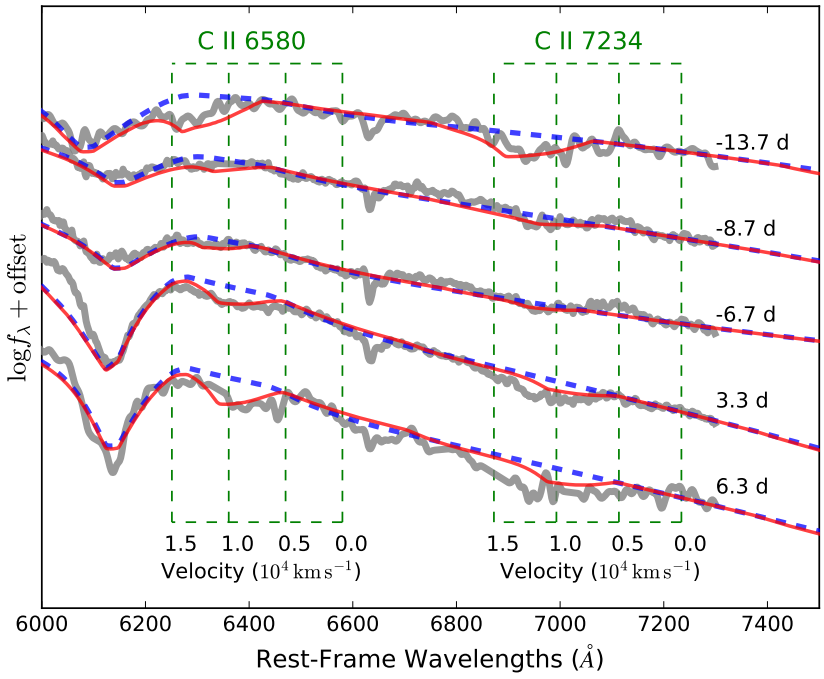

Figure 5.10: **Carbon features of iPTF13asv at different phases.** The numbers to the right of each spectrum indicate the phases in days. The observed spectra are shown in gray. The SYN++ spectra without C II are in blue and those with C II in red. The green dashed axes show velocities of C II 6580 and C II 7234 lines.

metallicity. The best-fit model gives a galaxy age of $10^{8.6}$ years and a stellar mass $\log_{10}(M_{\rm stellar}/M_\odot) = 7.85^{+0.5}_{-0.4}$ with a reduced $\chi^2 = 1.6$ (Figure 5.12). The best-fit model also shows no ongoing star-forming activity. Because SED fitting models are usually insensitive to very low star-forming rates, the best fit model is consistent with a low star-formation rate derived from the Hα flux. The derived star formation rate and the stellar mass of the iPTF13asv host galaxy follow the empirical relation between stellar mass and star formation rate (Foster *et al.*, 2012).

Since the host galaxy spectrum does not show [N II] lines, we estimate an upper limit of $\log([\text{N II}\,6548/\text{H}\alpha]) < -0.87$. Using Denicoló *et al.* (2002), we derived a metallicity upper limit of $12 + \log(\text{O/H}) < 8.3$. In fact, using the mass-metallicity relation (Foster *et al.*, 2012), we estimate a gas-phase metallicity of $12 + \log(O/H) \sim 8$ for the host galaxy. Compared to the host galaxy samples of Type Ia SNe in Pan *et al.* (2014) and Wolf *et al.* (2016),

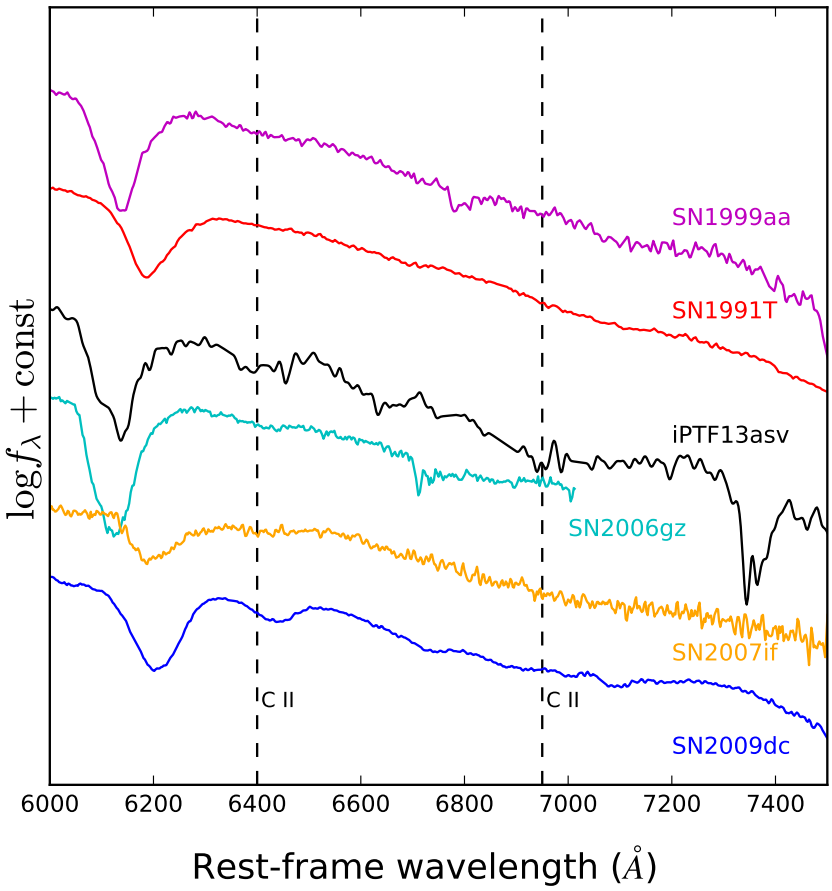

Figure 5.11: **Comparison of carbon features between iPTF13asv and well-studied overluminous events at one week after maximum.**

SDSS J162254.02+185733.8 is one of the least massive and most metal-poor galaxies that host Type Ia SNe.

5.4 Bolometric light curve and ejecta mass

Bolometric Light curve

Given the wavelength coverage of the iPTF13asv spectra, we first construct a pseudo-bolometric light curve between 3500 and 9700 Å. In order to calibrate the absolute fluxes of these spectra, we use interpolated optical light curves to "warp" the spectra. Then the spectra are integrated to derive the pseudo-bolometric light curve.

Due to the sparsely sampled UV and IR light curves, it is difficult to estimate

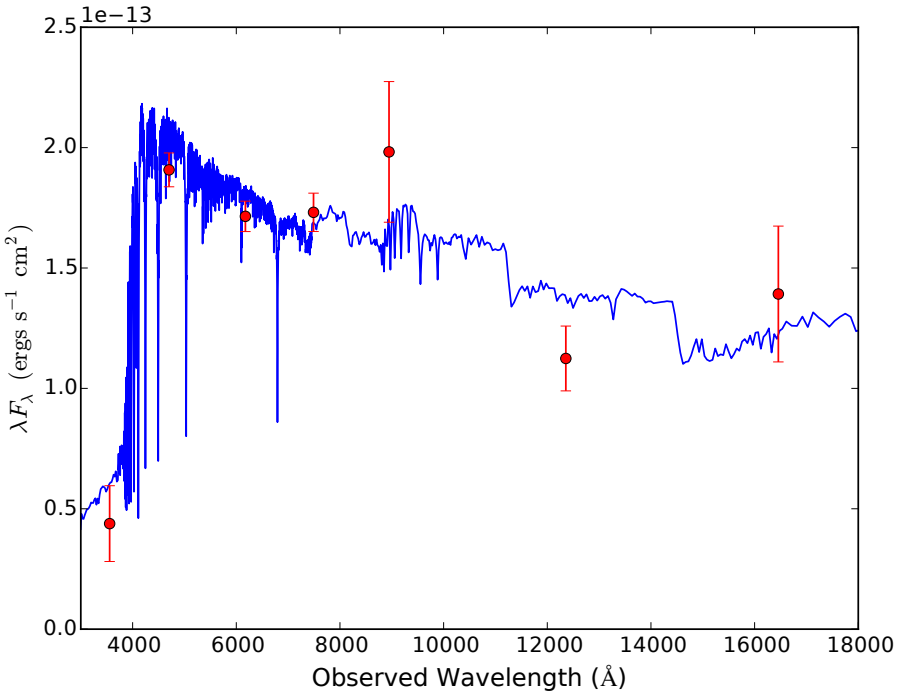

Figure 5.12: **SED fit of the host galaxy of iPTF13asv.** The data points (red) are SDSS model magnitudes in optical and aperture-photometric measurements in the near-IR RATIR reference images. The blue spectrum is the best fit from FAST.

the UV and IR radiation at different phases. Therefore we calculate optical-to-bolometric correction factors with a spectral template (Hsiao *et al.*, 2007). In this calculation, we find that the UV correction reaches about 25% before the B-band maximum and quickly drops to less than 5% around and after the B-band maximum. Given that the SN might be UV-luminous at early time and around maximum, our calculated correction probably underestimates the UV radiation. Using the *Swift* data around maximum, we estimate that this UV correction introduces a systematic uncertainty of a few percent to the bolometric luminosity. After maximum when the SN cools down, the UV contribution to the bolometric luminosity becomes even less important.

In the IR, the correction above 9700 Å is below 10% around the B-band maximum, and then reaches a maximum of 24% around the secondary maximum in the near-IR. At the epochs with IR data, we find that the calculated correction is consistent with the IR measurements.

The final bolometric light curve after UV and IR correction is shown in Figure

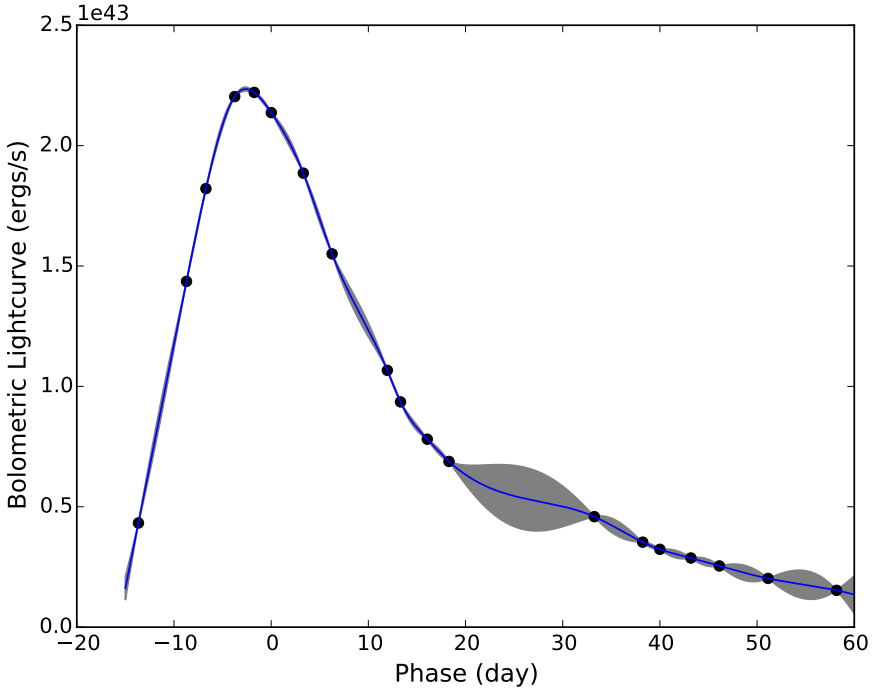

Figure 5.13: **Bolometric light curve of iPTF13asv**. The measured bolometric luminosities at different phases are in black circles. The blue curve is the best fit from the Gaussian process regression. The gray region represents the 1-σ uncertainty of the regression curve.

5.13. We further employ Gaussian process regression to derive a maximum bolometric luminosity $L_{max} = (2.2 \pm 0.2) \times 10^{43}\,\mathrm{erg\,s^{-1}}$ at -2.6 days.

^{56}Ni Mass and Ejecta Mass

Next, we follow the procedure in Scalzo *et al.* (2012, 2014c) to derive the ^{56}Ni mass and the total ejecta mass. First, the ^{56}Ni mass can be estimated through the following equation

$$L_{max} = \alpha S(t_R)\ , \tag{5.1}$$

where $S(t_R)$ is the instantaneous radioactive power at the bolometric luminosity maximum. α is an efficiency factor of order unity, depending on the distribution of ^{56}Ni (Jeffery *et al.*, 2006). We adopt a fiducial value of $\alpha = 1.3$ following Scalzo *et al.* (2012). The radioactive power of ^{56}Ni $\rightarrow^{56}$ Co $\rightarrow^{56}$ Fe is (Nadyozhin, 1994)

$$S(t_r) = \left[6.31\exp\left(-t_r/8.8\right) + 1.43\exp\left(-t_r/111\right)\right] M_{\mathrm{Ni}}\ , \tag{5.2}$$

where $S(t)$ is in units of $10^{43}\,\mathrm{erg\,s^{-1}}$ and $M_{\rm Ni}$ is in units of $M_\odot$. With the measured maximum bolometric luminosity $L_{max} = (2.2 \pm 0.2) \times 10^{43}\,\mathrm{erg\,s^{-1}}$ at -2.6 days, we obtain a ^{56}Ni mass of $(0.77 \pm 0.07) M_\odot$ directly from equation (5.1).

About one month after the SN maximum, the SN debris expands approximately in a homologous manner. At this time, most ^{56}Ni atoms have decayed to ^{56}Co. Thus the total luminosity can be approximated by

$$L(t) = \left[1 - \exp(-(t_0/t)^2)\right] S_\gamma(t) + S_{e^+}(t) \ , \tag{5.3}$$

where S_γ and S_{e^+} are the decay energy of ^{56}Co carried by γ-ray photons and positrons. In each ^{56}Co decay, a total energy of 3.61 MeV is emitted via γ photons and a total energy of 0.12 MeV is converted to the kinetic energy of positions. At time t_0, the mean optical path of γ-ray photons is unity. For a given density and velocity profile, t_0 reflects the column density along the line of sight. We fit equation (5.3) to the bolometric light curve of iPTF13asv after +20 days and obtained $t_0 = 44.2 \pm 2.0$ days.

Next, we derive the ^{56}Ni and total ejecta masses of iPTF13asv together by fitting L_{max} and t_0 simultaneously. If we assume a density profile $\rho(v) \propto \exp(-v/v_e)$ where v_e is a scale velocity, then the ejecta mass can be expressed as

$$M_{ej} = \frac{8\pi}{\kappa_\gamma q} \left(v_e t_0\right)^2 \ , \tag{5.4}$$

where κ_γ is the Compton scattering opacity for γ-ray photons . The value of κ_γ is expected to lie in the range between 0.025 and $0.033\,\mathrm{cm^2 g^{-1}}$ (Swartz *et al.*, 1995). We adopt a value of $0.025\,\mathrm{cm^2 g^{-1}}$ for the optically thin regime. The form factor q describes the distribution of ^{56}Ni and thus ^{56}Co (Jeffery, 1999). For evenly mixed ^{56}Ni, the value of q is close to one-third. Taking element stratification and mixing in the interfaces into account, Scalzo *et al.* (2014c) found that $q = 0.45 \pm 0.05$. Here, we adopt $q = 0.45$ in our estimation.

The value of v_e can be obtained by conservation of energy. The total kinetic energy of the ejecta is $6 M_{ej} v_e^2$. Neglecting the radiation energy, the total kinetic energy is equal to the difference between the nuclear energy released in the explosion and the binding energy of the exploding WD. The binding energy of a rotating WD with mass M_{ej} and central density ρ_c is given in Yoon and Langer (2005). Here we restrict the central density to lie between 10^7 and $10^{10}\,\mathrm{g\,cm^{-3}}$.

If we further assume that the ejecta is composed of unburned CO and synthesized Si, Fe and Ni, then the nuclear energy of the SN explosion is formulated in Maeda and Iwamoto (2009) as a function of mass M_{ej} and mass fractions $f_{\rm Fe}$, $f_{\rm Ni}$ and $f_{\rm Si}$. The ratio $\eta = f_{\rm Ni}/(f_{\rm Ni}+f_{\rm Fe})$ is also a function of ρ_c. Following Scalzo *et al.* (2014c), we adopt a Gaussian prior

$$\eta = 0.95 - 0.05\rho_{c,9} \pm 0.03\,\max(1, \rho_{c,9}) \ , \tag{5.5}$$

where $\rho_{c,9}$ is ρ_c in units of $10^9\,{\rm g\,cm^{-3}}$. In addition, we restrict the mass fraction $f_{\rm CO}$ less than 10%.

Based on the above assumptions, with a given set of ejecta mass M_{ej}, central density ρ_c and the mass fractions of different elements, we can calculate the peak bolometric luminosity L_{max} by equation (5.1) and t_0 by equation (5.4), and compare them with the measured values of iPTF13asv. Here we perform Markov-Chain Monte-Carlo simulations for a million steps and obtain $M_{Ni} = 0.81^{+0.10}_{-0.18}$ and $M_{ej} = 1.44^{+0.44}_{-0.12} M_\odot$ at a 95% confidence level.

Detached Shell Surrounding the SN

In order to explain the almost constant Si II velocity in super-Chandrasekhar events, Scalzo *et al.* (2010) and Scalzo *et al.* (2012) hypothesize a stationary shell detached from the ejecta. The shell is accelerated to a constant speed v_{sh} by colliding with fast-moving ejecta with velocities greater than v_{sh}. In fact, some simulations of WD mergers show that the outermost material forms such a stationary envelope that collides with fast-moving ejecta (Hoeflich and Khokhlov, 1996). Following the calculation procedure in Scalzo *et al.* (2010) and Scalzo *et al.* (2012), we derive an envelope mass of $0.15^{+0.11}_{-0.01} M_\odot$ for iPTF13asv. This shell increases the total mass of the system to $1.59^{+0.45}_{-0.12} M_\odot$ The ^{56}Ni, shell, and total masses of iPTF13asv are similar to those derived for SN20080522-000 in Scalzo *et al.* (2012). The large velocity and small mass make the detached shell have minor impacts to the γ-ray opacity, peak luminosity and the rise time of the SN.

5.5 Discussions

Origin of Strong UV Emission

Strong UV emission in a Type Ia SN could be powered by an extrinsic SN-companion collision (Kasen, 2010). In fact, in the UV-luminous SN2011de, Brown (2014) interpreted its UV light curve as possibly arising from collision

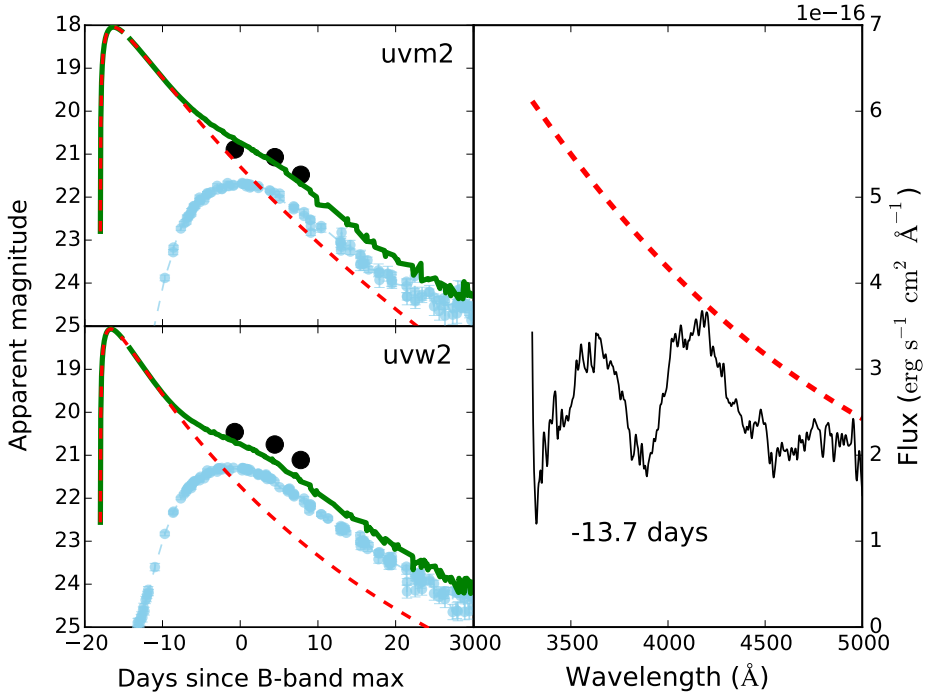

Figure 5.14: **Comparison between the SN-companion interaction signature model and iPTF13asv data.** *Left*: The $uvm2$ and $uvw2$ light curves of iPTF13asv (black circles) are compared to the total light curves (green) which combine the SN-companion interaction component (red; Kasen 2010) and the SN intrinsic emission (cyan). *Right*: the iPTF13asv spectrum at -13.7 days (black) is compared to the thermal spectrum of SN-companion collision (red).

between the SN ejecta and a companion star. Here we consider the same model for the strong UV emission of iPTF13asv.

We utilize the scaling relation in Kasen (2010) to fit the observed $uvm2$ light curve. In order to account for the non-negligible emission from the SN itself, we use the well-sampled $uvm2$ light curve of SN2011fe as a template. The fitting result shows that the companion star is located at 2×10^{13} cm away from the exploding WD (left panel of Figure 5.14). Given a typical mass ratio of a few and assuming Roche-lobe filling for stable mass transfer before explosion, we derive a companion radius of $\simeq 100 R_{\odot}$.

Although the model fit to the UV light curve looks plausible, it overpredicts the SN optical emission at very early phases. In the R-band light curve within a few days of explosion, the model-predicted SN flux (200 μJy) is higher than

the observed fluxes (the inset of Figure 5.1) by a factor of $> 30\%$ or equivalently brighter by 0.3 mag. Furthermore, at -13.7 days, the predicted thermal emission flux from the model below 4000 Å is also much higher than the observed spectrum (right panel of Figure 5.14). As such, we conclude that the strong UV emission seen in iPTF13asv is unlikely to arise from SN-companion collision.

As a result of the above analysis, we are forced to conclude that the strong UV emission is intrinsic. In fact, the strong UV emission and the lack of iron in early-phase spectra are probably causally related, as the iron group elements are the major absorbers of UV photons. These two observational facts, together with the near-IR secondary peak, strongly suggest that iPTF13asv has a stratified ejecta along the line of sight with concentration of iron group elements near the center of the explosion.

iPTF13asv as an Intermediate Case between Normal and Super-Chandrasekhar Subclasses

In Table 5.3, we summarize a comparison of normal SNe, iPTF13asv, and super-Chandrasekhar SNe. As can be seen from the table, on the one hand, iPTF13asv shares similar light curve shapes and a near-IR secondary peak with normal events. SNID also finds decent spectral matches between iPTF13asv and normal events. On the other hand, the peak radiation of iPTF13asv is as bright as super-Chandrasekhar events in both optical and UV. The evolution of Si II velocities of iPTF13asv is also similar to those of super-Chandrasekhar events. In addition, we derived an total ejecta mass slightly beyond the Chandrasekhar mass limit. Therefore, we tentatively classify iPTF13asv as an intermediate case between normal and super-Chandrasekhar subclasses.

In addition to the table, the H-band break, a sharp spectral feature formed by absorption of Fe II, Co II and Ni II (Hsiao *et al.*, 2013), is also distinctive between super-Chandrasekhar and normal events. The H-band break emerges around the maximum for normal SNe and decays to disappear within a month of maximum. In contrast, this feature does not appear in the super-Chandrasekhar events. However, the only near-IR spectrum of iPTF13asv is taken one month after the maximum. Therefore, we cannot determine whether iPTF13asv shows the H-band break or not.

Table 5.3. Comparison of iPTF13asv to normal and super-Chandrasekhar SNe

Feature	Normal	iPTF13asv	Super-Chandrasekhar	Section[a]
B-band absolute peak magnitude	-18 – -19.5	-19.97 ± 0.06	< -19.6	§5.3
UV absolute peak magnitude	$\gtrsim -15$	-15.25	$\lesssim -15$	§5.3 & Figure 5.7
B-band Δm_{15} (mag)	0.8 – 1.2	1.0	$\simeq 0.6$	§5.3
Near-IR secondary peak	strong	strong	weak or absent	§5.3 & Figure 5.6
SNID	normal	normal	super-Chandrasekhar	§5.3 & Table 5.2
Carbon feature after max	no	weak	strong	Figures 5.10 and 5.11
Si II 6355 velocity at max ($10^3\,\mathrm{km\,s^{-1}}$)[b]	10 – 14	10	8 – 12	Figure 5.8
Si II 6355 velocity gradient at max ($\mathrm{km\,s^{-1}\,day^{-1}}$)[b]	50 – 150	~ 0	-72 – 46	Figure 5.9
^{56}Ni mass ($M_\odot$)[c]	0.3 – 0.6	$0.81^{+0.10}_{-0.18}$	> 0.75	§5.4
Ejecta mass ($M_\odot$)[c]	0.8 – 1.5	$1.59^{+0.45}_{-0.12}$	> 1.5	§5.4

[a]This column points to sections in this paper that discuss corresponding features

[b]The velocity measurements of normal events are from Foley *et al.* (2011). Those of super-Chandrasekhar events are from Scalzo *et al.* (2012).

[c]The mass measurements of normal events are from Scalzo *et al.* (2014b). Those of super-Chandrasekhar events are from Scalzo *et al.* (2012).

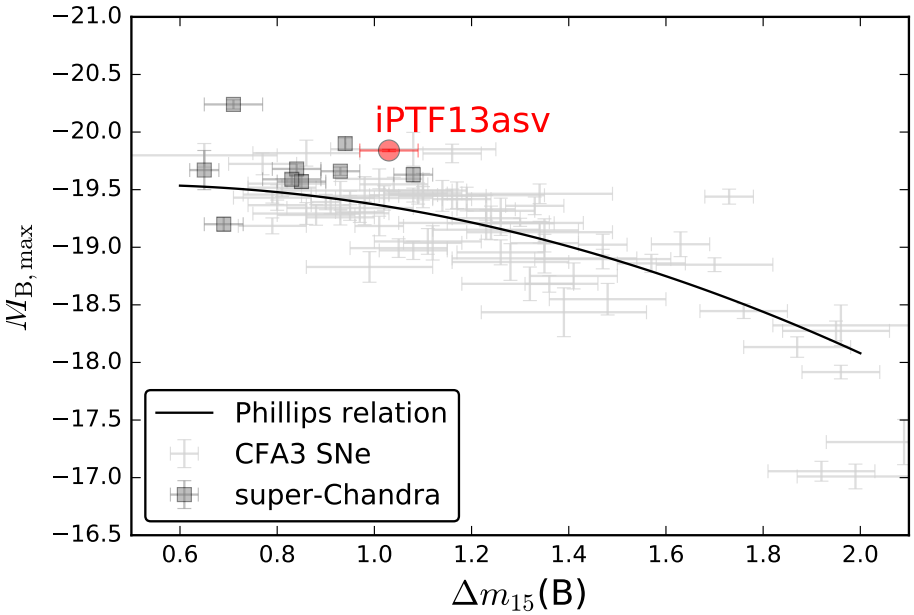

Figure 5.15: **iPTF13asv is an outlier from the the Phillips relation**. The Phillips relation is taken from Phillips *et al.* (1999). The CfA3 data are from Hicken *et al.* (2012). The super-Chandrasekhar events are from Scalzo *et al.* (2010) and Scalzo *et al.* (2012).

Progenitor

In this paragraph, we test the SD and DD progenitor scenarios to the case of iPTF13asv. In a SD system, a non-rotating WD cannot exceed the Chandrasekhar mass limit, and it is not clear in reality how rotation could increase this mass limit. Hydrodynamic simulations (e.g., Kromer *et al.* 2010; Sim *et al.* 2013) also show that explosions in a SD system cannot avoid a certain level of mixing in the ejecta. As such, these models do not easily concentrate the iron group elements in low velocity regions of the ejecta. For merging WDs, in contrast, simulations of prompt detonation (e.g., Moll *et al.* 2014) show strongly stratified ejecta structures along polar directions in asymmetric ejecta. In these directions, iron group elements are also confined to the low-velocity regions. Therefore, the large mass and stratification of the ejecta favor a DD progenitor system for iPTF13asv.

iPTF13asv in cosmology

Unsurprisingly, iPTF13asv is an outlier from the classical Phillips relation between peak magnitude and Δm_{15} (Phillips, 1993). As shown in Figure 5.15,

iPTF13asv is above the empirical relation by half a magnitude.

To have better calibration in cosmology, a third color term is introduced in the Phillips relation, i.e.,

$$\mu = m_B^* - (M_B - \alpha x_1 + \beta c) \ , \tag{5.6}$$

where μ is the distance modulus; m_B^* is the observed peak magnitude in the rest-frame B band; α, β and M_B are free parameters. x_1 and c are the shape and color parameters derived in the SALT2 fitting. In order to account for the dependence on the host galaxy properties, Sullivan *et al.* (2011) suggest to use different values of M_B for galaxies of stellar mass greater than and less than $10^{10} M_\odot$. Since the stellar mass of the iPTF13asv host galaxy is $\sim 10^{7.8} M_\odot$, we adopt the parameters from Betoule *et al.* (2014) for galaxies with stellar mass less than $10^{10} M_\odot$: $H_0 = 70\,\mathrm{km\,s^{-1}\,Mpc^{-1}}$, $M_B = -19.04 \pm 0.01$, $\alpha = 0.141 \pm 0.006$ and $\beta = 3.101 \pm 0.075$. Given the iPTF13asv measurements of $m_B^* = 16.28 \pm 0.03$, $x_1 = 0.37 \pm 0.09$ and $c = -0.16 \pm 0.02$, we find that iPTF13asv can still be included in this empirical relation and thus be useful for cosmographic measurements, whereas super-Chandrasekhar events are obvious outliers of this empirical relation (Scalzo *et al.*, 2012).

UV-luminous SNe at High Redshifts

Spectroscopic classification for high-redshift SNe requires very long integration on big telescopes. Therefore, in high-redshift SN surveys, an optical–UV "dropout" is introduced to preselect Type Ia candidates. For example, Riess *et al.* (2004, 2007) used the F850LP, F775W, and F606 filters on the *HST* Advanced Camera for Surveys (ACS) to search for SNe at redshifts up to 1.8.

The color preselection criteria may miss UV-luminous SNe. In Figure 5.16, we calculate the color difference in the F850LP, F775W, and F606 filters for normal SN1992a (Kirshner *et al.*, 1993), near-UV blue SN2011fe (Mazzali *et al.*, 2014), and UV-luminous iPTF13asv at maximum as a function of redshift. As can be seen, the three SNe show different colors at high redshifts. Although the rate of iPTF13asv-like events is probably low in the nearby Universe, such SNe might occur more frequently at high redshifts as there are more metal-poor dwarf galaxies. We speculate that it might become a non-negligible component in estimating the SN rate at high redshifts.

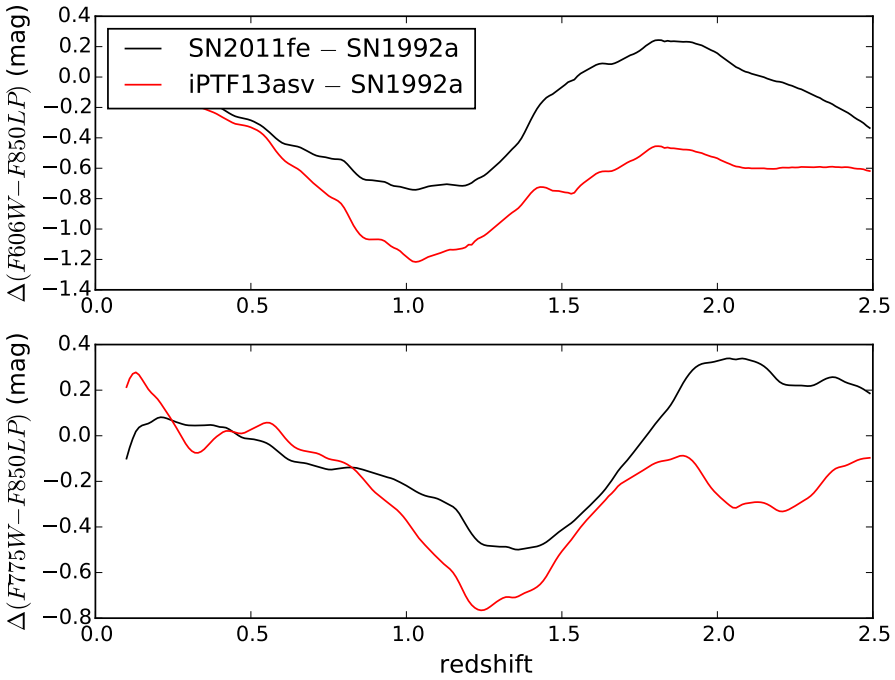

Figure 5.16: **Color difference as a function of redshift for three different Type Ia SNe.**

5.6 Conclusions

In this paper, we present multi-wavelength observations of a peculiar overluminous Type Ia supernova, iPTF13asv, discovered by the intermediate Palomar Transient Factory. While its light curve shape ($\Delta m_{15} = 1.03 \pm 0.01$ mag) and sharp secondary near-IR peak resemble characteristic features of normal Type Ia supernovae, iPTF13asv shows (1) peak optical and UV luminosities brighter than normal Type Ia supernova ($M_B = -19.84$ mag, $M_{uvm2} = -15.5$ mag) (2) low but almost constant expansion velocities and (3) persistent carbon absorption features after the maximum, which are commonly seen in super-Chandrasekhar events. We derive a ^{56}Ni mass of $0.81^{+0.10}_{-0.18} M_\odot$ and a total ejecta mass of $1.59^{+0.45}_{-0.12} M_\odot$. As a result, we suggest that iPTF13asv is an intermediate case between the normal and super-Chandrasekhar events.

Our observations of iPTF13asv also show an absence of iron absorption features in its early-phase spectra until several days before maximum and strong UV emission around peak. These observations, together with sharp near-IR secondary maxima, indicate that iPTF13asv has a stratified structure along the line of sight, with synthesized iron group elements concentrated in low-

velocity zones of its ejecta. Compared to hydrodynamic simulations, only WD mergers might produce the inferred ejecta structure along particular directions. Therefore, based on the large mass and stratification of the ejecta, we conclude that iPTF13asv favors a double-degenerate progenitor system.

Acknowledgement

We thank the anonymous referee for very useful comments and suggestions that substantially improved the manuscript. We are also grateful to M. Kromer for useful discussions about theoretic progenitor scenarios, and to A. De Cia, O. Yaron, D. Tal, D. Perley, K. Tinyanont, A. Waszczak, I. Arcavi, and S. Tang for performing observation and data reduction.

This research is partly supported by the *Swift* Guest Investigator program and by the National Science Foundation. Y.C. and M.M.K. acknowledge support from the National Science Foundation PIRE program grant 1545949. A.G. and R.A. acknowledge support from the Swedish Research Council and the Swedish Space Board. E.Y.H. acknowledges the support provided by the Danish Agency for Science and Technology and Innovation through a Sapere Aude Level 2 grant.

Some observations obtained with the SuperNova Integral Field Spectrograph on the University of Hawaii 2.2-m telescope as part of the Nearby Supernova Factory II project, a scientific collaboration between the Centre de Recherche Astronomique de Lyon, Institut de Physique Nucl'eaire de Lyon, Laboratoire de Physique Nucl'eaire et des Hautes Energies, Lawrence Berkeley National Laboratory, Yale University , University, University of Bonn , Max Planck Institute for Astrophysics, Tsinghua Center for Astrophysics, and Centre de Physique des Particules de Marseille.

Some data in this paper were obtained with ALFOSC, which is provided by the Instituto de Astrofisica de Andalucia (IAA) under a joint agreement with the University of Copenhagen and NOTSA.

We also thank the RATIR project team and the staff of the Observatorio Astronómico Nacional on Sierra San Pedro Mártir. RATIR is a collaboration between the University of California, the Universidad Nacional Autónoma de México, NASA Goddard Space Flight Center, and Arizona State University, benefiting from the loan of an H2RG detector and hardware and software support from Teledyne Scientific and Imaging. RATIR, the automation of the

Harold L. Johnson Telescope of the Observatorio Astronómico Nacional on Sierra San Pedro Mártir, and the operation of both is funded through NASA grants NNX09AH71G, NNX09AT02G, NNX10AI27G, and NNX12AE66G, CONACyT grants LN 260369, and UNAM PAPIIT grant IG100414.

A portion of this work was carried out at the Jet Propulsion Laboratory, California Institute of Technology, under a contract with the National Aeronautics and Space Administration.

Chapter 6

DISCOVERY, PROGENITOR AND EARLY EVOLUTION OF A TRIPPED ENVELOPE SUPERNOVA iPTF13bvn[†]

Yi Cao[1], Mansi M. Kasliwal[2], Iair Arcavi[3], Assaf Horesh[1], Paul Hancock[4,5], Stefano Valenti[6,7], S. Bradley Cenko[8], S. R. Kulkarni[1], Avishay Gal-Yam[3], Evgeny Gorbikov[3], Eran O. Ofek[3], David Sand[9], Ofer Yaron[3], Melissa Graham[6,7], Jeffrey M. Silverman[10], Craig Wheeler[10], G. H. Marion[10], Emma Walker[11], Paolo Mazzali[12,13,14], D. Andrew Howell[6,7], K. L. Li[15], A. K. H. Kong[15], Josh Bloom[16], Peter E. Nugent[16,17], Jason Surace[18], Frank Masci[19], John Carpenter[1], Nathalie Degenaar[20] & Christopher Gelino[19]

[1] Astronomy Department, California Institute of Technology, 1200 E. California Blvd., Pasadena, CA 91125, USA

[2] The Observatories, Carnegie Institution for Science, 813, Santa Barbara Street, Pasadena, CA 91101, USA

[3] Dept. of Particle Physics and Astrophysics, Weizmann Institute of Science, Rehovot, 76100, Israel

[4] Sydney Institute for Astronomy (SIfA), School of Physics, The University of Sydney, NSW 2006, Australia

[5] ARC Centre of Excellence for All-sky Astrophysics (CAASTRO), The University of Sydney, NSW 2006, Australia

[6] Las Cumbres Observatory Global Telescope Network, Goleta, CA 93117, USA

[7] Department of Physics, University of California, Santa Barbara, CA 93106, USA

[8] Astrophysics Science Division, NASA Goddard Space Flight Center, Mail Code 661, Greenbelt, MD, 20771, USA

[9] Department of Physics, Texas Tech University, Lubbock, TX 79409, USA

[10] Department of Astronomy, University of Texas at Austin, Austin, TX 78712, USA

[11] Department of Physics, Yale University, New Haven, CT 06511-8499, USA

[12] INAF-Padova Astronomical Observatory, Vicolo dell'Osservatorio 5 35122

[†]An edition of this chapter was published on the *Astrophysical Journal Letters*, vol. 775, 7 (2013).

Padova Italy
[13] Astrophysics Research Institute, Liverpool John Moores University, Liverpool, UK
[14] Max-Planck Institute for Astrophysics, D-85748 Garching, Germany
[15] Institute of Astronomy and Department of Physics, National Tsing Hua University, Hsinchu 30013, Taiwan
[16] Department of Astronomy, University of California Berkeley, B-20 Hearst Field Annex # 3411, Berkeley, CA, 94720-3411, USA
[17] Computational Cosmology Center, Computational Research Division, Lawrence Berkeley National Laboratory, 1 Cyclotron Road MS 50B-4206, Berkeley, CA, 94720, USA
[18] Spitzer Science Center, MS 220-6, California Institute of Technology, Jet Propulsion Laboratory, Pasadena, CA 91125, USA
[19] Infrared Processing and Analysis Center, California Institute of Technology, Pasadena, CA 91125, USA
[20] Department of Astronomy, University of Michigan, 500 Church Street, Ann Arbor, MI 48109, USA

Abstract

The intermediate Palomar Transient Factory reports our discovery of a young supernova, iPTF13bvn, in the nearby galaxy, NGC 5806 (22.5 Mpc). Our spectroscopic follow-up observations in the optical and infrared establish a Type Ib classification. We identify a blue progenitor candidate in *HST* pre-explosion images within a 2-σ error circle of 80 mas (8.7 pc). The candidate has a $M_{\rm B}$ luminosity of -5.52 ± 0.39 mag and a B$-$I color of 0.25 ± 0.25 mag. Fitting a power law to the early light curve, we find an extrapolated explosion date about 0.6 days before our first detection. We see no evidence of shock cooling. The pre-explosion detection limits constrain the radius of the progenitor to be smaller than several solar radii. iPTF13bvn is also detected in centimeter and millimeter wavelengths. Fitting a synchrotron self-absorption model to our radio data, we find a mass-loading parameter of $1.3 \times 10^{12}\,{\rm g\,cm^{-1}}$. Assuming a wind velocity of $10^3\,{\rm km\,s^{-1}}$, this mass-loading parameter leads to a progenitor mass-loss rate of $3 \times 10^{-5} M_\odot\,{\rm yr^{-1}}$. A post-explosion *HST* revisit to the site of iPTF13bvn two years after explosion has confirmed that the source detected at the location of iPTF13bvn in the pre-explosion images is at least part of the progenitor system.

6.1 Introduction

Supernovae (SNe) of Type Ibc constitute about one-third of core-collapse SNe (Li *et al.*, 2011b). Their spectra lack hydrogen (Filippenko, 1997), suggesting progenitors stripped of their hydrogen envelopes either due to mass transfer in a binary system or via copious stellar winds before the explosion. On theoretical grounds, the anticipated progenitors are Wolf-Rayet (WR) stars or less massive helium stars in binaries (e.g., Dessart *et al.*, 2012; Yoon *et al.*, 2012). The most straightforward way to test the above theoretical pictures is direct detection of the progenitor. This is possible for SNe occurring in nearby galaxies which have deep pre-explosion images (which means, in practice, *Hubble Space Telescope*, *HST*). Eldridge *et al.* (2013) comprehensively summarize searches for a dozen Ib/c progenitors, which are all non-detections. The deepest upper limit to date is $M_B = -4.4\,\mathrm{mag}$ for SN 2002ap, a Type Ic SN in the very nearby galaxy Messier 74 (Crockett *et al.*, 2007).

An alternative way to infer the progenitor properties is the post-shock-breakout cooling light curve at early phases of a SN, which is sensitive to the progenitor size, explosion energy, and the composition of the outermost envelope of the progenitor (e.g., Nakar and Sari, 2010; Rabinak and Waxman, 2011; Bersten *et al.*, 2012; Piro and Nakar, 2013), and in some propitious cases can even diagnose the presence of a binary companion (Kasen, 2010). For example, the shock cooling phase of SN 2008D (Type Ib) lasted about five days and the inferred radius of its progenitor is $< 14R_\odot$ (Soderberg *et al.*, 2008). No detection of shock cooling constrains the progenitor radius of PTF10vgv (Type Ic) to $< 6R_\odot$ (Corsi *et al.*, 2012; Piro and Nakar, 2013).

Radio measurements serve as another indirect probe of the progenitor system by characterizing the mass-loss history. Radio emission is produced by relativistic electrons accelerated in the supernova shock as they gyrate in the amplified magnetic field when the shock expands freely (Chevalier, 1998). The kinetic energy density of the post-shock gas $u_K = 9\rho v_s^2/8$, where ρ is the density and v_s is the constant shock speed. The magnetic energy density

$$\frac{B^2}{8\pi} = u_B = \epsilon_B u_K \simeq 6.8 \times 10^9 \epsilon_B \frac{\dot{M}}{v_w} t_d^{-2}\,\mathrm{ergs\,cm^{-3}}\ , \tag{6.1}$$

where ϵ_B is the ratio of the magnetic and thermal energy densities, $\dot{M}$ is the mass loss rate in $M_\odot\,\mathrm{yr}^{-1}$, v_w is the constant wind velocity from the progenitor, and t_d is the time post-explosion in days. Meanwhile, we assume a power

distribution of relativistic electrons, i.e., $N(\gamma) \propto \gamma^{-p}$ where γ is the Lorentz factor. The ratio between the electron energy density to the thermal energy density is denoted as ϵ_e. X-ray observations of the inverse Compton scattering of the SN emission by the non-thermal electrons from well-studied SNe have shown that $\epsilon_e \simeq 0.1$ (Chevalier and Fransson, 2006). We further assume energy equipartition between electrons and magnetic field, i.e., $\epsilon_e = \epsilon_B$. Following Chevalier (1998), the radio synchrotron luminosity in the optically thin regime is given by

$$L_\nu = \frac{(4\pi)^2 f R_s^3}{3} c_5 N_0 B^{(p+1)/2} \left(\frac{\nu}{2c_1}\right) \,\mathrm{ergs\,s^{-1}\,Hz^{-1}}\ , \tag{6.2}$$

and the synchrotron-self-absorption luminosity is

$$L_\nu = 4\pi^2 f R_s^3 \frac{c_5}{c_6} B^{-1/2} \left(\frac{\nu}{2c_1}\right)^{5/2} \,\mathrm{ergs\,s^{-1}\,Hz^{-1}}\ , \tag{6.3}$$

where the constants c_1, c_5 and c_6 can be found in Pacholczyk (1970). As such, radio observations allow us to measure the location of the SN shock at a given time, and the mass-loading parameter $A = \dot{M}/(4\pi v_w)$ where $\dot{M}$ is a constant mass-loss rate and v_w is the wind velocity from the progenitor (Chevalier, 1998). Chevalier and Fransson (2006) found that Type Ibc supernovae usually have $A \sim 10^{12}\,\mathrm{g\,cm^{-1}}$.

In this letter, we report the discovery of iPTF13bvn, a young Type Ib SN in the nearby galaxy NGC 5806. Archival *HST* images of NGC 5806 allow a direct progenitor search. We also present early photometric, spectroscopic, and radio observations and discuss implications on the progenitor.

6.2 Discovery

On 2013 June 16.238 (all times are in UT), the intermediate Palomar Transient Factory (iPTF; Law *et al.* 2009) identified a new transient source with $R = 18.6$ mag (AB) in the vicinity of NGC5806 (Cao *et al.*, 2013a). No source was detected at the same location down to 21.7 mag (3-σ) on June 15.240. Also there was no evidence for pre-outburst activity in 492 PTF images taken since 2009 June 29 to similar depths.

6.3 Progenitor identification

On June 20.276, we observed iPTF13bvn in H-band with OSIRIS (Larkin *et al.*, 2006) with the Laser Guide Star Adaptive Optics (LGS-AO) system

(Wizinowich *et al.*, 2006) mounted on the 10-m Keck I telescope. Registering the AO image to the archival *HST*/ACS image, we obtain a 1-σ uncertainty of 40 miniarcsec (mas). We find one source spatially coincident with the SN within the 2-σ (equivalently 8.7 pc in projection distance) error circle (Figure 6.1; Arcavi *et al.* 2013).

We perform point-spread function (PSF) photometry on the *HST*/ACS images with DOLPHOT (Dolphin, 2000). The photometry of the progenitor candidate is 26.50 ± 0.15 mag in F435W, 26.40 ± 0.15 mag in F555W and 26.10 ± 0.20 mag in F814W. To correct for extinction, we obtain a high-resolution spectrum (Section 6.4) and measure the equivalent widths of Na I D lines. We find local extinction of $E(B-V) = 0.0437$ and foreground extinction of 0.0278 (Poznanski *et al.*, 2012). Assuming $R_V = 3.1$ (Schlafly and Finkbeiner, 2011) and adopting a distance modulus of 31.76 ± 0.36 (22.5Mpc; Tully *et al.* 2009), we find $M_B = -5.52 \pm 0.39$ mag, $M_V = -5.55 \pm 0.39$ mag and $M_I = -5.77 \pm 0.41$ mag. Thus, the progenitor, if single, is no brighter than these values. The luminosity and colors are consistent with the compilation of WN and WC Wolf-Rayet stars in Eldridge *et al.* (2013).

However, WR stars are often in binaries (Tuthill *et al.*, 1999). Thus, the progenitor is possibly in a binary system and the optical emission might be dominated by the companion. We further note that color alone cannot be used as a discriminant. The B, V, and I filters are in the Rayleigh-Jeans tail of hot stars, including O-stars, WR stars, and blue supergiants. Moreover, given the $0.05''$ pixel size of *HST*/ACS, or equivalently 5.45 pc at the distance of NGC5806, the candidate can also be an unresolved young star cluster whose color is dominated by OB stars. Finally, we caution that the progenitor candidate may even be unrelated to the SN. The litmus test of whether this candidate is the progenitor or part of the progenitor system can only be undertaken by *HST* imaging after the SN fades.

6.4 Early photometric and spectroscopic evolution

Observations And Data Reduction

As part of regular iPTF operations, the field of iPTF13bvn was imaged twice every night by the Palomar 48 inch Oschin telescope (P48) with a Mould R-band filter (Ofek *et al.*, 2012a) during the spring quarter. Upon discovery of iPTF13bvn, the robotic Palomar 60 inch telescope (P60; Cenko *et al.* 2006)

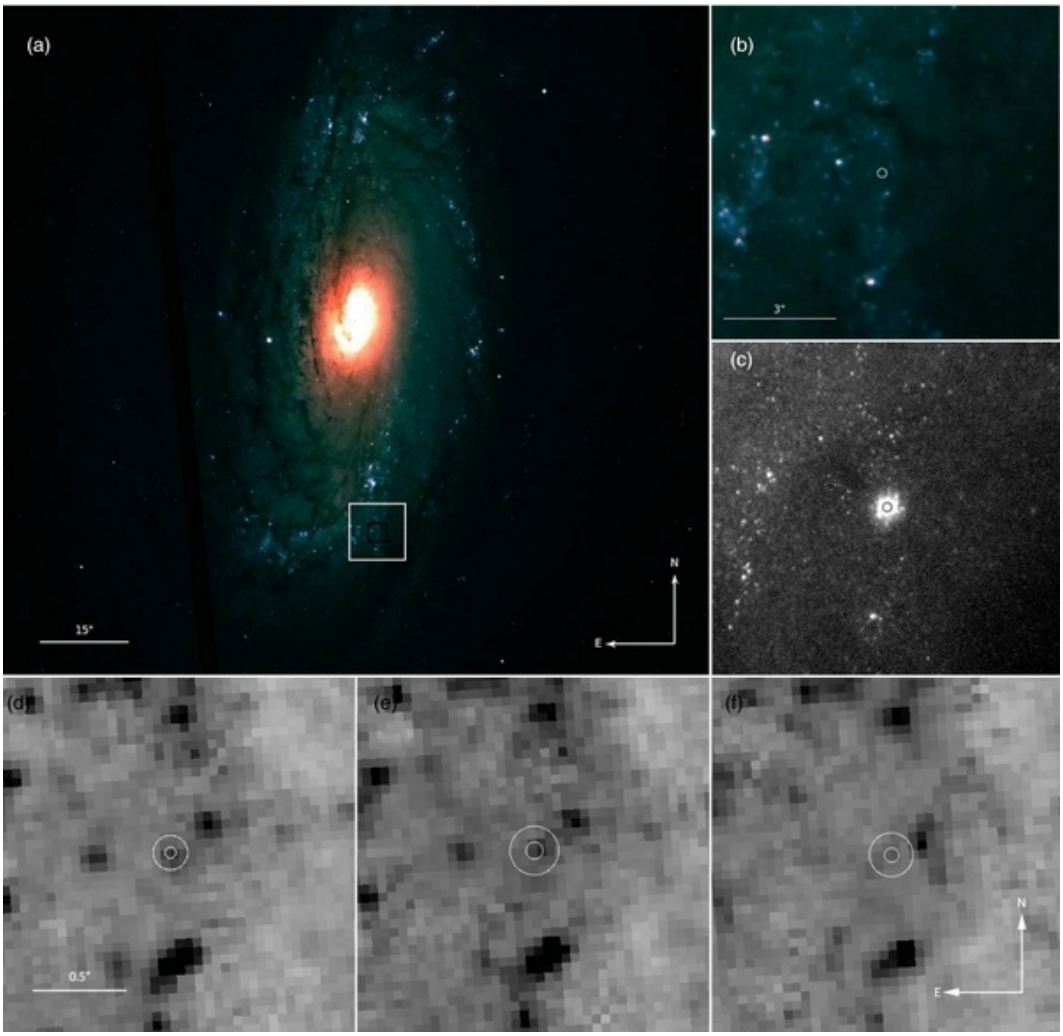

Figure 6.1: **Pre-explosion *HST* image and OSIRIS-AO image of iPTF13bvn.** The SN is located at $\alpha = 15^{\rm h}00^{\rm m}00\overset{\rm s}{.}152$, $\delta = +01°52'53''.17$ (J2000). Panel (a) shows the *HST* image of NGC 5806, taken on 2005 March 10 UT (*HST* proposal 10187, PI: Smartt). Panel (b) is a zoom-in of the *HST* image near the site of iPTF13bvn. Panel (c) is the composite image of the SN taken with OSIRIS and LGS-AO system. This is made by stacking sixty 15-second exposures. We align this image with the *HST*/ACS images with 15, 23, and 25 common stars in the F435W, F555W, and F814W filters and acquire registration uncertainties of 0.6, 0.9, and 0.8 *HST* pixel, respectively. Panels (d), (e), and (f) show the *HST* images at the position of the SN in F435W, F555W, and F814W filters. The position of iPTF13bvn is marked with 1-σ and 3-σ error circles. The progenitor candidate is 26.50 ± 0.15 mag in F435W (SNR= 11.2), 26.40 ± 0.15 mag in F555W (SNR= 9.9), and 26.10 ± 0.20 mag in F814W (SNR= 8.2).

was triggered for follow-up in the $g'r'i'z'$ bands. We obtained photometry with the Las Cumbres Observatory Global Telescope (LCOGT; Brown *et al.* 2013) network in the $UBVRIg'r'i'z'$ bands using the 1-m telescopes from Cerro Tololo (Chile), McDonald Observatory (USA), and Sutherland (South Africa), along with the 2-m Faulkes Telescope South (Siding Springs). As part of our ongoing iPTF-Swift program (PI Kasliwal), we triggered target-of-opportunity observations beginning on 2013 June 17 (Arcavi *et al.*, 2013). In the P48, P60, and *Swift* images, the host background is subtracted by using pre-explosion reference images, while in the LCOGT images a low-order polynomial fit is used to remove the background. PSF photometry is then performed in all the images. Photometry in the $g'r'i'z'$ bands is calibrated to Sloan Digital Sky Survey stars and that in the $UBVRI$ bands is calibrated with Landolt standard stars. The multi-color light curve of iPTF13bvn is illustrated in Figure 6.2.

Low-resolution spectroscopic follow-up of iPTF13bvn was undertaken with the DOLORES low-resolution spectrograph on Telescopio Nazionale Galileo (TNG), the Marcario Low-Resolution Spectrograph (Hill *et al.*, 1998) on the Hobby-Eberly Telescope (HET), the low-resolution, cross-dispersed spectrograph FLOYDS on the robotic Faulkes Telescope, the Dual Imaging Spectrograph on the ARC 3.5-m telescope, the Folded-Port InfraRed Echellete (Simcoe *et al.*, 2013) on the 6.5-m Magellan telescope, and SpeX (Rayner *et al.*, 2003) on the NASA Infrared Telescope Facility. We also obtained a high-resolution spectrum with High Resolution Echelle Spectrometer (HIRES; Vogt *et al.* 1994) on the 10 m Keck I telescope. The spectroscopic series of iPTF13bvn is displayed in Figure 6.3.

All photometry tables and spectroscopy data will be made public via WISeREP (Yaron and Gal-Yam, 2012).

Analysis: Photometry

In order to better constrain the explosion date, we fit a power-law model $f(t) \propto (t - t_0)^{\beta}$ to the P48 data of iPTF13bvn taken in the first five nights after explosion and constrain the parameters with the upper limits preceding the discovery. The best fit results in an explosion date $t_0 =$ June 15.67 and a power-law index $\beta = 1.01$ (Figure 6.2). The 95% confidence levels for t_0 and β are June [15.50, 15.76] and [0.923, 1.09], respectively. Note that the color

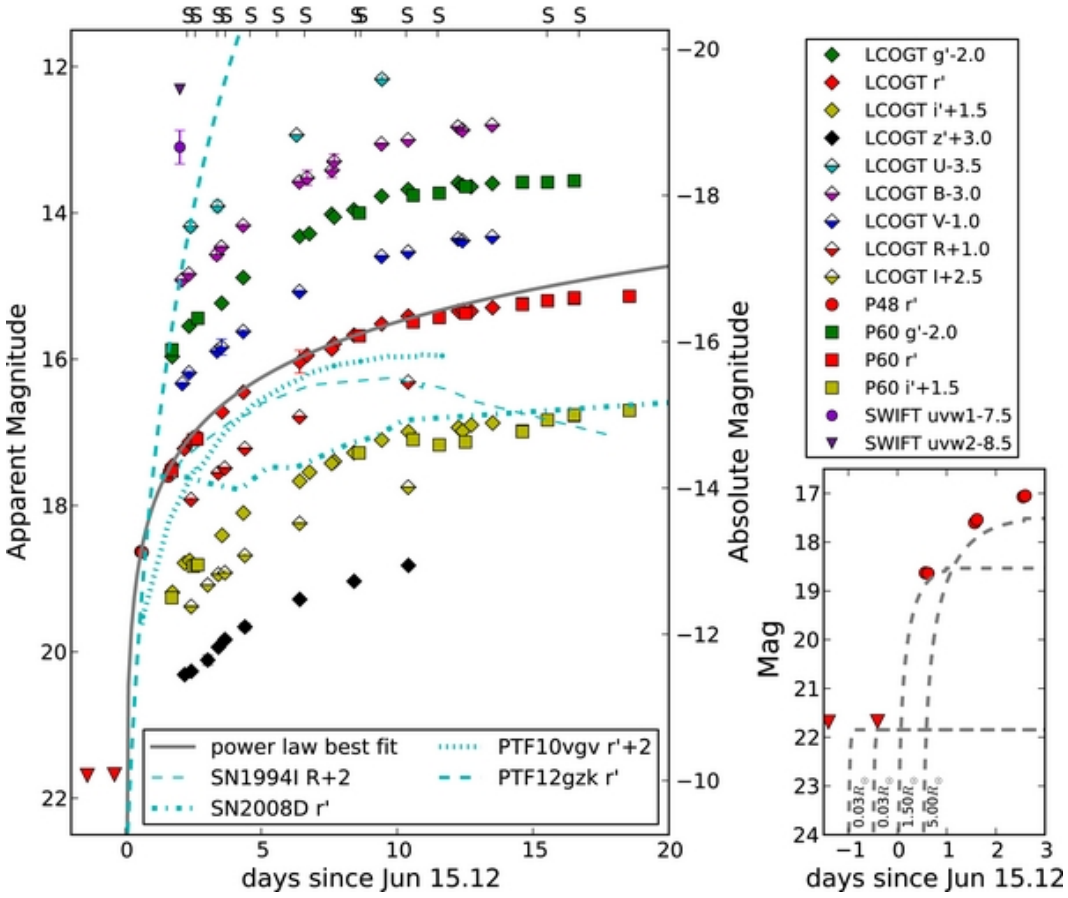

Figure 6.2: **Light curves of iPTF13bvn.** Left panel: multi-band light curve of iPTF13bvn (the color represents the filter, and the symbol shape represents the telescope). The upper limits are denoted in triangles. The origin $t = 0$ is set to the explosion date derived from the best power-law fit (solid gray curve). For comparison, r-band light curves of SN 1994I, SN 2008D, PTF10vgv, and PTF12gzk are also shown in cyan with different line styles. On the top axis, the epochs of spectroscopic follow-up are indicated by "S" In the right panel, the P48 R-band light curves are plotted against predicted light curves of shock cooling (gray dash curves) from Piro and Nakar (2013) for explosions starting at $t = -1,\ -0.5,\ 0.0,\ 0.5$ days with a "mean" velocity of $8,000\,\mathrm{km\,s^{-1}}$. The radius of the progenitor in each of the models is besides its corresponding light curve.

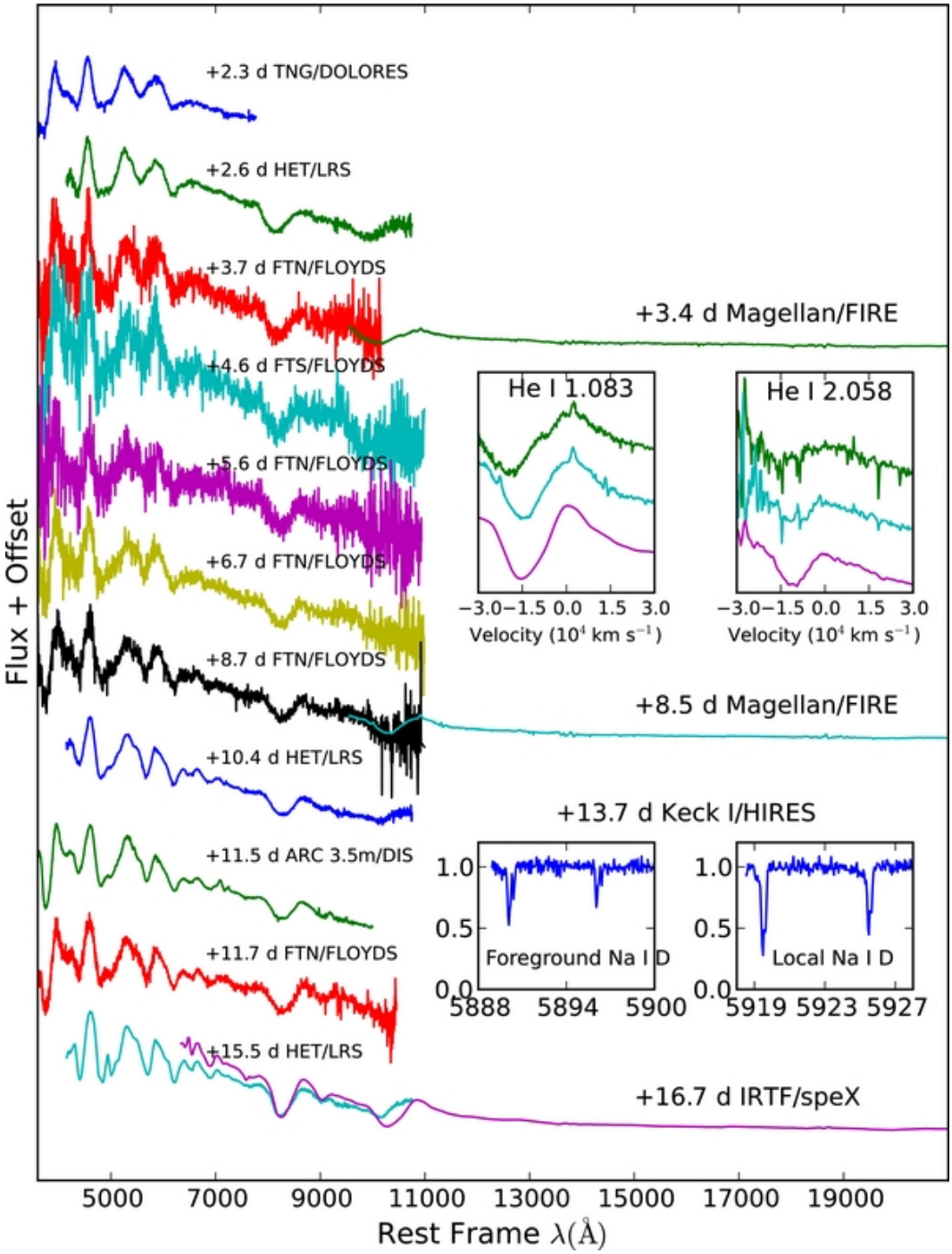

Figure 6.3: **Spectral sequence of iPTF13bvn.** Each spectrum is labeled with the observation date, the telescope, and the instrument. The upper two insets zoom-in to the infrared He I 10830 and He I 20581 lines. The lower two insets zoom-in to the Na I D doublet at high resolution.

evolution is minimal, suggesting that the R-band light curve is a reasonable proxy for the bolometric light curve. iPTF13bvn peaked at $R = -16.6$ mag at about $t_0 + 18$ days.

A comparison of R-band light curves between iPTF13bvn and other well-studied events, including SN1994I (Richmond *et al.*, 1996), SN2008D (Soderberg *et al.*, 2008), PTF10vgv (Corsi *et al.*, 2012), and PTF12gzk (Ben-Ami *et al.*, 2012), is shown in Figure 6.2. The type Ic SN1994I is much more luminous than iPTF13bvn while its rise rate is less than that of iPTF13bvn. The Type Ib SN 2008D has a five day cooling phase after its shock breakout before it slowly rises again, while we do not detect any shock cooling signature from iPTF13bvn. The energetic Type Ic SN PTF12gzk rises much faster than iPTF13bvn. Surprisingly, the closest match to the rise rate of iPTF13bvn through eight days is the high velocity Type Ic PTF10vgv (albeit about 2 mag fainter).

Following Piro and Nakar (2013), we derive a constraint on the progenitor radius based on our detection limits on shock cooling. The inferred radius is sensitive to the "mean" velocity of the ejecta $v = \sqrt{2E/M_{ej}}$ where E is the explosion energy and M_{ej} is the mass of the ejecta. Based on the measured photospheric velocities and line velocities (Section 6.4), we conservatively adopt the lowest velocity of $8,000\,\mathrm{km\,s^{-1}}$. If the velocity was higher, the radius of the progenitor would be constrained to be even smaller. The model also depends weakly on E and thus we assume $E = 10^{51}$ ergs. In the right bottom panel of Figure 6.2, the predicted R-band light curves (gray lines) of shock cooling with various explosion times are also plotted. We find the following: if the explosion had happened earlier than t_0, the progenitor radius would have to be unreasonably small ($\simeq 0.03 R_\odot$) because the luminosity of the shock breakout is tightly constrained by non-detection on June 14. If the explosion happened at t_0, the progenitor radius $< 1.5 R_\odot$. If the explosion happened at $t_0 + 0.5$ day, the progenitor radius $< 5 R_\odot$. Therefore we conclude that the progenitor radius was no larger than several solar radii, suggesting a stripped core such as WR stars.

Analysis: Spectroscopy

Figure 6.4 compares spectra of iPTF13bvn to those of well-studied Type Ibc supernovae.

The strongest features in the early spectra are the Ca II H+K and Ca II near-IR triplet absorption. The blends of Fe II lines at $\simeq 5,000$ Å and Fe II, Mg II and Ti II at $4,400$ Å are also prominent. The local minimum at about $5,500$ Å may be either He I or Na I and that at about $6,200$ Å may be interpreted as either Si II or Ne I. At +2.6 days after explosion (Figure 6.4), a SYNOW fit gives a photospheric velocity of $10,000\,\mathrm{km\,s^{-1}}$ and a Ca II line velocity of $14,000\,\mathrm{km\,s^{-1}}$. By +11.5 days, these velocities evolve to $8,000$ and $10,000\,\mathrm{km\,s^{-1}}$, respectively.

Helium lines are not expected to be prominent in early spectra of Type Ib SNe (Hachinger *et al.*, 2012). We begin to see weak wiggles at the location of He I ($5,876$ Å, $6,678$ Å and $7,065$ Å) in optical spectra after +10 days. However, SYNOW cannot fit a single expansion velocity to all the three lines simultaneously. In the IR spectra, we see a prominent absorption feature at $10,200$ Å, which may be explained by He I 10830 Å line blended with metal lines. The $20,581$ Å doublet is often used to confirm the presence of He (Taubenberger *et al.*, 2006; Marion *et al.*, 2014). By +16.7 days, we unambiguously detect this feature (see the inset of Figure 6.3). Therefore, we classify iPTF13bvn as a Type Ib SN (Milisavljevic *et al.*, 2013; Kasliwal *et al.*, 2013).

6.5 Radio follow-up

Promptly after discovery, we initiated radio follow-up observations at the Combined Array for Research in Millimeter-wave Astronomy (CARMA; PI Horesh) and requested Director's Discretionary Time at the Jansky Very Large Array (JVLA; PI Horesh). Our JVLA and CARMA data showed that the radio counterpart had a synchrotron self-absorption (SSA) spectrum. A few follow-up radio epochs were obtained with Australia Telescope Compact Array (ATCA; PI Hancock). The JVLA data were reduced using AIPS with J1505+0326 as a phase calibrator and 3C286 as a flux calibrator. The CARMA data were reduced using MIRIAD (Sault *et al.*, 1995) with J1549+026 as a phase calibrator and MWC349 as a flux calibrator. The ATCA data were reduced using MIRIAD with PKS B1921-293 as a bandpass calibrator, PKS B1508-055 as a phase calibrator, and PKS B1934-638 as a flux calibrator. All the radio data is presented in Figure 6.5.

We fit the multi-frequency multi-epoch data to the SSA model following Chevalier (1998).We assume that the electron energy distribution can be described

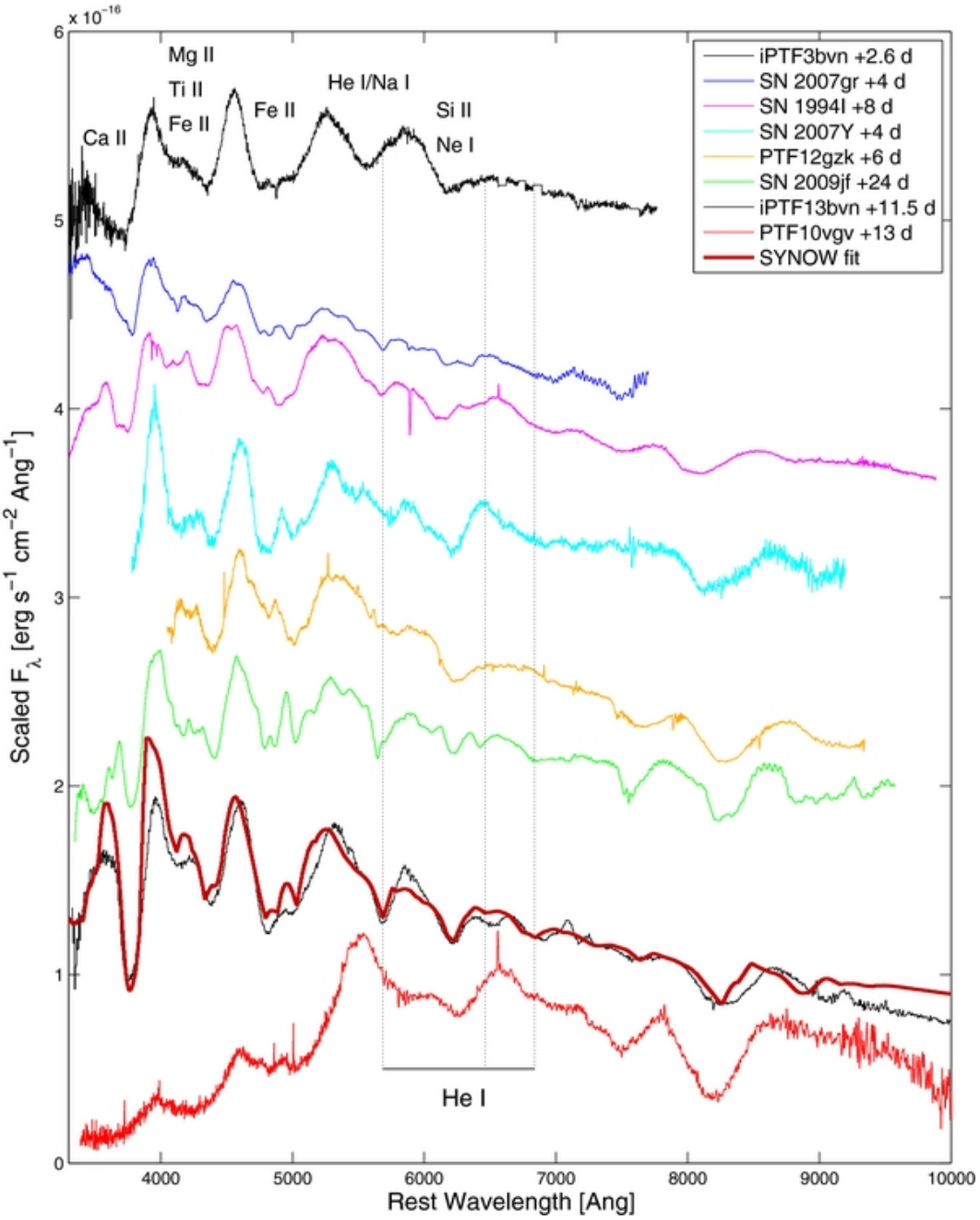

Figure 6.4: **Spectra of iPTF13bvn compared to other well-studied Type Ibc SNe.** All ages are reported in days since explosion. An early spectrum of iPTF13bvn shows strong similarity to early spectra of Type Ib/c SNe: SN 2007gr, Type Ic (Valenti *et al.*, 2008); SN 1994I, Type Ic (Filippenko *et al.*, 1995); SN 2007Y, Type Ib (Stritzinger *et al.*, 2009). The early spectrum of the energetic Type Ic PTF12gzk (Ben-Ami *et al.*, 2012) resembles that of iPTF13bvn, if a correction is made artificially for its remarkable blueshift. Later spectra of iPTF13bvn resemble the Type Ib SN 2009jf (Valenti *et al.*, 2011). Despite the light curve similarity, the high velocity Type Ic PTF10vgv bears no spectral resemblance to iPTF13bvn.

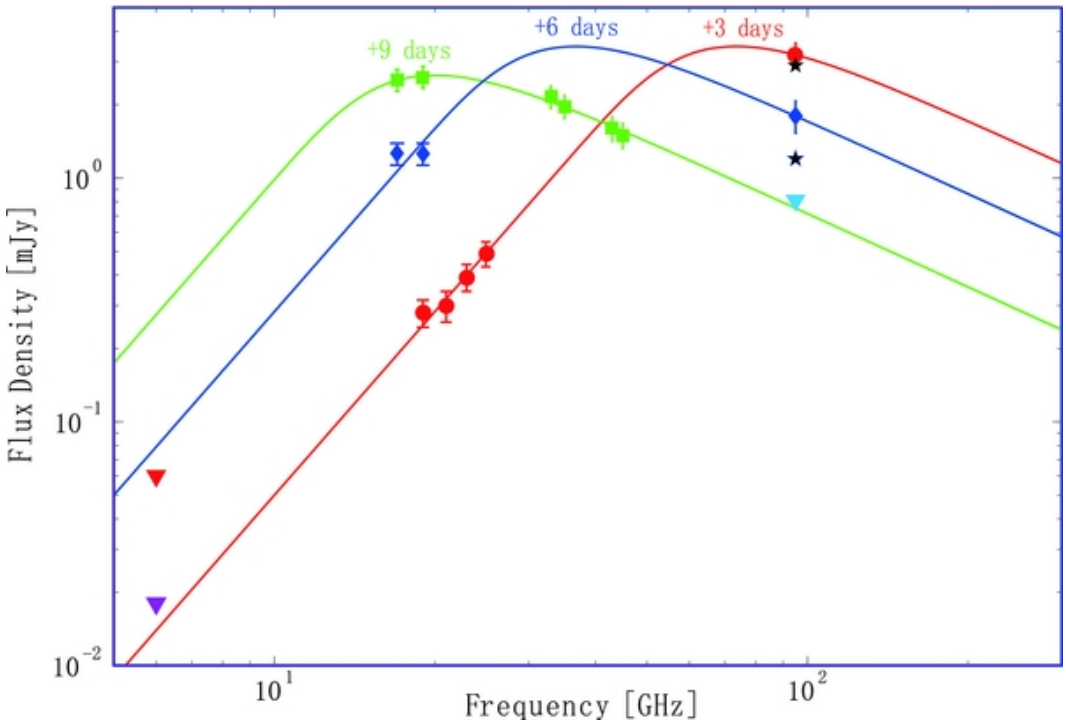

Figure 6.5: **Radio observations of iPTF13bvn.** Flux density as a function of frequency on +3 days (red circles; CARMA + JVLA), +6 days (blue diamonds; CARMA + ATCA), and +9 days (green squares; ATCA). The red triangle is our JVLA detection limit (3-σ) in C band (6 GHz) at +3 days. The purple triangle is the JVLA detection limit (3-σ) on +4 days obtained by (Kamble and Soderberg, 2013). The solid lines show our fits using synchrotron self-absorption models. Additional CARMA measurements on +4 days, and +8 days (black stars) and an upper limit on +10 days (cyan triangle) are also shown.

by a power law $N(\gamma) \propto \gamma^{-3}$. The fitted models are also presented in Figure 6.5.

We note that the SSA model alone is consistent with all our data including the null detection in C band on June 18. However, on June 19.1, Kamble and Soderberg (2013) observed iPTF13bvn with the JVLA in C band and announced a null detection with an rms of 6 μJy. Based on our SSA model, we estimate that Kamble and Soderberg should have detected iPTF13bvn at a level of $\sim$5-σ. Their null detection therefore may require additional free-free absorption at low frequencies. Based on inverse Compton scattering, we estimate the X-ray emission to be 10^{-15} ergs cm s^{-1}. This is consistent with our Swift/XRT upper limit of 1.0×10^{-13} ergs cm s^{-1} on June 17 (assuming a power-law spectrum with a photon index of 2.0). We note that Kong *et al.*

(2013) reported an X-ray detection by co-adding the XRT data from June 17 to July 13. We reprocessed the XRT data from the first ten days after the SN explosion and resulted in a 3-σ upper limit of $4 \times 10^{-14}\,\mathrm{ergs\,cm\,s^{-1}}$. This is also consistent with our expectation from inverse Compton scattering.

We find that the radio emission peaks at $\simeq 73.5,\ 37,\ 20\,\mathrm{GHz}$ with fluxes of $\simeq 3.5,\ 3.5,\ 2.7\,\mathrm{mJy}$ on June 18, 21 and 24, respectively. Following Chevalier (1998), we derive a shock wave radius $R_s \simeq 0.7,\ 1.4,\ 2.3 \times 10^{15}\,\mathrm{cm}$ and a magnetic field strength $B \simeq 8.2,\ 4.1,\ 2.3\,\mathrm{G}$. Using the explosion date determined in the optical data, we find a shock wave velocity of $2.7 \times 10^4 \mathrm{km\,s^{-1}}$, which is typical for SNe Ibc (Chevalier and Fransson, 2006).

Next, we derive a mass-loading parameter $A \simeq 1.3 \times 10^{12}\,\mathrm{g\,cm^{-1}}$. Assuming a typical wind velocity of $v_w \simeq 10^3\,\mathrm{km\,s^{-1}}$ from a WR star (Cappa *et al.*, 2004), the progenitor mass-loss rate $\dot{M} \simeq 3 \times 10^{-5} M_\odot\,\mathrm{yr^{-1}}$. This is consistent with the WR mass-loss rate in Cappa *et al.* (2004).

6.6 Conclusion

iPTF13bvn is a Type Ib SN that exploded on June 15.67 and rose to maximum luminosity of $M_R = -16.6\,\mathrm{mag}$ in about 18 days. The luminosity of the SN in the first 10 days is approximately proportional to t^{-1}. We identify a single progenitor candidate within a 2-σ error radius of 8.7 pc in pre-explosion *HST* imaging. The candidate has a M_B luminosity of $-5.52 \pm 0.39\,\mathrm{mag}$ and a $B-I$ color of $0.25 \pm 0.25\,\mathrm{mag}$. Future *HST* imaging, after the SN fades away, will determine whether this is a single star, a binary, or a star cluster. The non-detection of shock cooling in our light curve constrains the progenitor radius to smaller than a few solar radii. Our radio detections suggest a shock wave with velocity of $2.7 \times 10^4 \mathrm{km\,s^{-1}}$ and a progenitor mass-loss rate of $3 \times 10^{-5} M_\odot\,\mathrm{yr^{-1}}$. We conclude that the pre-explosion photometry of the detected candidate, the radius constraint based on absence of shock cooling, and the mass-loss rate derived from radio are all consistent with a WR progenitor.

6.7 Summary of follow-up research results

In this section, I summarize the follow-up results of iPTF13bvn and its possible progenitor, after an edition of this chapter is published on the ApJ Letters (Cao *et al.*, 2013b),

The spatial coincidence between the SN and the progenitor has later been

improved by aligning the *HST* image of the SN to the pre-explosion archival *HST* images (Fremling *et al.*, 2014). The uncertainty of the alignment was reduced to 0.18 *HST*/ACS pixels. Including the centroid uncertainty of the SN, the location of the SN on the pre-explosion *HST* image was narrowed down to an error circle of radius 9 mas (1-σ). The proposed progenitor candidate is only +1.7 mas in α and +3.6 mas in δ from the center of the error circle.

Based on our published photometry of the possible candidate, Groh *et al.* (2013) soon found that a single WR star within initial mass in the range 31–$35M_{\odot}$ fits the observed photometry. They further suggest that the progenitor likely has a luminosity of $10^{5.55}L_{\odot}$, effective temperature $\sim 45,000$ K, and mass $\sim 10.9M_{\odot}$ at the time of explosion. These models also indicate an uncertain ejecta mass of $\sim 8M_{\odot}$, which is higher than the average of the SN Ib ejecta mass that is derived from the light curve (2–$4M_{\odot}$).

The well-sampled photometry and spectroscopy data obtained allow different groups (Fremling *et al.*, 2014; Bersten *et al.*, 2014; Srivastav *et al.*, 2014) to build bolometric light curves of iPTF13bvn, and to derive its ^{56}Ni mass and ejecta mass. The derived ejecta mass ranges from $1.9M_{\odot}$ to $3.5M_{\odot}$, which is significantly lower than the mass of known WR stars (10–$15M_{\odot}$). As a result, a less massive progenitor in a binary system is preferred. This conclusion is also supported by the nebular spectra of the SN (Kuncarayakti *et al.*, 2015).

If the SN has no extra power resource in its late time evolution, its light curve will decline no slower than the light curve of ^{56}Co decay. By linear Extrapolation of the light curve of the SN (Figure 6.6), we find that iPTF13bvn would fall below the magnitude of the progenitor candidate by at least two magnitudes in June 2015.

On 2015 June 30, *HST*/ACS revisited the site of iPTF13bvn in the $F435W$ and $F555W$ filters. Eldridge and Maund (2016) reported that a source is detected at the location of the SN well below the detection level of the pre-explosion source and thus confirmed that the progenitor star has gone. However, comparing the light curve to that of another well-studied stripped-envelope SN2011dh (Type IIb), the late-time emission of iPTF13bvn might be dominated by the nebular line emission and detected in the most recent *HST* epoch. Another *HST*/ACS visit is needed in about a year to verify whether the SN has completely faded away.

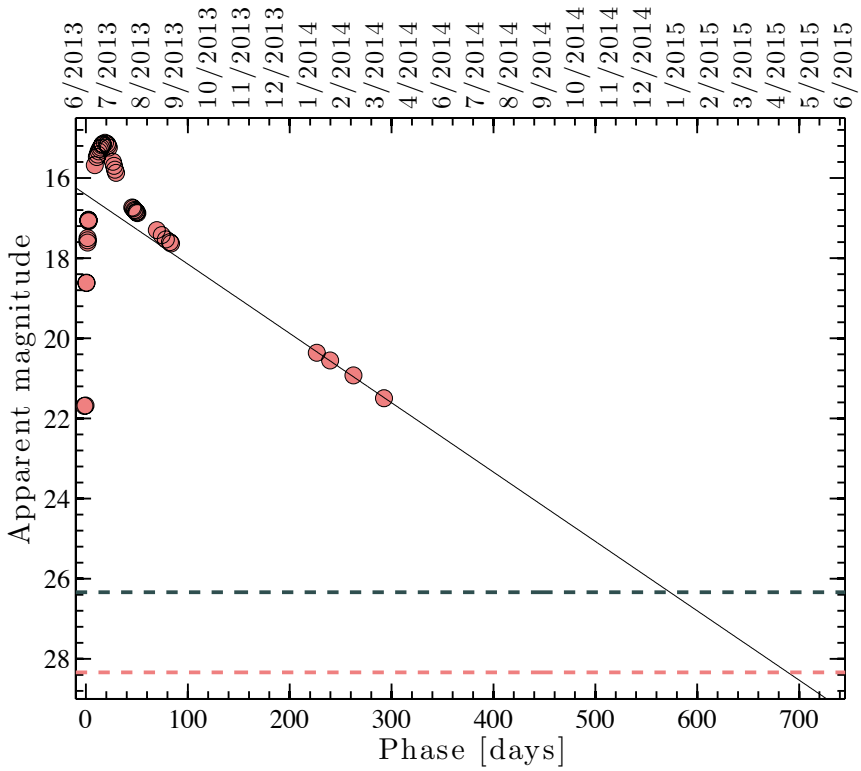

Figure 6.6: **Extrapolation of iPTF13bvn R-band light curve.** The black solid line is the linear extrapolation of the light curve. The black dashed line is the magnitude of the progenitor candidate and the red dashed line indicates two magnitude below the progenitor candidate.

Acknowledgement

We thank A. L. Piro for valuable discussions. We thank the following people for co-operating with our target of opportunity or queue observations: M. Roth (Magellan), A. Hartuynan (TNG), J. Johnson (Keck), and J. Caldwell (HET). We thank A. Howard and H. Isaacson for HIRES data reduction. We thank R. Campbell, Hien Tran, and S. Tendulkar for helping with OSIRIS LGS-AO observation and data reduction. We thank P. Vreeswijk for assisting with HST image registration. We thank J. Vinko, R. Foley, B. Kirshner, D. Perley, A. Corsi, and K. Mooley as proposal co-Is. We thank J. Swift, B. Montet, M. Bryan, R. Jensen-Clem, D. Polishook, and S. Tinyanont for assisting with observations.

M.M.K. acknowledges generous support from the Hubble Fellowship and Carnegie-Princeton Fellowship. J.M.S. is supported by an NSF Astronomy and Astrophysics Postdoctoral Fellowship under award AST-1302771. N.D. acknowl-

edges the Hubble Fellowship. Research by A.G.Y. and his group was supported by grants from the ISF, BSF, GIF, Minerva, the EU/FP7 via an ERC grant and the Kimmel award. The research of J.C.W. is supported by NSF Grant AST 11-09801.

The National Energy Research Scientific Computing Center, supported by the Office of Science of the U.S. Department of Energy, provided staff, computational resources, and data storage for this project. The Australia Telescope is funded by the Commonwealth of Australia for operation as a National Facility managed by CSIRO. This research has been supported by the Australian Research Council through Super Science Fellowship grant FS100100033. The Centre for All-sky Astrophysics is an Australian Research Council Centre of Excellence, funded by grant CE110001020. The National Radio Astronomy Observatory is a facility of the National Science Foundation operated under cooperative agreement by Associated Universities, Inc. Ongoing CARMA development and operations are supported by the National Science Foundation under a cooperative agreement, and by the CARMA partner universities.

Chapter 7

SUMMARY AND FUTURE DIRECTIONS

Supernova emission in the first days of explosions contains rich information about the physical properties of their progenitors. This motivated me to conduct fast-cadence transient surveys in the intermediate Palomar Transient Factory (iPTF), with the scientific goal of constraining the poorly-understood progenitor systems of hydrogen-free supernovae. In the following, I summarize the major results of this thesis:

1. In these fast-cadence surveys, fast discovery and rapid follow-up observations are equally important for infant supernovae (Chapter 2). I showed that (1) the nightly survey cadences were strictly maintained to ensure the young age of discovered supernovae, (2) our realtime image subtraction pipeline managed to deliver supernova candidates within ten minutes of images being taken, and (3) we successfully performed comprehensive follow-up observations of interesting transients within hours of discovery through our pre-approved target-of-opportunity programs on a variety of ground-based and space telescopes. In the years 2013 – 2015, we discovered over a hundred supernovae within a few days of their explosions, forty-nine of which we performed spectroscopic follow-up observations to within the same night or next night following discoveries.

2. A strong and declining ultraviolet pulse was detected from a low-velocity (subclass prototype: SN2002es) Type Ia supernova iPTF14atg within four days of its explosion (Chapter 3). The pulse had a peak luminosity $\gtrapprox 3 \times 10^{41}\,\mathrm{ergs\,s^{-1}}$ and decayed in a few days. This pulse can be best interpreted as the diffusive thermal emission produced by collision between the supernova ejecta and a companion star. This result provides evidence that at least some Type Ia supernovae arise from the single degenerate channel in which accretion onto a white dwarf from a nondegenerate companion star triggers the supernova explosion of the white dwarf.

3. Although iPTF14atg and a sibling low-velocity event iPTF14dpk both resemble the prototypical event SN2002es in optical light curve and spectra around and after maximum, they show distinct early-rise behavior (Chapter 4): the early rising R-band light curve in iPTF14atg before -17 days with respect to its maximum is completely missing in iPTF14dpk. Instead, iPTF14dpk abruptly jumped to $R = -17$ mag with a rise rate of $> 2\,\mathrm{mag\,day^{-1}}$ at -17 days. I showed that the early emission from iPTF14atg can be entirely attributed to the supernova-companion collision. If SN2002es-like events all arise from the single degenerate channel, the missing early emission from iPTF14dpk can be explained as a natural consequence of an unfavored viewing angle along which the supernova-companion interaction is shaded by the optically thick ejecta. I also show that a supernova has a dark phase between its explosion (as estimated by the supernova-explosion collision date) and the first light of its radioactively-powered light curve. The duration of the dark phase depends on the depth of the shallowest ejecta layer in which ^{56}Ni is deposited.

4. A peculiar Type Ia supernova iPTF13asv (Chapter 5) showed strong near-UV emission and absence of iron in the early-phase optical spectra, which implies weak mixing of iron group elements in the fast-moving ejecta and thus a stratified ejecta structure. Compared to the state-of-the-art simulations, I showed that the stratification probably results from a prompt explosion of a white dwarf merger. I further showed that iPTF13asv resembles the super-Chandrasekhar Type Ia supernovae in the large peak luminosity, low expansion velocity, and persistent carbon absorption, and derived a total ejecta mass of about $1.6 M_{\odot}$. Such a super-Chandrasekhar ejecta mass also supports the double-degenerate origin of iPTF13asv.

5. I reported the first direct detection of the progenitor system of a Type Ib supernova iPTF13bvn in the pre-explosion *HST* archival images (Chapter 6). This progenitor has been confirmed by a post-explosion *HST* revisit to the site of the supernova. Separately, comparing the early-phase optical light curve of the supernova to post-shock-breakout cooling models, I constrained the radius of the progenitor being no larger than several solar radii. From the early-phase radio observations of the supernova,

I also derived a mass loss rate of $3 \times 10^{-5} M_{\odot}\,\mathrm{yr}^{-1}$ for the progenitor star in its last few years prior to the supernova explosion. The identified progenitor system in the pre-explosion image and the constraints on the radius and mass loss rate of the progenitor form a comprehensive dataset that Type Ib supernova explosion theories need be tested on.

6. Flash spectroscopy of Type II supernovae is outside the scope of this thesis. However, I briefly summarize it here for completeness, as it is another major result from our fast-cadence surveys. If a supernova explodes within a dense circumstellar medium which is established by the mass loss of its progenitor, the high-energy photons released in the supernova shock breakout may ionize the circumstellar medium. Before the supernova ejecta sweeps over the circumstellar medium, we anticipate to observe a hot thermal continuum emission from the supernova photosphere superposed by recombination lines from the ionized circumstellar medium. In 2013 – 2015, my colleagues and I have observed these recombination lines in a dozen young Type II supernovae (Gal-Yam *et al.*, 2014; Khazov *et al.*, 2016). The line shapes and their evolution provide new diagnostics to the density profile, the wind velocity and the chemical abundance of the circumstellar medium and thus the properties of the mass loss history of the progenitors.

Moving forward, the next frontier in the young supernova field is to expand these single-object results into sample studies. Specifically, early ultraviolet observations of a large sample of thermonuclear supernovae are warranted to determine the fraction of events of different subtypes with early-phase ultraviolet pulses. Then we can estimate the fraction of supernovae arising from the single degenerate channel and constrain the binary geometry of these progenitor systems. This study will enhance our understanding towards the population of white dwarf binaries and potentially improve the measurement precision of supernova cosmology.

In the core-collapse supernovae, the early optical light curves of a large number of supernovae will put constraints on the radii of their progenitors. The early-phase flash spectra and radio observations will determine the physical properties of the mass loss from their progenitors at last stages. The last-stage mass loss of massive stars is a key to understanding the core-collapse

supernovae, because it is probably driven by the core-collapse mechanism and because it sets up the initial condition for the core collapse. Compared to the direct pre-explosion imaging, these new methods can be applied to supernovae in a much larger volume and therefore collect a sample within a reasonable timescale.

iPTF will cease operation in February 2017 and will make way for the Zwicky Transient Facility (ZTF; Smith *et al.* 2014) which equipped with a new camera of 47 $\deg^2$ field of view. ZTF survey speed will be order-of-magnitude faster than that of iPTF and is expected to find one young supernova every night (the exact survey strategy is yet to be determined). The newly commissioned SED Machine (an imager and integrated field unit) on the Palomar 60-inch will automatically undertake immediate follow-up observations of interesting transients discovered in ZTF to provide color information and spectroscopic classification. In parallel to ZTF, a few space missions of large-area fast-cadence ultraviolet surveys, such as ULTRASAT (Sagiv *et al.*, 2014), have also been proposed. These ultraviolet surveys will be more sensitive to high-temperature phases of cosmic explosions, such as the supernova shock breakout and supernova-companion interaction.

In a broad picture, large-scale astronomical surveys including iPTF and ZTF are transforming astronomy from a data-starved to a data-swamped discipline, fundamentally changing traditional methodologies. The data volume that will be collected in the next decade will supersede everything accumulated over the preceding four thousand years of astronomy. Our experience in the iPTF era has demonstrated that applying advanced technologies in computer and data sciences to processing, analyzing and storing the big volume of data will lead to incredible astronomical discoveries in near future.

Appendix A

CLASSICAL NOVAE IN ANDROMEDA: LIGHT CURVES FROM THE PALOMAR TRANSIENT FACTORY AND GALEX†

Yi Cao[1,2], Mansi M. Kasliwal[2,3] , James D. Neill[2], S. R. Kulkarni[2], Yu-Qing Lou[1], Sagi Ben-Ami[4], Joshua S. Bloom[5], S. Bradley Cenko[5], Nicholas M. Law[6], Peter E. Nugent[5,7], Eran O. Ofek[8], Dovi Poznanski[9] & Robert M. Quimby[2,10]

[1] Tsinghua Center for Astrophysics (THCA), Department of Physics, Tsinghua University, Beijing 100084, China

[2] Astronomy Department, California Institute of Technology, 1200 East California Boulevard, Pasadena, CA 91125, USA

[3] Observatories of the Carnegie Institution for Science, 813 Santa Barbara Street, Pasadena, CA 91101, USA

[4] Department of Particle Physics and Astrophysics, The Weizmann Institute of Science, Rehovot 76100, Israel

[5] Department of Astronomy, University of California, Berkeley, CA 94720-3411, USA

[6] Dunlap Institute for Astronomy and Astrophysics, University of Toronto, 50 St. George Street, Toronto, M5S 3H4 Ontario, Canada

[7] Computational Cosmology Center, Lawrence Berkeley National Laboratory, 1 Cyclotron Road, Berkeley, CA 94720, USA

[8] Benoziyo Center for Astrophysics, Faculty of Physics, The Weizmann Institute of Science, Rehovot 76100, Israel

[9] School of Physics and Astronomy, Tel-Aviv University, Tel Aviv 69978, Israel

[10] IPMU, University of Tokyo, Kashiwanoha 5-1-5, Kashiwa-shi, Chiba, Japan

†An edition of this chapter was published on the *Astrophysical Journal*, vol. 752, 133 (2012).

Abstract

We present optical light curves of 29 novae in M31 during the 2009 and 2010 observing seasons of the Palomar Transient Factory (PTF). The dynamic and rapid cadences in PTF monitoring of M31, from one day to ten minutes, provide excellent temporal coverage of nova light curves, enabling us to record the photometric evolution of M31 novae in unprecedented detail. We also detected eight of these novae in the near-ultraviolet (UV) band with the Galaxy Evolution Explorer satellite. Novae M31N 2009-10b and M31N 2010-11a show prominent UV emission peaking a few days prior to their optical maxima, possibly implying aspherical outbursts. Additionally, our blueshifted spectrum of the recent outburst of PT And (M31N 2010-12a) indicates that it is a recurrent nova in M31 and not a dwarf nova in the Milky Way as was previously assumed. Finally, we systematically searched for novae in all confirmed globular clusters (GCs) of M31 and found only M31N 2010-10f associated with Bol 126. The specific nova rate in the M31 GC system is thus about one per year, which is not enhanced relative to the rate outside the GC system.

A.1 Introduction

Classical novae (CNe) are interesting for at least two reasons: first, they provide a laboratory to investigate thermonuclear runaways in semidegenerate conditions (e.g., Bode and Evans, 2008); second, they have been proposed as progenitors of type Ia supernovae (e.g., Starrfield *et al.*, 1988). Observations of Galactic novae are limited due to extinction and distance determination. Given the fact that nova outbursts are about 10^3 to 10^4 times more frequent and 10^3 to 10^4 times less luminous than supernovae, nova searches are limited to the nearest galaxies.

CNe in M31 (The Andromeda Galaxy) have been observed for nearly a century (Hubble, 1929; Arp, 1956; Rosino, 1964, 1973; Ciardullo *et al.*, 1987; Rosino *et al.*, 1989; Sharov and Alksnis, 1991; Tomaney and Shafter, 1992; Rector *et al.*, 1999; Cassatella *et al.*, 2004; Shafter and Irby, 2001; Darnley *et al.*, 2004, 2006; Kasliwal *et al.*, 2011; Shafter *et al.*, 2011a). The published nova rates for M31 range between 24 yr^{-1} (Arp, 1956) and 65 yr^{-1} (Darnley *et al.*, 2004).

The Palomar Transient Factory (PTF) (Law *et al.*, 2009; Rau *et al.*, 2009) acquired nearly daily monitoring of M31 in the R band during the 2009 and

2010 observing seasons. It provides three advantages for the study of novae in M31: first, the large field of view (FoV) of 7.2 square degrees covers the main region of M31 in one snapshot. Second, PTF has fast and dynamic cadences from one day to as short as ten minutes. This temporal coverage gives unprecedentedly detailed light curves. Third, the limiting magnitude is $R \simeq 20\,\mathrm{mag}$ (a little worse near the center of M31 where the background is strong and the gradient is steep). Hence, given the mean distance modulus of 24.36 for M31 (Vilardell *et al.*, 2010), PTF can detect all but the most heavily extincted novae in M31 (weather-permitting) and follow them up down to a magnitude of $\mathrm{M}_R \sim -4.4$.

The PTF data also offer an opportunity to explore known recurrent novae (RNe) in M31 and perhaps discover new ones. According to the catalog maintained by Pietsch (2010), about thirteen recurrent novae have been discovered in M31. The white dwarf masses of RNe are thought to be closer to the Chandrasekhar mass limit than those of ordinary CNe (Starrfield *et al.*, 1988)

Another issue related to novae that can be assessed with PTF archives is whether the nova rate in the globular cluster (GC) system is enhanced relative to that outside the globular cluster system. Ciardullo *et al.* (1990b) did a search for novae in fifty-four M31 GCs based on the Hα surveys of Ciardullo *et al.* (1987) and Ciardullo *et al.* (1990a). In a mean effective survey time of approximate two years, they did not find any nova outbursts in any of the M31 GCs. Tomaney *et al.* (1992) reported another one-year search of over two hundred M31 GCs with Hα emission but did not find any nova outbursts, providing an upper limit on the rate of 0.005 nova yr^{-1} GC^{-1}. The only GC nova found in M31 is M31N 2007-06b (Shafter and Quimby, 2007). Henze *et al.* (2009c) then derived a rate of 1.1 nova yr^{-1} for the M31 GC system, which is comparable to the rate (per unit mass) outside the globulars.

In a nova outburst, except for a short "fireball" phase where radiation is given out by the thermal emission of the photosphere, UV photons are thought to originate at the surface of the white dwarf (WD), deep within the nova envelope, while optical photons are released near the surface of the envelope and result from absorption and re-emission of relatively low ionization species such as Cr II, Fe II and other heavy elements in the envelope. These species are either from secular evolution of the WD progenitor or due to the mass transfer from the companion (Williams *et al.*, 2008). Nova shells therefore serve as

passive photon converters whose spectra reflect the reprocessing of incident UV light to longer wavelength bands. Eventually, the expansion decreases the temperature and dilutes absorbing species to finally reveal the UV photons (Kato and Hachisu, 1994; González-Riestra and Krautter, 1998). Therefore, to explore the UV light powering the nova emission, we searched in parallel for any contemporaneous UV observations of CNe in M31 with the *GALEX* satellite (Martin *et al.*, 2005). We obtained near UV-optical light curves for eight novae in M31.

This paper is arranged as follows. Section A.2 describes PTF and *GALEX* observation and data reduction as well as data from other sources. Section A.3 presents light curves of CNe and describes their morphology. Section A.4 discusses novae in GCs. Section A.5 focuses on RNe. Section A.6 discusses ordinary and bizarre novae observed in the UV band. Section A.7 revisits the relation between the maximum magnitude and the rate of decline (MMRD) with our nova sample. Finally we conclude this paper in Section A.8.

A.2 Observations

Nova Sample

We examined all novae as reported by Pietsch (2010)[1] in the PTF image archives and obtained light curves for twenty-nine novae. Among them, eight novae also have UV light curves from *GALEX*. Table A.1 gives main parameters of PTF and *GALEX* observations. Table A.2 describes the nova sample and Figure A.1 illustrates their spatial distribution.

PTF

PTF (Law *et al.*, 2009) employs the 1.2-m Oschin Telescope at Palomar Observatory with an array of twelve CCD chips, each having 4K×2K pixels. One of the chips does not function for unknown reasons. The pixel size is $1''.0$/pixel and thus the total FoV is 7.2 square degrees.

The time coverage of PTF observations of M31 during the 2009 and 2010 seasons is shown in Figure A.2. The first observing season is from 2009 August 18 to 2010 January 17 and the second is from 2010 June 30 to 2010 December 15. From 2010 August 28 to 2010 September 7, PTF observed M31 with a fast

[1] http://www.mpe.mpg.de/∼m31novae/opt/m31/index.php. This site maintains a comprehensive catalog of novae in M31.

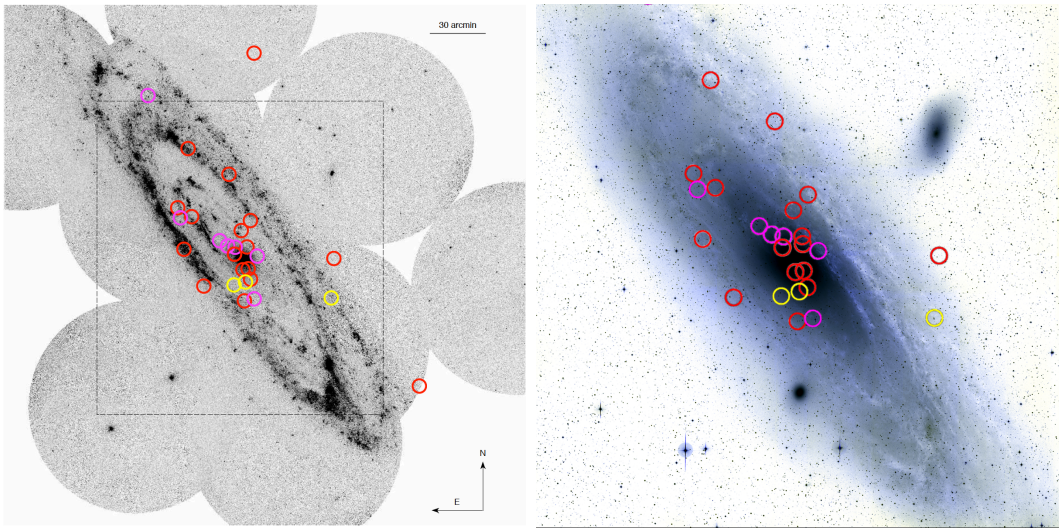

Figure A.1: **Spatial distribution of the nova sample in M31.** The left panel is an image of M31 taken by *GALEX* (Gil de Paz *et al.*, 2007). The right panel is a mosaic image of M31 from PTF (Credit: P. Nugent). The dashed box in the upper panel shows the physical size of the bottom one. The actual FoV is larger than the size of this image. The red circles denote positions of novae only observed in PTF. RNe are highlighted by the yellow circles. The magenta circles denote novae observed by both PTF and *GALEX*.

Table A.1. M31 observation summary

	PTF	*GALEX*
Filter	Mould R	NUV
$\lambda_{\rm effect}$ (Å)	6581	2316
$\Delta\lambda$ (Å)	1251	1060
$t_{\rm expose}$ (s)	60	740-1703
FoV (deg^2)	7.2	1.2
Cadence	10min to days	1-2 days
Epoch	726	51 (the center field) 22-27 (outskirt fields)

Table A.2. M31 nova Sample

Nova Name	α (J2000)	δ (J2000)	Discovery Date by Others	Magnitude at Discovery	PTF First Detection Date	Spectral Type	Reference
M31N 2009-08b	$00^h44^m09^s.87$	$+41°48'50''.8$	2009/08/09.780	17.2(U)[1]	2009/08/18.423	...	1
M31N 2009-08e	$00^h42^m36^s.23$	$+41°18'01''.6$	2009/08/25.896	17.9(R)	2009/08/26.400	Fe II	2
M31N 2009-09a	$00^h42^m26^s.08$	$+41°04'01''.0$	2009/09/02.078	17.1(U)	2009/08/18.454	Fe II	3
M31N 2009-10a	$00^h45^m14^s.04$	$+42°04'38''.8$	2009/10/03.619	17.1(U)	2009/09/30.494	Fe II	4
M31N 2009-10b	$00^h42^m20^s.77$	$+41°16'44''.5$	2009/10/11.414	18.8(R)	2009/10/10.376	Fe II	5
M31N 2009-11a	$00^h43^m04^s.76$	$+41°41'08''.2$	2009/11/03.559	17.8(U)	2009/10/31.321	Fe II	6
M31N 2009-11b[2]	$00^h42^m39^s.61$	$+41°09'03''.2$	2009/11/06.523	18.6(R)	2009/11/07.199	...	7
M31N 2009-11d	$00^h44^m16^s.85$	$+41°18'53''.6$	2009/11/19.194	18.1(R)	2009/12/01.201	Fe II	8
M31N 2009-11e	$00^h42^m35^s.31$	$+41°12'59''.1$	2009/11/21.138	18.8(*Swift* uvw2)	2009/12/01.201	Fe II	9
M31N 2009-12a	$00^h40^m19^s.40$	$+41°15'47''.6$	2009/12/22.488	16.6(U)	2009/12/24.078	...	10
M31N 2010-01a[3]	$00^h42^m56^s.74$	$+41°17'21''.0$	2010/01/11.13	17.6(R)	2010/01/11.130	Fe II	11
M31N 2010-06a	$00^h43^m07^s.56$	$+41°19'49''.0$	2010/06/28.014	18.1(R)	2010/06/30.397	Fe II	12
M31N 2010-06b	$00^h44^m22^s.46$	$+41°28'14''.5$	2010/06/28.014	19.1(R)	2010/06/30.353	Fe II	13
M31N 2010-06c	$00^h44^m04^s.48$	$+41°28'34''.2$	2010/06/26.084	17.8(R)	2010/06/30.353	...	14
M31N 2010-06d	$00^h42^m55^s.61$	$+41°19'26''.0$	2010/06/24.02	19.5(*Swift* uvw1)	2010/07/04.397	Fe II	15
M31N 2010-07a	$00^h43^m20^s.11$	$+41°21'23''.7$	2010/07/07.036	20.6(*Swift* uvw1)	2010/07/07.328	Fe II	16
M31N 2010-09a	$00^h42^m23^s.32$	$+42°17'08''.6$	2010/09/04.552	17.2(U)	2010/09/01.372	Fe II	17
M31N 2010-09b	$00^h43^m45^s.53$	$+41°07'54''.7$	2010/09/30.412	17.7(R)	2010/09/30.230	Fe II	18
M31N 2010-09c	$00^h38^m09^s.06$	$+40°37'25''.9$	2010/09/03.30	18.7(U)	2010/08/13.235	Fe II	19
M31N 2010-10a	$00^h42^m45^s.84$	$+41°24'22''.2$	2010/10/05.551	17.6(R)	2010/10/08.163	Fe II	20
M31N 2010-10b	$00^h42^m41^s.51$	$+41°03'27''.3$	2010/08/19.055	18.9(R)	2010/10/08.163	Fe II	21
M31N 2010-10c	$00^h44^m26^s.56$	$+41°31'13''.8$	2010/10/13.557	17.8(U)	2010/10/13.113	Fe II	22
M31N 2010-10d	$00^h42^m36^s.91$	$+41°19'29''.6$	2010/10/29.478	17.8(U)	2010/10/29.213	Fe II	23
M31N 2010-10e[4]	$00^h42^m57^s.76$	$+41°08'12''.3$	2010/10/31.727	18.1(R)	2010/11/01.158	He/N	24
M31N 2010-10f[5]	$00^h42^m43^s.58$	$+41°12'42''.6$	2010/11/07.06	0.02 cts/s (XRT)	2010/10/12.189	...	25

Table A.2. M31 nova Sample (continued)

Nova Name	α (J2000)	δ (J2000)	Discovery Date by Others	Magnitude at Discovery	PTF First Detection Date	Spectral Type	Reference
M31N 2010-11a	$00^h42^m31^s.60$	$+41°09'51''.5$	2010/11/23.05	18.2(*Swift* uvw1)	2010/12/01.250	He/N	26
M31N 2010-12a[6]	$00^h40^m24^s.37$	$+41°04'03''.5$	2010/12/01.15	16.7(U)	2010/12/01.270	Fe II	27
M31N 2010-12b	$00^h42^m31^s.08$	$+41°27'20''.3$	2010/12/11.095	16.7(U)	2010/12/10.115	...	28
M31N 2010-12c[3]	$00^h42^m56^s.67$	$+41°17'21''.2$	2010/12/15.528	17.2(U)	2010/12/15.093	He/N	29

References. — (1) Rodríguez-Gil *et al.*, 2009; Ovcharov *et al.*, 2009; (2) Ovcharov *et al.*, 2009; Henze *et al.*, 2009b; Medvedev *et al.*, 2009; (3) Henze *et al.*, 2009a; Barsukova *et al.*, 2009b; (4) Fabrika *et al.*, 2009a; (5) Nakano and Yusa, 2009; Podigachoski *et al.*, 2009b; Hornoch and Kusnirak, 2009; Fabrika *et al.*, 2009b; Hornoch *et al.*, 2009a; Nakano *et al.*, 2009; Nakano and Itagaki, 2009; Yamaoka *et al.*, 2009; Martignoni *et al.*, 2009; Di Mille *et al.*, 2009; Barsukova *et al.*, 2009a; Henze *et al.*, 2009b; (6) Nishiyama and Kabashima, 2009a; Burwitz *et al.*, 2009; Hornoch *et al.*, 2009c; (7) Nishiyama *et al.*, 2009a; Henze *et al.*, 2009e; Kasliwal, 2009; Henze *et al.*, 2009d; Kasliwal *et al.*, 2009; (8) Nishiyama and Kabashima, 2009b; Podigachoski *et al.*, 2009d; Hornoch *et al.*, 2009b; Podigachoski *et al.*, 2009c; (9) Green, 2009; Pietsch *et al.*, 2009b; Cagas, 2009; Kusnirak *et al.*, 2009; Hornoch and Pejcha, 2009; Pietsch *et al.*, 2009a; (10) Nishiyama *et al.*, 2009b; (11) **Atel2383**; Burwitz *et al.*, 2010a; Hornoch *et al.*, 2010j,i; Green, 2010e; Pietsch and Henze, 2010a; Hornoch *et al.*, 2010g; Pietsch and Henze, 2010b; (12) Hornoch *et al.*, 2010d,l,a,h,f; Henze *et al.*, 2010d; Pietsch *et al.*, 2010k; (13) Hornoch *et al.*, 2010c,a,h; (14) Burwitz *et al.*, 2010b; Pietsch *et al.*, 2010a; Hornoch, 2010; Hornoch *et al.*, 2010a,f; Burwitz *et al.*, 2010c; (15) Pietsch *et al.*, 2010b; Hornoch *et al.*, 2010k; Pietsch *et al.*, 2010f; Henze *et al.*, 2010d; Barsukova *et al.*, 2010; Pietsch *et al.*, 2010k; (16) Hornoch and Zasche, 2010; Henze *et al.*, 2010a; Hornoch *et al.*, 2010a,h; Henze *et al.*, 2010b,d; Pietsch *et al.*, 2010k; (17) Yusa, 2010a; Shafter *et al.*, 2010d; (18) Yusa, 2010b; Pietsch *et al.*, 2010j; Shafter *et al.*, 2010f,h; (19) Romadan *et al.*, 2010; Shafter *et al.*, 2010c; Krushinski *et al.*, 2010; (20) Yusa, 2010c; Shafter *et al.*, 2010h; Pietsch *et al.*, 2010k; (21) Corral-Santana *et al.*, 2010; Shafter *et al.*, 2010i; (22) Nakano and Yusa, 2010; Shafter *et al.*, 2010g; (23) Nishiyama and Kabashima, 2010; Sun *et al.*, 2010; Hornoch *et al.*, 2010e; Hornochova and Wolf, 2010; Shafter *et al.*, 2010b; (24) Hornochova *et al.*, 2010; Pietsch *et al.*, 2010d; Shafter *et al.*, 2010a; Pietsch *et al.*, 2010g (25) Pietsch *et al.*, 2010i; Henze *et al.*, 2010c; Shafter *et al.*, 2010e; (26) Pietsch *et al.*, 2010h; Cao *et al.*, 2010; Fabrika *et al.*, 2010; (27) Zheng *et al.*, 2010; (28) Green, 2010a; Koishikawa, 2010; Pietsch *et al.*, 2010c; Green, 2010b,c; Yusa, 2010d; Koishikawa *et al.*, 2010; Pietsch *et al.*, 2010e; (29) Prieto *et al.*, 2010a; Yusa, 2010e; Green, 2010d,f; Prieto *et al.*, 2010b;

[1]The bracket following the magnitude indicates the observation band and U represents unfiltered observation.

[2]RN; 1997-11k=2001-12b=2009-11b.

[3]According to CBET 2610, 2010-01a and 2010-12c are two different objects within 0".8.

[4]RN; 1963-09c=1968-09a=2001-07b=2010-10e.

[5]The nova 2010-10f is probably inside the GC Bol 126.

[6]Another recurrent burst of PT And.

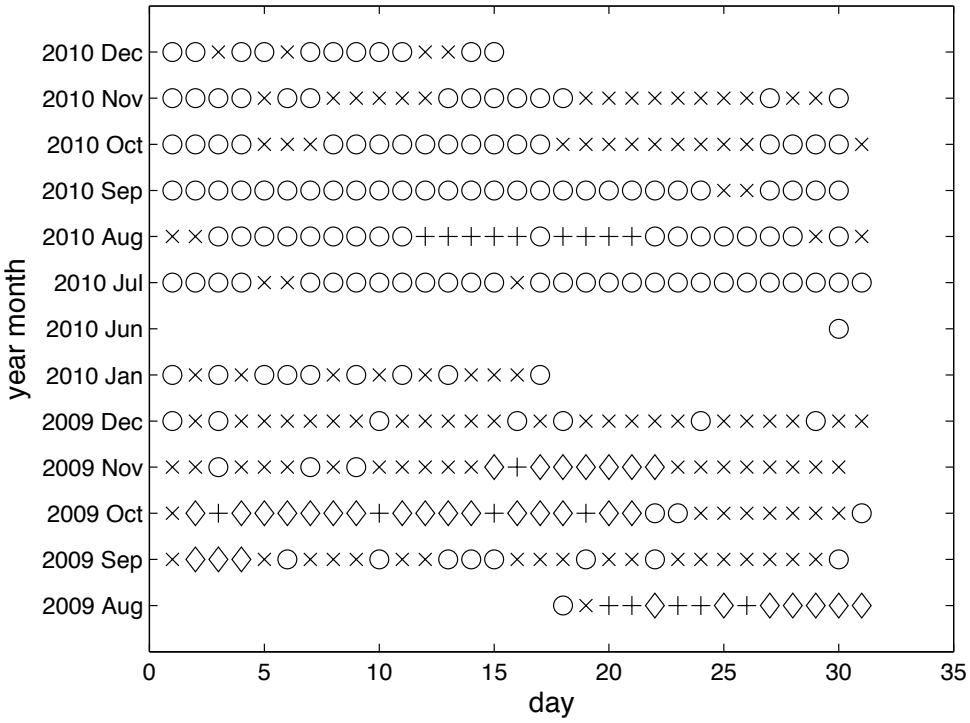

Figure A.2: **Temporal coverage of both PTF and *GALEX*.** A plus sign indicates an epoch observed by both PTF and *GALEX* while a cross indicates an epoch observed by neither. PTF-only observations are denoted with circles. *GALEX*-only observations are represented by diamonds. Statistically, during the first observing season, PTF observed M31 for 20% of 156 total nights, *GALEX* observed for 21% nights and the two overlapped on 6% nights. In the second season, PTF observed for 75% of 169 nights and *GALEX* overlapped with PTF on nine nights.

Table A.3. M31 novae observed with *GALEX*

Name	Epochs	UT start	UT end
M31N 2009-09a	63	2009/08/20.429	2009/10/15.707
M31N 2009-10a	13	2009/10/02.629	2009/10/21.457
M31N 2009-10b	22	2009/10/08.587	2009/11/15.725
M31N 2009-11b	63	2009/08/20.429	2009/11/15.725
M31N 2010-06a	13	2010/08/12.894	2010/08/21.998
M31N 2010-06b	13	2010/08/12.894	2010/08/21.998
M31N 2010-06d	13	2010/08/12.894	2010/08/21.998
M31N 2010-07a	13	2010/08/12.894	2010/08/21.998

Table A.4. X-ray and spectroscopic observation epochs of M31 novae

Novae	Observation UT Spectrum	X-Ray	Reference
M31N 2009-08e	2009/09/18.014		Medvedev *et al.*, 2009
M31N 2009-09a	2009/09/18.18		Barsukova *et al.*, 2009b
M31N 2009-10a	2009/10/09.91		Fabrika *et al.*, 2009a
M31N 2009-10b	2009/10/09.820		Fabrika *et al.*, 2009b
	2009/10/15.5		Yamaoka *et al.*, 2009
	2009/10/19.936		Barsukova *et al.*, 2009a
M31N 2009-11a	2009/11/25.32		Hornoch *et al.*, 2009c
M31N 2009-11b	2009/11/08.35		Kasliwal, 2009
	2009/11/09.82		Kasliwal *et al.*, 2009
M31N 2009-11d	2009/11/21.31		Hornoch *et al.*, 2009b
M31N 2009-11e	2009/11/22.19		Hornoch and Pejcha, 2009
M31N 2010-01a	2010/01/13.08		Hornoch *et al.*, 2010j
	2010/01/15.09		Hornoch *et al.*, 2010i
M31N 2010-06a	2010/07/19		Hornoch *et al.*, 2010f
M31N 2010-06b	2010/07/19		Hornoch *et al.*, 2010f
M31N 2010-06d	2010/08/08.86		Barsukova *et al.*, 2010
M31N 2010-07a	2010/07/19		Hornoch *et al.*, 2010f
M31N 2010-09a	2010/09/07.23		Shafter *et al.*, 2010d
M31N 2010-09b	2010/10/01.39		Shafter *et al.*, 2010f
	2010/10/06.40		Shafter *et al.*, 2010h
M31N 2010-09c	2010/09/14.23		Shafter *et al.*, 2010c
M31N 2010-10a	2010/10/06.38		Shafter *et al.*, 2010h
M31N 2010-10b	2010/10/28.31		Shafter *et al.*, 2010i
	2010/11/03.31		Shafter *et al.*, 2010i
	2010/11/11.28		Shafter *et al.*, 2010i
M31N 2010-10c	2010/10/17.35		Shafter *et al.*, 2010g
M31N 2010-10d	2010/10/30.31		Shafter *et al.*, 2010b
M31N 2010-10e	2010/11/04.32		Shafter *et al.*, 2010a
		2010/11/15.16	Pietsch *et al.*, 2010g
		2010/11/17.09	Pietsch *et al.*, 2010g
M31N 2010-10f	2010/11/13.285		Shafter *et al.*, 2010e
		2010/11/03.04	Pietsch *et al.*, 2010i
		2010/11/06.20	Pietsch *et al.*, 2010i
		2010/11/07.06	Pietsch *et al.*, 2010i
M31N 2010-11a	2010/12/05.74		Fabrika *et al.*, 2010
M31N 2010-12a	2010/12/30.24		this paper
M31N 2010-12c	2010/12/30.25		this paper

cadence of about ten minutes. All PTF images were taken with a R-band filter. The average seeing during the two seasons is $2''.5$ with a median value of $2''.4$. We discarded $< 1\%$ of the images with seeing worse than $3''.5$, because the high stellar density in M31 leads to strong blending among adjacent objects under bad seeing conditions. Our final image database samples over seven hundred epochs on 7987 individual CCD images.

Data Reduction and Photometry

All images were processed through the PTF pipeline at the Lawrence Berkeley National Laboratory (see Law *et al.*, 2009) with astrometric solutions of $1''.0$ accuracy. The relative photometry is calibrated as follows. We first use SExtractor to make a source catalog for each image. We then choose the catalog with the largest number of $14\,\mathrm{mag} < R < 17\,\mathrm{mag}$ sources as reference. Then, other non-reference catalogs are spatially matched to the reference using source positions and forced to agree with the reference photometry after variable sources are removed with a standard outlier procedure[2]. The resulting photometric uncertainty is usually around 0.05 mag. The absolute magnitudes are calibrated to the catalog in Massey *et al.* (2006).

Photometry is also done with SExtractor. The background is estimated in a region of $20'' \times 20''$ centered at each target. Fluxes are measured within a Kron-like elliptical aperture. The first order moment of each object determines the Kron radius r (Kron, 1980) and the second order moment determines ellipticity and position angle. The aperture has an area of $6.25\pi r^2$. For a null detection, a 3-σ limiting magnitude is estimated.

In order to assess the quality of photometric results from SExtractor, we constructed light curves of three novae (M31N 2009-09a, M31N 2009-10a and M31N 2009-11a) with two alternative methods: 1) aperture photometry with an aperture radius of seeing and with constant local background; 2) aperture photometry with an aperture radius of seeing and with local background estimation by linear regression. All three methods lead to consistent magnitude measurements.

[2] *NIST/SMATCH e-Handbook of Statistical Methods* at http://www.itl.nist.gov/div898/handbook/eda/section3/ea35h.htm

Photometric and Spectroscopic Follow-up

Photometric follow-up of M31N 2010-11a was triggered for the Palomar 60-inch telescope (Cenko *et al.*, 2006) on 2010 December 4. On 2010 December 30, we also used the Low Resolution Imaging Spectrometer (LRIS; Oke *et al.*, 1995) mounted on the Keck I telescope to obtain spectra of M31N 2010-12a and M31N 2010-12c. These spectra were obtained with a configuration of the 560 dichroic, the 400/3400 grism in the blue side and the 400/8500 grating in the red side with a central wavelength of 7800 .

GALEX

GALEX is a wide-field imaging UV space telescope that was originally launched with near-UV (NUV and far-UV (FUV) detectors. Unfortunately, the FUV detector failed before the start of the PTF survey of M31. The NUV detector effective wavelength is 2316 Å and the band width is 1060 Å (Martin *et al.*, 2005; Morrissey *et al.*, 2007). This channel has a FoV of 1.2 square degrees (Morrissey *et al.*, 2007).

GALEX Observation Summary

The visibility of M31 for *GALEX* is defined by the Sun, Moon and Earth-limb constraints that limit the observations more than for ground-based observatories. The result is that *GALEX* was able to intensively monitor M31 in several campaigns that overlap with the PTF campaigns of 2009 and 2010 (2009 August 08 to 2009 September 04; 2009 October 02 to 2009 October 21; 2009 November 15 to 2009 November 22; 2010 August 12 to 2010 August 21). Figure A.2 illustrates *GALEX* temporal coverage and its overlap with PTF. A field centered in M31 is monitored daily, while ten outskirt fields in M31 are observed every other day. So we have fifty-one epochs of the center field while about 22−27 epochs of the outskirt fields. The exposures were all taken during single orbit pointings and thus have durations close to 1500 seconds with a range from 740 seconds to 1703 seconds. Table A.1 summarizes parameters of observations.

Photometry

Photometry was done with an aperture with 6″ in radius at each nova position, and was calibrated using the standard *GALEX* zero-points to the AB

magnitude system (Morrissey *et al.*, 2007). Eight novae were detected; see Table A.3.

Data from Other Sources

For completeness in optical and UV bands, we incorporate photometric measurements of novae from ATel and CBET reports (see the reference column in Table A.2). This includes optical photometry in R, B, V, r', i' and Hα bands as well as unfiltered data. We also include data published in Shafter *et al.* (2011a) where several novae in 2009 are well-sampled. The UV data in ATel reports are mainly obtained by *Swift* (Gehrels *et al.*, 2004). For consistency of data between *GALEX* and *Swift*, all *Swift* data are calibrated onto the AB magnitude system (Siegel *et al.*, 2010). When data from different sources are used, due to difference of filters, data may have systematical errors among different projects.

In addition, we include X-ray and spectroscopic information of novae in M31 from *Swift* from either ATel reports or our own analysis (see Table A.4).

Missing Novae

During the two seasons presented here, we did not find three announced novae in the PTF archive: M31N 2009-10c, M31N 2009-11c and M31N 2010-07b.

M31N 2009-10c took place at $\alpha = 00^h42^m45^s8$, $\delta = +41°15'57''$. (J2000), less than thirty arcseconds from the center of M31. This nova reached maximum light, $R = 17.2$, on Oct 9, 2009 (Podigachoski *et al.*, 2009a). PTF observed M31 on Oct 10, 2009. In the vicinity of the nova position, if we fit a constant background, each pixel has a count $\sim$ 50000 with a standard deviation of $\sigma \sim 6000$. Given that the seeing then was about three arcseconds and that the zeropoint is 27.6, the local 3-σ limiting magnitude is 15.2. If the background is fit with a plane, the standard deviation is roughly 1500 and the limiting magnitude is 16.8. Thus this nova is not detected in these images. In the subtraction image, the circle of $30''$ in radius in the center of M31 is excluded in the subtraction algorithm where the algorithm does not work well. As a result, we missed this nova in our PTF data.

There are gaps of forty arcseconds between adjacent CCDs. M31N 2009-11c unfortunately fell in the gap between two adjacent CCDs.

M31N 2010-07b showed strong Hα emission in July. However, its luminosities

in R and r' bands were about 20.7 mag in June and July (Hornoch *et al.*, 2010b). This fact suggested that this nova likely peaked much earlier and decayed in June and July. The second observing season of PTF started at the end of June (see Figure A.1). This nova thus was below our single-image detection threshold.

Admittedly, we did not carry out a real-time search of novae in M31 in the first two seasons of PTF. Our nova sample inherits the sensitivity and incompleteness of those projects that discovered these novae.

Special Novae

M31 2010-09c

This nova has a faint and close neighbor with R= 19.85 ± 0.2 within two arcseconds. In SDSS Data Release 8, we found two nearby sources within two arcseconds. With the empirical relation between photometry of *ugriz* and UBVRI systems (Jordi *et al.*, 2006), we obtain that the neighbors have R= 20.53 and R= 20.33, giving a total magnitude of 19.67 that is consistent with our measurements. The uncertainty caused by the neighbors has been included in the nova light curve. The spectroscopic confirmation in Shafter *et al.* (2010c) identified the M31N 2010-09c as a real nova of Fe II type.

M31 2010-10f

This nova is spatially associated with the M31 GC Bol 126 (Wirth *et al.*, 1985). In Figure A.4, we clearly see a brightening of the GC by about one magnitude on around 2010 October 10 (Julian Date: 2455480). The luminosity of the GC before the nova is 16.8 ± 0.2. The light curve of the nova is obtained by subtracting the GC brightness. One possible reason for the large uncertainty in the photometry measurements is that the nova is only a few pixels away from the edge of the CCD.

M31N 2010-01a and M31N 2010-12c

These two novae occurred within one arcsecond of each other, a separation which is less than the pixel scale of PTF ($\simeq 1''.0$). A highly accurate astrometric solution shows that they are indeed two separate objects (Green, 2010f).

We obtained a spectrum of 2010-12c with LRIS on 2010 December 30 (Figure A.3, bottom panel). The spectrum shows a weak continuum superposed with many emission lines, illustrating that the nova has already entered the nebular phase. We identified Hα, Hβ, Hγ, Hδ, OI 8446 and several He and N lines. Hδ has a slight P Cygni profile. The emission lines suggest the nova is of the He/N type. After fitting each emission line with a Gaussian profile, we find that Hα is centered at 6556 Å, Hβ at 4858 Å, Hδ at 4338 Å, and OI 8446 at 8437 Å, suggesting a blueshifted velocity in the range from -200 to -300 km s^{-1}. From the full width at zero intensity (FWZI) of the Balmer lines, we derived an expansion velocity of $\simeq 3000$ km/s. On the other hand, the systemic velocity of M31 is -300 km s^{-1}. The nova lies about $2'$ northeast of the center of M31. The HI 21 cm line (Chemin *et al.*, 2009; Corbelli *et al.*, 2010) suggests a rotation velocity of about 260 km s^{-1} receding from us. However, the nova is apparently close to the center of the galaxy, and therefore may not follow the motion of the disk measured by the HI 21cm line. Another measurement of a nearby planetary nebula (Merrett *et al.*, 2006) at $\alpha = 00^h42^m57^s.4$ and $\delta = +41°17'26''$. (J2000) suggests a radial velocity of -300 km s^{-1} along the line of sight. Consequently, we conclude that 2010-12c is a real nova in M31.

Additionally, these two novae have two more historical neighboring novae within $10''$.: nova 30 (discovered in 1986) from Ciardullo *et al.* (1987) and M31N 2009-08a. Generally speaking, our sample includes more novae in the central region of M31 than in the outskirt. This might result from the high stellar density in the center of the galaxy.

A.3 Light curves of classical novae

Except three recurrent events, light curves of twenty-six CNe are presented in Figures A.5 to A.9. An electronic version of the PTF and *GALEX* data is online[3] in a machine-readable format. An example of M31N 2010-12a is illustrated in Table A.5.

The nova light curves are presented in groups based on their features described below. Figures A.5 presents novae with smooth decline. Figure A.6 illustrates novae with jittery decline. Novae with well-sampled rise stages are displayed in Figure A.7. Figure A.8 highlights two novae recorded during the PTF 10min-cadence observations where their rise histories were recorded in great detail.

[3]http://www.astro.caltech.edu/∼ycao/m31novae/index.html

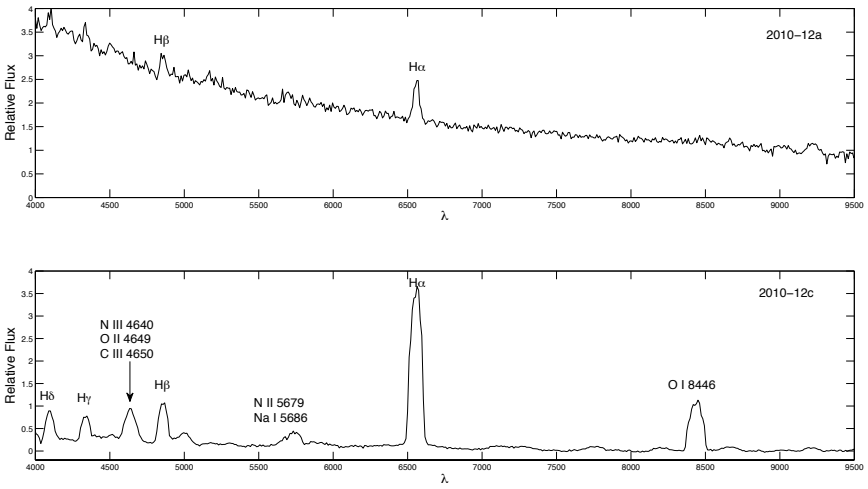

Figure A.3: Spectra of M31N 2010-12a (top) and M31N 2010-12c (bottom), obtained with LRIS on Keck-I telescope on December 30th, 2010.

Figure A.4 shows the light curves of the only GC nova M31N 2010-10f and its host Bol 126. All other under-sampled light curves are collected in Figure A.9.

Table A.6 summarizes the photometric and morphological features of these novae.

Morphological classification

The shape of each light curve can be characterized by several parameters: the rise rate, the rise time to the maximum magnitude, the rise morphology, the maximum magnitude, the decline rate that is represented by $t_n (n = 1,\ 2,\ 3,\ \ldots)$ which is defined as the time interval during which a nova decays from its maximum by n magnitudes, and the decline morphology. Since PTF samples the M31 nova luminosity distribution down to $M_R \sim -4.5$ (see §1) and the peak absolute magnitude of a nova can range from -5 to -9, we use t_2 to indicate the decline rate. In our measurements, t_2 is estimated by linear interpolation of the light curves. Other parameters are defined as follows: the rise rate is the mean rate from the first detection to the first local maximum; the rise time is the interval from first detection in PTF to its global maximum. All measurements are done with PTF R-band data.

For novae inside our Galaxy, Strope *et al.* (2010) classified the diverse light curves morphologically according to their decline light curves. With a median

Table A.5. Light curve of M31N 2010-12a

Julian Date	Magnitude	Magnitude Error[1]
2455530.702	20.190	99.000
2455531.770	16.763	0.030
2455532.780	15.581	0.023
2455532.825	15.561	0.025
2455535.681	16.013	0.024
2455537.578	16.325	0.024
2455537.622	16.346	0.025
2455538.577	16.526	0.024
2455538.621	16.496	0.025
2455539.577	16.636	0.026
2455539.620	16.638	0.025
2455540.615	16.721	0.027
2455540.659	16.776	0.026
2455541.613	16.817	0.027
2455541.656	16.899	0.031
2455544.593	17.243	0.029
2455544.639	17.175	0.032
2455545.593	17.283	0.038
2455545.637	17.303	0.034

[1]99.000 in Magnitude Error indicates that a 3σ upper limit is given in Magnitude.

coverage extending to 8.0 mag below peak, novae were grouped into seven classes. In their sample of 93 nova light curves, 38% decline smoothly, 21% have plateau phase, 18% show dust dips, 1% rebrighten with a cusp-shaped secondary maxima, 4% oscillate quasi-sinusoidally on smooth decline, 2% are flat-topped and 16% have irregular jitters or flared during decline. However, PTF is unable to follow M31 novae to such late times in the light curve evolution. We, instead, roughly classify our M31 novae into two major classes: S-class for smooth light curves and J-class for jittery light curves or for light curves with flares superposed on the decline. Statistically in our nova sample, 60% show S-class decline and 40% belong to the J-class. Given that our sample is quite small, this result is roughly consistent with the Galactic population. We do not see any flat-topped nova.

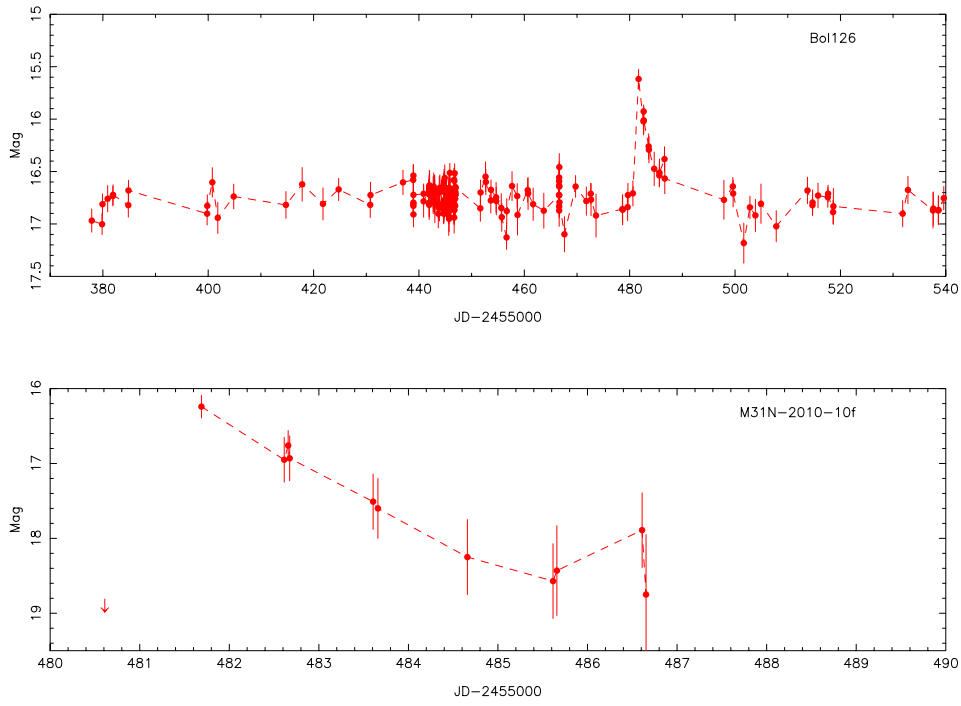

Figure A.4: Light curve of GC Bol 126 is shown in the top panel. The subtracted light curve of M31N 2010-10f is presented in the bottom panel.

Similarly, thanks to the rapid cadences, PTF sampled the rising stages of several novae very well. This enables us to employ the same S-J classification to describe the rising parts of the light curves (see Table A.6). We find that the S-class novae rise very fast (e.g., M31N 2010-09b rose within two days) while the J-class novae rise more slowly (e.g., M31N 2010-10b took thirty days to reach its maximum). But we do not see any relation between the rise time and peak magnitudes. Luminous M31N 2010-09b and subluminous M31N 2009-11a rose rapidly while luminous M31N 2010-07a and subluminous M31N 2009-09a both rose very slowly.

During an extremely-fast-cadence (tens of minutes) experiment in PTF, we observed the rising stages of M31N 2010-09a and M31N 2010-09c in unprecedented detail, as shown in the bottom panels of Figure A.8. The rise of both novae is smooth over a timescale of tens of minutes.

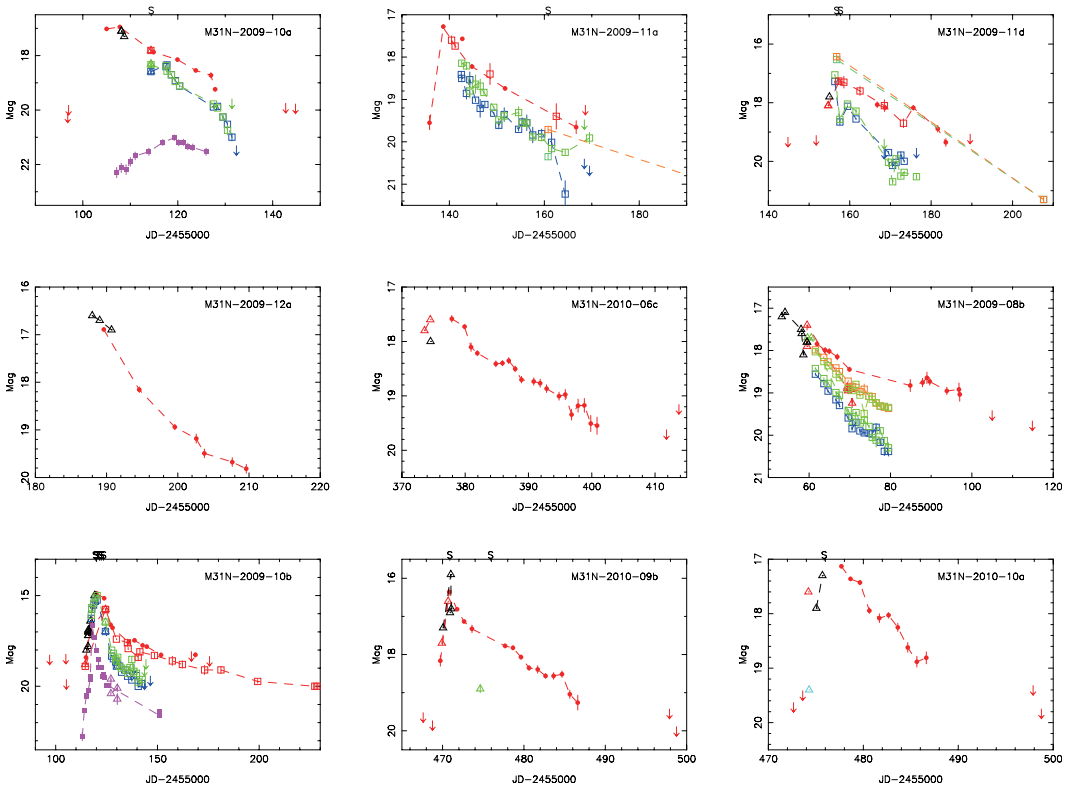

Figure A.5: **Light curves of nine smoothly declining novae.** Different symbol shapes mean data from different sources. PTF and *GALEX* data are shown in filled circles and squares, respectively. Data collected from ATel and CBET reports are in empty triangles and data read from Shafter *et al.* (2011b) are in empty squares. Data in different filters are illustrated by colors. R band data are in red; B band data in blue; V band data in green; r' band data in orange; i' band data in Chartreuse; Hα narrow band data in cyan; NUV band data in magenta; and unfiltered data in black. Along the top horizontal axis, an "X" indicates an X-ray observation at that time and an "S" indicates a spectrum of the nova taken at that time.

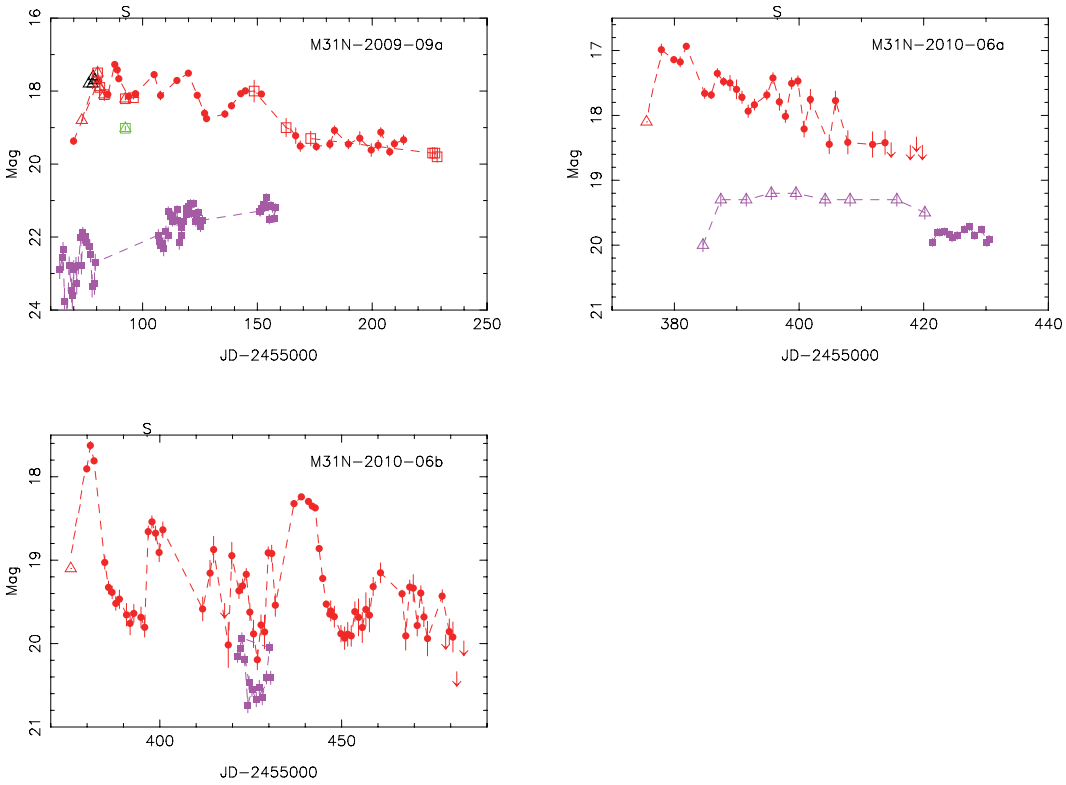

Figure A.6: **Light curves of novae with jittering decay.** Symbol designations are the same as those in Figure A.5.

Super-Eddington Phase

Some novae around maxima exhibit super-Eddington phases. Theorists (e.g., Shaviv, 2001) model this phase with a porous structure in the nova wind that reduces the effective opacity and raises the Eddington luminosity. Kato and Hachisu (2005) produced a light-curve model based on this idea that successfully matched the super-Eddington phase of Nova V1974 Cyg, and demonstrated the importance of the relationship between the optical and UV light curves. They isolated a portion of the UV continuum near 1455 Å that had a duration that was well correlated with the decline rate of the nova in the optical. This continuum UV light curve combined with the model of how the UV light is reprocessed into the optical light curve allows an estimate of the precursor WD mass and distance to be made, based on certain assumptions about the chemical composition of the envelope (Kato and Hachisu, 2007).

One might assume that the clumpy wind responsible for the lower opacity and higher Eddington luminosities of the brightest novae might produce other

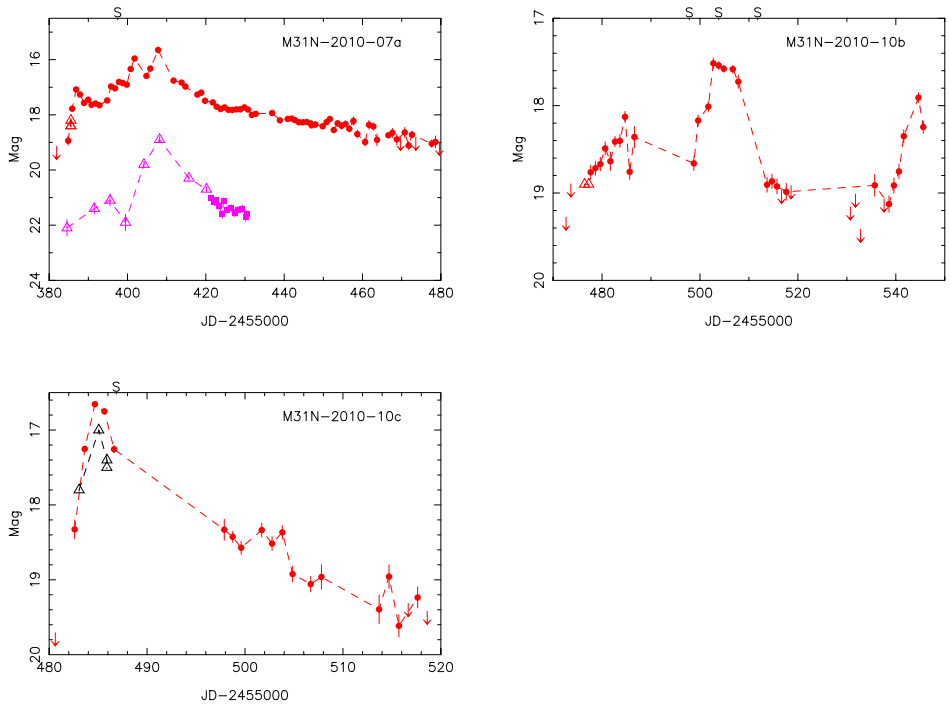

Figure A.7: **Light curves of M31 Novae with well-sampled rise phases.** Symbol designations are the same as those in Figure A.5.

observable signatures. Small-scale structure in the rising light curve could be observed as the clumps are non-uniformly heated and accelerated by the ongoing eruption and as radiation is diffused through them. We have very high-cadence observations of the rising phases of two novae (M31N 2010-09a and M31N 2010-09c), both of which have peak brightnesses ≥ -7.5 and are thus mildly super-Eddington novae (Duerbeck, 1981). Nova 2010-09c exhibits a very smooth and steady rise and a smooth decline, consistent with a uniform nova wind, 2010-09a has considerable structure in its rising light curve with multiple peaks both near and after the maximum light. Our observations of M31N 2009-09a, M31N 2010-07a, M31N 2009-09a and M31N 2009-09c also show several peaks around maxima. The multiple peaks could arise when different winds are blown out from the center successively during an outburst. Each peak is formed when the pseudo-photosphere meets the shock wave at the head of the corresponding wind. These novae tend to be mildly to strongly

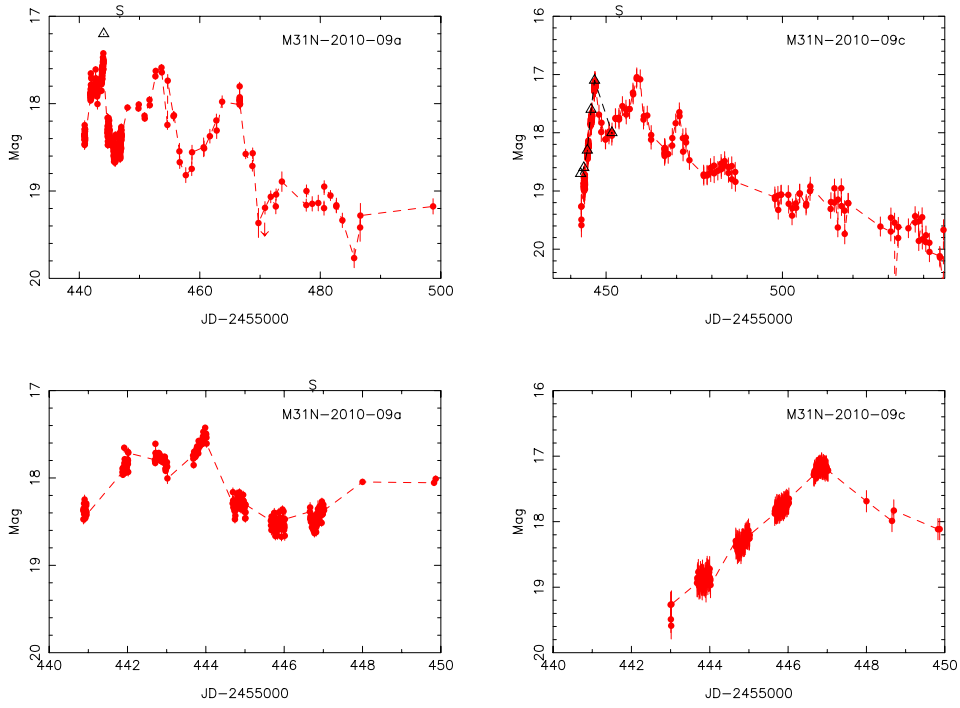

Figure A.8: **Fast-cadence light curves of two M31 novae** M31N 2010-09a and M31N 2010-09c were observed during the PTF 10min-cadence experiments. In the top two panels, we show both full light curves. In the bottom two panels, rising phases are highlighted. Symbol designations are the same as those in Figure A.5.

super-Eddington, however, many of our novae with smooth, well-sampled light curves also fall into the range of mildly to strongly super-Eddington luminosity (e.g., M31N 2009-08b, but especially M31N 2010-09b). We therefore conclude that structures in the nova wind and thus in the light curve can arise regardless of the luminosity of the outburst.

A.4 Novae in globular clusters

M31N 2010-10f was spatially associated with the GC Bol 126 to within one arcsecond. A supersoft X-ray source (SSS) was also reported in the vicinity (Henze *et al.*, 2010c). This event is similar to M31N 2007-06b (Shafter and Quimby, 2007) in Bol 111 which was confirmed spectroscopically during the outburst. A SSS counterpart was also found for this object (Henze *et al.*,

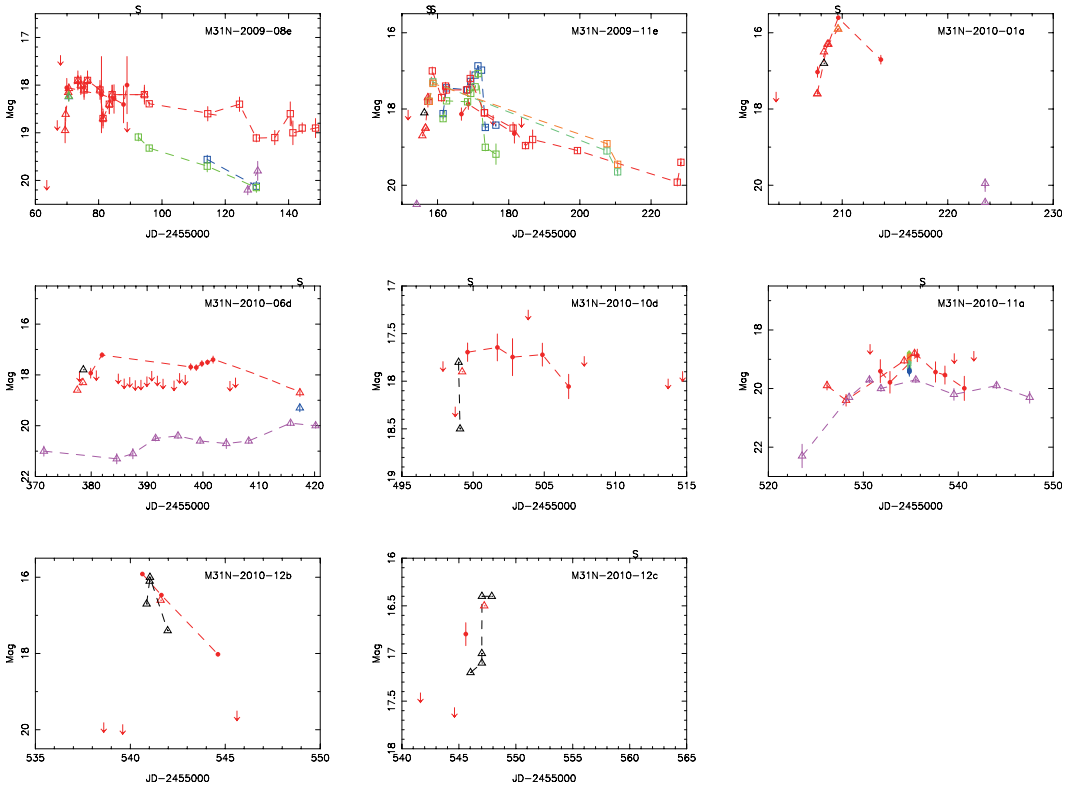

Figure A.9: **Under-sampled nova light curves**. Symbol designations are the same as those in Figure A.5.

2009c). They are the only two events in M31 that are associated with GCs.

Several previous searches for GC novae obtained null results (e.g., Ciardullo *et al.*, 1990b; Tomaney *et al.*, 1992). We examined our PTF image database at the positions of all confirmed M31 GCs from the Revised Bologna Catalog (V.4, Dec 2009, Galleti *et al.*, 2004). Magnitudes of these GCs range from R=13 mag to R=20 mag. We do not find any other GC novae candidates. Given an effective survey time of M31 in PTF for roughly one year, we obtain a GC nova rate of about 1 yr^{-1}.

Is the nova rate enhanced in GCs? The total stellar mass of M31 is $\sim 6 \times 10^{10} M_{\odot}$ (Tamm *et al.*, 2007). Using the highest published nova rate for M31 of 65 yr^{-1} from Darnley *et al.* (2006), we estimate a maximum global specific nova rate of $\sim 1/(10^{9} M_{\odot})$ yr^{-1} in M31. Given a typical GC mass of $10^{6} M_{\odot}$ and about seven hundred confirmed M31 GCs, the nova rate in the M31 GC system is $\sim 1/(10^{9} M_{\odot})$ yr^{-1}. We conclude that the M31 GC specific nova rate is not significantly higher than the M31 galaxy specific nova rate.

Low mass X-ray binaries (LMXBs) — mass transferring binaries with a neutron star receiving matter from a companion — can be viewed, in some ways, as surrogates for CNe and RNe. Since the early days of X-ray astronomy it has been known that at least in our Galaxy that the rate of brightest LMXBs (per unit mass) are nearly two orders of magnitude larger than that for the disk of the Milky Way. This trend appears to be even more acute for M31 (Trudolyubov and Priedhorsky, 2004). In part this may be because M31 possesses a more extensive cluster system than our own Galaxy. Thus, naively, we would expect far more CNe and RNe in the GC system of M31. Over the period of investigation (2009-2010), a total of three RNe were found in the disk/bulge of M31. If we assume the mass fraction of GCs is $\sim 1\%$, we would have expected to see a similar number in the cluster system. Within small number systems, the detection of a RN associated with the cluster would be consistent with this expectation. Separately, given that seven hundred CNe are known, over 2009 and 2010 we should have seen many tens of CNe in the GCs. but only one was found. Indeed, over the last hundred years only one CN that has been associated with a GC of M31 has been spectroscopically confirmed (Shafter and Quimby, 2007). In summary we cannot arrive at a sensible conclusion with the presently available data.

A.5 Recurrent novae

According to the catalog maintained by Pietsch (2010), 26 RNe in M31 are known. During the two seasons we report on, three recurrent events were reported: M31N 2009-11b, M31N 2010-10e and M31N 2010-12a. Figure A.10 presents their light curves. Besides these, we examined the PTF archive by putting an aperture at each position of more than 800 old novae in M31 from the list of Pietsch (2010) in order to find more recurrent events. None were found. Therefore, given an effective observing time of roughly one year in PTF, the recurrent nova rate in M31 is $\sim 3\,\mathrm{novae\,year^{-1}}$. Given a total number of 29 novae in our sample, we derived an outburst ratio of RNe and CNe to be about 0.1, consistent with that of della Valle and Livio (1996).

We examined M31N 2010-12a in some detail, as another outburst of PT And. This object has recorded outbursts in 1957, 1983, 1986, 1988 and 1998. Alksnis and Zharova (2000) collected its previous outbursts and found that all light curves can be fit by one template. The average decline rate of previous outbursts is 0.09 to 0.11 mag per day. The light curve of this most recent out-

Table A.6. Properties of PTF well-sampled nova light curves

Nova	Rising rate (mag/day)	Rising Time (days)	Rising Morphology	t_2 (days)	Decline Morphology	R-Band Peak Magnitude
2009-08b	...	...	...	>35	J	17.76
2009-09a	...	26	J	79	J	17.26
2009-10a	...	...	...	20	S	16.95
2009-10b	0.6	5	S	8	S	14.84
2009-11a	0.8	3	S	22	S	17.23
2009-11b	...	...	...	>37	J	18.25
2009-11d	...	...	...	>17	J	17.72[1]
2009-12a	...	...	...	10	S	16.88
2010-06a	...	...	...	>31	J	16.88
2010-06b	0.4	...	...	8	J	17.62
2010-06c	...	...	...	19	S	17.57
2010-07a	0.7	26	J	15	S	15.65
2010-09a	0.5	14	J	40	J	17.42
2010-09b	1.6	2	S	10	S	16.36
2010-09c	0.4	18	J	57	J	17.04
2010-10a	...	...	...	>9	S	17.03
2010-10b	...	30	...	>41	...	17.44
2010-10c	1.0	3	S	20	S	16.65
2010-10e	...	...	...	>5	S	17.84
2010-12a	1.0	3	S	>13	S	15.56
2010-12b	...	...	...	3	S	15.70

[1]The maximum magnitude is from ATel reports because PTF missed the peak magnitude.

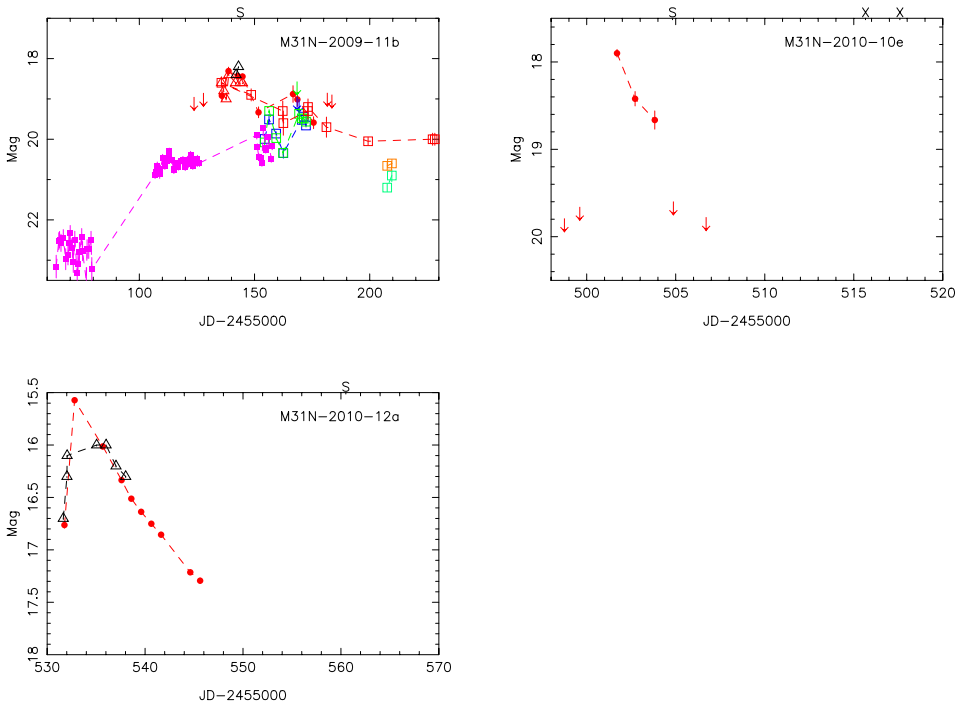

Figure A.10: **Light curves of three RNe detected in PTF.** Symbol designations are the same as those in Figure A.5.

burst (M31N 2010-12a) can also be fit by the template. Figure A.11 shows the similarity between light curves of the recent and 1988 outbursts. The decline rate of the recent outburst is around 0.10 mag per day consistent with previous ones. This invariance property is also observed in Galactic RNe (Schaefer, 2010). Such characteristics of RNe suggests that RN outbursts only depend on system parameters like the WD mass and its composition.

Because of its luminous and frequent outbursts, PT And was assumed to be a dwarf nova inside the Milky Way (Alksnis and Zharova, 2000). However, no direct evidence of this object's nature was available until we obtained a spectrum of its most recent outburst with LRIS in Keck-I telescope. This spectrum (see the top panel of Figure A.3) shows a very blue continuum superposed with prominent Hα and Hβ lines as well as several weak Fe lines. Fitting the red part of the spectrum with a Planck function yields a temperature of $7 \sim 8 \times 10^3\,K$. We fit the Hα and Hβ lines with Gaussian profiles and

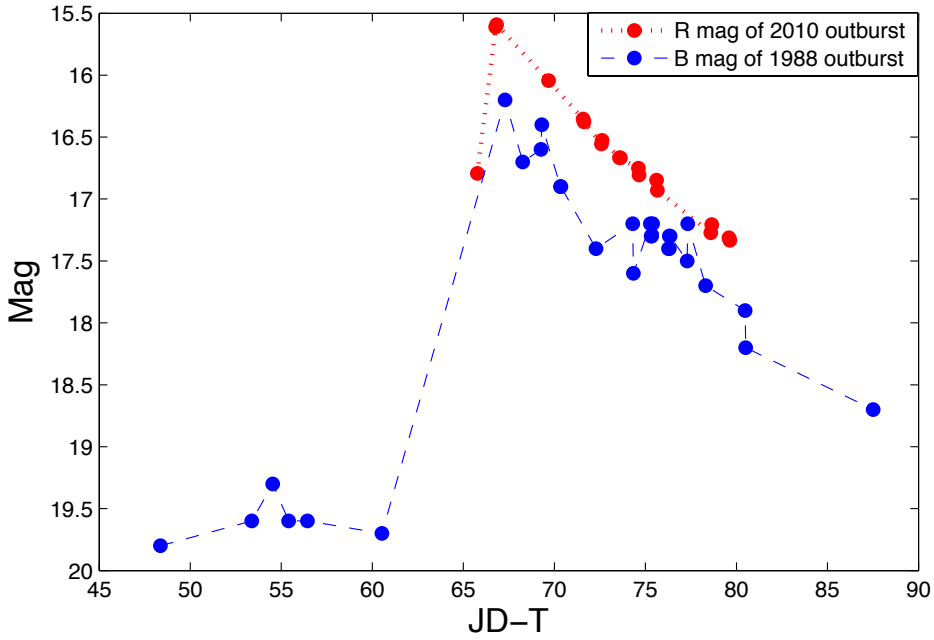

Figure A.11: **Light curve comparison of two outbursts of PT And.** A comparison of the light curves of outbursts of PT And in 1988 and 2010 is shown in the figure, where $T = 2455466$ for the 2010 outburst and $T = 2455100$ for the 1988 one. Though with different filters, the light curve of the recent outburst (M31N 2010-12a) resembles that of the 1988 outburst.

obtained the following observed wavelengths: Hα is centered at $\lambda = 6558\,\text{Å}$ and Hβ at $\lambda = 4857\,\text{Å}$. These correspond to blue-shifts with radial velocities of $\sim -200\,\text{km s}^{-1}$ and $\sim -300\,\text{km s}^{-1}$. The systemic velocity of M31 is $\sim -300\,\text{km s}^{-1}$. We assume that this object is not located in the disk of M31, thus we do not take the rotation velocity of M31 disk into account. We conclude that the blue-shifts are roughly consistent with the motion of M31. Our spectrum evidently supports the conclusion that PT And resides in M31 instead of in the Milky Way. This can also be tested by observing its proper motion. It is of only galactic sources that we may observe proper motion. The FWZI of the Balmer lines suggest an expansion velocity of $\simeq 2000\,\text{km/s}$. In addition, given very weak iron lines, we tentatively classify the nova into the Fe II type.

The association of PT And with M31 leads to a peak absolute magnitude of about -9, which makes it the brightest RN ever known.

The decline rates of RNe vary over a large range in M31. M31N 2009-11b has

$t_2 > 37$ days and M31N 2010-10e has $t_2 > 5$ days. Consider that M31N 2010-12a has a decline rate of ~ 0.1 mag/day, so its t_2 is possibly around twenty days. The t_2 values of Galactic RNe also range from one day to fifty days (Schaefer, 2010).

A.6 UV light curves of novae

Theoretically, the UV emission after the optical maximum light is characterized by a delayed UV peak after the optical peak, because most UV photons are absorbed and re-emitted in the optical in the outer envelope (Kato and Hachisu, 1994; González-Riestra and Krautter, 1998; Cassatella *et al.*, 2002). However in our sample, we see some deviation from this general picture: 2009-10b has a peak in the *GALEX* NUV over two days prior to its peak in the optical (see Figure A.12). The recurrent nova 2009-11b was seen in the *GALEX* NUV about forty days before it was visible in optical bands (although this could be due to cadence and weather, see Figure A.10). The nova 2010-06d was detected in *Swift* (Pietsch *et al.*, 2010f) about six days before optical detection (see Figure A.9). *Swift* also detected 2010-11a several days before optical detection (Pietsch *et al.*, 2010h; Cao *et al.*, 2010, also Figure A.9). For 2010-07a, the optical and UV maxima were nearly simultaneous as measured by PTF and by *Swift* (Henze *et al.*, 2010b, see Figure A.7).

Admittedly the detection in the optical and UV involves many factors including survey sensitivities, temporal coverage and observing weather. In a few cases, however, it is clear that the UV peak coincides with or precedes the optical peak. These cases demonstrate that not all UV photons are re-processed and that the absorption in the UV will vary considerably depending on factors such as physical geometry or chemical abundances in the envelope. These variations will produce a range of optical/UV peak offsets and luminosity ratios. We also point out that multi-band optical data show that three of these UV novae have red colors: 2009-10b has $R - V \sim 1.4$ at decline (Shafter *et al.*, 2011b); 2009-11b has $R - V \sim 0.7$ at decline (Shafter *et al.*, 2011b); 2010-11a has $g - i \sim 0.2$ around its optical peak from our photometric follow-up.

M31N 2009-10b and M31N 2010-11a

The novae 2009-10b and 2010-11a are two peculiar cases in that their UV peaks lead the optical maxima by a few days. Moreover, at the early decay stage of UV emission, the optical colors of both novae look quite red.

Of the two, 2009-10b is brighter, has better light curve coverage in PTF, *GALEX* and other bands, and is thus a better case for further examination. Figure A.12 zooms in on the early multi-band light curve. Table A.8 lists the rise rate, maximum magnitudes, dates and decline rates by t_2 and t_3 in the NUV, B, V and R bands. The NUV data are from *GALEX*. Part of R band data are from PTF. B, V and part of R band data are published in Shafter *et al.* (2011b). We can see clearly that the NUV peak is earlier than the B, V and R peaks by two to three days. The rise rates in B, V and R band are consistent while NUV emission rises swiftly. The decline rates of NUV, B and V are similar while R band emission decays slower.

2010-11a is possibly the faintest nova in our sample with a peak observed magnitude of $R \sim 18.8$ (see Figure A.9). It was first detected by *Swift* (Pietsch *et al.*, 2010h) and then we reported its optical counterpart (Cao *et al.*, 2010). The strong UV emission peaked several days prior to its optical maximum. Near its optical maximum, we carried out a photometric follow-up in i', r', g' and B bands with the Palomar 60-inch telescope and observed that this nova had red optical colors, as shown in Table A.7.

The UV observations and the color information suggest that UV and optical emission originates from different radiative regions because they cannot be simply interpreted as the thermal radiation of a receding spherical photosphere which has a large optical depth in local thermal equilibrium. Because UV emission is only generated deep inside the envelope, the result may suggest that the envelope has holes from which we can see deep inside.

The models of Shaviv (2001) and Kato and Hachisu (2005, 2007) propose a reduced effective opacity of the nova envelope to explain the super-Eddington phase, resulting from a porous structure of the envelope caused by flow instabilities. We may use a similar scenario of asphericity of nova outbursts to qualitatively explain the red UV novae. UV photons are generated deep under the envelope at the surface of the WD. In the envelope, the bottom is heated to very high temperatures by thermonuclear runaway, and thus instabilities like Rayleigh-Bénard convection are likely to occur. This instability causes the mass distribution in the nova envelope to deviate from a spherical distribution. Thus, along some lines of sight to the center of the outburst, the mass is less and so is the opacity. The UV photons then escape from these directions and are observed by us if we are observing along one of these lines of sight.

Table A.7. P60 photometric follow-up of M31N 2010-11a

JD-2455500(days)	Bands	Magnitude	Magnitude Error
34.817	i'	18.80	0.10
34.819	i'	18.84	0.09
34.822	i'	18.89	0.09
34.824	r'	18.91	0.08
34.826	r'	19.04	0.09
34.838	r'	18.96	0.08
34.831	r'	18.89	0.09
34.833	r'	19.04	0.11
34.835	g'	19.20	0.09
34.838	g'	19.32	0.11
34.840	g'	19.12	0.09
34.842	B	19.40	0.13
34.844	B	19.37	0.16
34.847	B	19.43	0.15

The red optical emission still comes from the reprocessing of the envelope in the other directions. The ratio between the UV and optical fluxes reflects the angular size of the cone. If the instability produces an extreme feature with very low mass and very low opacity along the line of sight, we may detect the central UV photons directly. This might be what we are observing in 2009-10b and 2010-11a. Another possible explanation could be very low abundances of chemical species that absorb in the UV, although this may not explain the red optical colors.

The uniqueness of the UV-optical light curves of 2009-10b and 2010-11a suggest either their super-Eddington phases or their chemical abundances (or both) are very different from the majority of novae (Cassatella *et al.*, 2002). They may possibly represent a population that deviates from any empirical relation derived from large nova samples, such as MMRD relation. In fact, 2009-10b is a luminous outlier of the MMRD relation (see Figure A.13). Unfortunately, due to its faintness, we were unable to measure the t_2 decline rate for the nova 2010-11a.

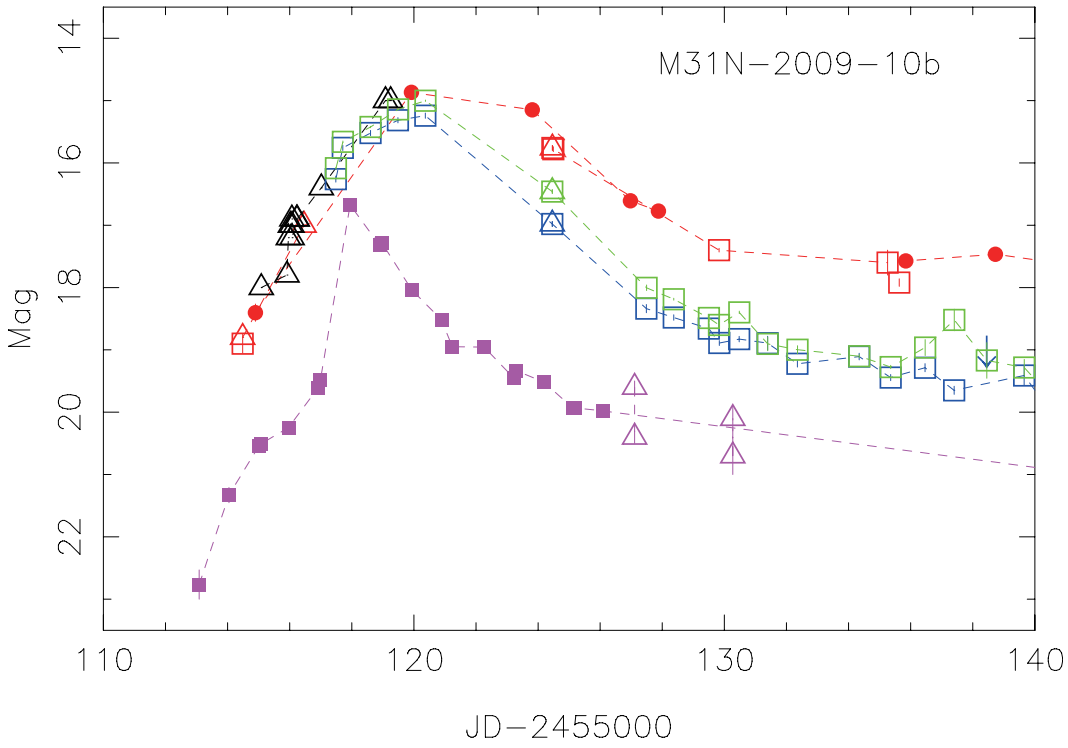

Figure A.12: **Multiband early-phase light curve of M31 N2009-10b.** We can clearly see that the UV peaks prior to the peaks in B, V and R bands by about two days. When the UV decays, the optical part is quite red. Symbol designations are the same as those in Figure A.5.

Table A.8. 2009-10b NUV and optical properties

Bands	NUV[1]	B[2]	V[2]	R[3]
rise rate (mag/day)	1.2	0.4	0.4	0.7
peak magnitude	16.68	15.24	15.00	14.84
peak date (JD-2455110)	7.95	10.37	10.37	9.95
t_2(days)	3	5	5	8
t_3(days)	7	7	7	17

[1] *GALEX* observations;

[2] data from Shafter *et al.* (2011b);

[3] data from PTF and Shafter *et al.* (2011b).

A.7 MMRD revisited

Novae exhibit a MMRD relation (della Valle and Livio, 1995; Kasliwal *et al.*, 2011). We can assess this relation with our nova sample in M31.

One of main issues in evaluating the MMRD relation is estimating the dust extinction. A multitude of methods using color and Balmer decrement have been used in literature to estimate the extinction (Darnley *et al.*, 2006; Kogure, 1961; Kasliwal *et al.*, 2011). The PTF nova observations, however, provide no color information, being done only in the R band. Thus, we apply a mean foreground dust extinction. The foreground extinction of M31, $E(B-V) = 0.062$mag (Schlegel *et al.*, 1998), leads to

$$A_g = 3.793 \times E(B-V) = 0.234. \tag{A.1}$$

For a better comparison with previous results (e.g., Kasliwal *et al.*, 2011), following Shafter et al.(2009), we use the colors of an A5V star ($T = 8200K$) to transform R magnitudes to g magnitudes (Jordi *et al.*, 2006). In Kasliwal *et al.* (2011), the total extinction correction for M31 novae is roughly $A_g = 0.24$ except that two of them (20%) have a correction of $A_g > 1.0$. It is possible that local extinction for most novae in our sample is small.

In Figure A.13, we can see five significant outliers from the MMRD region in our sample. The brightest outlier is M31N 2010-10b (see discussion in Section A.6). The other outlier above the relation is PT And (=M31N 2010-12a). M31N 2009-12a, M31N 2010-06b and M31N 2010-06c lie in the faint and fast-decline rate zone below the MMRD relation. Kasliwal *et al.* (2011) also found several novae in this zone. Kasliwal *et al.* (2011) proposed the possibility that the outliers may be RNe. However, none of the three faint outliers in our sample are known to be recurrent. The remaining novae reside roughly along the MMRD region.

M31N 2010-10b resides near the brightest end of novae, which resembles "superbright" novae that have been observed in M31, the Large Magellanic Cloud and the Galaxy (e.g., della Valle, 1991). The energy budget for these objects is not clear. It could be related to the Common Envelope phase in nova systems (e.g., Iben and Livio, 1993) or a very cold low-mass WD accreting through Roche lobe from a close low-mass companion (Iben and Tutukov, 1992). In either scenario, as the outer part of the system comes from the companion, the UV observation of M31N 2010-10b requires very low metallicity of the common

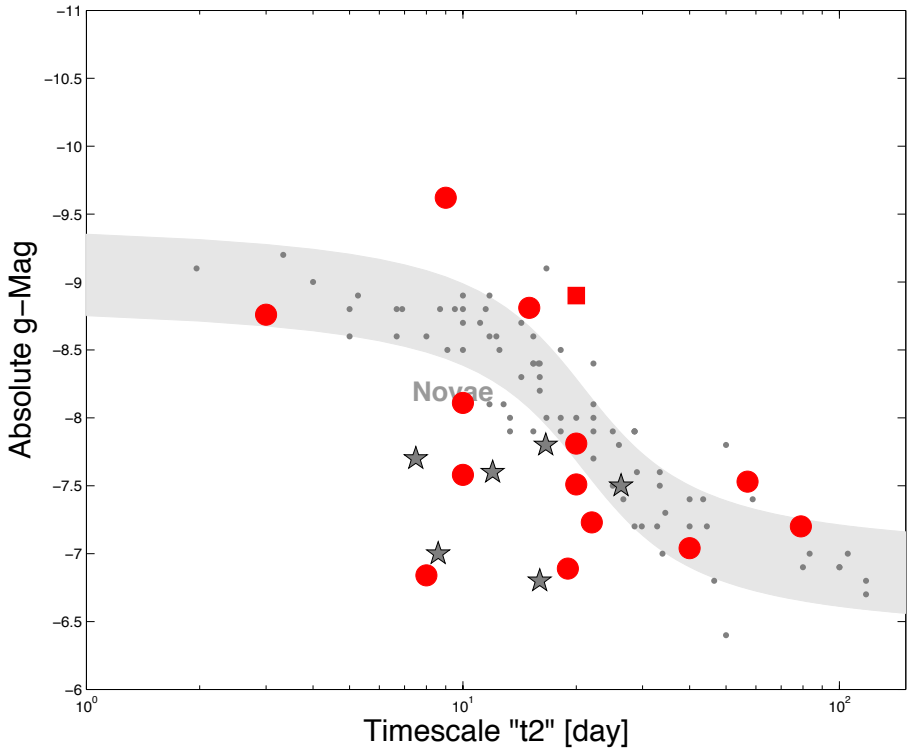

Figure A.13: **The empirical relation for novae between the maximum magnitude and the rate of decline (MMRD).** The gray region denotes the MMRD from della Valle and Livio (1995), while the small dark gray solid dots represents their nova sample. The six gray stars show the sample from Kasliwal *et al.* (2011). Red circles and a red square are the M31 novae from this paper. The red square denotes the bright recurrent nova M31N 2010-12a.

envelope of the binary system or the outer envelope of the nova. Therefore, correlations between spatial distributions of stellar population and "superbright" novae will be helpful.

A.8 Conclusion

In this paper, we construct light curves of twenty-nine classical novae in M31 from PTF data, eight of which also have joint UV-optical light curves from both PTF and *GALEX*. The main findings are as follows:

1. We detected three recurrent novae. They show similar properties to recurrent novae in the Galaxy (Schaefer, 2010). We obtained a spectrum of the recent outburst of PT And (also known as M31N 2010-12a). While

previously identified as a dwarf nova in the Milky Way (Alksnis and Zharova, 2000), we find the blueshifts in our spectrum to be consistent with the event being a recurrent nova in M31. The light curve of 2010-12a resembles those of previous outbursts, suggesting the same physical conditions in the recurrent outbursts. Our search at all other historical nova positions finds no additional outburst candidates. From this we derive a recurrent nova rate of about three per year in M31.

2. The rise behaviors of M31 classical novae are diverse and we classify them morphologically into S (smooth) and J (jittering) classes. We find that the S-class novae rise significantly faster than the J-class novae. We see no dependence between rise-time and maximum magnitude.

3. During the ten minute cadence PTF observations the rising light curve of two novae were recorded with unprecedented detail. These novae showed smooth and consistent rising light curves without large amplitude variability.

4. The declining light curves are also divided morphologically into S and J classes. The relative population of different classes in M31 is roughly consistent with that in the Galaxy.

5. Three quarters of the well-sampled novae obey the empirical MMRD relation. The remaining one quarter (five events) are consistent with the "faint and fast" outliers found by Kasliwal *et al.* (2011).

6. Some novae have UV detections prior to or at the same time as the first optical detection. Moreover, 2009-10b and 2010-11a have UV peaks prior to optical maxima while both are quite red in the UV decay phases. These observations are inconsistent with theoretical predictions of delayed UV emission in the iron curtain stage, possibly suggesting extreme density or abundance variations for these novae.

7. Apart from 2010-10f in Bol 126, we find no other novae in all the cataloged M31 GCs. We derive a GC nova rate in M31 of $\sim$ 1 yr^{-1}. This nova rate is not enhanced relative to the rate in M31 outside of the GC system.

We realize the novae reported here are only a subset of all the classical novae in M31 as the number is smaller than expected (e.g., 65 nova yr^{-1} according

to Darnley *et al.*, 2006). We did not undertake a systematic search for classical novae in PTF images during the 2009 and 2010 seasons. Since the FoV and survey depth of PTF should be sensitive to all classical novae (weather-permitting), we have started a more complete search for classical novae in M31 in the 2011 season. For 2012, we intend to run a real-time search for novae. Our photometric and spectroscopic follow-up will enable us to better understand their properties and to estimate the local extinction correction.

Besides optical bands, future UV surveys are warranted for nova studies. Some novae peak in the UV before the optical. Such novae could provide important insights into the development and structure of the nova wind. It is also important to know if novae like M31N 2009-10b and M31N 2010-11a are rare or common and if they are always outliers in the MMRD diagram.

Ongoing and upcoming synoptic surveys (e.g., Palomar Transient Factory and Next Generation Transient Facilities) will continue to monitor the Andromeda Galaxy. The long time baseline will give us a larger sample of recurrent novae. As noted earlier, recurrent novae could be the progenitors of Ia supernovae. Thus the increased sample and timely follow-up will give us a comprehensive understanding of rate of recurrent novae–an important clue to their endpoint.

Acknowledgments

We thank the referee, Dr. Massimo Della Valle, for very helpful comments and suggestions to improve the manuscript. We thank Marina Orio and Sumin Tang for valuable discussions. We thank the Weizmann Monitoring Team (A. Gal-Yam, I. Arcavi, D. Polishook, A. Sternberg, O. Yaron, D. Xu) for daily monitoring of transient candidates from the PTF discovery stream.

MMK acknowledges support from the Hubble Fellowship and the Carnegie-Princeton Fellowship. SBC wishes to acknowledge generous support from Gary and Cynthia Bengier, the Richard and Rhoda Goldman Fund, National Aeronautics and Space Administration (NASA)/*Swift* grant NNX10AI21G, NASA/*Fermi* grant NNX1OA057G, and National Science Foundation (NSF) grant AST–0908886.

This research was supported in part by Tsinghua Center for Astrophysics (THCA), by the National Natural Science Foundation of China (NSFC) grants 10373009, 10533020 and 11073014 at Tsinghua University, by the Ministry of Science and Technology (MOST) under State Key Development Program for

Basic Research grant 2012CB821800, by the Tsinghua University Initiative Scientific Research Program, by the SRFDP 20050003088, 200800030071 and 20110002110008, and by the Yangtze Endowment from the Ministry of Education at Tsinghua University.

GALEX (Galaxy Evolution Explorer) is a NASA Small Explorer, launched in 2003 April. We gratefully acknowledge NASA's support for construction, operation, and science analysis for the GALEX mission, developed in cooperation with the Centre National d'Etudes Spatiales of France and the Korean Ministry of Science and Technology.

The National Energy Research Scientific Computing Center, which is supported by the Office of Science of the U.S. Department of Energy under Contract No. DE-AC02-05CH11231, provided staff, computational resources and data storage for PTF.

This research has made use of the NASA/IPAC Extragalactic Database (NED) which is operated by the Jet Propulsion Laboratory, California Institute of Technology, under contract with the National Aeronautics and Space Administration.

BIBLIOGRAPHY

1. C. W. Akerlof, R. L. Kehoe, T. A. McKay, *et al.*, *PASP* **115**, 132–140 (2003).
2. G. Aldering, P. Antilogus, S. Bailey, *et al.*, *ApJ* **650**, 510–527 (2006).
3. A. Alksnis, A. V. Zharova, *Information Bulletin on Variable Stars* **4909**, 1–+ (2000).
4. I. Arcavi, S. B. Cenko, A. Gal-Yam, E. Ofek, *The Astronomer's Telegram* **5146**, 1 (2013).
5. H. C. Arp, *AJ* **61**, 15–34 (1956).
6. P. Astier, J. Guy, N. Regnault, *et al.*, *A&A* **447**, 31–48 (2006).
7. R. L. Barone-Nugent, C. Lidman, J. S. Wyithe, *et al.*, *MNRAS* **425**, 1007–1012 (2012).
8. E. A. Barsukova, A. F. Valeev, O. Sholukhova, *et al.*, *The Astronomer's Telegram* **2789**, 1 (2010).
9. E. Barsukova, V. Afanasiev, S. Fabrika, *et al.*, *The Astronomer's Telegram* **2251**, 1 (2009).
10. E. Barsukova, A. Valeev, O. Sholukhova, *et al.*, *The Astronomer's Telegram* **2205**, 1 (2009).
11. E. C. Bellm, S. R. Kulkarni, ZTF Collaboration, presented at the American Astronomical Society Meeting Abstracts, vol. 225, p. 328.04.
12. S. Ben-Ami, A. Gal-Yam, A. V. Filippenko, *et al.*, *ApJ* **760**, L33 (2012).
13. M. C. Bersten, O. G. Benvenuto, G. Folatelli, *et al.*, *AJ* **148**, 68 (2014).
14. M. C. Bersten, O. G. Benvenuto, K. Nomoto, *et al.*, *ApJ* **757**, 31 (2012).
15. M. Betoule, R. Kessler, J. Guy, *et al.*, *A&A* **568**, A22 (2014).
16. F. B. Bianco, D. A. Howell, M. Sullivan, *et al.*, *ApJ* **741**, 20 (2011).
17. S. Blinnikov, P. Lundqvist, O. Bartunov, K. Nomoto, K. Iwamoto, *ApJ* **532**, 1132–1149 (2000).
18. S. Blondin, T. Matheson, R. P. Kirshner, *et al.*, *AJ* **143**, 126 (2012).
19. S. Blondin, J. L. Tonry, *ApJ* **666**, 1024–1047 (2007).
20. J. S. Bloom, D. Kasen, K. J. Shen, *et al.*, *ApJ* **744**, L17 (2012).
21. M. F. Bode, A. Evans, *Classical Novae*.
22. A. S. Bolton, D. J. Schlegel, É. Aubourg, *et al.*, *AJ* **144**, 144 (2012).

23. A. A. Breeveld, W. Landsman, S. T. Holland, *et al.*, presented at the American Institute of Physics Conference Series, ed. by J. E. McEnery, J. L. Racusin, N. Gehrels, vol. 1358, pp. 373–376, DOI: 10.1063/1.3621807, arXiv: 1102.4717 [astro-ph.IM].

24. H. Brink, J. W. Richards, D. Poznanski, *et al.*, *MNRAS* **435**, 1047–1060 (2013).

25. P. J. Brown, *ApJ* **796**, L18 (2014).

26. P. J. Brown, K. S. Dawson, M. de Pasquale, *et al.*, *ApJ* **753**, 22 (2012).

27. P. J. Brown, K. S. Dawson, D. W. Harris, *et al.*, *ApJ* **749**, 18 (2012).

28. P. J. Brown, P. Kuin, R. Scalzo, *et al.*, *ApJ* **787**, 29 (2014).

29. T. M. Brown, N. Baliber, F. B. Bianco, *et al.*, *PASP* **125**, 1031–1055 (2013).

30. C. R. Burns, M. Stritzinger, M. M. Phillips, *et al.*, *AJ* **141**, 19 (2011).

31. C. R. Burns, M. Stritzinger, M. M. Phillips, *et al.*, *ApJ* **789**, 32 (2014).

32. V. Burwitz, W. Pietsch, M. Henze, *et al.*, *Central Bureau Electronic Telegrams* **2124**, 1 (2010).

33. V. Burwitz, W. Pietsch, M. Henze, *et al.*, *Central Bureau Electronic Telegrams* **2343**, 1 (2010).

34. V. Burwitz, W. Pietsch, M. Henze, *et al.*, *The Astronomer's Telegram* **2697**, 1 (2010).

35. V. Burwitz, J. Rodriguez, S. Holmes, U. Kolb, R. Lucas, *Central Bureau Electronic Telegrams* **2003**, 2 (2009).

36. P. Cagas, *Central Bureau Electronic Telegrams* **2061**, 3 (2009).

37. Y. Cao, E. Gorbikov, I. Arcavi, *et al.*, *The Astronomer's Telegram* **5137**, 1 (2013).

38. Y. Cao, M. M. Kasliwal, I. Arcavi, *et al.*, *ApJ* **775**, L7 (2013),

39. Y. Cao, M. M. Kasliwal, S. R. Kulkarni, *The Astronomer's Telegram* **3066**, 1 (2010).

40. Y. Cao, S. R. Kulkarni, D. A. Howell, *et al.*, *Nature* **521**, 328–331 (2015),

41. C. Cappa, W. M. Goss, K. A. van der Hucht, *AJ* **127**, 2885–2897 (2004).

42. R. Cartier, M. Hamuy, G. Pignata, *et al.*, *ApJ* **789**, 89 (2014).

43. A. Cassatella, A. Altamore, R. González-Riestra, *A&A* **384**, 1023–1029 (2002).

44. A. Cassatella, H. J. L. Lamers, C. Rossi, A. Altamore, R. González-Riestra, *A&A* **420**, 571–588 (2004).

45. S. B. Cenko, D. B. Fox, D.-S. Moon, *et al.*, *PASP* **118**, 1396–1406 (2006).

46. S. B. Cenko, A. L. Urban, D. A. Perley, *et al.*, *ApJ* **803**, L24 (2015).

47. L. Chemin, C. Carignan, T. Foster, *ApJ* **705**, 1395–1415 (2009).

48. R. A. Chevalier, *ApJ* **499**, 810–819 (1998).

49. R. A. Chevalier, C. Fransson, *ApJ* **651**, 381–391 (2006).

50. L. Chomiuk, *PASA* **30**, e046 (2013).

51. R. Ciardullo, H. C. Ford, J. D. Neill, G. H. Jacoby, A. W. Shafter, *ApJ* **318**, 520–530 (1987).

52. R. Ciardullo, A. W. Shafter, H. C. Ford, *et al.*, *ApJ* **356**, 472–482 (1990).

53. R. Ciardullo, P. Tamblyn, A. C. Phillips, *PASP* **102**, 1113–1119 (1990).

54. E. Corbelli, S. Lorenzoni, R. Walterbos, R. Braun, D. Thilker, *A&A* **511**, A89+ (2010).

55. J. Corral-Santana, J. Casares, P. Hornochova, M. Wolf, *Central Bureau Electronic Telegrams* **2487**, 1 (2010).

56. A. Corsi, E. O. Ofek, A. Gal-Yam, *et al.*, *ApJ* **747**, L5 (2012).

57. R. M. Crockett, S. J. Smartt, J. J. Eldridge, *et al.*, *MNRAS* **381**, 835–850 (2007).

58. P. A. Crowther, *ARA&A* **45**, 177–219 (2007).

59. M. J. Darnley, M. F. Bode, E. Kerins, *et al.*, *MNRAS* **353**, 571–588 (2004).

60. M. J. Darnley, M. F. Bode, E. Kerins, *et al.*, *MNRAS* **369**, 257–271 (2006).

61. M. della Valle, *A&A* **252**, L9–L12 (1991).

62. M. della Valle, M. Livio, *ApJ* **452**, 704 (1995).

63. M. della Valle, M. Livio, *ApJ* **473**, 240 (1996).

64. G. Denicoló, R. Terlevich, E. Terlevich, *MNRAS* **330**, 69–74 (2002).

65. L. Dessart, D. J. Hillier, C. Li, S. Woosley, *MNRAS* **424**, 2139–2159 (2012).

66. F. Di Mille, S. Ciroi, H. Navasardyan, *et al.*, *The Astronomer's Telegram* **2248**, 1 (2009).

67. R. Di Stefano, R. Voss, J. S. Claeys, *ApJ* **738**, L1 (2011).

68. A. E. Dolphin, *PASP* **112**, 1383–1396 (2000).

69. A. J. Drake, S. G. Djorgovski, A. Mahabal, *et al.*, *ApJ* **696**, 870–884 (2009).

70. H. W. Duerbeck, *PASP* **93**, 165–175 (1981).

71. J. J. Eldridge, M. Fraser, S. J. Smartt, J. R. Maund, R. M. Crockett, *MNRAS* **436**, 774–795 (2013).

72. J. J. Eldridge, J. R. Maund, *ArXiv e-prints*, arXiv: 1604.05050 [astro-ph.SR] (2016).

73. J. J. Eldridge, C. A. Tout, *MNRAS* **353**, 87–97 (2004).

74. L. Ensman, A. Burrows, *ApJ* **393**, 742–755 (1992).

75. S. M. Faber, A. C. Phillips, R. I. Kibrick, *et al.*, presented at the Instrument Design and Performance for Optical/Infrared Ground-based Telescopes, ed. by M. Iye, A. F. Moorwood, vol. 4841, pp. 1657–1669, DOI: 10.1117/12.460346.

76. S. Fabrika, E. A. Barsukova, A. F. Valeev, *et al.*, *The Astronomer's Telegram* **3068**, 1 (2010).

77. S. Fabrika, O. Sholukhova, A. Valeev, K. Hornoch, W. Pietsch, *The Astronomer's Telegram* **2239**, 1 (2009).

78. S. Fabrika, O. Sholukhova, A. Valeev, *et al.*, *Central Bureau Electronic Telegrams* **1971**, 3 (2009).

79. S. W. Falk, *ApJ* **225**, L133–L136 (1978).

80. A. V. Filippenko, *ARA&A* **35**, 309–355 (1997).

81. A. V. Filippenko, A. J. Barth, T. Matheson, *et al.*, *ApJ* **450**, L11 (1995).

82. A. V. Filippenko, M. W. Richmond, D. Branch, *et al.*, *AJ* **104**, 1543–1556 (1992).

83. A. V. Filippenko, M. W. Richmond, T. Matheson, *et al.*, *ApJ* **384**, L15–L18 (1992).

84. R. E. Firth, M. Sullivan, A. Gal-Yam, *et al.*, *MNRAS* **446**, 3895–3910 (2015).

85. E. L. Fitzpatrick, *PASP* **111**, 63–75 (1999).

86. R. J. Foley, P. J. Brown, A. Rest, *et al.*, *ApJ* **708**, L61–L65 (2010).

87. R. J. Foley, P. J. Challis, R. Chornock, *et al.*, *ApJ* **767**, 57 (2013).

88. R. J. Foley, P. J. Challis, A. V. Filippenko, *et al.*, *ApJ* **744**, 38 (2012).

89. R. J. Foley, C. McCully, S. W. Jha, *et al.*, *ApJ* **792**, 29 (2014).

90. R. J. Foley, N. E. Sanders, R. P. Kirshner, *ApJ* **742**, 89 (2011).

91. C. Foster, A. M. Hopkins, M. Gunawardhana, *et al.*, *A&A* **547**, A79 (2012).

92. C. Fremling, J. Sollerman, F. Taddia, *et al.*, *A&A* **565**, A114 (2014).

93. J. A. Frieman, B. Bassett, A. Becker, *et al.*, *AJ* **135**, 338–347 (2008).

94. S. Galleti, L. Federici, M. Bellazzini, F. Fusi Pecci, S. Macrina, *A&A* **416**, 917–924 (2004).

95. A. Gal-Yam, I. Arcavi, E. O. Ofek, *et al.*, *Nature* **509**, 471–474 (2014).

96. V. N. Gamezo, A. M. Khokhlov, E. S. Oran, A. Y. Chtchelkanova, R. O. Rosenberg, *Science* **299**, 77–81 (2003).

97. M. Ganeshalingam, W. Li, A. V. Filippenko, *et al.*, *ApJ* **751**, 142 (2012).

98. G. Garavini, G. Folatelli, A. Goobar, *et al.*, *AJ* **128**, 387–404 (2004).

99. N. Gehrels, G. Chincarini, P. Giommi, *et al.*, *ApJ* **611**, 1005–1020 (2004).

100. A. Gil de Paz, S. Boissier, B. F. Madore, *et al.*, *ApJS* **173**, 185–255 (2007).

101. J. I. González Hernández, P. Ruiz-Lapuente, H. M. Tabernero, *et al.*, *Nature* **489**, 533–536 (2012).

102. R. González-Riestra, J. Krautter, presented at the Ultraviolet Astrophysics Beyond the IUE Final Archive, ed. by W. Wamsteker, R. Gonzalez Riestra, B. Harris, vol. 413, p. 367.

103. A. Goobar, J. Johansson, R. Amanullah, *et al.*, *ApJ* **784**, L12 (2014).

104. A. Goobar, M. Kromer, R. Siverd, *et al.*, *ApJ* **799**, 106 (2015).

105. E. Gorbikov, A. Gal-Yam, E. O. Ofek, *et al.*, *MNRAS* **443**, 671–677 (2014).

106. D. W. Green, *Central Bureau Electronic Telegrams* **2061**, 1 (2009).

107. D. W. Green, *Central Bureau Electronic Telegrams* **2582**, 1 (2010).

108. D. W. Green, *Central Bureau Electronic Telegrams* **2582**, 4 (2010).

109. D. W. Green, *Central Bureau Electronic Telegrams* **2582**, 5 (2010).

110. D. W. Green, *Central Bureau Electronic Telegrams* **2597**, 2 (2010).

111. D. W. Green, *Central Bureau Electronic Telegrams* **2187**, 1 (2010).

112. D. W. Green, *Central Bureau Electronic Telegrams* **2610**, 1 (2010).

113. J. H. Groh, C. Georgy, S. Ekström, *A&A* **558**, L1 (2013).

114. J. Guy, P. Astier, S. Baumont, *et al.*, *A&A* **466**, 11–21 (2007).

115. S. Hachinger, P. A. Mazzali, M. Sullivan, *et al.*, *MNRAS* **429**, 2228–2248 (2013).

116. S. Hachinger, P. A. Mazzali, S. Taubenberger, *et al.*, *MNRAS* **422**, 70–88 (2012).

117. I. Hachisu, M. Kato, K. Nomoto, *ApJ* **756**, L4 (2012).

118. B. T. Hayden, P. M. Garnavich, D. Kasen, *et al.*, *ApJ* **722**, 1691–1698 (2010).

119. M. Henze, V. Burwitz, W. Pietsch, *et al.*, *Central Bureau Electronic Telegrams* **2358**, 2 (2010).

120. M. Henze, V. Burwitz, W. Pietsch, *et al.*, *The Astronomer's Telegram* **2727**, 1 (2010).

121. M. Henze, F. Kaduk, W. Pietsch, *et al.*, *The Astronomer's Telegram* **2189**, 1 (2009).

122. M. Henze, W. Pietsch, V. Burwitz, *et al.*, *The Astronomer's Telegram* **3019**, 1 (2010).

123. M. Henze, W. Pietsch, F. Haberl, *The Astronomer's Telegram* **2787**, 1 (2010).

124. M. Henze, W. Pietsch, F. Haberl, M. Orio, *The Astronomer's Telegram* **2274**, 1 (2009).

125. M. Henze, W. Pietsch, F. Haberl, *et al.*, *A&A* **500**, 769–779 (2009).

126. M. Henze, W. Pietsch, P. Podigachoski, *et al.*, *The Astronomer's Telegram* **2286**, 1 (2009).

127. M. Henze, W. Pietsch, P. Podigachoski, *et al.*, *Central Bureau Electronic Telegrams* **2015**, 2 (2009).

128. M. Hicken, P. Challis, R. P. Kirshner, *et al.*, *ApJS* **200**, 12 (2012).

129. M. Hicken, P. M. Garnavich, J. L. Prieto, *et al.*, *ApJ* **669**, L17–L20 (2007).

130. G. J. Hill, H. E. Nicklas, P. J. MacQueen, *et al.*, presented at the Optical Astronomical Instrumentation, ed. by S. D'Odorico, vol. 3355, pp. 375–386.

131. W. Hillebrandt, J. C. Niemeyer, *ARA&A* **38**, 191–230 (2000).

132. P. Hoeflich, A. Khokhlov, *ApJ* **457**, 500 (1996).

133. T. W.-S. Holoien, B. J. Shappee, K. Z. Stanek, *et al.*, *The Astronomer's Telegram* **6168** (2014).

134. I. M. Hook, I. Jørgensen, J. R. Allington-Smith, *et al.*, *PASP* **116**, 425–440 (2004).

135. K. Hornoch, *Central Bureau Electronic Telegrams* **2343**, 3 (2010).

136. K. Hornoch, J. M. Corral-Santana, J. Casares, *Central Bureau Electronic Telegrams* **2391**, 1 (2010).

137. K. Hornoch, M. Corral-Santana, J. Casares, *et al.*, *Central Bureau Electronic Telegrams* **2411**, 1 (2010).

138. K. Hornoch, P. Hornochova, J. Gallagher, P. Garnavich, *Central Bureau Electronic Telegrams* **2342**, 1 (2010).

139. K. Hornoch, P. Hornochova, P. Kubanek, *et al.*, *Central Bureau Electronic Telegrams* **2341**, 1 (2010).

140. K. Hornoch, P. Hornochova, M. Wolf, *Central Bureau Electronic Telegrams* **2516**, 4 (2010).

141. K. Hornoch, P. Hornochova, P. Zasche, M. Wolf, *Central Bureau Electronic Telegrams* **2391**, 3 (2010).

142. K. Hornoch, P. Kubanek, J. Gorosabel, *et al.*, *Central Bureau Electronic Telegrams* **2187**, 3 (2010).

143. K. Hornoch, P. Kusnirak, *Central Bureau Electronic Telegrams* **1971**, 2 (2009).

144. K. Hornoch, P. Kusnirak, O. Pejcha, *Central Bureau Electronic Telegrams* **1971**, 4 (2009).

145. K. Hornoch, O. Pejcha, *Central Bureau Electronic Telegrams* **2061**, 5 (2009).

146. K. Hornoch, O. Pejcha, P. Kusnirak, *Central Bureau Electronic Telegrams* **2058**, 3 (2009).

147. K. Hornoch, O. Pejcha, M. Wolf, *Central Bureau Electronic Telegrams* **2062**, 1 (2009).

148. K. Hornoch, J. L. Prieto, O. Pejcha, *et al.*, *Central Bureau Electronic Telegrams* **2391**, 2 (2010).

149. K. Hornoch, J. Prieto, R. Khan, O. Pejcha, *Central Bureau Electronic Telegrams* **2136**, 1 (2010).

150. K. Hornoch, J. Prieto, R. Khan, *et al.*, *Central Bureau Electronic Telegrams* **2127**, 1 (2010).

151. K. Hornoch, M. Wolf, P. Garnavich, *et al.*, *Central Bureau Electronic Telegrams* **2347**, 2 (2010).

152. K. Hornoch, P. Zasche, *Central Bureau Electronic Telegrams* **2358**, 1 (2010).

153. K. Hornoch, P. Zasche, K. Hornoch, *et al.*, *Central Bureau Electronic Telegrams* **2341**, 2 (2010).

154. P. Hornochova, K. Hornoch, M. Wolf, P. Kusnirak, O. Pejcha, *Central Bureau Electronic Telegrams* **2573**, 1 (2010).

155. P. Hornochova, M. Wolf, *Central Bureau Electronic Telegrams* **2571**, 1 (2010).

156. D. A. Howell, M. Sullivan, P. E. Nugent, *et al.*, *Nature* **443**, 308–311 (2006).

157. D. A. Howell, M. Sullivan, K. Perrett, *et al.*, *ApJ* **634**, 1190–1201 (2005).

158. E. Y. Hsiao, C. R. Burns, C. Contreras, *et al.*, *A&A* **578**, A9 (2015).

159. E. Y. Hsiao, A. Conley, D. A. Howell, *et al.*, *ApJ* **663**, 1187–1200 (2007).

160. E. Y. Hsiao, G. H. Marion, M. M. Phillips, *et al.*, *ApJ* **766**, 72 (2013).

161. E. P. Hubble, *ApJ* **69**, 103–158 (1929).

162. J. P. Huchra, L. M. Macri, K. L. Masters, *et al.*, *ApJS* **199**, 26 (2012).

163. I. Iben Jr., M. Livio, *PASP* **105**, 1373–1406 (1993).

164. I. Iben Jr., A. V. Tutukov, *ApJ* **389**, 369–374 (1992).

165. D. J. Jeffery, *ArXiv Astrophysics e-prints*, eprint: `astro-ph/9907015` (1999).

166. D. J. Jeffery, D. Branch, E. Baron, *ArXiv Astrophysics e-prints*, eprint: `astro-ph/0609804` (2006).

167. S. Jha, D. Branch, R. Chornock, *et al.*, *AJ* **132**, 189–196 (2006).

168. K. Jordi, E. K. Grebel, K. Ammon, *A&A* **460**, 339–347 (2006).

169. S. Justham, *ApJ* **730**, L34 (2011).

170. P. M. Kalberla, W. B. Burton, D. Hartmann, *et al.*, *A&A* **440**, 775–782 (2005).

171. A. Kamble, A. Soderberg, *The Astronomer's Telegram* **5154**, 1 (2013).

172. D. Kasen, *ApJ* **649**, 939–953 (2006).

173. D. Kasen, *ApJ* **708**, 1025–1031 (2010).

174. D. Kasen, P. Nugent, R. C. Thomas, L. Wang, *ApJ* **610**, 876–887 (2004).

175. M. M. Kasliwal, *Central Bureau Electronic Telegrams* **2015**, 3 (2009).

176. M. M. Kasliwal, PhD thesis, California Institute of Technology, 2011.

177. M. M. Kasliwal, S. B. Cenko, S. R. Kulkarni, *et al.*, *ApJ* **735**, 94 (2011).

178. M. M. Kasliwal, S. B. Cenko, L. P. Singer, *et al.*, *ArXiv e-prints*, arXiv: `1602.08764 [astro-ph.IM]` (2016).

179. M. M. Kasliwal, N. Degenaar, D. Polishook, *The Astronomer's Telegram* **5151**, 1 (2013).

180. M. M. Kasliwal, R. Quimby, M. Shara, *et al.*, *The Astronomer's Telegram* **2290**, 1 (2009).

181. M. Kato, I. Hachisu, *ApJ* **437**, 802–826 (1994).

182. M. Kato, I. Hachisu, *ApJ* **633**, L117–L120 (2005).

183. M. Kato, I. Hachisu, *ApJ* **657**, 1004–1012 (2007).

184. P. L. Kelly, O. D. Fox, A. V. Filippenko, *et al.*, *ApJ* **790**, 3 (2014).

185. R. C. Kennicutt Jr., *ARA&A* **36**, 189–232 (1998).

186. D. Khazov, O. Yaron, A. Gal-Yam, *et al.*, *ApJ* **818**, 3 (2016).

187. R. P. Kirshner, D. J. Jeffery, B. Leibundgut, *et al.*, *ApJ* **415**, 589 (1993).

188. T. Kogure, *PASJ* **13**, 335–+ (1961).

189. M. Koishikawa, *Central Bureau Electronic Telegrams* **2582**, 2 (2010).

190. M. Koishikawa, W. Pietsch, T. Yusa, *Central Bureau Electronic Telegrams* **2582**, 7 (2010).

191. A. K. Kong, K. L. Li, E. Ofek, *The Astronomer's Telegram* **5210**, 1 (2013).

192. M. Kriek, P. G. van Dokkum, I. Labbé, *et al.*, *ApJ* **700**, 221–231 (2009).

193. K. Krisciunas, N. C. Hastings, K. Loomis, *et al.*, *ApJ* **539**, 658–674 (2000).

194. M. Kromer, S. A. Sim, M. Fink, *et al.*, *ApJ* **719**, 1067–1082 (2010).

195. R. G. Kron, *ApJS* **43**, 305–325 (1980).

196. V. Krushinski, I. Zalozhnich, T. Kopytova, A. Popov, *The Astronomer's Telegram* **2844**, 1 (2010).

197. H. Kuncarayakti, K. Maeda, M. C. Bersten, *et al.*, *A&A* **579**, A95 (2015).

198. D. Kushnir, B. Katz, S. Dong, E. Livne, R. Fernández, *ApJ* **778**, L37 (2013).

199. P. Kusnirak, K. Hornoch, P. Zasche, M. Wolf, *Central Bureau Electronic Telegrams* **2061**, 4 (2009).

200. N. Langer, *ARA&A* **50**, 107–164 (2012).

201. B. Lantz, G. Aldering, P. Antilogus, *et al.*, presented at the Optical Design and Engineering, ed. by L. Mazuray, P. J. Rogers, R. Wartmann, vol. 5249, pp. 146–155, DOI: 10.1117/12.512493.

202. J. Larkin, M. Barczys, A. Krabbe, *et al.*, presented at the Society of Photo-Optical Instrumentation Engineers (SPIE) Conference Series, vol. 6269, 62691A, DOI: 10.1117/12.672061.

203. N. M. Law, S. R. Kulkarni, R. G. Dekany, *et al.*, *PASP* **121**, 1395–1408 (2009).

204. W. D. Li, A. V. Filippenko, R. R. Treffers, *et al.*, presented at the American Institute of Physics Conference Series, ed. by S. S. Holt, W. W. Zhang, vol. 522, pp. 103–106, DOI: 10.1063/1.1291702, eprint: astro-ph/9912336.

205. W. Li, J. S. Bloom, P. Podsiadlowski, *et al.*, *Nature* **480**, 348–350 (2011).

206. W. Li, R. Chornock, J. Leaman, *et al.*, *MNRAS* **412**, 1473–1507 (2011).

207. W. Li, A. V. Filippenko, R. Chornock, *et al.*, *PASP* **115**, 453–473 (2003).

208. W. Li, J. Leaman, R. Chornock, *et al.*, *MNRAS* **412**, 1441–1472 (2011).

209. P. Lundqvist, A. Nyholm, F. Taddia, *et al.*, *A&A* **577**, A39 (2015).

210. K. Maeda, K. Iwamoto, *MNRAS* **394**, 239–249 (2009).

211. D. Maoz, F. Mannucci, G. Nelemans, *ARA&A* **52**, 107–170 (2014).

212. R. Margutti, J. Parrent, A. Kamble, *et al.*, *ApJ* **790**, 52 (2014).

213. G. H. Marion, P. J. Brown, J. Vinkó, *et al.*, *ApJ* **820**, 92 (2016).

214. G. H. Marion, J. Vinko, R. P. Kirshner, *et al.*, *ApJ* **781**, 69 (2014).

215. M. Martignoni, K. Itagaki, H. Yamaoka, *Central Bureau Electronic Telegrams* **1980**, 2 (2009).

216. D. C. Martin, J. Fanson, D. Schiminovich, *et al.*, *ApJ* **619**, L1 (2005).

217. P. Massey, K. A. Olsen, P. W. Hodge, *et al.*, *AJ* **131**, 2478–2496 (2006).

218. T. Matheson, R. P. Kirshner, P. Challis, *et al.*, *AJ* **135**, 1598–1615 (2008).

219. P. A. Mazzali, I. J. Danziger, M. Turatto, *A&A* **297**, 509 (1995).

220. P. A. Mazzali, M. Sullivan, S. Hachinger, *et al.*, *MNRAS* **439**, 1959–1979 (2014).

221. C. McCully, S. W. Jha, R. J. Foley, *et al.*, *Nature* **512**, 54–56 (2014).

222. A. Medvedev, E. Barsukova, A. Valeev, *et al.*, *The Astronomer's Telegram* **2213**, 1 (2009).

223. H. R. Merrett, M. R. Merrifield, N. G. Douglas, *et al.*, *MNRAS* **369**, 120–142 (2006).

224. D. Milisavljevic, R. Fesen, T. Pickering, *et al.*, *The Astronomer's Telegram* **5142**, 1 (2013).

225. P. A. Milne, P. J. Brown, P. W. Roming, F. Bufano, N. Gehrels, *ApJ* **779**, 23 (2013).

226. P. A. Milne, P. J. Brown, P. W. Roming, *et al.*, *ApJ* **721**, 1627–1655 (2010).

227. R. Moll, C. Raskin, D. Kasen, S. E. Woosley, *ApJ* **785**, 105 (2014).

228. V. Morozova, A. L. Piro, M. Renzo, *et al.*, *ApJ* **814**, 63 (2015).

229. P. Morrissey, T. Conrow, T. A. Barlow, *et al.*, *ApJS* **173**, 682–697 (2007).

230. D. K. Nadyozhin, *ApJS* **92**, 527–531 (1994).

231. S. Nakano, K. Itagaki, *Central Bureau Electronic Telegrams* **1973**, 1 (2009).

232. S. Nakano, K. Itagaki, J. Nicolas, *Central Bureau Electronic Telegrams* **1971**, 5 (2009).

233. S. Nakano, T. Yusa, *Central Bureau Electronic Telegrams* **1967**, 1 (2009).

234. S. Nakano, T. Yusa, *Central Bureau Electronic Telegrams* **2500**, 1 (2010).

235. E. Nakar, A. L. Piro, *ApJ* **788**, 193 (2014).

236. E. Nakar, R. Sari, *ApJ* **725**, 904–921 (2010).

237. K. Nishiyama, F. Kabashima, *Central Bureau Electronic Telegrams* **2003**, 1 (2009).

238. K. Nishiyama, F. Kabashima, *Central Bureau Electronic Telegrams* **2058**, 1 (2009).

239. K. Nishiyama, F. Kabashima, *Central Bureau Electronic Telegrams* **2516**, 2 (2010).

240. K. Nishiyama, F. Kabashima, K. Hornoch, *et al.*, *Central Bureau Electronic Telegrams* **2015**, 1 (2009).

241. K. Nishiyama, F. Kabashima, T. Yusa, *Central Bureau Electronic Telegrams* **2100**, 1 (2009).

242. S. Nobili, A. Goobar, *A&A* **487**, 19–31 (2008).

243. K. Nomoto, I. Iben Jr., *ApJ* **297**, 531–537 (1985).

244. P. E. Nugent, M. Sullivan, S. B. Cenko, *et al.*, *Nature* **480**, 344–347 (2011).

245. P. Nugent, E. Baron, D. Branch, A. Fisher, P. H. Hauschildt, *ApJ* **485**, 812–819 (1997).

246. P. Nugent, A. Kim, S. Perlmutter, *PASP* **114**, 803–819 (2002).

247. E. O. Ofek, R. Laher, N. Law, *et al.*, *PASP* **124**, 62–73 (2012).

248. E. O. Ofek, R. Laher, J. Surace, *et al.*, *PASP* **124**, 854–860 (2012).

249. J. B. Oke, J. G. Cohen, M. Carr, *et al.*, *PASP* **107**, 375 (1995).

250. J. B. Oke, J. E. Gunn, *PASP* **94**, 586 (1982).

251. E. Ovcharov, A. Valcheva, T. Georgiev, *et al.*, *The Astronomer's Telegram* **2176**, 1 (2009).

252. A. G. Pacholczyk, *Radio astrophysics. Nonthermal processes in galactic and extragalactic sources.*

253. K.-C. Pan, P. M. Ricker, R. E. Taam, *ApJ* **750**, 151 (2012).

254. Y.-C. Pan, M. Sullivan, K. Maguire, *et al.*, *MNRAS* **438**, 1391–1416 (2014).

255. J. T. Parrent, D. A. Howell, B. Friesen, *et al.*, *ApJ* **752**, L26 (2012).

256. J. T. Parrent, R. C. Thomas, R. A. Fesen, *et al.*, *ApJ* **732**, 30 (2011).

257. F. Patat, P. Chandra, R. Chevalier, *et al.*, *Science* **317**, 924– (2007).

258. B. Paxton, L. Bildsten, A. Dotter, *et al.*, *ApJS* **192**, 3 (2011).

259. R. Pereira, R. C. Thomas, G. Aldering, *et al.*, *A&A* **554**, A27 (2013).

260. S. Perlmutter, G. Aldering, G. Goldhaber, *et al.*, *ApJ* **517**, 565–586 (1999).

261. M. M. Phillips, *ApJ* **413**, L105–L108 (1993).

262. M. M. Phillips, P. Lira, N. B. Suntzeff, *et al.*, *AJ* **118**, 1766–1776 (1999).

263. W. Pietsch, *Astronomische Nachrichten* **331**, 187–+ (2010).

264. W. Pietsch, M. Henze, *Central Bureau Electronic Telegrams* **2187**, 2 (2010).

265. W. Pietsch, M. Henze, *The Astronomer's Telegram* **2435**, 1 (2010).

266. W. Pietsch, M. Henze, V. Burwitz, *et al.*, *Central Bureau Electronic Telegrams* **2343**, 2 (2010).

267. W. Pietsch, M. Henze, V. Burwitz, *et al.*, *Central Bureau Electronic Telegrams* **2347**, 1 (2010).

268. W. Pietsch, M. Henze, V. Burwitz, *et al.*, *Central Bureau Electronic Telegrams* **2582**, 3 (2010).

269. W. Pietsch, M. Henze, V. Burwitz, *et al.*, *The Astronomer's Telegram* **3001**, 1 (2010).

270. W. Pietsch, M. Henze, V. Burwitz, *et al.*, *The Astronomer's Telegram* **3076**, 1 (2010).

271. W. Pietsch, M. Henze, V. Burwitz, *et al.*, *The Astronomer's Telegram* **2713**, 1 (2010).

272. W. Pietsch, M. Henze, F. Haberl, V. Burwitz, *The Astronomer's Telegram* **3038**, 1 (2010).

273. W. Pietsch, M. Henze, F. Haberl, V. Burwitz, *The Astronomer's Telegram* **3061**, 1 (2010).

274. W. Pietsch, M. Henze, F. Haberl, V. Burwitz, *The Astronomer's Telegram* **3013**, 1 (2010).

275. W. Pietsch, J. Lloyd, M. Henze, *et al.*, *The Astronomer's Telegram* **2896**, 1 (2010).

276. W. Pietsch, J. Lloyd, M. Henze, *et al.*, *The Astronomer's Telegram* **2964**, 1 (2010).

277. W. Pietsch, P. Podigachoski, F. Haberl, *et al.*, *The Astronomer's Telegram* **2308**, 1 (2009).

278. W. Pietsch, P. Podigachoski, F. Haberl, *et al.*, *Central Bureau Electronic Telegrams* **2061**, 2 (2009).

279. A. L. Piro, *ApJ* **679**, 616–625 (2008).

280. A. L. Piro, *ApJ* **759**, 83 (2012).

281. A. L. Piro, *ApJ* **808**, L51 (2015).

282. A. L. Piro, P. Chang, N. N. Weinberg, *ApJ* **708**, 598–604 (2010).

283. A. L. Piro, V. S. Morozova, *ArXiv e-prints*, arXiv: `1512.03442 [astro-ph.HE]` (2015).

284. A. L. Piro, E. Nakar, *ApJ* **769**, 67 (2013).

285. A. L. Piro, E. Nakar, *ApJ* **784**, 85 (2014).

286. Planck Collaboration, P. A. Ade, N. Aghanim, *et al.*, *A&A* **571**, A16 (2014).

287. P. Podigachoski, M. Henze, W. Pietsch, *et al.*, *The Astronomer's Telegram* **2234**, 1 (2009).

288. P. Podigachoski, M. Henze, W. Pietsch, *et al.*, *Central Bureau Electronic Telegrams* **1971**, 1 (2009).

289. P. Podigachoski, W. Pietsch, M. Henze, *et al.*, *The Astronomer's Telegram* **2304**, 1 (2009).

290. P. Podigachoski, W. Pietsch, M. Henze, *et al.*, *Central Bureau Electronic Telegrams* **2058**, 2 (2009).

291. D. Poznanski, J. X. Prochaska, J. S. Bloom, *MNRAS* **426**, 1465–1474 (2012).

292. J. Prieto, R. Khan, P. Garnavich, J. Pagnini, T. Yusa, *Central Bureau Electronic Telegrams* **2594**, 1 (2010).

293. J. Prieto, R. Khan, P. Hornochova, *Central Bureau Electronic Telegrams* **2610**, 2 (2010).

294. I. Rabinak, E. Waxman, *ApJ* **728**, 63 (2011).

295. A. Rau, S. R. Kulkarni, N. M. Law, *et al.*, *PASP* **121**, 1334–1351 (2009).

296. J. T. Rayner, D. W. Toomey, P. M. Onaka, *et al.*, *PASP* **115**, 362–382 (2003).

297. U. Rebbapragada, B. Bue, P. R. Wozniak, presented at the American Astronomical Society Meeting Abstracts, vol. 225, p. 434.02.

298. T. A. Rector, G. H. Jacoby, D. L. Corbett, M. Denham, presented at the Bulletin of the American Astronomical Society, vol. 31, pp. 1420–1421.

299. A. Rest, D. Scolnic, R. J. Foley, *et al.*, *ApJ* **795**, 44 (2014).

300. M. W. Richmond, S. D. van Dyk, W. Ho, *et al.*, *AJ* **111**, 327 (1996).

301. A. G. Riess, A. V. Filippenko, P. Challis, *et al.*, *AJ* **116**, 1009–1038 (1998).

302. A. G. Riess, L.-G. Strolger, S. Casertano, *et al.*, *ApJ* **659**, 98–121 (2007).

303. A. G. Riess, L.-G. Strolger, J. Tonry, *et al.*, *ApJ* **600**, L163–L166 (2004).

304. P. Rodríguez-Gil, R. Ferrando, D. Rodríguez, *et al.*, *The Astronomer's Telegram* **2166**, 1 (2009).

305. A. Romadan, N. Whallon, W. Zheng, *et al.*, *The Astronomer's Telegram* **2840**, 1 (2010).

306. L. Rosino, *Annales d'Astrophysique* **27**, 498–505 (1964).

307. L. Rosino, *A&AS* **9**, 347 (1973).

308. L. Rosino, M. Capaccioli, M. D'Onofrio, M. della Valle, *AJ* **97**, 83–96 (1989).

309. A. Rubin, A. Gal-Yam, A. De Cia, *et al.*, *ApJ* **820**, 33 (2016).

310. I. Sagiv, A. Gal-Yam, E. O. Ofek, *et al.*, *AJ* **147**, 79 (2014).

311. H. Saio, K. Nomoto, *ApJ* **615**, 444–449 (2004).

312. H. Sana, S. E. de Mink, A. de Koter, *et al.*, *Science* **337**, 444 (2012).

313. R. J. Sault, P. J. Teuben, M. C. Wright, presented at the Astronomical Data Analysis Software and Systems IV, ed. by R. A. Shaw, H. E. Payne, J. J. Hayes, vol. 77, p. 433, eprint: `astro-ph/0612759`.

314. R. A. Scalzo, G. Aldering, P. Antilogus, *et al.*, *ApJ* **713**, 1073–1094 (2010).

315. R. A. Scalzo, M. Childress, B. Tucker, *et al.*, *MNRAS* **445**, 30–48 (2014).

316. R. A. Scalzo, A. J. Ruiter, S. A. Sim, *MNRAS* **445**, 2535–2544 (2014).

317. R. Scalzo, G. Aldering, P. Antilogus, *et al.*, *ApJ* **757**, 12 (2012).

318. R. Scalzo, G. Aldering, P. Antilogus, *et al.*, *MNRAS* **440**, 1498–1518 (2014).

319. B. E. Schaefer, *ApJS* **187**, 275–373 (2010).

320. E. F. Schlafly, D. P. Finkbeiner, *ApJ* **737**, 103 (2011).

321. D. J. Schlegel, D. P. Finkbeiner, M. Davis, *ApJ* **500**, 525–553 (1998).

322. M. Scodeggio, R. Giovanelli, M. P. Haynes, *AJ* **116**, 2728–2737 (1998).

323. A. W. Shafter, M. F. Bode, M. J. Darnley, R. Ciardullo, K. A. Misselt, *The Astronomer's Telegram* **3006**, 1 (2010).

324. A. W. Shafter, M. F. Bode, M. J. Darnley, *et al.*, *ApJ* **727**, 50–+ (2011).

325. A. W. Shafter, R. Ciardullo, M. F. Bode, M. J. Darnley, K. A. Misselt, *The Astronomer's Telegram* **2987**, 1 (2010).

326. A. W. Shafter, R. Ciardullo, M. F. Bode, M. J. Darnley, K. A. Misselt, *The Astronomer's Telegram* **2843**, 1 (2010).

327. A. W. Shafter, R. Ciardullo, M. F. Bode, M. J. Darnley, K. A. Misselt, *The Astronomer's Telegram* **2834**, 1 (2010).

328. A. W. Shafter, R. Ciardullo, M. J. Darnley, M. F. Bode, K. A. Misselt, *The Astronomer's Telegram* **3074**, 1 (2010).

329. A. W. Shafter, R. Ciardullo, M. J. Darnley, M. F. Bode, K. A. Misselt, *The Astronomer's Telegram* **2898**, 1 (2010).

330. A. W. Shafter, R. Ciardullo, M. J. Darnley, M. F. Bode, K. A. Misselt, *The Astronomer's Telegram* **2949**, 1 (2010).

331. A. W. Shafter, R. Ciardullo, M. J. Darnley, M. F. Bode, K. A. Misselt, *The Astronomer's Telegram* **2909**, 1 (2010).

332. A. W. Shafter, M. J. Darnley, K. Hornoch, *et al.*, *ApJ* **734**, 12 (2011).

333. A. W. Shafter, K. Hornoch, M. J. Darnley, *et al.*, *The Astronomer's Telegram* **3039**, 1 (2010).

334. A. W. Shafter, B. K. Irby, *ApJ* **563**, 749–767 (2001).

335. A. W. Shafter, R. M. Quimby, *ApJ* **671**, L121–L124 (2007).

336. B. J. Shappee, K. Z. Stanek, R. W. Pogge, P. M. Garnavich, *ApJ* **762**, L5 (2013).

337. A. S. Sharov, A. Alksnis, *Ap&SS* **180**, 273–286 (1991).

338. N. J. Shaviv, *MNRAS* **326**, 126–146 (2001).

339. M. H. Siegel, E. A. Hoversten, P. W. Roming, *et al.*, *ApJ* **725**, 1215–1225 (2010).

340. J. M. Silverman, A. V. Filippenko, *MNRAS* **425**, 1917–1933 (2012).

341. J. M. Silverman, M. Ganeshalingam, W. Li, *et al.*, *MNRAS* **410**, 585–611 (2011).

342. S. A. Sim, I. R. Seitenzahl, M. Kromer, *et al.*, *MNRAS* **436**, 333–347 (2013).

343. R. A. Simcoe, A. J. Burgasser, P. L. Schechter, *et al.*, *PASP* **125**, 270–286 (2013).

344. L. P. Singer, S. B. Cenko, M. M. Kasliwal, *et al.*, *ApJ* **776**, L34 (2013).

345. L. P. Singer, M. M. Kasliwal, S. B. Cenko, *et al.*, *ApJ* **806**, 52 (2015).

346. S. J. Smartt, *ARA&A* **47**, 63–106 (2009).

347. S. J. Smartt, *PASA* **32**, e016 (2015).

348. R. M. Smith, R. G. Dekany, C. Bebek, *et al.*, presented at the Ground-based and Airborne Instrumentation for Astronomy V, vol. 9147, p. 914779, DOI: 10.1117/12.2070014.

349. A. M. Soderberg, E. Berger, K. L. Page, *et al.*, *Nature* **453**, 469–474 (2008).

350. S. Srivastav, G. C. Anupama, D. K. Sahu, *MNRAS* **445**, 1932–1941 (2014).

351. V. Stanishev, A. Goobar, R. Amanullah, *et al.*, *ArXiv e-prints*, arXiv: 1505.07707 (2015).

352. S. Starrfield, W. M. Sparks, G. Shaviv, *ApJ* **325**, L35–L38 (1988).

353. A. Sternberg, A. Gal-Yam, J. D. Simon, *et al.*, *MNRAS* **443**, 1849–1860 (2014).

354. M. Stritzinger, P. Mazzali, M. M. Phillips, *et al.*, *ApJ* **696**, 713–728 (2009).

355. R. J. Strope, B. E. Schaefer, A. A. Henden, *AJ* **140**, 34–62 (2010).

356. M. Sullivan, J. Guy, A. Conley, *et al.*, *ApJ* **737**, 102 (2011).

357. G. Sun, Wenzhou, Zhejiang, X. Gao, *Central Bureau Electronic Telegrams* **2516**, 3 (2010).

358. D. A. Swartz, P. G. Sutherland, R. P. Harkness, *ApJ* **446**, 766 (1995).

359. A. Tamm, E. Tempel, P. Tenjes, *ArXiv e-prints*, arXiv: 0707.4375 (2007).

360. S. Taubenberger, S. Benetti, M. Childress, *et al.*, *MNRAS* **412**, 2735–2762 (2011).

361. S. Taubenberger, A. Pastorello, P. A. Mazzali, *et al.*, *MNRAS* **371**, 1459–1477 (2006).

362. R. C. Thomas, G. Aldering, P. Antilogus, *et al.*, *ApJ* **743**, 27 (2011).

363. R. C. Thomas, P. E. Nugent, J. C. Meza, *PASP* **123**, 237–248 (2011).

364. A. B. Tomaney, A. Crotts, A. Shafter, presented at the American Astronomical Society Meeting Abstracts, vol. 24, pp. 1237–+.

365. A. B. Tomaney, A. W. Shafter, *ApJS* **81**, 683–714 (1992).

366. S. Trudolyubov, W. Priedhorsky, *ApJ* **616**, 821–844 (2004).

367. R. B. Tully, L. Rizzi, E. J. Shaya, *et al.*, *AJ* **138**, 323–331 (2009).

368. P. G. Tuthill, J. D. Monnier, W. C. Danchi, *Nature* **398**, 487–489 (1999).

369. S. Valenti, N. Elias-Rosa, S. Taubenberger, *et al.*, *ApJ* **673**, L155 (2008).

370. S. Valenti, M. Fraser, S. Benetti, *et al.*, *MNRAS* **416**, 3138–3159 (2011).

371. F. Vilardell, I. Ribas, C. Jordi, E. L. Fitzpatrick, E. F. Guinan, *A&A* **509**, A70+ (2010).

372. J. Vinkó, K. Sárneczky, K. Takáts, *et al.*, *A&A* **546**, A12 (2012).

373. S. S. Vogt, S. L. Allen, B. C. Bigelow, *et al.*, presented at the Instrumentation in Astronomy VIII, ed. by D. L. Crawford, E. R. Craine, vol. 2198, p. 362.

374. R. M. Wagner, A. Kaur, A. Porter, *et al.*, *The Astronomer's Telegram* **6203** (2014).

375. M. G. Walker, M. Mateo, E. W. Olszewski, *et al.*, *ApJ* **667**, L53–L56 (2007).

376. B. Wang, Z. Han, *New A Rev.* **56**, 122–141 (2012).

377. E. Waxman, P. Mészáros, S. Campana, *ApJ* **667**, 351–357 (2007).

378. J. Whelan, I. Iben Jr., *ApJ* **186**, 1007–1014 (1973).

379. C. J. White, M. M. Kasliwal, P. E. Nugent, *et al.*, *ApJ* **799**, 52 (2015).

380. R. Williams, E. Mason, M. Della Valle, A. Ederoclite, *ApJ* **685**, 451–462 (2008).

381. A. Wirth, L. L. Smarr, T. L. Bruno, *ApJ* **290**, 140–153 (1985).

382. P. L. Wizinowich, J. Chin, E. Johansson, *et al.*, presented at the Society of Photo-Optical Instrumentation Engineers (SPIE) Conference Series, vol. 6272, p. 627209, DOI: 10.1117/12.672104.

383. R. C. Wolf, C. B. D'Andrea, R. R. Gupta, *et al.*, *ArXiv e-prints*, arXiv: 1602.02674 (2016).

384. M. Yamanaka, K. S. Kawabata, K. Kinugasa, *et al.*, *ApJ* **707**, L118–L122 (2009).

385. H. Yamaoka, K. Ayani, S. Honda, K. Kinugasa, *Central Bureau Electronic Telegrams* **1980**, 1 (2009).

386. O. Yaron, A. Gal-Yam, *PASP* **124**, 668–681 (2012).

387. N. Yasuda, M. Fukugita, *AJ* **139**, 39–52 (2010).

388. S.-C. Yoon, *PASA* **32**, e015 (2015).

389. S.-C. Yoon, G. Gräfener, J. S. Vink, A. Kozyreva, R. G. Izzard, *A&A* **544**, L11 (2012).

390. S.-C. Yoon, N. Langer, *A&A* **419**, 623–644 (2004).

391. S.-C. Yoon, N. Langer, *A&A* **435**, 967–985 (2005).

392. F. Yuan, R. M. Quimby, J. C. Wheeler, *et al.*, *ApJ* **715**, 1338–1343 (2010).

393. T. Yusa, *Central Bureau Electronic Telegrams* **2448**, 1 (2010).

394. T. Yusa, *Central Bureau Electronic Telegrams* **2472**, 1 (2010).

395. T. Yusa, *Central Bureau Electronic Telegrams* **2483**, 1 (2010).

396. T. Yusa, *Central Bureau Electronic Telegrams* **2582**, 6 (2010).

397. T. Yusa, *Central Bureau Electronic Telegrams* **2597**, 1 (2010).

398. W. Zheng, A. Romadan, N. Whallon, *et al.*, *Central Bureau Electronic Telegrams* **2574**, 1 (2010).

399. L. Zhou, X. Wang, K. Zhang, *et al.*, *Central Bureau Electronic Telegrams* **3543**, 1 (2013).